Tracing impurities and illuminating their impact

Surveying and characterizing liquid argon with LLAMA for LEGEND and beyond

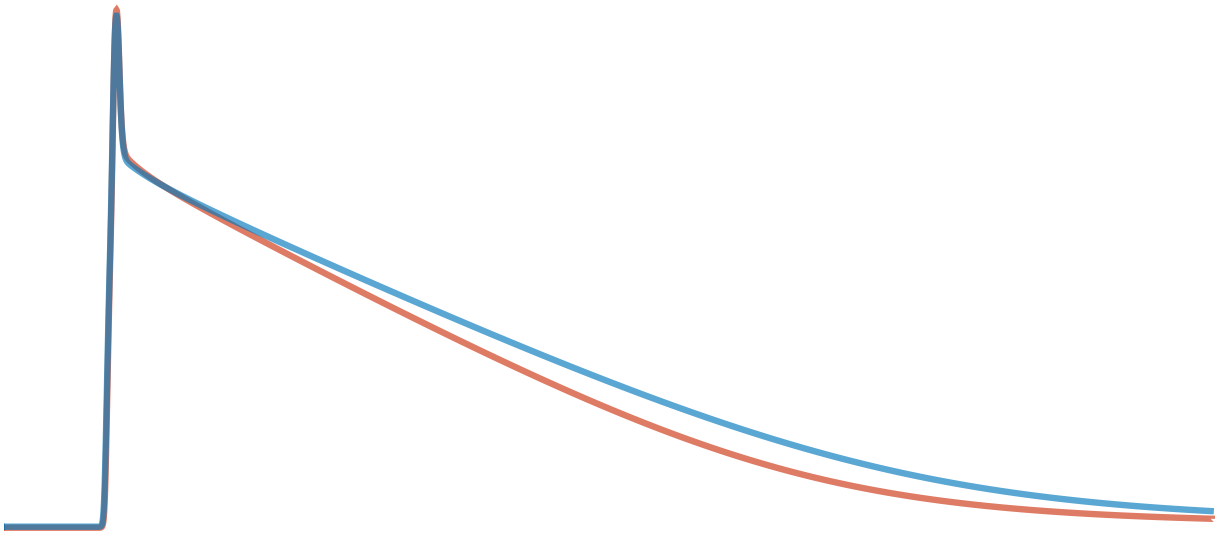

Mario Schwarz

2024

TECHNISCHE UNIVERSITÄT MÜNCHEN

TUM School of Natural Sciences

Tracing impurities and illuminating their impact: Surveying and characterizing liquid argon with LLAMA for LEGEND and beyond

Mario Schwarz

Vollständiger Abdruck der von der TUM School of Natural Sciences der Technischen Universität München zur Erlangung des akademischen Grades eines

Doktors der Naturwissenschaften (Dr. rer. nat.)

genehmigten Dissertation.

Vorsitz:	Prof. Dr. Alejandro Ibarra
Prüfer der Dissertation:	1. Prof. Dr. Stefan Schönert
	2. Priv.-Doz. Dr. Béla Majorovits

Die Dissertation wurde am 03.05.2024 bei der Technischen Universität München eingereicht und durch die TUM School of Natural Sciences am 18.06.2024 angenommen.

Abstract

The matter-antimatter asymmetry of the universe constitutes a critical yet unresolved question bridging cosmology and particle physics. A discovery of neutrinoless double beta ($0\nu\beta\beta$) decay would shed light on this puzzle, as it would be an unambiguous detection of a process creating matter unbalanced by antimatter. This observation would further imply that neutrinos are Majorana particles, i.e. identical to antineutrinos. Thus motivated, the search for this decay is being conducted with great effort. LEGEND pursues this search using high-purity germanium detectors enriched in the $0\nu\beta\beta$ decay candidate isotope ^{76}Ge. The germanium detectors are suspended in a scintillating liquid argon (LAr) volume. The LAr features a light readout instrumentation, transforming it into a full-fledged detector: a vital building block of LEGEND's background reduction scheme.

Variable quantities of trace impurities affect the LAr detector by altering LAr's key optical properties: the light yield, the effective triplet lifetime, and the attenuation length for its own scintillation light. A continuous model of the response and performance of the LAr detector requires permanent knowledge of these parameters. To this end, the dedicated LEGEND Liquid Argon Monitoring Apparatus (LLAMA) was developed and integrated into LEGEND-200. LLAMA constitutes the main part of this dissertation work. During the commissioning of LEGEND-200, impurities were introduced by frequent payload insertions. LLAMA evaluated the introduced absorption, leading to an additional component of the absorption length of $l_{abs} = (5.2 \pm 1.8)\,\mathrm{m}$. At the same time, the introduced quenching is limited to $< 4\,\%$. The subsequent undisturbed LEGEND-200 data-taking phase has stable LAr properties. Under these conditions, LLAMA limited the potential decrease in light intensity to less than 10 % over 4 years. Moreover, LLAMA proved to be a valuable quality control system during cryostat filling, saving the experiment from an excessive influx of nitrogen. Based on this data, nitrogen-doped LAr was studied in the sub-ppm regime, deriving an unprecedentedly precise quenching rate constant of $k_{Q,\mathrm{N}_2} = (0.120 \pm 0.007)\,\mu\mathrm{s}^{-1}\,\mathrm{ppm}^{-1}$. Furthermore, the scintillation time profile of purified LAr was investigated, providing evidence for an intermediate component currently disputed in literature. Its relative contribution and the recombination time are $I_i/I_{sig} = 0.08 \pm 0.03$ and $\tau_{rec} = (290 \pm 140)\,\mathrm{ns}$, respectively. Additionally, in dedicated measurements in a test cryostat, the impact of xenon doping on the aforementioned optical properties was observed. The comprehensive understanding of LAr properties gained by LLAMA is crucial for the optical model of LEGEND-200 and, hence, to the upcoming physics analysis, informs the next-generation LEGEND-1000 stage, and profits other large-scale LAr detectors. Its successful operation supports further applications of LLAMA in LEGEND-1000 and beyond.

A further part of this dissertation discusses ordinary muon capture for nuclear theory of $0\nu\beta\beta$ decay with MONUMENT. This experiment employs the so-called ALPACA data acquisition (DAQ) system, incorporating the DAQ software originally developed for LLAMA. ALPACA distinguishes itself through its trigger scheme and offline analysis approach from another DAQ system that works in parallel. Its performance during the 2021 measurement campaign is described in this dissertation.

Zusammenfassung

Die Asymmetrie zwischen Materie und Antimaterie im Universum stellt eine entscheidende ungelöste Frage in der Kosmologie und Teilchenphysik dar. Eine Entdeckung des neutrinolosen doppelten Betazerfalls ($0\nu\beta\beta$-Zerfall) würde Licht in das Rätsel bringen, da es ein Prozesses ist, welcher Materie ohne Ausgleich durch Antimaterie erzeugt. Außerdem würde es zeigen, dass Neutrinos Majorana-Teilchen sind, d.h. identisch mit ihren Antiteilchen sind. Die Suche nach diesen Zerfall wird daher mit großem Aufwand betrieben. LEGEND führt die Suche mit hochreinen Germaniumdetektoren durch, die mit dem $0\nu\beta\beta$-Zerfallskandidaten ^{76}Ge angereichert sind. Die Detektoren befinden sich in einem szintillierenden Flüssigargon(LAr)-Volumen. Die Licht-detektierende Instrumentierung im LAr verwandelt es in einen vollwertigen Detektor: ein unverzichtbarer Baustein für die Hintergrundreduktion in LEGEND.

Veränderliche Mengen an Spurenverunreinigungen beeinflussen den LAr-Detektor indem sie optische Eigenschaften des LAr verändern: die Lichtausbeute, die effektive Triplett-Lebensdauer und die Abschwächlänge für das eigene Szintillationslicht. Ein fortwährendes Modell für die Reaktion und die Performanz des LAr-Detektors benötigt ständiges Wissen über diese Parameter. Zu diesem Zweck wurde LLAMA (LEGEND Liquid Argon Monitoring Apparatus) eigens entwickelt und in LEGEND-200 eingebaut. LLAMA stellt den Hauptteil dieser Dissertation dar. Während der Inbetriebnahme von LEGEND-200 wurden durch häufige Einbringungen des Detektor-Arrays Verunreinigungen eingetragen. LLAMA ermittelte die verstärkte Absorption, die einer zusätzlichen Absorptionslänge von $l_{abs} = (5.2 \pm 1.8)\,\mathrm{m}$ entspricht. Das Quenching konnte dabei auf $< 4\,\%$ limitiert werden. Die anschließende Datennahmephase von LEGEND-200 hat stabile LAr-Eigenschaften. Unter diesen Bedingungen limitierte LLAMA die mögliche Reduktion der Lichtintensität auf weniger als 10 % über 4 Jahre. Darüber hinaus bewies sich LLAMA als wertvolles Qualitätskontrollsystem während des Füllens des Kryostaten, wobei es das Experiment vor einem starken Zufluss an Stickstoff bewahrte. Basierend auf diesen Daten wurde Stickstoff-gedoptes LAr im sub-ppm-Bereich studiert, wobei eine präzise Quenching-Rate von $k_{Q,\mathrm{N}_2} = (0.120{\pm}0.007)\,\mu\mathrm{s}^{-1}\,\mathrm{ppm}^{-1}$ ermittelt wurde. Außerdem wurde das Zeitspektrum von gereinigtem LAr untersucht und dabei die sog. Intermediate-Komponente nachgewiesen, dessen Existenz gegenwärtig umstritten ist. Für dessen Anteil und die Rekombinationsdauer wurden $I_i/I_{sig} = 0.08 \pm 0.03$ bzw. $\tau_{rec} = (290 \pm 140)\,\mathrm{ns}$ gemessen. Zusätzlich wurde in Messungen in einem Test-Kryostaten der Einfluss von Xenon auf die bereits erwähnten optischen Eigenschaften ermittelt. Das durch LLAMA gewonnene umfassende Verständnis von LAr-Eigenschaften ist wichtig für das optische Modell und die Analyse von LEGEND-200, und informiert die LEGEND-1000-Stufe und weitere Anwendungen großskaliger LAr-Detektoren. Der erfolgreiche Betrieb von LLAMA unterstützt weitere Anwendungen von LLAMA in LEGEND-1000 und darüber hinaus.

Ein weiterer Teil dieser Dissertation diskutiert den gewöhnlichen Myoneneinfang für die Theorie der Kernphysik im $0\nu\beta\beta$-Zerfall mit MONUMENT. Dieses Experiment benutzt das sog. ALPACA-Datenaufzeichnungs(DAQ)-System, das die ursprünglich für LLAMA entwickelte DAQ-Software inkorporiert. ALPACA unterscheidet sich durch sein Triggerschema und die Offline-Analyse von einem parallelen DAQ-System. Seine Performanz während der Messkampagne 2021 ist in dieser Dissertation beschrieben.

Contents

Part I

Physics of the neutrinoless double beta decay

Chapter 1

Neutrinos in and beyond the Standard Model

The universe contains matter, forming galaxies, stars, and planets. Matter vastly dominates over the negligible antimatter fraction, as observed by several studies [1–3]. This asymmetry constitutes an outstanding and challenging open question in particle physics and cosmology since all physics processes observed so far yield a perfect balance between matter and antimatter, both for their creation and destruction [4].

The Standard Model of particle physics respects the global $B-L$ symmetry, with the baryon number B and the lepton number L, and thus allows to distinguish between matter and antimatter[1] [4]. Hence, any answer to the asymmetry question has to lie beyond the Standard Model. Regarding beyond-Standard-Model (BSM) physics, neutrino oscillations already demonstrated the violation of both other global symmetries in the Standard Model: $L_e - L_\mu$ and $L_\mu - L_\tau$. Also, neutrinos are perfectly suited to provide a portal between matter and antimatter. They are the only fermions in the Standard Model lacking both charge and a magnetic moment and thus might be their own antiparticles, in which case L is violated and hence $B-L$ is broken.

Neutrinoless double beta ($0\nu\beta\beta$) decay provides a direct experimental probe for these properties; hence, the search for it is of paramount interest for the field [4]. The current chapter summarizes[2] the properties of the neutrino in and beyond the Standard Model, and concludes with theory aspects of the $0\nu\beta\beta$ decay, including a description of relevant

[1] Both B and L individually are not expected to be exactly obeyed, as they are not exact symmetries (so-called *anomalous symmetries*) and are thus violated by quantum fluctuations [4].

[2] The summary is focused on critical aspects relevant for later parts of this dissertation. A more comprehensive description can be found e.g. in [5].

nuclear structure theory. Experimental aspects of the $0\nu\beta\beta$ decay search are covered in the following chapter, which combines general considerations with present and future efforts in real-world applications.

1.1 History and theory

Intriguingly, the neutrino, a superior candidate for shedding light on the matter-antimatter asymmetry puzzle, was first postulated to solve other fundamental particle physics problems. In 1930, Pauli proposed a new particle - the neutrino - to restore energy conservation in beta decays [6]. Fermi then embedded it into his theory of beta decay [7].

In current knowledge, three *flavors* of neutrinos exist, in analogy to charged leptons and quarks. The first experimental discovery of neutrinos succeeded in 1956 by Cowan and Reines [8], by detecting electron (anti)neutrinos. Later, in 1962, Lederman, Schwartz, and Steinberger discovered the muon neutrino [9], and at last, the tau neutrino was observed by the DONUT collaboration in 2000 [10].

1.1.1 Mass mechanisms

In the Standard Model, neutrinos are spin-1/2 particles described by four-component wavefunctions $\psi(x)$ solving the Dirac equation. A priori, these four components distinguish particles and antiparticles, as well as two helicities. So far, the formalism equals the one of charged leptons.

The fundamental difference is brought up by the fact that only left-handed neutrinos (ν_L) and right-handed antineutrinos ($\bar{\nu}_R$) exist in the Standard Model, as only those take part in the weak interaction. This has immediate consequences for the mass generation mechanism. From the Dirac equation, the Dirac mass term can be derived as:

$$\mathscr{L} = m_D \bar{\psi}\psi = m_D \left(\bar{\psi}_L \psi_R + \bar{\psi}_R \psi_L\right). \tag{1.1}$$

Thus, neutrinos cannot acquire a Dirac mass in the Standard Model, as both chiral states would have to exist, each for both neutrinos and antineutrinos.

However, the discovery of neutrino oscillation (further mentioned later) gives evidence for non-zero neutrino masses, and thus, a mass mechanism is required. A minimal

Standard Model extension is possible, in which a right-handed neutrino and left-handed antineutrino are added, in which case m_D can be generated by Yukawa couplings to the Higgs field. Though possible, this mechanism is disfavored as the associated coupling strength would be around twelve orders of magnitude smaller than the one of any other Standard Model particle [11].

Conversely, the Majorana mass term is a supreme candidate for the new mass-generating mechanism and can be expressed as:

$$\mathscr{L} = \frac{1}{2} m_M \bar{\psi} \psi^C + h.c., \tag{1.2}$$

where ψ^C is the charge-conjugated version of ψ and $h.c.$ denotes the Hermitian conjugate. The existence of this term would require the neutrino to be a Majorana particle, i.e. being identical to its own antiparticle.

The Dirac-Majorana mass term provides a generalization:

$$\mathscr{L} = \frac{1}{2} \begin{pmatrix} \bar{\psi}_L & \bar{\psi}_L^C \end{pmatrix} \begin{pmatrix} m_L & m_D \\ m_D & m_R \end{pmatrix} \begin{pmatrix} \psi_R^C \\ \psi_R \end{pmatrix} + h.c., \tag{1.3}$$

from which Dirac and Majorana mass terms can be recovered by demanding $m_R = m_L = 0$ and $m_D = 0$, respectively.

One can identify neutrino states in the role they take in the weak interaction: active neutrinos ($\nu_L = \psi_L$ and $\nu_R^C = \psi_R^C$) and sterile neutrinos ($N_R = \psi_R$ and $N_L^C = \psi_L^C$). Now, one can require $m_L = 0$ and $m_R \gg m_D$. This generates two very different neutrino masses:

$$m_\nu \approx \frac{m_D^2}{m_R}, \quad m_N \approx m_R. \tag{1.4}$$

This is the so-called *seesaw* mechanism, which explains the smallness of active neutrino masses while allowing for m_D to share the mass scale of all other fermions [12, 13].

1.1.2 Neutrino mixing and mass ordering

Before continuing with experimental probes for a Majorana nature of neutrinos, neutrino mixing and mass ordering are introduced to provide a basis for the mass observables required in the later explanations.

Neutrino oscillation[3], i.e. the change of a given neutrino's flavor state while traveling, was observed in several independent experiments, e.g. [14–18]. Following from this, it is known that neutrino flavor eigenstates are a mixture of the mass eigenstates and that the differences between the mass eigenvalues are non-vanishing. The unitary Pontecorvo–Maki–Nakagawa–Sakata (PMNS) matrix describes the flavor eigenstates ν_α, $\alpha \in e, \mu, \tau$ as a mixture of three mass eigenstates ν_i, $i \in 1, 2, 3$ [19]:

$$\nu_\alpha = \sum_i U_{\alpha i} \nu_i. \tag{1.5}$$

The PMNS matrix can be fully parametrized by three mixing angles (θ_{12}, θ_{13} and θ_{23}), and three CP-violating phases (δ, α and β). Only δ has physical meaning regardless of the neutrino nature. Conversely, α and β are only relevant in the case of Majorana neutrinos and can be absorbed into the other terms in the case of Dirac neutrinos.

Neutrino oscillation experiments yield results of the mass squared differences $\Delta m^2_{ij} = m^2_i - m^2_j$. Additionally, the sign of Δm_{21} is known from adiabatic flavor conversions within the sun [20, 21]. The sign of Δm_{31} is unknown, which allows for two possible constellations: the *normal ordering* $m_1 < m_2 < m_3$ and the *inverted ordering* $m_3 < m_1 < m_2$. Currently, global fits favor normal ordering at $\approx 2.5\sigma$ [22, 23].

1.2 Double beta decay with and without neutrino emission

Returning to the quest for solving the matter-antimatter asymmetry puzzle, discovering a Majorana character of neutrinos would imply the violation of L conservation and further $B - L$, the only remaining global symmetry of the Standard Model. Neutrinoless double beta ($0\nu\beta\beta$) decay provides the most promising probe for the Majorana nature of neutrinos, and the process can be expressed as[4]:

$${}^A X_Z \rightarrow {}^A Y_{Z+2} + 2\, e^-. \tag{1.6}$$

[3] For an overview about neutrino oscillation, see e.g. [5].

[4] Precisely, the shown process is the $0\nu\beta^-\beta^-$ decay. Additionally, $0\nu\beta^+\beta^+$, $0\nu\beta^+$EC and 0νECEC processes potentially exist but are studied less intensively. For a review, see [24].

This decay was first proposed by Furry in 1939 [25] and violates the lepton number conservation by two units. To stress its importance, the term "creation of matter without antimatter" is coined for this process [4]. Its experimental discovery is thus of paramount interest to the field and is pursued by several experiments around the globe. Chapter 2 discusses experimental efforts further.

$0\nu\beta\beta$ decay competes with the two-neutrino double beta ($2\nu\beta\beta$) decay

$$ {}^{A}X_{Z} \rightarrow {}^{A}Y_{Z+2} + 2\,e^{-} + 2\,\bar{\nu}_{e}, \tag{1.7} $$

which was first conceived by Goeppert-Mayer in 1935 [26] and is allowed by the Standard Model, though suppressed due to being a second-order weak process with half-lives ranging from 10^{18} to 10^{24} years [27]. Nevertheless, it has already been observed, first in ^{82}Se [28] and succeedingly by different groups and experiments in several isotopes [29–34]. The general name double beta ($\beta\beta$) decay is introduced here and addresses both $0\nu\beta\beta$ and $2\nu\beta\beta$ decays.

An observation of $\beta\beta$ decay and thus $0\nu\beta\beta$ decay is only possible for certain isotopes. First, the decay itself has to be energetically allowed. Second, single beta decay has to be forbidden or strongly suppressed[5], as they would compete with $\beta\beta$ decay, which is a second order weak process. Typically, $0\nu\beta\beta$ decay candidate isotopes have even numbers of protons and neutrons (even-even), as they are more strongly bound than the odd-odd daughter of a hypothetical beta decay but can be less strongly bound than the even-even second neighbor.

As an example, figure 1.1 shows the mass parabulas for even-even and odd-odd nuclei of $A = 76$ isobars for the $0\nu\beta\beta$ candidate isotope ^{76}Ge. Single beta decays are forbidden, while $\beta\beta$ decays are allowed and have a Q-value of $Q_{\beta\beta}$.

Figure 1.2a shows the Feynman diagram of the $2\nu\beta\beta$ decay, which effectively equals two simultaneous beta decays. Figure 1.2b sketches the $0\nu\beta\beta$ decay mediated by the virtual exchange of light Majorana neutrinos. This process constitutes the minimal extension of the Standard Model necessary for allowing $0\nu\beta\beta$ decay. All light neutrino mass eigenstates contribute to the neutrino propagator, and each mass m_i gives the amount of opposite helicity required. Thus, the so-called effective Majorana neutrino

[5] A large mismatch in total angular momentum between the initial and final nucleus can suppress beta decay to rates comparable to $\beta\beta$ decay [35].

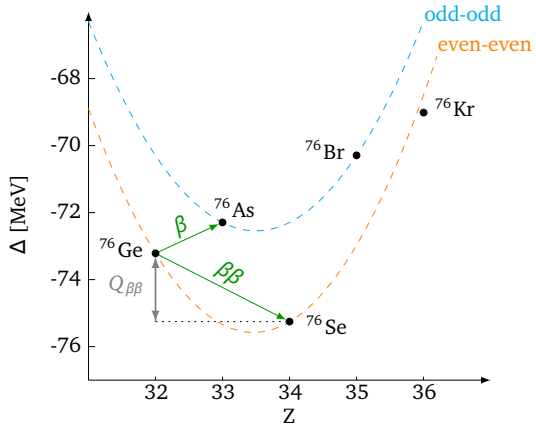

Figure 1.1: Mass excess $\Delta = (m_A - A)\,u$ for nuclei of mass number $A = 76$ and mass m_A, with u denoting the atomic mass unit. The single beta decay of the $0\nu\beta\beta$ candidate isotope ^{76}Ge is energetically forbidden, while a double beta decay is possible. Taken from [4].

mass, commonly written as

$$m_{\beta\beta} = \left| \sum_i U_{ei}^2 \, m_i \right|, \tag{1.8}$$

contributes linearly to the amplitude of $0\nu\beta\beta$ decay.

The term can be expanded to

$$m_{\beta\beta} = \left| m_1 \, |U_{e1}|^2 + m_2 \, e^{2i\alpha} \, |U_{e2}|^2 + m_3 \, e^{2i\beta} \, |U_{e3}|^2 \right|, \tag{1.9}$$

which makes the impact of both Majorana phases α and β explicit. In principle, full cancellation is possible for normal ordering and in a certain mass range of m_1; however, at the cost of fine-tuning.

Though light neutrino exchange likely contributes dominantly to $0\nu\beta\beta$ decay [4], other lepton number non-conserving BSM physics processes possibly contribute. The so-called *black box* or *Schechter-Valle* theorem provides a mechanism for particle-antiparticle transition for any operator leading to $0\nu\beta\beta$ decay [36]. However, the neutrino mass induced by this mechanism is too small to solely explain neutrino masses [37].

Fermi's golden rule allows to derive the rate $\Gamma^{0\nu}$ and half-live $T_{1/2}^{0\nu}$ in case of several

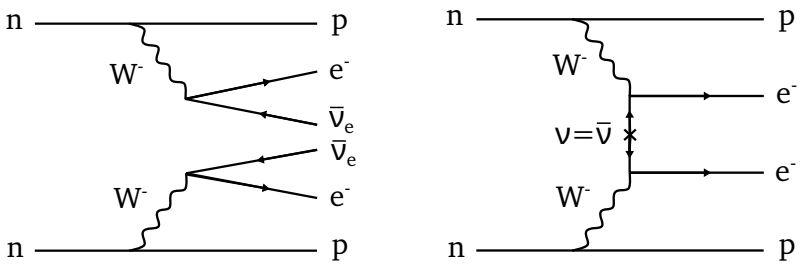

(a) $2\nu\beta\beta$ decay.

(b) $0\nu\beta\beta$ decay mediated by light neutrino exchange.

Figure 1.2

BSM mechanisms i at scale Λ leading to $0\nu\beta\beta$ decay [4]:

$$\frac{\Gamma^{0\nu}}{\ln(2)} = \frac{1}{T^{0\nu}_{1/2}} = \sum_i \mathcal{G}_i \, g_i^4 \, |\mathcal{M}_i|^2 \, f_i(\Lambda) + \text{interference terms.} \tag{1.10}$$

Here, $\mathcal{G}_i$ denote the phase space factors, g_i are the hadronic matrix elements, and $\mathcal{M}_i$ are the nuclear matrix elements (NMEs). $f_i(\Lambda)$ are dimensionless functions encompassing the individual strengths of BSM physics.

In case of only light neutrino exchange, the formula simplifies to:

$$\frac{1}{T^{0\nu}_{1/2}} = \mathcal{G}^{0\nu} \, g_A^4 \, |\mathcal{M}^{0\nu}|^2 \, \frac{m^2_{\beta\beta}}{m^2_e}, \tag{1.11}$$

where g_A is the axial vector coupling constant, and both $\mathcal{G}^{0\nu}$ and $\mathcal{M}^{0\nu}$ are specific to light neutrino exchange. While $\mathcal{G}^{0\nu}$ can be calculated with high precision [38, 39], the NMEs, and potentially g_A, currently carry large uncertainties. These values are essential, as equation 1.11 is required to convert experimental isotope-specific sensitivities, limits, and possibly results of $T^{0\nu}_{1/2}$ into the absolute $m_{\beta\beta}$ scale, facilitating comparisons. Details about the motivation, challenges, and efforts of nuclear theory to provide these quantities are further addressed in section 1.3.

1.2.1 Neutrino mass observables

Predictions on $m_{\beta\beta}$ are crucial for designing $0\nu\beta\beta$ decay experiments. Equation 1.9 contains seven degrees of freedom for calculating $m_{\beta\beta}$: the mixing angles θ_{12} and θ_{13},

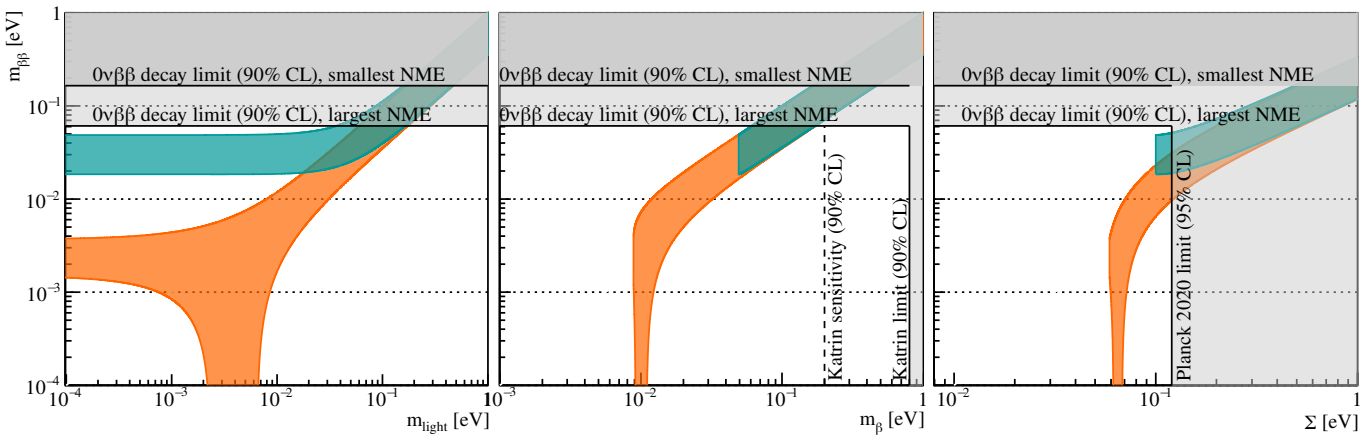

Figure 1.3: Maximally allowed parameter space for $m_{\beta\beta}$ parametrized by either m_{light}, m_β or Σ. Orange and green shaded areas refer to normal and inverted ordering, respectively. The central values of neutrino oscillation parameters from [41] are used. Grey areas are excluded by current experiments (see text). Taken from [4].

both Majorana phases as well as all three neutrino masses [4]. Neutrino oscillation experiments allow constraining only four of those - both mixing angles, as well as two mass squared differences - leaving three degrees of freedom fully unbound. Until the neutrino mass ordering is identified, it constitutes another free parameter.

Predictions on $m_{\beta\beta}$ based on the remaining degrees of freedom were first done by Vissani [40]. The maximally allowed parameter range for $m_{\beta\beta}$ is obtained by leaving both Majorana phases unconstrained. Commonly, the lightest neutrino mass m_{light} parametrizes the remaining degree of freedom.

The left plot of figure 1.3 shows the entire parameter range using this parametrization. The results for normal and inverted orderings are drawn in orange and green, respectively. Grey areas show current exclusion limits from $0\nu\beta\beta$ decay experiments, here KamLAND-Zen [42], with different NME assumptions.

Parametrizing the allowed parameter space using other neutrino mass observables demonstrates the exciting synergy with different types of experiments. Beta decay endpoint studies use kinematics of the beta decay to constrain the effective (electron)

neutrino mass m_β, defined as

$$m_\beta = \sqrt{\sum_i |U_{ei}^2|\, m_i^2}. \tag{1.12}$$

Currently, KATRIN is leading the field with the current best limit being 0.8 eV (90 % C.L.) [43]; the final sensitivity goal is 0.2 eV [44]. The interplay of m_β with $m_{\beta\beta}$ is shown in the center panel of figure 1.3, also marking the current limit and sensitivity of KATRIN. As of now, $0\nu\beta\beta$ decay excludes the parameter range probed by KATRIN, and any measurement of m_β in this region would disfavor light neutrino exchange mediating $0\nu\beta\beta$ decay [4].

Another bound is set by cosmology because neutrinos impact large-scale structure formation, which imprints on Baryon Acoustic Oscillation (BAO) power spectra of the Cosmic Microwave Background (CMB) [45]. Constraints from cosmology must be taken with a grain of salt, for they depend on the Standard Model of cosmology, ΛCDM. The current limit from Planck [46] is $\Sigma < 0.12\,\text{eV}$. It has to be noted that a lower bound[6] exists at $\Sigma > 0.059\,\text{eV}$, hence upcoming surveys will measure Σ given that ΛCDM and Standard Model assumptions hold [4]. This bound refers to the normal ordering scenario; inverted ordering is only possible for $\Sigma > 0.10\,\text{eV}$, i.e. inverted ordering gets disfavored in case a lower Σ is measured [47]. Figure 1.3 (right panel) shows the relation to $m_{\beta\beta}$ and predicts, that a measurement of Σ close to the current limit would force $m_{\beta\beta}$ above 10 meV, i.e. in reach for next-generation experiments in case of favorable NMEs [4].

Next-generation $0\nu\beta\beta$ decay experiments target discovery and will fully cover the parameter space of the inverted ordering scenario, which extends down to $(18.4 \pm 1.3)\,\text{meV}$ [48]. At the same time, a significant fraction of the parameter space allowed for normal ordering will be probed. As previously stated, $m_{\beta\beta}$ has no lower bound for normal ordering since fine-tuned Majorana phases can make it vanish for a patricular mass range. However, it has to be noted that the double-logarithmic representation in figure 1.3 might over-emphasize low $m_{\beta\beta}$ [4].

Future $0\nu\beta\beta$ decay experiments demand profound predictions on the probability distribution of $m_{\beta\beta}$, especially for the slightly favored normal ordering scenario. These require, however, several assumptions on prior distributions. For example, demanding

[6] Lower bounds for normal and inverted ordering assume central values for neutrino oscillation parameters from [41].

flat priors on the Majorana phases disfavors vanishing $m_{\beta\beta}$ values [49]. Additionally, a model-dependent study by [4] uses the solar and atmospheric neutrino mass scales to motivate $m_{\beta\beta}$ values in the range from 8 meV to 10 meV. This region "can constitute a challenging, and yet conceivable goal for the experimental community" [4].

1.3 Nuclear structure effects

1.3.1 Nuclear models

Going back to equation 1.11, one remembers that a relation from $m_{\beta\beta}$ to the experimentally accessible $T^{0\nu}_{1/2}$ requires knowledge of nuclear properties. Designing $0\nu\beta\beta$ decay experiments hence relies on these quantities for several reasons [50]:

- The exposure required for reaching a certain $m_{\beta\beta}$ goal needs to be estimated.
- NMEs facilitate selecting a $0\nu\beta\beta$ decay candidate isotope based on its expected half-live.
- Once a $T^{0\nu}_{1/2}$ is measured, NMEs are needed to accurately derive the neutrino mass scale.

High-precision results on $\mathcal{G}^{0\nu}$ are available and thus are no concern [38, 39]. Conversely, NMEs and a potentially quenched g_A carry large uncertainties and must be addressed.

NMEs depend on the wavefunctions of the parent and daughter nuclei, the virtual states of the intermediate nucleus, and the specific $0\nu\beta\beta$ decay process. Since $0\nu\beta\beta$ decay has not been observed so far and the $0\nu\beta\beta$ decay parameters are unknown, NMEs have to be derived through theoretical nuclear structure calculations. Most $0\nu\beta\beta$ decay candidate isotopes contain a medium-to-high number of nucleons and thus NME calculations employ many-body calculations, which use different approximations and truncations. The following compiles summaries of the usual approaches, while a comprehensive discussion is available in [50]:

- The nuclear shell model (NSM) is a standard technique to describe medium-to-heavy nuclei [51, 52]. It restricts itself to treating nucleons close to the Fermi surface but features the full set of correlations between them. Commonly, a single harmonic oscillator shell is used, which fails to cover all states required to fully

describe proton-neutron pairing correlations, which have significant impacts on $0\nu\beta\beta$ decay [50, 53]. Recently, calculations with two oscillator shells tackled the problem and showed moderate enhancements of NMEs [54].

- While the quasiparticle random phase approximation (QRPA) overcomes the NSM's limitation of handling a restricted set of states, it covers only a reduced set of correlations, modeled as particle-hole excitations [50]. Apart from the missing correlations, deformations of nuclei are also usually not treated. Only recently, deformations are included in calculations leading to reduced NMEs [55], which are, however, presumably under-estimated as they lack mixing of deformation states [4].

- Energy-density functional (EDF) theory yields ground state properties by minimizing an energy density functional and allows for a mean-field description [4, 50]. Currently, NMEs are overestimated due to missing correlations [4, 50] including proton-neutron pairing [56], which can be handled by an approach proposed by [57].

- The interacting boson model (IBM) treats pairs of nucleons as bosons, and its variant IBM-II distinguishes between neutrons and protons and is used to calculate $0\nu\beta\beta$ decay NMEs [50]. Like the NSM and the EDF theory, missing proton-neutron pairing correlations lead to overestimated NMEs [4] and are included in [58].

In conclusion, all phenomenological models implement simplifications required to describe medium-to-heavy nuclei, impacting the resulting NMEs.

Recently, ab initio methods become powerful enough to provide $0\nu\beta\beta$ decay NMEs even for medium-to-heavy nuclei used in experiments. They build models from first principles, treating all nucleons in a nucleus explicitly and with realistic nuclear forces [4]. As the complexity scales with the number of nucleons, more methods are available for lighter nuclei than heavier ones. Currently, three ab initio approaches are successfully applied to ^{48}Ca, the lightest $0\nu\beta\beta$ decay candidate usable in experiments: the in-medium generator coordinate method (IM-GCM) [59], the valence-space formulation of the in-medium similarity renormalization group (VS-IMSRG) [60] and coupled-cluster (CC) theory [61]. The results agree within uncertainties [62].

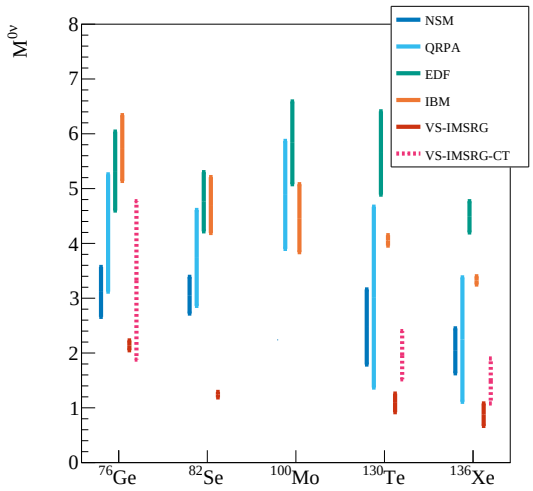

Figure 1.4: Ranges of NMEs for light neutrino exchange derived by different many-body methods. No g_A quenching is assumed. Continuous (dashed) lines indicate models using the long-range component only (long-range and contact term combined). Data sources for phenomenological methods: NSM: [64–66]; QRPA: [55, 67–69]; EDF theory: [70–72] and IBM: [73, 74], from which [73] contains a modification [4] suggested by [74]. Ab initio results using VS-IMSRG (long range only): ^{76}Ge and ^{82}Se: [60]; ^{130}Te and ^{136}Xe: [63]. Calculations including the contact term ("VS-IMSRG-CT"): ^{76}Ge: [62] (VS-IMSRG & IM-GCM); ^{130}Te and ^{136}Xe: [63] (VS-IMSRG).

For ^{76}Ge, two methods are applied so far, IM-GCM and VS-IMSRG, from which uncertainties stemming from the many-body method are obtained [62]. Only VS-IMSRG has been performed for ^{130}Te and ^{136}Xe to date [63].

Figure[7] 1.4 shows ranges encompassing the spread of all values of individual NME calculation methods and isotopes. Isotopes selected for the plot are under consideration for next-generation $0\nu\beta\beta$ decay experiments [4].

[7] This figure, as well as the majority of all figures in this work, use the "vibrant" color scheme from Paul Tol, which is apt for color-blind vision: `https://personal.sron.nl/~pault/`

1.3.2 Novel short-range contribution and g_A quenching

The matrix element can be split into a long-range and a short-range component:

$$\mathcal{M}^{0\nu} = \mathcal{M}^{0\nu}_{\text{long}} + \mathcal{M}^{0\nu}_{\text{short}}. \tag{1.13}$$

Traditionally, only the long-range component is used, as for all models marked with continuous lines in figure 1.4. However, [75, 76] introduced a novel short-range contact term, which may be a leading-order contribution [4]. Currently, ab initio calculations by [62, 63] include the contact term for NMEs of ^{130}Te, ^{136}Xe and ^{76}Ge; they are drawn in dashed in figure 1.4.

The figure further assumes an unquenched g_A value. A phenomenological correction $g_A \approx 1.27$ to an effective value g_A^{eff} was introduced to describe beta decay rates [77]. There, g_A is quenched to around 70 % of its "bare" value, and the factor depends on the mass number of the decaying nucleus [50]. As long as the source of the quenching is unknown, it is unclear whether it applies to $0\nu\beta\beta$ decay, leaving the possibility that its rate is strongly reduced, as it depends on g_A to the fourth power [50].

However, recent ab initio calculations yield vanishing discrepancies for beta [78] and $0\nu\beta\beta$ decays [63], suggesting g_A quenching to be obsolete. Instead, specific nuclear properties missing from traditional calculations seem responsible for the apparent quenching [63]. The decrease of NMEs from phenomenological models to ab initio calculations visible in figure 1.4 can be attributed to the impact of the inclusion of these properties [60]. Including the novel short-range term might somewhat cure this reduction, as visible in the same figure.

It becomes clear that current nuclear structure calculations show deficits in delivering NME values with an accuracy sufficient for next-generation $0\nu\beta\beta$ decay searches. An improvement requires experimental benchmarks. Unique properties of $0\nu\beta\beta$ decay render benchmarks from beta or $2\nu\beta\beta$ decays insufficient. Specifically, the high momentum transfer in $0\nu\beta\beta$ decays makes all states of the intermediate odd-odd nucleus relevant. In contrast, only 1^+ multipole states are reached via $2\nu\beta\beta$ decay, and the beta decay probes only the ground state [79]. Ordinary muon capture (OMC) offers a similar momentum transfer and thus was proposed to provide said benchmark [79].

1.4 Structure of this dissertation

At this point, this dissertation is branching into its two main parts. One branch is following up on OMC as a benchmark for $0\nu\beta\beta$ decay NMEs and covers MONUMENT, a current OMC experiment. That part provides theoretical background on OMC in chapter 13 and a description of the MONUMENT experiment in chapter 14. Two chapters follow, presenting details about the implementation and performance of a data acquisition system, which is part of MONUMENT and has been developed and characterized in the scope of this work.

The other branch continues with experimental efforts in $0\nu\beta\beta$ decay. The following chapter provides a general overview of experimental aspects, while chapter 3 covers LEGEND, a staged $0\nu\beta\beta$ decay experiment using high-purity germanium (HPGe) detectors enriched in ^{76}Ge. Then, part III describes the LEGEND Liquid Argon Monitoring Apparatus (LLAMA), which is the core topic of this dissertation. Its setup and working principle are explained after a theoretical description of liquid argon scintillation, and various results from its application in LEGEND and beyond are provided and discussed.

References

[1] A. G. Cohen, A. De Rujula, and S. L. Glashow, "A Matter - antimatter universe?" *Astrophys. J.*, vol. 495, pp. 539–549, 1998. DOI: 10.1086/305328. arXiv: astro-ph/9707087.

[2] L. Canetti, M. Drewes, and M. Shaposhnikov, "Matter and Antimatter in the Universe," *New J. Phys.*, vol. 14, p. 095 012, 2012. DOI: 10.1088/1367-2630/14/9/095012. arXiv: 1204.4186 [hep-ph].

[3] B. D. Fields, K. A. Olive, T.-H. Yeh, and C. Young, "Big-Bang Nucleosynthesis after Planck," *JCAP*, vol. 03, p. 010, 2020, [Erratum: JCAP 11, E02 (2020)]. DOI: 10.1088/1475-7516/2020/03/010. arXiv: 1912.01132 [astro-ph.CO].

[4] M. Agostini, G. Benato, J. A. Detwiler, J. Menéndez, and F. Vissani, "Toward the discovery of matter creation with neutrinoless $\beta\beta$ decay," *Rev. Mod. Phys.*, vol. 95, no. 2, p. 025 002, 2023. DOI: 10.1103/RevModPhys.95.025002. arXiv: 2202.01787 [hep-ex].

[5] K. Zuber, *Neutrino Physics*. CRC Press, Taylor & Francis Group, 2020, ISBN: 978-1-315-19561-2. DOI: 10.1201/9781315195612.

[6] W. Pauli, "Dear radioactive ladies and gentlemen," *Phys. Today*, vol. 31N9, p. 27, 1978.

[7] E. Fermi, "Versuch einer Theorie der β-Strahlen. I," *Zeitschrift für Physik*, vol. 88, no. 3, pp. 161–177, 1934, ISSN: 0044-3328. DOI: 10.1007/BF01351864.

[8] C. L. Cowan, F. Reines, F. B. Harrison, H. W. Kruse, and A. D. McGuire, "Detection of the free neutrino: A Confirmation," *Science*, vol. 124, pp. 103–104, 1956. DOI: 10.1126/science.124.3212.103.

[9] G. Danby *et al.*, "Observation of High-Energy Neutrino Reactions and the Existence of Two Kinds of Neutrinos," *Phys. Rev. Lett.*, vol. 9, pp. 36–44, 1962. DOI: 10.1103/PhysRevLett.9.36.

[10] K. Kodama *et al.*, "Observation of tau neutrino interactions," *Phys. Lett. B*, vol. 504, pp. 218–224, 2001. DOI: 10.1016/S0370-2693(01)00307-0. arXiv: hep-ex/0012035.

[11] A. de Gouvêa, "Neutrino Mass Models," *Annu. Rev. Nucl. Part. Sci.*, vol. 66, no. 1, pp. 197–217, 2016. DOI: 10.1146/annurev-nucl-102115-044600.

[12] R. N. Mohapatra and G. Senjanović, "Neutrino Mass and Spontaneous Parity Nonconservation," *Phys. Rev. Lett.*, vol. 44, no. 14, pp. 912–915, 1980. DOI: 10.1103/PhysRevLett.44.912.

[13] B. Kayser and R. N. Mohapatra, "The Nature of Massive Neutrinos," in *Current Aspects of Neutrino Physics*. Springer Berlin Heidelberg, 2001, pp. 17–38, ISBN: 978-3-662-04597-8. DOI: 10.1007/978-3-662-04597-8_2.

[14] K. Abe *et al.*, "Solar neutrino measurements using the full data period of Super-Kamiokande-IV," 2023. arXiv: 2312.12907 [hep-ex].

[15] B. Aharmim *et al.*, "Combined Analysis of all Three Phases of Solar Neutrino Data from the Sudbury Neutrino Observatory," *Phys. Rev. C*, vol. 88, p. 025 501, 2013. DOI: 10.1103/PhysRevC.88.025501. arXiv: 1109.0763 [nucl-ex].

[16] R. Abbasi *et al.*, "Measurement of atmospheric neutrino mixing with improved IceCube DeepCore calibration and data processing," *Phys. Rev. D*, vol. 108, no. 1, p. 012 014, 2023. DOI: 10.1103/PhysRevD.108.012014. arXiv: 2304.12236 [hep-ex].

[17] Z. Chen, "Latest results from Daya Bay using the full dataset," in *31st International Symposium on Lepton Photon Interactions at High Energies*, 2023. arXiv: 2309.05989 [hep-ex].

[18] E. Catano-Mur, "Recent results from NOvA," in *56th Rencontres de Moriond on Electroweak Interactions and Unified Theories*, 2022. arXiv: 2206.03542 [hep-ex].

[19] Z. Maki, M. Nakagawa, and S. Sakata, "Remarks on the unified model of elementary particles," *Prog. Theor. Phys.*, vol. 28, pp. 870–880, 1962. DOI: 10.1143/PTP.28.870.

[20] L. Wolfenstein, "Neutrino Oscillations in Matter," *Phys. Rev. D*, vol. 17, pp. 2369–2374, 1978. DOI: 10.1103/PhysRevD.17.2369.

[21] S. P. Mikheev and A. Y. Smirnov, "Resonant amplification of neutrino oscillations in matter and solar neutrino spectroscopy," *Nuovo Cim. C*, vol. 9, pp. 17–26, 1986. DOI: 10.1007/BF02508049.

[22] I. Esteban, M. C. Gonzalez-Garcia, M. Maltoni, T. Schwetz, and A. Zhou, "The fate of hints: updated global analysis of three-flavor neutrino oscillations," *JHEP*, vol. 09, p. 178, 2020. DOI: 10.1007/JHEP09(2020)178. arXiv: 2007.14792 [hep-ph].

[23] F. Capozzi, E. Di Valentino, E. Lisi, A. Marrone, A. Melchiorri, and A. Palazzo, "Unfinished fabric of the three neutrino paradigm," *Phys. Rev. D*, vol. 104, no. 8, p. 083 031, 2021. DOI: 10.1103/PhysRevD.104.083031. arXiv: 2107.00532 [hep-ph].

[24] J. Maalampi and J. Suhonen, "Neutrinoless Double β^+/ EC Decays," *Adv. High Energy Phys.*, vol. 2013, p. 505 874, 2013. DOI: 10.1155/2013/505874.

[25] W. H. Furry, "On Transition Probabilities in Double Beta-Disintegration," *Phys. Rev.*, vol. 56, no. 12, pp. 1184–1193, 1939. DOI: 10.1103/PhysRev.56.1184.

[26] M. Goeppert-Mayer, "Double Beta-Disintegration," *Phys. Rev.*, vol. 48, no. 6, pp. 512–516, 1935. DOI: 10.1103/PhysRev.48.512.

[27] A. S. Barabash, "Average and recommended half-life values for two-neutrino double beta decay: upgrade-2019," *AIP Conf. Proc.*, vol. 2165, no. 1, p. 020 002, 2019. DOI: 10.1063/1.5130963. arXiv: 1907.06887 [nucl-ex].

[28] S. R. Elliott, A. A. Hahn, and M. K. Moe, "Direct evidence for two-neutrino double-beta decay in ^{82}Se," *Phys. Rev. Lett.*, vol. 59, no. 18, pp. 2020–2023, 1987. DOI: 10.1103/PhysRevLett.59.2020.

[29] J. B. Albert *et al.*, "Improved measurement of the $2\nu\beta\beta$ half-life of ^{136}Xe with the EXO-200 detector," *Phys. Rev. C*, vol. 89, no. 1, p. 015 502, 2014. DOI: 10.1103/PhysRevC.89.015502.

[30] A. Gando *et al.*, "Precision Analysis of the ^{136}Xe Two-Neutrino $\beta\beta$ Spectrum in KamLAND-Zen and Its Impact on the Quenching of Nuclear Matrix Elements," *Phys. Rev. Lett.*, vol. 122, no. 19, p. 192 501, 2019. DOI: 10.1103/PhysRevLett.122.192501.

[31] C. Augier *et al.*, "Measurement of the $2\nu\beta\beta$ Decay Rate and Spectral Shape of Mo100 from the CUPID-Mo Experiment," *Phys. Rev. Lett.*, vol. 131, no. 16, p. 162 501, 2023. DOI: 10.1103/PhysRevLett.131.162501. arXiv: 2307.14086 [nucl-ex].

[32] O. Azzolini *et al.*, "Measurement of the $2\nu\beta\beta$ Decay Half-Life of Se82 with the Global CUPID-0 Background Model," *Phys. Rev. Lett.*, vol. 131, no. 22, p. 222 501, 2023. DOI: 10.1103/PhysRevLett.131.222501. arXiv: 2306.14654 [nucl-ex].

[33] I. Nutini *et al.*, "New results from the CUORE experiment," *Int. J. Mod. Phys. A*, vol. 37, no. 07, p. 2 240 014, 2022. DOI: 10.1142/S0217751X22400140.

[34] M. Agostini *et al.*, "Final Results of GERDA on the Two-Neutrino Double-β Decay Half-Life of Ge76," *Phys. Rev. Lett.*, vol. 131, no. 14, p. 142 501, 2023. DOI: 10.1103/PhysRevLett.131.142501. arXiv: 2308.09795 [nucl-ex].

[35] M. Alanssari *et al.*, "Single and Double Beta-Decay Q Values among the Triplet ^{96}Zr, ^{96}Nb, and ^{96}Mo," *Phys. Rev. Lett.*, vol. 116, no. 7, p. 072 501, 2016. DOI: 10.1103/PhysRevLett.116.072501.

[36] J. Schechter and J. W. F. Valle, "Neutrinoless double-β decay in SU(2)×U(1) theories," *Phys. Rev. D*, vol. 25, no. 11, pp. 2951–2954, 1982. DOI: 10.1103/PhysRevD.25.2951.

[37] M. Duerr, M. Lindner, and A. Merle, "On the Quantitative Impact of the Schechter-Valle Theorem," *JHEP*, vol. 06, p. 091, 2011. DOI: 10.1007/JHEP06(2011)091. arXiv: 1105.0901 [hep-ph].

[38] J. Kotila and F. Iachello, "Phase-space factors for double-β decay," *Phys. Rev. C*, vol. 85, no. 3, p. 034 316, 2012. DOI: 10.1103/PhysRevC.85.034316.

[39] S. Stoica and M. Mirea, "Phase Space Factors for Double-Beta Decays," *Front. in Phys.*, vol. 7, p. 12, 2019. DOI: 10.3389/fphy.2019.00012.

[40] F. Vissani, "Signal of neutrinoless double beta decay, neutrino spectrum and oscillation scenarios," *JHEP*, vol. 06, p. 022, 1999. DOI: 10.1088/1126-6708/1999/06/022. arXiv: hep-ph/9906525.

[41] P. D. Group, P. A. Zyla, R. M. Barnett, J. Beringer, O. Dahl, Dwyer, *et al.*, "Review of Particle Physics," *Progress of Theoretical and Experimental Physics*, vol. 2020, no. 8, p. 083C01, 2020, ISSN: 2050-3911. DOI: 10.1093/ptep/ptaa104.

[42] A. Gando *et al.*, "Search for Majorana Neutrinos near the Inverted Mass Hierarchy Region with KamLAND-Zen," *Phys. Rev. Lett.*, vol. 117, no. 8, p. 082 503, 2016, [Addendum: Phys.Rev.Lett. 117, 109903 (2016)]. DOI: 10.1103/PhysRevLett.117.082503. arXiv: 1605.02889 [hep-ex].

[43] M. Aker *et al.*, "Direct neutrino-mass measurement with sub-electronvolt sensitivity," *Nature Phys.*, vol. 18, no. 2, pp. 160–166, 2022. DOI: 10.1038/s41567-021-01463-1. arXiv: 2105.08533 [hep-ex].

[44] M. Aker *et al.*, "KATRIN: status and prospects for the neutrino mass and beyond," *J. Phys. G*, vol. 49, no. 10, p. 100 501, 2022. DOI: 10.1088/1361-6471/ac834e. arXiv: 2203.08059 [nucl-ex].

[45] M. Lattanzi and M. Gerbino, "Status of neutrino properties and future prospects - Cosmological and astrophysical constraints," *Front. in Phys.*, vol. 5, p. 70, 2018. DOI: 10.3389/fphy.2017.00070. arXiv: 1712.07109 [astro-ph.CO].

[46] N. Aghanim *et al.*, "Planck 2018 results. VI. Cosmological parameters," *Astron. Astrophys.*, vol. 641, A6, 2020, [Erratum: Astron.Astrophys. 652, C4 (2021)]. DOI: 10.1051/0004-6361/201833910. arXiv: 1807.06209 [astro-ph.CO].

[47] S. Dell'Oro, S. Marcocci, M. Viel, and F. Vissani, "The contribution of light Majorana neutrinos to neutrinoless double beta decay and cosmology," *JCAP*, vol. 12, p. 023, 2015. DOI: 10.1088/1475-7516/2015/12/023. arXiv: 1505.02722 [hep-ph].

[48] M. Agostini, G. Benato, J. A. Detwiler, J. Menéndez, and F. Vissani, "Testing the inverted neutrino mass ordering with neutrinoless double-β decay," *Phys. Rev. C*, vol. 104, no. 4, p. L042501, 2021. DOI: 10.1103/PhysRevC.104.L042501. arXiv: 2107.09104 [hep-ph].

[49] M. Agostini, G. Benato, and J. Detwiler, "Discovery probability of next-generation neutrinoless double- β decay experiments," *Phys. Rev. D*, vol. 96, no. 5, p. 053 001, 2017. DOI: 10.1103/PhysRevD.96.053001. arXiv: 1705.02996 [hep-ex].

[50] J. Engel and J. Menéndez, "Status and future of nuclear matrix elements for neutrinoless double-beta decay: a review," *Reports on Progress in Physics*, vol. 80, no. 4, p. 046 301, 2017. DOI: 10.1088/1361-6633/aa5bc5.

[51] E. Caurier, G. Martínez-Pinedo, F. Nowacki, A. Poves, and A. P. Zuker, "The shell model as a unified view of nuclear structure," *Rev. Mod. Phys.*, vol. 77, no. 2, pp. 427–488, 2005. DOI: 10.1103/RevModPhys.77.427.

[52] B. A. Brown, "The nuclear shell model towards the drip lines," *Prog. Part. Nucl. Phys.*, vol. 47, pp. 517–599, 2001. DOI: 10.1016/S0146-6410(01)00159-4.

[53] P. Vogel, "Nuclear structure and double beta decay," *J. Phys. G*, vol. 39, p. 124 002, 2012. DOI: 10.1088/0954-3899/39/12/124002. arXiv: 1208.1992 [nucl-th].

[54] Y. Iwata *et al.*, "Large-Scale Shell-Model Analysis of the Neutrinoless $\beta\beta$ Decay of ^{48}Ca," *Phys. Rev. Lett.*, vol. 116, no. 11, p. 112 502, 2016. DOI: 10.1103/PhysRevLett.116.112502.

[55] D.-L. Fang, A. Faessler, and F. Šimkovic, "$0\nu\beta\beta$-decay nuclear matrix element for light and heavy neutrino mass mechanisms from deformed quasiparticle random-phase approximation calculations for ^{76}Ge,^{82} Se,^{130} Te,^{136} Xe, and ^{150}Nd with isospin restoration," *Phys. Rev. C*, vol. 97, no. 4, p. 045 503, 2018. DOI: 10.1103/PhysRevC.97.045503.

[56] N. Hinohara and J. Engel, "Proton-neutron pairing amplitude as a generator coordinate for double-β decay," *Phys. Rev. C*, vol. 90, no. 3, p. 031 301, 2014. DOI: 10.1103/PhysRevC.90.031301.

[57] B. Bally, A. Sánchez-Fernández, and T. R. Rodríguez, "Symmetry-projected variational calculations with the numerical suite TAURUS: I. Variation after particle-number projection," *Eur. Phys. J. A*, vol. 57, no. 2, p. 69, 2021, [Erratum: Eur.Phys.J.A 57, 124 (2021)]. DOI: 10.1140/epja/s10050-021-00369-z. arXiv: 2010.14169 [nucl-th].

[58] P. Van Isacker, J. Engel, and K. Nomura, "Neutron-proton pairing and double-β decay in the interacting boson model," *Phys. Rev. C*, vol. 96, no. 6, p. 064 305, 2017. DOI: 10.1103/PhysRevC.96.064305.

[59] J. M. Yao, B. Bally, J. Engel, R. Wirth, T. R. Rodríguez, and H. Hergert, "*AbInitio* Treatment of Collective Correlations and the Neutrinoless Double Beta Decay of ^{48}Ca," *Phys. Rev. Lett.*, vol. 124, no. 23, p. 232 501, 2020. DOI: 10.1103/PhysRevLett.124.232501. arXiv: 1908.05424 [nucl-th].

[60] A. Belley, C. G. Payne, S. R. Stroberg, T. Miyagi, and J. D. Holt, "*AbInitio* Neutrinoless Double-Beta Decay Matrix Elements for ^{48}Ca , ^{76}Ge , and ^{82}Se," *Phys. Rev. Lett.*, vol. 126, no. 4, p. 042 502, 2021. DOI: 10.1103/PhysRevLett.126.042502. arXiv: 2008.06588 [nucl-th].

[61] S. Novario *et al.*, "Coupled-Cluster Calculations of Neutrinoless Double-β Decay in ^{48}Ca," *Phys. Rev. Lett.*, vol. 126, no. 18, p. 182 502, 2021. DOI: 10.1103/PhysRevLett.126.182502. arXiv: 2008.09696 [nucl-th].

[62] A. Belley *et al.*, "Ab initio uncertainty quantification of neutrinoless double-beta decay in ^{76}Ge," 2023. arXiv: 2308.15634 [nucl-th].

[63] A. Belley, T. Miyagi, S. R. Stroberg, and J. D. Holt, "Ab initio calculations of neutrinoless $\beta\beta$ decay refine neutrino mass limits," 2023. arXiv: 2307.15156 [nucl-th].

[64] J. Menéndez, "Neutrinoless $\beta\beta$ decay mediated by the exchange of light and heavy neutrinos: The role of nuclear structure correlations," *J. Phys. G*, vol. 45, no. 1, p. 014 003, 2018. DOI: 10.1088/1361-6471/aa9bd4. arXiv: 1804.02105 [nucl-th].

[65] M. Horoi and A. Neacsu, "Shell model predictions for ^{124}Sn double-β decay," *Phys. Rev. C*, vol. 93, no. 2, p. 024 308, 2016. DOI: 10.1103/PhysRevC.93.024308.

[66] L. Coraggio, A. Gargano, N. Itaco, R. Mancino, and F. Nowacki, "Calculation of the neutrinoless double-β decay matrix element within the realistic shell model," *Phys. Rev. C*, vol. 101, no. 4, p. 044 315, 2020. DOI: 10.1103/PhysRevC.101.044315.

[67] M. T. Mustonen and J. Engel, "Large-scale calculations of the double-β decay of ^{76}Ge, ^{130}Te, ^{136}Xe, and ^{150}Nd in the deformed self-consistent Skyrme quasiparticle random-phase approximation," *Phys. Rev. C*, vol. 87, no. 6, p. 064 302, 2013. DOI: 10.1103/PhysRevC.87.064302.

[68] J. Hyvärinen and J. Suhonen, "Nuclear matrix elements for $0\nu\beta\beta$ decays with light or heavy Majorana-neutrino exchange," *Phys. Rev. C*, vol. 91, no. 2, p. 024 613, 2015. DOI: 10.1103/PhysRevC.91.024613.

[69] J. Terasaki, "Strength of the isoscalar pairing interaction determined by a relation between double-charge change and double-pair transfer for double-β decay," *Phys. Rev. C*, vol. 102, no. 4, p. 044 303, 2020. DOI: 10.1103/PhysRevC.102.044303.

[70] T. R. Rodríguez and G. Martínez-Pinedo, "Energy Density Functional Study of Nuclear Matrix Elements for Neutrinoless $\beta\beta$ Decay," *Phys. Rev. Lett.*, vol. 105, no. 25, p. 252 503, 2010. DOI: 10.1103/PhysRevLett.105.252503.

[71] N. L. Vaquero, T. R. Rodríguez, and J. L. Egido, "Shape and Pairing Fluctuation Effects on Neutrinoless Double Beta Decay Nuclear Matrix Elements," *Phys. Rev. Lett.*, vol. 111, no. 14, p. 142 501, 2013. DOI: 10.1103/PhysRevLett.111.142501.

[72] L. S. Song, J. M. Yao, P. Ring, and J. Meng, "Nuclear matrix element of neutrinoless double-β decay: Relativity and short-range correlations," *Phys. Rev. C*, vol. 95, no. 2, p. 024 305, 2017. DOI: 10.1103/PhysRevC.95.024305.

[73] J. Barea, J. Kotila, and F. Iachello, "$0\nu\beta\beta$ and $2\nu\beta\beta$ nuclear matrix elements in the interacting boson model with isospin restoration," *Phys. Rev. C*, vol. 91, no. 3, p. 034 304, 2015. DOI: 10.1103/PhysRevC.91.034304.

[74] F. F. Deppisch, L. Graf, F. Iachello, and J. Kotila, "Analysis of light neutrino exchange and short-range mechanisms in $0\nu\beta\beta$ decay," *Phys. Rev. D*, vol. 102, no. 9, p. 095 016, 2020. DOI: 10.1103/PhysRevD.102.095016.

[75] V. Cirigliano *et al.*, "New Leading Contribution to Neutrinoless Double-β Decay," *Phys. Rev. Lett.*, vol. 120, no. 20, p. 202 001, 2018. DOI: 10.1103/PhysRevLett.120.202001.

[76] V. Cirigliano *et al.*, "New Leading Contribution to Neutrinoless Double-β Decay," *Phys. Rev. Lett.*, vol. 120, no. 20, p. 202 001, 2018. DOI: 10.1103/PhysRevLett.120.202001.

[77] I. S. Towner, "Quenching of spin matrix elements in nuclei," *Phys. Rept.*, vol. 155, pp. 263–377, 1987. DOI: 10.1016/0370-1573(87)90138-4.

[78] P. Gysbers *et al.*, "Discrepancy between experimental and theoretical β-decay rates resolved from first principles," *Nature Phys.*, vol. 15, no. 5, pp. 428–431, 2019. DOI: 10.1038/s41567-019-0450-7. arXiv: 1903.00047 [nucl-th].

[79] M. Kortelainen and J. Suhonen, "Ordinary muon capture as a probe of virtual transitions of $\beta\beta$ decay," *Europhysics Letters*, vol. 58, no. 5, p. 666, 2002. DOI: 10.1209/epl/i2002-00401-5.

Chapter 2

Experimental $0\nu\beta\beta$ decay search

The isotope employed is the core element of any experimental search for $0\nu\beta\beta$ decay. While several isotopes can undergo $\beta\beta$ decays, only a fraction qualifies for experimental applications due to their favorable properties. The expected $0\nu\beta\beta$ decay rate is a crucial property, increasing with both NMEs and the $Q_{\beta\beta}$ value. Further, natural abundance and commercial availability are relevant. The detector design depends on the material properties of the isotope used, bringing in unique advantages and challenges and rendering experimental methods in this field very diverse and quickly developing.

2.1 Unique signature

All experiments share the requirement to detect the unique signature of $0\nu\beta\beta$ decay. Only the final state leptons provide means to distinguish $0\nu\beta\beta$ decay from the competing $2\nu\beta\beta$ decay and are further utilized to discriminate against other backgrounds. Due to the elusive nature of neutrinos, both electrons emitted by $\beta\beta$ decays must provide the necessary information via their individual energy or momentum direction.

The summed electron energy provides a common way to distinguish between $0\nu\beta\beta$ and $2\nu\beta\beta$ decays. The distributions for both cases are shown in figure 2.1. $0\nu\beta\beta$ decays lead to a mono-energetic peak at $Q_{\beta\beta}$, as it is a three-body decay, where the nucleus receives negligible recoil energy due to its large mass. Conversely, $2\nu\beta\beta$ decay is a five-body process (again, with a negligible nuclear recoil energy), and the sum of the electrons' energies follows a continuous distribution. The width of the $0\nu\beta\beta$ decay peak is set by the detector resolution, which needs to be sufficient to separate it from the continuous $2\nu\beta\beta$ distribution.

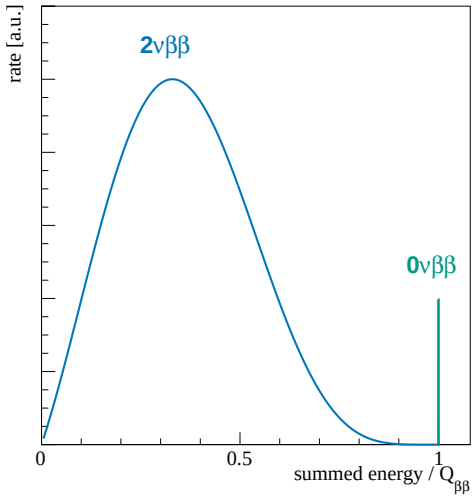

Figure 2.1: Summed electron energy spectrum for $2\nu\beta\beta$ and $0\nu\beta\beta$ decays. The mono-energetic peak of $0\nu\beta\beta$ decay provides a clear signature, distinguishing it from the continuous distribution of $2\nu\beta\beta$ decay. The relative scaling of the two distributions is unknown. The analytic formula of the $2\nu\beta\beta$ decay spectrum is taken from [1].

2.2 General considerations

Discriminating between $0\nu\beta\beta$ and $2\nu\beta\beta$ decays is required but by far not sufficient for a successful experiment. The extremely low count rate expected for $0\nu\beta\beta$ decay constitutes a major challenge and drives the experimental design choices.

A high amount of the $\beta\beta$ decay isotope material has to be used, which puts requirements on its availability and affordability on the world market. As the natural abundances of typically used $0\nu\beta\beta$ decay candidate isotopes are less than[1] 10 % [2], isotopic enrichment is commonly performed. The detection efficiency is maximized to make maximal use of the precious material, typically either by using detectors built out of the isotope or by having the isotope embedded in the detector.

Nevertheless, the expected signal rate is tiny, and refined background reduction techniques must be implemented to be sensitive. In a *quasi-background-free* scenario, in which less than one background count mimicking $0\nu\beta\beta$ decay is expected, the half-life

[1] Except for ^{130}Te, which has a natural abundance of around 34 %.

sensitivity scales as

$$T_{1/2}^{0\nu} \propto m\,t, \tag{2.1}$$

where the product of mass m and measurement time t is commonly referred to as *exposure*. Conversely, in the presence of a sizable background expectation, the half-life sensitivity only scales as

$$T_{1/2}^{0\nu} \propto \sqrt{\frac{m\,t}{BI\,\Delta E}}. \tag{2.2}$$

Here, *BI* denotes the *background index*, given in terms of the expected number of background counts in the region of interest (ROI) around $Q_{\beta\beta}$ per exposure and energy interval. The energy region ΔE searched for $0\nu\beta\beta$ decays is given by the detector resolution, which is thus a key performance parameter. Experiments strive to push the background index as low as possible using radiopure structural materials, active background suppression, fiducialization, pulse-shape analysis and placing the experiment in underground laboratories.

2.3 Current and future efforts

The experimental landscape of $0\nu\beta\beta$ search is vast and characterized by the usage of a diverse set of technologies. This section presents an overview, while [3] gives a more complete and elaborate description.

The present-generation experiments set exclusion limits on $T_{1/2}^{0\nu}$ and thus on $m_{\beta\beta}$. A selection is compiled in table 2.1, which provides the exclusion sensitivities, defined as the median half-live excluded, given a true no-signal hypothesis.

Since the next-generation experiments target discovery, 3σ discovery sensitivities are quoted in table 2.2. The 3σ discovery sensitivity is defined as the half-life, leading to a 50 % chance for a 3σ discovery.

2.3.1 Large liquid scintillator detectors

Dissolving or loading $0\nu\beta\beta$ isotopes in liquid scintillators provides highly scalable and low-radioactive experiments, often re-purposing existing infrastructure. Photodetectors, typically photomultiplier tubes (PMTs), surround the liquid scintillator volume, providing energy and position reconstruction. The latter allows for fiducialization, utilizing the

Table 2.1: Selection of finished or running (*) $0\nu\beta\beta$ experiments with their limits and sensitivities corresponding to 90 % C.L.

experiment	isotope	sensitivity	limit		ref.
		$T^{0\nu}_{1/2}$[yr]	$T^{0\nu}_{1/2}$[yr]	$m_{\beta\beta}$[meV]	
GERDA	^{76}Ge	$>1.8\times10^{26}$	$>1.8\times10^{26}$	$<79-180$	[4]
MAJORANA	^{76}Ge	$>8.1\times10^{25}$	$>8.3\times10^{25}$	$<113-269$	[5]
CUPID-0	^{82}Se	$>7.0\times10^{24}$	$>4.6\times10^{24}$	$<263-545$	[6]
CUPID-Mo	^{100}Mo		$>1.8\times10^{24}$	$<280-490$	[7]
CUORE*	^{130}Te	$>2.8\times10^{25}$	$>2.2\times10^{25}$	$<90-305$	[8]
KamLAND-Zen*	^{136}Xe	$>1.3\times10^{26}$	$>2.3\times10^{26}$	$<36-156$	[9]
EXO-200	^{136}Xe	$>5.0\times10^{25}$	$>3.5\times10^{25}$	$<93-286$	[10]

Table 2.2: Selection of next-generation $0\nu\beta\beta$ experiments with their 3σ discovery sensitivities.

experiment	isotope	3σ discovery sensitivity		ref.
		$T^{0\nu}_{1/2}$[yr]	$m_{\beta\beta}$[meV]	
LEGEND-1000	^{76}Ge	$>1.3\times10^{28}$	$<9-21$	[11]
CUPID	^{100}Mo	$>1\times10^{27}$	$<12-20$	[12]
KamLAND2-Zen	^{136}Xe	$>1.1\times10^{27}$	$<17-71$	[3]
nEXO	^{136}Xe	$>7.4\times10^{27}$	$<6-27$	[3, 13]

detectors' self-shielding capabilities.

The low energy resolution due to the low number of photons produced around $Q_{\beta\beta}$ presents a major challenge. Especially the endpoint of the $2\nu\beta\beta$ spectrum overlaps with the expected distribution of $0\nu\beta\beta$ events, requiring spectral analysis [3]. Currently, KamLAND-Zen takes data and is loaded with 750 kg of ^{136}Xe. [9] The KamLAND2-Zen stage is foreseen, which will use 1 t of ^{136}Xe and plans to improve the energy resolution [14, 15]. Also, SNO+ presents a two-staged approach using a liquid scintillator loaded with natural tellurium. The first stage uses 1.3 t of ^{130}Te and the deployment is anticipated to commence in 2024 [16], and a second stage with 6.6 t of ^{130}Te is planned [17].

2.3.2 Time projection chambers

Xenon time-projection chambers (TPCs) offer higher energy resolutions. A static electric field is applied to a liquid or high-pressure gas volume, allowing a measurement of the ionization signal in addition to the scintillation light, facilitating particle identification and 3D position reconstruction. ^{136}Xe is a $0\nu\beta\beta$ decay candidate, providing a source = detector approach. EXO-200 was the most sensitive experiment adopting this design choice, using 161 kg ^{136}Xe in a liquid-phase TPC [10]. Its next-generation successor nEXO plans to use 5 t of xenon, enriched to 90 % in ^{136}Xe [13]. Tagging of the ^{136}Ba daughter ion after the decay is proposed for this experiment [18].

2.3.3 Cryogenic calorimeters

Cryogenic calorimeters, or bolometers, are frequently used in rare event searches, including $0\nu\beta\beta$ decay projects and dark matter experiments. They use small crystals made from various materials with attached thermometers to measure the heat signals produced by energy depositions. Like TPCs, bolometers for $0\nu\beta\beta$ decay use a source = detector approach, however, their small size of typically 0.2 kg to 0.8 kg severely limits their scalability [3]. In the case of scintillating crystals, the additional photon channel offers particle identification.

The next-generation experiment CUPID plans to use a total isotope mass of 250 kg in the shape of Li_2MoO_4 crystals enriched in ^{100}Mo. In total, 1500 crystals will be equipped with heat and light readout [12]. The experiment builds on the knowledge gained by CUORE and will use its cryogenic infrastructure. CUORE did not feature the two-channel readout and was dominated by alpha backgrounds. Two further precursor experiments, CUPID-0 [19] and CUPID-Mo [7], benchmark the CUORE detector technology and provide a robust background model.

2.3.4 High-purity germanium detectors

The use of HPGe detectors enriched in ^{76}Ge follows the source = detector paradigm. They provide the leading energy resolution of the field, reaching $\sigma = 1.1$ keV at $Q_{\beta\beta}$ [20]. Further, their intrinsic radiopurity makes them ideally suited for applications in $0\nu\beta\beta$

experiments, with dates back as far as 1967 [21][2].

Classically, HPGe detectors were operated in shielded vacuum cryostats [22], with the pinnacle of this technology being demonstrated by the MAJORANA collaboration [5]. GERDA introduced the operation of bare HPGe detectors in liquid argon (LAr), serving as a coolant and, most importantly, acting as a passive and active shield, allowing GERDA to reach unprecedented background levels [4].

Building on the success of both experiments and combining their key technological achievements, the LEGEND collaboration will continue the search. The LEGEND experiment is separated into two stages, of which LEGEND-200 is currently taking data and provides vital experience paving the way for the next-generation LEGEND-1000 stage. The integer suffixes of each stage indicate the planned germanium mass in kg. A more detailed description of LEGEND is presented in chapter 3.

2.3.5 Tracking calorimators

Only tracking calorimeters separate the $0\nu\beta\beta$ decay candidate isotope from the detector. The source takes the form of thin foils, which are surrounded by drift chambers and, beyond those, calorimeters. The drift chambers feature a magnetic field for discriminating electrons and positrons and provide a unique tool for studying the $0\nu\beta\beta$ decay kinematics. Apart from the difficult scalability, the design principle renders $0\nu\beta\beta$ decay identification and the separation from $2\nu\beta\beta$ decays challenging since emitted electrons inevitably lose part of their kinetic energy within the source foils.

NEMO-3 was the most sensitive experiment to date and used seven target isotopes, of which ^{100}Mo had the largest mass [23]. Currently, its successor, SuperNEMO, is in preparation, which foresees a stage using 100 kg of ^{82}Se [24]. Its expected discovery sensitivity after 10 yr runtime is 8×10^{25} yr [3], which does not reach the regions explored by next-generation experiments. However, further phases with more mass and different isotopes are still open [3, 24].

[2] Note, that this early experiment used fully lithium diffused germanium detectors (GeLi) rather than the currently used HPGe detectors.

References

[1] V. Tretyak and Y. Zdesenko, "Tables of double beta decay data," *Atomic Data and Nuclear Data Tables*, vol. 61, no. 1, pp. 43–90, 1995, ISSN: 0092-640X. DOI: 10.1016/S0092-640X(95)90011-X.

[2] J. Meija *et al.*, "Isotopic compositions of the elements 2013 (IUPAC Technical Report)," *Pure and Applied Chemistry*, vol. 88, no. 3, pp. 293–306, 2016. DOI: 10.1515/pac-2015-0503.

[3] M. Agostini, G. Benato, J. A. Detwiler, J. Menéndez, and F. Vissani, "Toward the discovery of matter creation with neutrinoless $\beta\beta$ decay," *Rev. Mod. Phys.*, vol. 95, no. 2, p. 025 002, 2023. DOI: 10.1103/RevModPhys.95.025002. arXiv: 2202.01787 [hep-ex].

[4] M. Agostini *et al.*, "Final Results of GERDA on the Two-Neutrino Double-β Decay Half-Life of Ge76," *Phys. Rev. Lett.*, vol. 131, no. 14, p. 142 501, 2023. DOI: 10.1103/PhysRevLett.131.142501. arXiv: 2308.09795 [nucl-ex].

[5] I. J. Arnquist *et al.*, "Final Result of the Majorana Demonstrator's Search for Neutrinoless Double-β Decay in ^{76}Ge," *Phys. Rev. Lett.*, vol. 130, no. 6, p. 062 501, 2023. DOI: 10.1103/PhysRevLett.130.062501.

[6] O. Azzolini *et al.*, "Final Result on the Neutrinoless Double Beta Decay of ^{82}Se with CUPID-0," *Phys. Rev. Lett.*, vol. 129, no. 11, p. 111 801, 2022. DOI: 10.1103/PhysRevLett.129.111801.

[7] C. Augier *et al.*, "Final results on the $0\nu\beta\beta$ decay half-life limit of ^{100}Mo from the CUPID-Mo experiment," *Eur. Phys. J. C*, vol. 82, no. 11, p. 1033, 2022. DOI: 10.1140/epjc/s10052-022-10942-5. arXiv: 2202.08716 [nucl-ex].

[8] D. Q. Adams *et al.*, "Search for Majorana neutrinos exploiting millikelvin cryogenics with CUORE," *Nature*, vol. 604, no. 7904, pp. 53–58, 2022. DOI: 10.1038/s41586-022-04497-4. arXiv: 2104.06906 [nucl-ex].

[9] S. Abe *et al.*, "Search for the Majorana Nature of Neutrinos in the Inverted Mass Ordering Region with KamLAND-Zen," *Phys. Rev. Lett.*, vol. 130, no. 5, p. 051 801, 2023. DOI: 10.1103/PhysRevLett.130.051801. arXiv: 2203.02139 [hep-ex].

[10] G. Anton *et al.*, "Search for Neutrinoless Double-β Decay with the Complete EXO-200 Dataset," *Phys. Rev. Lett.*, vol. 123, no. 16, p. 161 802, 2019. DOI: 10.1103/PhysRevLett.123.161802. arXiv: 1906.02723 [hep-ex].

[11] N. Abgrall *et al.*, "The Large Enriched Germanium Experiment for Neutrinoless $\beta\beta$ Decay: LEGEND-1000 Preconceptual Design Report," 2021. arXiv: 2107.11462 [physics.ins-det].

[12] K. Alfonso *et al.*, "CUPID: The Next-Generation Neutrinoless Double Beta Decay Experiment," *J. Low Temp. Phys.*, vol. 211, no. 5-6, pp. 375–383, 2023. DOI: 10.1007/s10909-022-02909-3.

[13] G. Adhikari *et al.*, "nEXO: neutrinoless double beta decay search beyond 10^{28} year half-life sensitivity," *J. Phys. G*, vol. 49, no. 1, p. 015 104, 2022. DOI: 10.1088/1361-6471/ac3631. arXiv: 2106.16243 [nucl-ex].

[14] A. Giuliani *et al.*, "Double Beta Decay APPEC Committee Report," 2019. arXiv: 1910.04688 [hep-ex].

[15] J. Shirai, "Results and future plans for the KamLAND-Zen experiment," *J. Phys. Conf. Ser.*, vol. 888, no. 1, p. 012 031, 2017. DOI: 10.1088/1742-6596/888/1/012031.

[16] B. Tam, "The SNO+ Experiment: Reactor & Solar ν Prospects," *PoS*, vol. NOW2022, p. 033, 2023. DOI: 10.22323/1.421.0033. arXiv: 2211.05538 [hep-ex].

[17] C. Grant, *Results from KamLAND-ZEN and SNO+*, 2020. DOI: 10.5281/zenodo.4142683.

[18] K. Twelker *et al.*, "An apparatus to manipulate and identify individual Ba ions from bulk liquid Xe," *Rev. Sci. Instrum.*, vol. 85, p. 095 114, 2014. DOI: 10.1063/1.4895646. arXiv: 1407.0618 [physics.ins-det].

[19] O. Azzolini *et al.*, "Background Model of the CUPID-0 Experiment," *Eur. Phys. J. C*, vol. 79, no. 7, p. 583, 2019. DOI: 10.1140/epjc/s10052-019-7078-8. arXiv: 1904.10397 [nucl-ex].

[20] C. E. Aalseth *et al.*, "Search for Neutrinoless Double-β Decay in ^{76}Ge with the Majorana Demonstrator," *Phys. Rev. Lett.*, vol. 120, no. 13, p. 132 502, 2018. DOI: 10.1103/PhysRevLett.120.132502. arXiv: 1710.11608 [nucl-ex].

[21] E. Fiorini, A. Pullia, G. Bertolini, F. Cappellani, and G. Restelli, "A Search for Lepton Nonconservation in Double Beta Decay With a Germanium Detector," *Phys. Lett. B*, vol. 25, pp. 602–603, 1967. DOI: 10.1016/0370-2693(67)90127-X.

[22] F. T. Avignone and S. R. Elliott, "The Search for Double Beta Decay With Germanium Detectors: Past, Present, and Future," *Front. in Phys.*, vol. 7, p. 6, 2019. DOI: 10.3389/fphy.2019.00006. arXiv: 1901.02805 [nucl-ex].

[23] R. Arnold *et al.*, "Results of the search for neutrinoless double-β decay in ^{100}Mo with the NEMO-3 experiment," *Phys. Rev. D*, vol. 92, no. 7, p. 072 011, 2015. DOI: 10.1103/PhysRevD.92.072011. arXiv: 1506.05825 [hep-ex].

[24] F. Piquemal, "The SuperNEMO project," *Phys. Atom. Nucl.*, vol. 69, pp. 2096–2100, 2006. DOI: 10.1134/S1063778806120131.

Part II

Next generation $0\nu\beta\beta$ decay search in ^{76}Ge

Chapter 3

The LEGEND project

3.1 Physics goals

LEGEND (Large Enriched Germanium Experiment for Neutrinoless $\beta\beta$ Decay) pursues the search for $0\nu\beta\beta$ decay using HPGe detectors enriched in ^{76}Ge in a staged approach. The next-generation LEGEND-1000 stage is designed to achieve a 3σ discovery sensitivity fully spanning the parameter space in the inverted ordering scenario and also probes a considerable part of the parameter space in case of normal ordering. The $0\nu\beta\beta$ decay half-live discovery sensitivity aimed for is $T_{1/2}^{0\nu} = 1.3 \times 10^{28}$ yr, which translates to an effective Majorana neutrino mass of $m_{\beta\beta}$ in the range of $9-21$ meV [1, 2].

In 10 yr of runtime and with 1000 kg of HPGe detector mass, LEGEND-1000 will acquire 10 t yr of exposure. With an energy resolution of 2.5 keV (full width at half maximum (FWHM)) at $Q_{\beta\beta}$ and a background index of less than 1×10^{-5} cts/(keV kg yr), the background expectation within $\pm 2\sigma$ around $Q_{\beta\beta}$ is approximately 0.4 counts. Thus, LEGEND-1000 will stay quasi-background-free, a crucial condition that allows the sensitivity to scale linearly with the exposure gain. Reaching this unprecedented background level requires efforts on various aspects of the experiment - from choosing the underground site and selecting low-radioactive materials over active and passive shielding technologies to pulse shape analysis.

In this matter, LEGEND-1000 can build on its predecessor stage LEGEND-200, which provides valuable experience. LEGEND-200 is the first stage of LEGEND and will eventually operate 200 kg of HPGe detectors over a runtime of 5 yr. The total exposure of 1 t yr provides a 3σ discovery sensitivity of $T_{1/2}^{0\nu} \approx 1 \times 10^{27}$ yr and an exclusion sensitivity at 90 % C.L. of $T_{1/2}^{0\nu} > 1.5 \times 10^{27}$ yr. In order to ensure a quasi-background-free search,

LEGEND-200 targets a background index of not more than 2×10^{-4} cts/(keV kg yr), i.e. only about one order of magnitude above LEGEND-1000. This allows LEGEND-200 to act as a test bench for developing leading-edge technologies in an extremely low-background environment and to demonstrate the feasibility of the background goal of LEGEND-1000.

In turn, the design of LEGEND-200 was informed by its successful predecessor experiments GERDA and MAJORANA DEMONSTRATOR. With a background index of 5.2×10^{-4} cts/(keV kg yr) [3], i.e. less than a factor of 3 away from the LEGEND-200 goal, GERDA provided a strong proof that LEGEND can build on well-performing background-reduction techniques. The energy resolution of around 2.5 keV (FWHM) at $Q_{\beta\beta}$ reached by MAJORANA DEMONSTRATOR is sufficient for both stages of LEGEND.

3.2 LEGEND-200

LEGEND-200 is currently taking data with around 140 kg of installed HPGe detector mass. It took over the water tank and the cryogenic infrastructure from GERDA, which finished data taking in 2019. Also, main design principles follow GERDA's approach, such as operating bare HPGe detectors in LAr. In addition to providing cooling and passive shielding, the scintillating LAr volume becomes an active detector by being instrumented with a light-readout system. These main paradigms shape the design of the LEGEND-200 setup, which is described in the following.

3.2.1 Setup overview

LEGEND-200 is located in Hall A of the Laboratori Nazionali del Gran Sasso (LNGS) underground laboratory in Italy. The rock overburden of 1400 m thickness, corresponding to 3500 m water equivalent (m.w.e.), provides shielding against cosmic radiation. Most importantly, the cosmic muon flux is reduced to around $3.5 \times 10^{-4}\,\mathrm{m^{-2}\,s^{-1}}$ [4].

The experimental setup is pictured in figure 3.1a. The outermost part is a PMT-instrumented water tank. Apart from providing passive shielding by attenuating gamma radiation and moderating neutrons, it yields a veto against cosmic muons, creating Cherenkov radiation. It has a diameter of 10 m, a volume of 590 $\mathrm{m^3}$, and has an internal lining of VM2000 reflector foil enhancing light collection. Together with the cryostat, it was taken over from the GERDA experiment and received only minor modifications

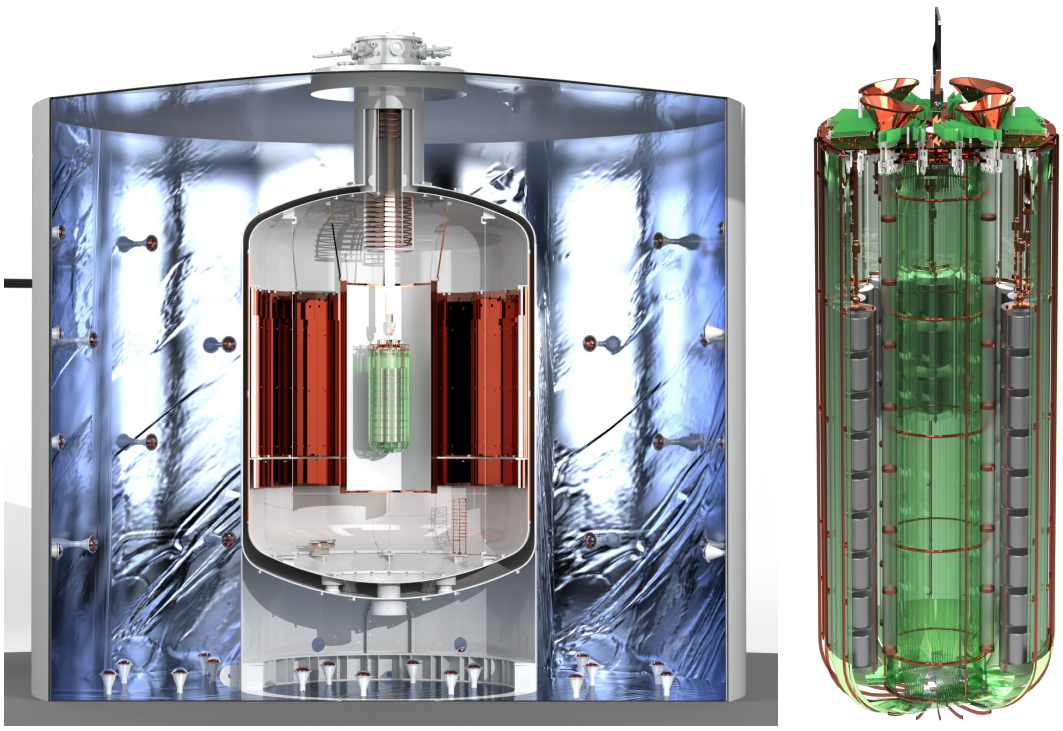

(a) (b)

Figure 3.1: Renders of the LEGEND-200 setup.
(a): The full setup including the PMT-instrumented water tank surrounding the LAr cryostat. A LAr pump, LLAMA, and the WLSR are directly mounted in the cryostat.
(b): The suspended payload consists of a ring of 12 HPGe detector strings surrounded by two coaxial barrels consisting of WLS fibers read out by SiPMs. See text for details. Renders by P. Krause.

restricted to the placement and number of PMTs.

The LAr cryostat is located in the center of the water tank. The steel vessel has an inner diameter of 4 m and contains 64 m^3 of LAr [5]. An internal copper lining of up to 6 mm shields the detectors from gammas emitted by radioactive trace impurities in the steel. LAr was filled in during the LEGEND-200 commissioning in Summer 2021. Using online liquid-phase purification with the LEGEND Liquid Argon purification System (LLArS) [6], the LAr quality of LEGEND-200 surpasses what has been achieved for GERDA. However, the present LAr contains a significant nitrogen contamination from a spoiled LAr batch

delivered. The current effective triplet lifetime[1] is around[2] 1.16 µs, which exceeds the best quality achieved in GERDA Phase-II of 1.00 µs [7]. Details about the LAr filling are presented in section 6.3.

The LEGEND Liquid Argon Monitoring Apparatus (LLAMA) is mounted on the bottom of the cryostat. It measures the optical properties of LAr permanently and in-situ and played a crucial role in the cryostat filling campaign. The setup and working principle are described in chapter 5 and its application as a monitor in LEGEND-200 in chapter 6. Part III moreover contains analysis results of LLAMA data, partly obtained during its application in LEGEND-200. The LEGEND-200 cryostat further features a submerged LAr pump to facilitate on-demand loop-mode purification using LLArS [8].

The immersed payload (see figure 3.1b) is located in the center of the cryostat. Its final configuration will contain the HPGe detectors in a 12-string ring-shaped configuration. The detector array is surrounded by two coaxial barrels consisting of wavelength-shifting (WLS) fibers read out by SiPM arrays: the core part of the LAr instrumentation. The payload enters and leaves the cryostat through a dedicated lock system at its top.

The wavelength-shifting reflector (WLSR) is suspended in the cryostat and surrounds the payload. It reflects outgoing photons to enhance the LAr instrumentations' light collection capability. In the following, the HPGe detector array and the LAr instrumentation, including the WLSR, are explained.

3.2.2 Germanium detectors

LEGEND-200 uses HPGe detectors, which exhibit excellent energy resolution [9] and extremely high intrinsic radiopurity [10]. Energy depositions from ionizing radiation create clusters of electron-hole pairs. The applied bias voltage forces the charges to the electrodes, creating a measurable signal. In LEGEND-200, p-type detectors are used, with a grounded p^+ electrode collecting holes, while the n^+ electrode is biased to a positive high voltage and attracts electrons.

The time structure of the signals allows discriminating events via pulse-shape analysis. The finite charge drift speed enables distinguishing point-like $\beta\beta$ events from gamma events, creating multiple energy depositions in the same detector, and alpha and beta

[1] The effective triplet lifetime is a common measure for the LAr purity, as it decreases in the presence of trace impurities inducing quenching. See section 4.3.1.
[2] See section 7.4.3.

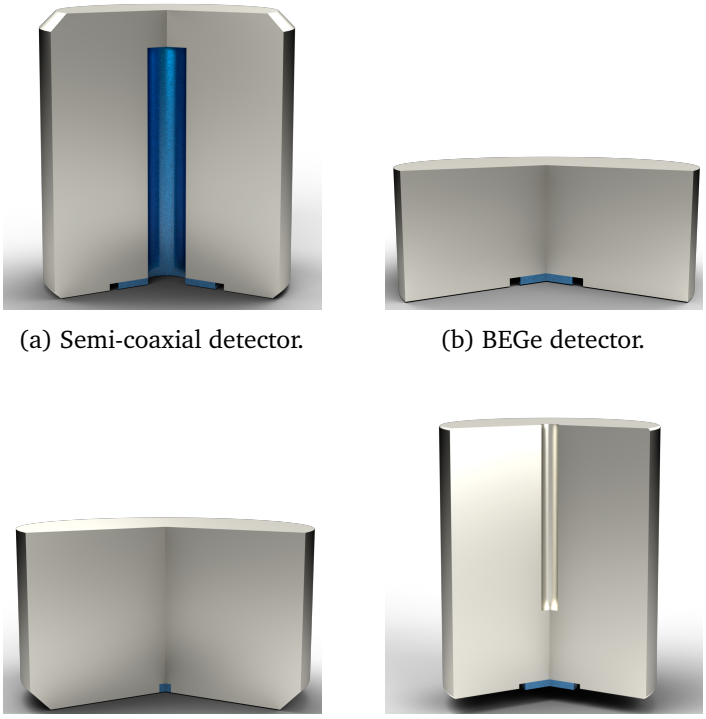

(a) Semi-coaxial detector. (b) BEGe detector.

(c) PPC detector. (d) IC detector.

Figure 3.2: Renders of HPGe detector types employed in LEGEND-200. In all cases, the p^+ electrode is marked in blue. All renders by P. Krause.

events at the detector's surface. For a detailed description of pulse-shape discrimination in HPGe detectors, see e.g. [11, 12].

In addition to pulse-shape discrimination performance, a high mass of individual HPGe detectors is advantageous for low-background experiments, as it reduces the total mass of read-out electronics close to the detectors. The electronics components inevitably have higher quantities of intrinsic radioactivity than e.g. structural materials or the HPGe detectors themselves.

LEGEND-200 features four different types of HPGe detectors, which are shown in figure 3.2 and are briefly[3] described in the following:

- **Semi-coaxial** detectors have a deep p^+ borehole, providing a strong drift field even across large detectors. Its pulse-shape discrimination performance is inferior

[3] A more in-depth description is available in [12].

to the other detector types.

- The **broad energy germanium (BEGe)** detectors were originally produced for GERDA Phase-II [13, 14] and have a circular p^+ contact on one side. They offer superior pulse-shape performance, but cannot be produced with high masses.
- Similar to BEGes, **p-type point contact (PPC)** detectors exhibit good pulse-shape performance at the cost of being restricted in mass. They have been taken over from MAJORANA DEMONSTRATOR.
- **Inverted coaxial (IC)** [12, 15] detectors share the electrode structure with BEGes, while having a n^+-doped borehole. This allows ICs to have a pulse shape similar to BEGes while being about three times more massive. Five of these detectors were characterized in GERDA before their application in LEGEND-200 [16].

Due to their advantages, all detectors produced specifically for LEGEND-200 are of the IC type. Currently, around 142 kg of HPGe detectors are installed in LEGEND-200, from which approximately 65 kg are taken over from GERDA and MAJORANA DEMONSTRATOR. Future detector insertions are foreseen.

The final LEGEND-200 configuration has an array of 12 HPGe detector strings in a circular arrangement. This design maximizes the distance between strings while allowing for efficient scintillation light collection by the surrounding fiber barrels. The structural parts of the strings are manufactured from two materials: All rods are made from underground electroformed copper, which exhibits ultra-low intrinsic backgrounds [17]. The HPGe detectors rest on baseplates made from polyethylene naphthalate (PEN), whose scintillating and wavelength-shifting capabilities boost the light collection in the detectors' vicinity [18, 19].

3.2.3 LAr instrumentation

Energy depositions from ionizing radiation cause LAr to scintillate with a peak emission wavelength of around 128 nm, which is in the vacuum-ultraviolet (VUV) region. Details about LAr scintillation are provided in chapter 4. By detecting light emitted by LAr and any other scintillating material around the HPGe detectors, backgrounds causing coincident energy emissions in both the detectors and the scintillating materials can be

identified. Since $\beta\beta$ decays from ^{76}Ge are confined in a single HPGe detector, an anti-coincidence condition with a light detection provides strong background discrimination.

Light propagation in LAr is enhanced by WLS materials since light of longer wavelengths gets attenuated less than the VUV light directly emitted by LAr [7, 20]. Apart from the PEN baseplates, this also applies to surfaces coated with tetraphenyl butadiene (TPB), which shifts the VUV light to the visible blue region [21]. Nylon mini-shrouds (MSs) surround all individual detector strings and are coated with TPB [22], aiding light collection close to the detectors.

Additionally, the WLSR, which was coated in-situ with TPB [8, 23], surrounds the array and boosts the light collection efficiency by shifting and reflecting outgoing photons [24]. Its diameter is 1.4 m, which was optimized in a dedicated Monte Carlo campaign conducted together with P. Krause and is described in his dissertation [8].

WLS fibers[4] coated with TPB collect photons - VUV or previously shifted - and guide them towards arrays of SiPMs mounted at their ends. While any TPB surface shifts the initial wavelength to visible blue, the fiber material itself shifts it further to the visible green [7]. The green photons are trapped in the fiber, which has two cladding layers, boosting the trapping efficiency.

The fibers are arranged in two barrels, both of which are in coaxial arrangement with the HPGe array (see figure 3.1b.). The inner and outer barrels are inside and outside the HPGe array, respectively, and act as low-radioactive light collectors in the HPGe detectors' vicinity. The outer barrel is bent inwards at its bottom, providing a light-collecting floor to detect photons traveling downwards along the array.

All fibers are read out with SiPMs[5] mounted on both ends. As the fibers have a cross-section of 1x1 mm^2, always nine of them are coupled to one 3x3 mm^2 SiPM. In turn, nine SiPMs form one SiPM array, in which the individual SiPMs are electrically connected in parallel.

A top-bottom pair of SiPM arrays and their attached fibers form a fiber module. The inner barrel comprises nine fiber modules, while the outer barrel contains 20 modules, leading to 58 channels. See [8] for an elaborate description of all parts of the LEGEND-200 LAr instrumentation.

[4] Saint Gobain (BCF-91A) [8].
[5] KETEK PM33100T [8].

3.2.4 Active background suppression

To achieve the required background level, LEGEND-200 employs a powerful and diverse set of background reduction techniques. The signal of interest manifests itself as a point-like energy deposition in the bulk of a single HPGe detector. This signature allows to discriminate background events via the following techniques:

- The aforementioned pulse-shape analysis allows the identification of multiple energy depositions in the same detector, typically originating from Compton-scattering gammas, as well as alpha or beta events at the detector's surface.
- Detector anti-coincidence tags coincident energy depositions in multiple detectors.
- Signals in a HPGe detector can be accompanied by energy depositions in LAr, allowing to discriminate those via the LAr instrumentation.

These methods act in synergy, as certain background sources are tagged with higher efficiencies via specific approaches [7]. To avoid spoiling the background suppression with "dark spots," the amount of non-active materials such as copper has to be kept at a minimum, especially close to the detectors.

The LEGEND-200 collaboration invests great efforts in simulating the performance in suppressing various background components. On the one hand, this is required for investigating background sources around $Q_{\beta\beta}$, i.e. of immediate relevance for the $0\nu\beta\beta$ decay search. Apart from the impact on the LEGEND-200 design, this is also done to inform the LEGEND-1000 stage based on the experience in LEGEND-200. On the other hand, physics studies apart from $0\nu\beta\beta$ decay require expectations of backgrounds surviving analysis cuts, as they target different and possibly more extended energy regions where background contributions are not flat. For example, the search for exotic physics[6] in GERDA uses the energy range from 560 keV to 2000 keV and employs LAr anti-coincidence [25, 26].

Currently, the Geant4-based [27] Monte Carlo framework MAJORANA-GERDA (MaGe) [28] provides a base to obtain background estimations for LEGEND-200 and LEGEND-1000. It generates energy depositions in HPGe detectors and scintillating materials

[6] These include Majoron emission, Lorentz violation, and the emission of sterile neutrinos or double fermions.

originating from various background sources. Post-processing then yields detector responses, which provide the final background estimations.

The generation of simulated HPGe detector waveforms uses the SigGen program [29], which provides signals of drifting charges in the detectors, together with the electric field. The simulation is benchmarked against measurements with an ^{241}Am source [12]. Currently, the simulation of pulse-shape discrimination (PSD) based on these waveforms is limited to bulk events, while rejection efficiencies for surface events are manually tuned to data [2].

The simulation of the LAr instrumentation response uses photon detection probabilities throughout the LAr volume, which takes the form of a pre-generated 3D map to efficiently use computing time. MaGe is used to produce these maps, using the optical properties of different surfaces and the optical and scintillation properties of LAr. Especially the properties of LAr are a critical input, which is further discussed in section 4.5. In summary, the concentration of impurities can alter the optical properties. The possibility[7] of time-varying impurity concentrations calls for a permanent in-situ monitor for LAr, realized by LLAMA.

3.2.5 Data taking and analysis

LEGEND-200 uses an offline data-taking and analysis scheme. Waveforms are acquired for individual HPGe detectors and SiPM arrays, which are connected to a FlashCam-based readout system [2]. Data taking is segmented into runs lasting one week each, which feature physics data taking interrupted by a single calibration.

In physics mode, the data acquisition (DAQ) triggers on any energy deposition in one or multiple HPGe detectors and on the LAr instrumentation. The latter condition requires a considerable amount of detected photoelectrons (PE) to avoid high rates due to ^{39}Ar decays. Every trigger in physics mode leads to a readout of all HPGe detectors and LAr instrumentation channels.

The weekly calibration uses four ^{228}Th sources, which are lowered into the array [30]. Only HPGe channels exhibiting a non-zero energy deposition are read out to limit the data rate. The SiPMs of the LAr instrumentation and LLAMA are not biased to prevent

[7] The optical properties of LEGEND-200's LAr did indeed change during commissioning, which is attributed to increased impurity concentrations. See section 7.3.

harm from excessive scintillation light production.

Similar to GERDA, LEGEND-200 blinds the region around $Q_{\beta\beta}$ to prevent biasing the analysis. The offline analysis is tuned to the blinded data, and frozen before every un-blinding stage. Digital signal processing of HPGe and LAr instrumentation data uses the Python-based pygama[8] package.

3.3 LEGEND-1000

The next-generation LEGEND-1000 stage is currently in its planning and R&D phase. Since it profits from the experience gained by its predecessor stage LEGEND-200, which shares its main design principles, LEGEND-1000 can build on mature technologies. This section summarizes the most essential aspects of LEGEND-1000. A much more in-depth description is currently available in [1], while a more recent report is in preparation [2].

3.3.1 Site selection and cosmogenic background

Several sites are in consideration to host LEGEND-1000. With a depth of 6010 m.w.e., the Sudbury Neutrino Observatory Laboratory (SNOLAB) provides a very low remaining muon flux of $3 \times 10^{-6}\,\mathrm{m}^{-2}\,\mathrm{s}^{-1}$ [31]. Access is restricted to a vertical shaft, posing a challenge for the construction of LEGEND-1000.

Conversely, LNGS provides access via a road tunnel, facilitating the delivery of setup components via trucks, which allows for off-site production of several components. Thus, LNGS is currently the preferred location [2]. LEGEND-1000 can be placed in Hall C, at the location formerly occupied by the Borexino detector [32].

In comparison to SNOLAB, the cosmic muon flux at LNGS is about two orders of magnitude higher, around $3.5 \times 10^{-4}\,\mathrm{m}^{-2}\,\mathrm{s}^{-1}$ [4]. While the prompt muon-induced background is subdominant, delayed muon-induced backgrounds constitute a major concern for LEGEND-1000 and are thus studied extensively. Precisely, the in-situ production of ^{77}Ge and ^{77m}Ge by captures of muon-induced neutrons on ^{76}Ge are expected to exceed the background goal even after standard background suppression techniques [2]. However, delayed coincidence cuts are foreseen, sufficiently suppressing the muon-induced background without hampering the $0\nu\beta\beta$ decay search [2, 33].

[8] Pygama is open source and available at GitHub: `https://github.com/legend-exp/pygama`.

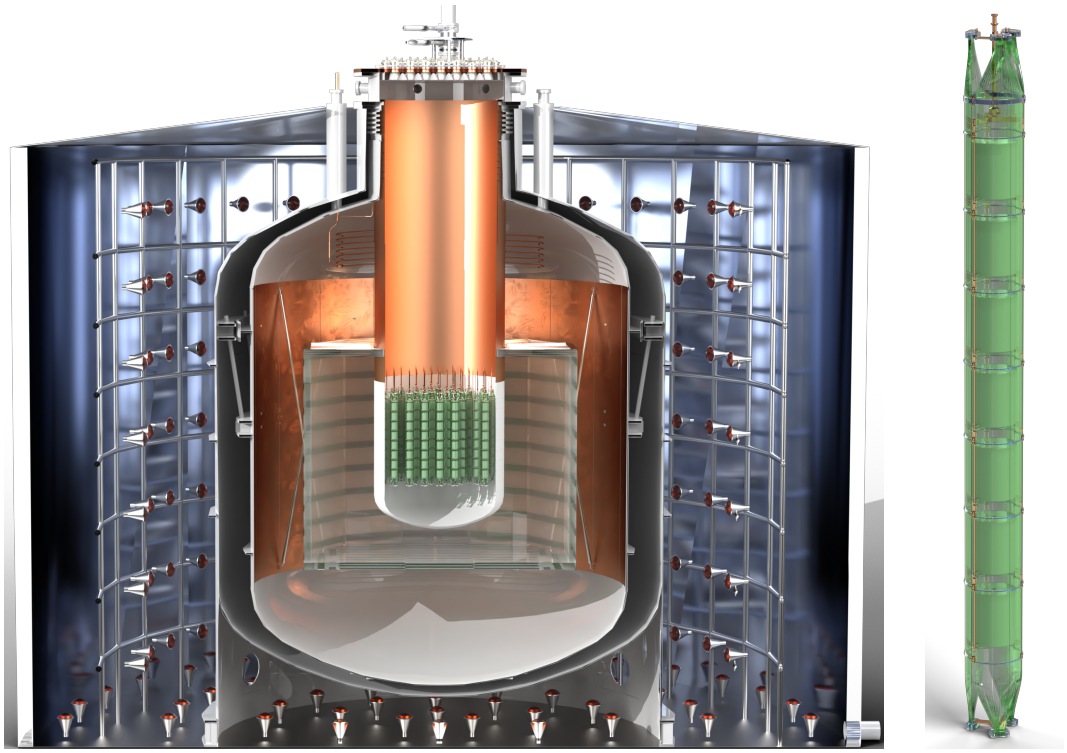

(a) (b)

Figure 3.3: Renders of the LEGEND-1000 setup in the current LNGS design.
(a): The entire setup, including the water tank and the cryostat, which is separated into an outer AAr and an inner UAr volume. The outer volume features instrumented neutron moderators. The reentrant tube houses the detector strings and has an inner WLSR lining.
(b): A single string holding several HPGe detectors together with a LAr instrumentation consisting of three fiber modules.
See text for details. Renders by P. Krause.

3.3.2 Design choices and challenges

The general design of LEGEND-1000 is based on LEGEND-200. Figure 3.3a shows an overview of the current design considered for the LNGS site option. An instrumented water tank will surround a LAr cryostat. In contrast to LEGEND-200, a copper reentrant tube will separate the cryostat into two LAr volumes.

The outer volume will be filled with atmospheric argon (AAr) and acts as an additional

active and passive shield against cosmogenic backgrounds [2]. It contains poly(methyl methacrylate) (PMMA)[9] neutron moderators reducing the fraction of neutron captures in germanium. The moderators carry a dedicated LAr instrumentation, detecting neutron captures crucial for the delayed coincidence cuts mentioned previously. WLSRs line the reentrant tube's outer surface and the cryostat wall's inner surface.

The inner volume will be presumably filled with underground argon (UAr) [2]. Compared to AAr, UAr contains around three orders of magnitude less[10] ^{39}Ar and ^{42}Ar, which would constitute a significant background source for the LAr instrumentation and HPGe detectors, respectively. The novel lock system allows the deployment (and retrieval) of individual detector strings into the UAr volume while leaving all other strings untouched. A rendering of a detector string is shown in figure 3.3b. LEGEND-1000 will employ IC detectors exclusively. Each string has its own LAr instrumentation, composed of three fiber modules [8]. Similar to LEGEND-200, LEGEND-1000 uses a WLSR, which lines the inner surface of the reentrant tube at the height of the detector strings.

LEGEND-1000 foresees doping the AAr volume with trace amounts of xenon to boost the light collection performance. The increased attenuation length will be especially beneficial given the large dimension of the outer vessel. Additionally, xenon doping is under consideration for the UAr volume.

3.3.3 LLAMA for LEGEND-1000

Understanding the impact of xenon doping on the optical properties of LAr is crucial for deciding the target concentration and modeling the expected LAr instrumentation performance. Thus, dedicated measurements have been performed in the Subterranean Cryogenic Argon Research Facility (SCARF), a test cryostat at the Technical University of Munich (TUM), in which LLAMA measured relevant optical properties. Further measurements are planned. Details about the measurement and its analysis are presented in chapter 11, while section 12.3 works out the predicted impact on the LAr instrumentation performance.

Further, the optical properties of LEGEND-200's LAr are among the lessons learned from that stage. Especially, the stability during commissioning informs the LEGEND-1000

[9] While PMMA is preferred, also other materials are under consideration, including polyethylene and PEN.
[10] Due to lack of cosmogenic activation, the UAr's ^{39}Ar content is reduced by a factor of around 1400 compared to AAr [34]. For the same reason, a similar reduction is expected for ^{42}Ar [2].

stage, impacting design choices of the string integration procedure and LAr purification efforts (see chapter 7).

The positive experience in LEGEND-200 strongly suggests the application of LLAMA in both LAr volumes of LEGEND-1000, supervising the filling and subsequent operation phases. Since the failing of some of LLAMA's SiPMs in LEGEND-200 (see appendix B) highlighted the limitations of an unretrievable setup, LLAMA systems in LEGEND-1000 should offer access in case of similar issues. Installing LLAMA in a dedicated string entering the reentrant tube solves this problem for the UAr volume but necessitates changes to the LLAMA setup to fit the smaller diameter of such a string. A retrievable in-situ installation of LLAMA into the AAr volume is more challenging and will presumably require a dedicated lock.

References

[1] N. Abgrall *et al.*, "The Large Enriched Germanium Experiment for Neutrinoless $\beta\beta$ Decay: LEGEND-1000 Preconceptual Design Report," 2021. arXiv: 2107.11462 [physics.ins-det].

[2] N. Abgrall *et al.*, "The Large Enriched Germanium Experiment for Neutrinoless $\beta\beta$ Decay: LEGEND-1000 Conceptual Design Report," internal draft.

[3] M. Agostini *et al.*, "Final Results of GERDA on the Two-Neutrino Double-β Decay Half-Life of Ge76," *Phys. Rev. Lett.*, vol. 131, no. 14, p. 142 501, 2023. DOI: 10.1103/PhysRevLett.131.142501. arXiv: 2308.09795 [nucl-ex].

[4] M. Agostini *et al.*, "Flux Modulations seen by the Muon Veto of the GERDA Experiment," *Astropart. Phys.*, vol. 84, pp. 29–35, 2016. DOI: 10.1016/j.astropartphys.2016.08.002. arXiv: 1601.06007 [physics.ins-det].

[5] K. T. Knöpfle and B. Schwingenheuer, "Design and performance of the GERDA low-background cryostat for operation in water," *JINST*, vol. 17, no. 02, P02038, 2022. DOI: 10.1088/1748-0221/17/02/P02038. arXiv: 2202.03847 [physics.ins-det].

[6] M. Haranczyk *et al.*, "Purification of large volume of liquid argon for LEGEND-200," *PoS*, vol. PANIC2021, p. 102, 2022. DOI: 10.22323/1.380.0102.

[7] C. Wiesinger, "No neutrinos not found," Ph.D. dissertation, Munich, Tech. U., 2020.

[8] P. Krause, "Shining Light on Backgrounds," Ph.D. dissertation, Technische Universität München, 2023.

[9] C. E. Aalseth *et al.*, "Search for Neutrinoless Double-β Decay in ^{76}Ge with the Majorana Demonstrator," *Phys. Rev. Lett.*, vol. 120, no. 13, p. 132 502, 2018. DOI: 10.1103/PhysRevLett.120.132502. arXiv: 1710.11608 [nucl-ex].

[10] M. Agostini *et al.*, "Limits on uranium and thorium bulk content in GERDA Phase I detectors," *Astropart. Phys.*, vol. 91, pp. 15–21, 2017. DOI: 10.1016/j.astropartphys.2017.03.003. arXiv: 1611.06884 [physics.ins-det].

[11] M. Agostini *et al.*, "Pulse shape analysis in Gerda Phase II," *Eur. Phys. J. C*, vol. 82, no. 4, p. 284, 2022. DOI: 10.1140/epjc/s10052-022-10163-w. arXiv: 2202.13355 [physics.ins-det].

[12] T. Comellato, "Inverted Coaxial Detectors for Legend," Ph.D. dissertation, Technische Universität München, 2022, p. 188.

[13] D. Budjas, M. Barnabe Heider, O. Chkvorets, N. Khanbekov, and S. Schönert, "Pulse shape discrimination studies with a Broad-Energy Germanium detector for signal identification and background suppression in the GERDA double beta decay experiment," *JINST*, vol. 4, P10007, 2009. DOI: 10.1088/1748-0221/4/10/P10007. arXiv: 0909.4044 [nucl-ex].

[14] M. Agostini *et al.*, "Production, characterization and operation of ^{76}Ge enriched BEGe detectors in GERDA," *Eur. Phys. J. C*, vol. 75, no. 2, p. 39, 2015. DOI: 10.1140/epjc/s10052-014-3253-0. arXiv: 1410.0853 [physics.ins-det].

[15] R. J. Cooper, D. C. Radford, P. A. Hausladen, and K. Lagergren, "A novel HPGe detector for gamma-ray tracking and imaging," *Nucl. Instrum. Meth. A*, vol. 665, pp. 25–32, 2011. DOI: 10.1016/j.nima.2011.10.008.

[16] M. Agostini *et al.*, "Characterization of inverted coaxial ^{76}Ge detectors in GERDA for future double-β decay experiments," *Eur. Phys. J. C*, vol. 81, no. 6, p. 505, 2021. DOI: 10.1140/epjc/s10052-021-09184-8. arXiv: 2103.15111 [physics.ins-det].

[17] N. Abgrall *et al.*, "The Majorana Demonstrator radioassay program," *Nucl. Instrum. Meth. A*, vol. 828, pp. 22–36, 2016. DOI: 10.1016/j.nima.2016.04.070. arXiv: 1601.03779 [physics.ins-det].

[18] L. Manzanillas *et al.*, "Optical properties of low background PEN structural components for the Legend-200 experiment," *JINST*, vol. 17, no. 09, P09007, 2022. DOI: 10.1088/1748-0221/17/09/P09007. arXiv: 2204.13747 [physics.ins-det].

[19] L. Manzanillas *et al.*, "Usage of PEN as self-vetoing structural material in the LEGEND experiment," *JINST*, vol. 17, no. 03, p. C03031, 2022. DOI: 10.1088/1748-0221/17/03/C03031.

[20] M. Agostini *et al.*, "Liquid argon light collection and veto modeling in GERDA Phase II," *Eur. Phys. J. C*, vol. 83, no. 4, p. 319, 2023, ISSN: 1434-6052. DOI: 10.1140/epjc/s10052-023-11354-9.

[21] C. Benson, G. Orebi Gann, and V. Gehman, "Measurements of the intrinsic quantum efficiency and absorption length of tetraphenyl butadiene thin films in the vacuum ultraviolet regime," *Eur. Phys. J. C*, vol. 78, no. 4, p. 329, 2018. DOI: 10.1140/s10052-018-5807-z. arXiv: 1709.05002 [physics.ins-det].

[22] A. Lubashevskiy *et al.*, "Mitigation of ^{42}Ar/^{42}K background for the GERDA Phase II experiment," *Eur. Phys. J. C*, vol. 78, no. 1, p. 15, 2018. DOI: 10.1140/epjc/s10052-017-5499-9. arXiv: 1708.00226 [physics.ins-det].

[23] G. R. Araujo, "Advancing Neutrinoless Double Beta Decay Search with LEGEND and MONUMENT, and Exploring Passive Neutrino Detectors with PALEOCCENE," Ph.D. dissertation, Universität Zürich, 2023.

[24] A. Leonhardt, "Characterization of Wavelength Shifters for Rare-Event Search Experiments with a VUV Spectrofluorometer," *Master's thesis, TUM*, 2021. DOI: 10.13140/RG.2.2.25067.87849.

[25] M. Agostini *et al.*, "Search for exotic physics in double-β decays with GERDA Phase II," *JCAP*, vol. 12, p. 012, 2022. DOI: 10.1088/1475-7516/2022/12/012. arXiv: 2209.01671 [nucl-ex].

[26] E. Bossio, "Beyond the Standard Model physics searches with double-beta decays," Ph.D. dissertation, Munich, Tech. U., 2022.

[27] S. Agostinelli *et al.*, "Geant4—a simulation toolkit," *Nucl. Instrum. Meth. A*, vol. 506, no. 3, pp. 250–303, 2003, ISSN: 0168-9002. DOI: 10.1016/S0168-9002(03)01368-8.

[28] M. Boswell *et al.*, "MaGe-a Geant4-Based Monte Carlo Application Framework for Low-Background Germanium Experiments," *IEEE Transactions on Nuclear Science*, vol. 58, no. 3, pp. 1212–1220, 2011. DOI: 10.1109/TNS.2011.2144619.

[29] D. C. Radford. "Siggen." (2014), [Online]. Available: https://github.com/radforddc/icpc_siggen (visited on 01/29/2024).

[30] L. Baudis *et al.*, "Calibration sources for the LEGEND-200 experiment," *JINST*, vol. 18, no. 02, P02001, 2023. DOI: 10.1088/1748-0221/18/02/P02001. arXiv: 2211.05026 [physics.ins-det].

[31] N. J. T. Smith, "The SNOLAB deep underground facility," *Eur. Phys. J. Plus*, vol. 127, p. 108, 2012. DOI: 10.1140/epjp/i2012-12108-9.

[32] G. Alimonti *et al.*, "The Borexino detector at the Laboratori Nazionali del Gran Sasso," *Nucl. Instrum. Meth. A*, vol. 600, pp. 568–593, 2009. DOI: 10.1016/j.nima.2008.11.076. arXiv: 0806.2400 [physics.ins-det].

[33] C. Wiesinger, L. Pandola, and S. Schönert, "Virtual depth by active background suppression: Revisiting the cosmic muon induced background of GERDA Phase II," *Eur. Phys. J. C*, vol. 78, no. 7, p. 597, 2018. DOI: 10.1140/epjc/s10052-018-6079-3. arXiv: 1802.05040 [hep-ex].

[34] P. Agnes *et al.*, "Results from the first use of low radioactivity argon in a dark matter search," *Phys. Rev. D*, vol. 93, no. 8, p. 081 101, 2016. DOI: 10.1103/PhysRevD.93.081101.

Part III

Optical properties of liquid argon in LEGEND-200

Chapter 4

Theory of liquid argon scintillation

4.1 Advantages and applications

Being clean, scalable, and efficient in light output makes liquid noble gases an attractive detection medium in low-background experiments. Contemporary detectors almost[1] exclusively use liquid argon or xenon targets. These elements are highly dense and can be cooled passively with liquid nitrogen.

Radioactive isotopes pose a critical constituent. Krypton is rendered practically unusable for low-background applications due to substantial amounts of the beta emitter ^{85}Kr [2]. The main radioisotope present in LAr extracted from the atmosphere is ^{39}Ar, having a specific activity of about 1 Bq/kg [3]. As mitigation, underground sources such as CO_2 wells [4] are conceived and employed by large-scale experiments like DarkSide-50 [5]. Xenon has no long-lived radioisotope except from ^{136}Xe, which undergoes double beta decay only [6].

With detectors such as XENONnT [7], and LUX-ZEPLIN (LZ) [8], the multi-ton era of xenon-based experiments was reached, despite the comparably high cost due to the low atmospheric abundance of xenon. The faster photon emission time of liquid xenon (LXe) compared to LAr [9] is advantageous for applications that face high rates and hence have to reduce dead times. Furthermore, the primary emission wavelength of LXe is at 175 nm [10], which is easier to detect with state-of-the-art light readout systems than the 128 nm [9] of LAr [11]. Doping LAr with LXe at ppm levels has been proposed to combine the mentioned advantages of LXe with the cost-efficiency of LAr [12, 13].

The direct search for dark matter is an important field of application for liquid noble gas

[1] MiniCLEAN is a notable exception, designed to exchange the liquid argon target with liquid neon [1].

detectors [7, 8, 14–19]. Current and future experiments exist in single-phase (detecting only scintillation light) or dual-phase TPC (ionization is recorded additionally) geometry. LAr TPCs are also applied for high-intensity neutrino beam experiments [20–22]. Since xenon can be enriched in the $0\nu\beta\beta$ decay candidate isotope ^{136}Xe, $0\nu\beta\beta$ decay search is conducted with LXe TPC technology [23, 24]. Furthermore, LAr is applied in a secondary detector system of $0\nu\beta\beta$ decay search in ^{76}Ge [25–27], as presented in chapter 3.

4.2 Optical properties of pure liquid argon

4.2.1 Scintillation mechanism

This section focuses on the key aspects of liquid argon scintillation. More extensive descriptions of the mechanisms involved can be found e.g. in [28, 29]. A simplified sketch of the processes described in the following is presented in figure 4.1.

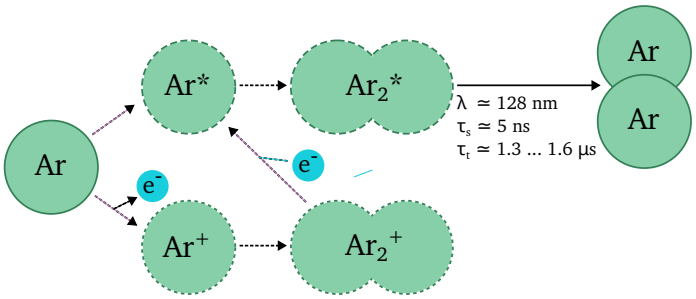

Figure 4.1: Simplified sketch of argon excimer formation and decay. Non-radiative energy transfers are drawn in dashed, while the radiative decay of the excimer Ar_2^* is drawn with a continuous line.

Ionizing radiation depositing energy within LAr creates ionized (Ar^+) or highly excited (Ar^{**}) argon atoms. The Ar^{**} atoms de-excite to the lowest excited state Ar^* [30]. The resonance lines from the direct decay of Ar^* to the ground state are invisible in liquid argon since the photons are immediately re-absorbed by Ar atoms [29]. Instead, excited dimers (excimers) Ar_2^* are formed in either the singlet ($^1\Sigma_u^+$) or triplet ($^3\Sigma_u^+$) state [31]. Both states decay to the ground state ($^1\Sigma_g^+$) via emission of a VUV photon; the emission spectrum is around 10 nm broad and centered at 128 nm [9]. The ground state of the Ar_2 molecule is not stable and thus disintegrates into two neutral Ar atoms, which prevents

re-absorption of the VUV emission [30]. The Ar^+ ions and neutral Ar atoms form Ar_2^+ molecular ions. Theose recombine with electrons to form Ar^{**} and a neutral argon atom [32].

Both spin configurations have distinct lifetimes. The lifetime of the singlet state (τ_s) is around 4.4 ns to 10 ns (see table 1 in [33] and references therein). For the triplet state, the experimentally measured lifetimes τ_t range from 1300 ns to 1600 ns [33]. Values below 1300 ns have been measured but can be explained by unrecognized impurities [34]. The lifetimes were found to be independent of energy and particle type of the incident radiation [9, 12, 33, 35]. However, the ratio of singlet to triplet light emission depends on the primary particle and its energy [33], enabling PSD [12, 35]. The redistribution of excitation energy between both spin states with hot electrons immediately after excitation yields a possible explanation [36]:

$$^1\Sigma_u^+ + e^- \longleftrightarrow ^3\Sigma_u^+ + (e^-)'. \tag{4.1}$$

The much faster decay of the singlet state leads to a dominant transition of excitation from triplet to singlet in the early phase, in the presence of high electron densities [33]. Thus, particles leading to a high linear energy transfer (LET), such as ions, show an increased ratio of singlet to triplet emission, e.g. around 3 for a beam of sulfur ions [33]. For very low LET, mixing is subdominant and a singlet-to-triplet ratio of around 0.3 is observed [28].

Literature reports an additional intermediate component affecting the pulse shape in the time region around 30 ns to 100 ns [9, 12, 33, 35, 37–40]. The origin is still the context of discussion. Since most experiments employ wavelength shifters such as TPB, delayed emissions of these substances can cause this component, as explored by [40, 41]. However, it is also found in detectors devoid of wavelength shifters ([33] and this work: see chapter 9). In [33], it is attributed to finite recombination times of the ionized molecules with electrons. Following [42], the time dependence of this component is described by

$$I_i(t) = \frac{C}{(1 + t/\tau_{rec})^2}, \tag{4.2}$$

with τ_{rec} referred to as the recombination time constant. The factor C is independent of t but depends on the temperature and the initial electron density.

4.2.2 VUV light propagation

Photons in liquid argon are subject to absorption and scattering; both processes can be combined in *attenuation*. Detectors unable to disentangle absorption and scattering will see the effective attenuation length (mean free path length) l_{att}:

$$\frac{1}{l_{att}(\lambda)} = \frac{1}{l_{abs}(\lambda)} + \frac{1}{l_{scat}(\lambda)}, \tag{4.3}$$

where l_{abs} and l_{scat} denote the absorption and scattering length, respectively. The wavelength-dependent intensity I' after traveling a path of length x is then described by the Beer-Lambert-Law [43]:

$$I'(x,\lambda) = I(\lambda)\, e^{-\frac{x}{l_{att}(\lambda)}}. \tag{4.4}$$

In [44], a vanishing absorption cross-section for pure LAr for its own scintillation light is motivated by the first excited energy levels exceeding those photons' energies. Impurities are, however, responsible for a finite absorption length for scintillation photons [45] in LAr volumes not highly purified, which is discussed in detail in section 4.3.2. In contrast, Rayleigh scattering of LAr scintillation photons is present in the pure medium. In this process, photons elastically scatter off particles much smaller than their wavelength. Impurities do not alter the process due to being scarce. The cross-section of Rayleigh scattering is proportional to the fourth power of the photons' wavelength [46], thus varying significantly over the LAr scintillation peak. The Rayleigh scattering length can be obtained from attenuation length measurements without impurities causing absorption [47]. An attenuation length of (66 ± 3) cm was measured in a wavelength-integrated measurement [48]. However, a later wavelength-resolved study finds a lower threshold of the attenuation at 128 nm of 110 cm [49].

Alternatively, the Rayleigh scattering length can be calculated from material properties such as dielectric constant, temperature, and density. A value of 90 cm at 128 nm was obtained by [47]. The result's relative uncertainty of 35 % is dominated by the extrapolation of the dielectric constant from the gas to the liquid phase. More recently, the measurement of the group velocity of 128 nm photons in LAr allows determining the dielectric constant and hence the Rayleigh scattering length of (99.1 ± 2.3) cm with improved accuracy [50].

4.3 Influence of impurities

Real-world applications of LAr have to cope with impurities altering the production and propagation of VUV photons. Studying the impact of impurities has become increasingly important since

- larger detectors are proposed; thus, the attenuation length becomes more critical,
- higher energy resolution is required; hence, minimizing quenching is paramount, and
- advanced PSD algorithms require a precise understanding of the time structure of light emission.

Thus motivated, several measurements of optical parameters of LAr containing different concentrations[2] of various impurities have been conducted [11, 44, 51–55]. Though technically an impurity, the effects of xenon traces in LAr differ strongly due to re-emission and wavelength-shifting features. Thus, the properties of argon-xenon mixtures are discussed later in section 4.4. Conversely, the affected LAr properties due to non-radiative impurities (such as O_2 and N_2) are discussed in the following.

4.3.1 Quenching of primary emission

Via the two-body reaction

$$\mathrm{Ar}_2^* + \chi \rightarrow 2\mathrm{Ar} + \chi\,, \tag{4.5}$$

argon excimers are quenched by an impurity χ non-radiatively [51]. This applies to e.g. N_2, whose excited states are unlikely reached by this process [52], thus no visible photons[3] are observed [51]. The quenching process competes with the radiative de-excitation of Ar_2^*. Thus, the observed emission time constants are reduced, and effective lifetimes $\tau'_{s,t}$ can be introduced [51]

$$\frac{1}{\tau'_j} = \frac{1}{\tau_j} + k_{Q,\chi}\,[\chi\,], \tag{4.6}$$

[2] Concentrations in this work are generally given in terms of mole fractions. A detailed description of different definitions of this quantity in literature is presented in appendix A.

[3] Those photons appear in the gas phase of N_2-doped Ar and are known as the second positive group [51]

with $j = s, t$ referring to the singlet and triplet state, respectively. $k_{Q,\chi}$ denotes the *rate constant* for a specific impurity. The time-integrated intensity is reduced from I_j to $I'_{Q,j}([\chi])$:

$$I'_{Q,j}([\chi]) = I_j \frac{\tau'_j([\chi])}{\tau_j}. \tag{4.7}$$

Since the lifetime of $^3\Sigma_u^+$ is much longer, a reduction of the effective triplet lifetime takes place, while the effect on the singlet emission is negligible [51]. With that, the quenched total intensity can be written as

$$I'_Q([\chi]) = I\left(\eta_s + \frac{\eta_t}{1 + \tau_t\, k_{Q,\chi}\,[\chi]}\right), \tag{4.8}$$

where η_s and η_t denote the singlet and triplet fractions for pure LAr, respectively ($\eta_j = \frac{I_j}{I}$) and $\eta_s + \eta_t = 1$ holds.

4.3.2 Absorption of liquid argon scintillation light

Once emitted, LAr scintillation photons can be subject to absorption caused by diluted contaminants. In contrast to quenching effects, this leads to a reduction of the overall light output regardless of the emitting excimer's spin configuration. The shape of the photon time spectrum is not affected in contrast to the quenching process[4]. The mean free path length of photons in a transparent medium containing an absorbing substance χ in concentration $[\chi]$, which has an *absorption coefficient* $k_{A,\chi}$ reads:

$$l_{abs,\chi}(\lambda, [\chi]) = \frac{1}{k_{A,\chi}(\lambda)[\chi]}. \tag{4.9}$$

Using the Beer-Lambert-Law (eq. 4.4), the intensity remaining after absorption-induced losses is:

$$I'_A(x, \lambda, [\chi]) = I(\lambda)\, e^{-x\, k_{A,\chi}(\lambda)[\chi]}. \tag{4.10}$$

[4]This is true if the absorbed energy is not re-emitted in photons. For example, in the case of oxygen in a liquid medium, the energy is mainly dissipated as heat [44].

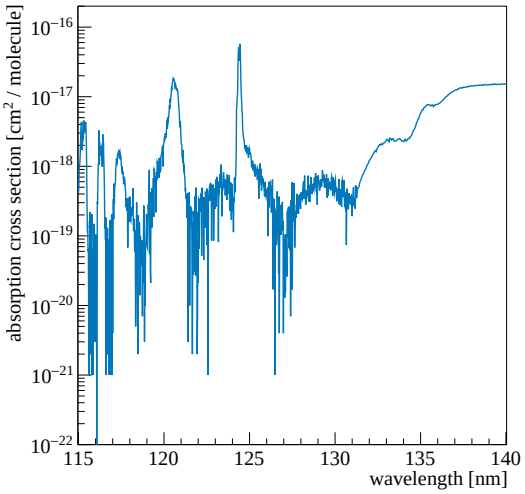

Figure 4.2: Absorption spectrum of gaseous oxygen from [56]. The absorption bands from photo-dissociation dominate lower wavelengths, while at higher wavelengths, the Schumann-Runge continuum takes over [44].

The potentially wavelength-dependent absorption coefficient can be obtained from the *absorption cross-section* $\sigma_{A,\chi}$ [44]:

$$k_{A,\chi}(\lambda) = \sigma_{A,\chi}(\lambda)\, 10^{-6}\, \rho_{LAr}\, \frac{N_A}{A_{Ar}}, \tag{4.11}$$

where ρ_{LAr} is the mass density of LAr, A_{Ar} is its molar mass and N_A denotes Avogadro's number.

Absorption cross-sections typically show absorption bands in the region of LAr emission caused by photo-dissociation. This is shown for gaseous oxygen in figure 4.2, where also the so-called Schumann-Runge continuum at higher wavelengths is visible [44]. Since the absorption cross-section varies over several orders of magnitude, the wavelength-integrated intensity over the distance traveled does not follow a single exponential decay. This was pointed out by [45] after observing attenuation features later attributed to xenon [49]. A model of the absorption of LAr scintillation photons can be established with one of the following two inputs:

- **Wavelength-resolved** determination of $k_{A,\chi}(\lambda)$ over the full LAr VUV emission range. Ideally, this information is provided by measurements in doped LAr, like in

xenon-doped liquid argon [49], since some absorption features are only present in the mixture. This is, e.g. the case for an absorption band found in xenon-doped liquid argon, which is attributed to a Wannier-Mott[5] impurity state [49].

Since such measurements are scarce, an alternative approach is to estimate the absorption cross-section of a LAr impurity from measurements in its pure, warm gas state[6]. Apart from being unable to predict mixture-exclusive absorption features, the spectral distortions caused by the transition to the cold and dense state are not precisely known. For oxygen-doped argon, an arbitrary broadening of the absorption cross-section spectrum was shown to fit wavelength-integrated measurements [44]. Motivated by the observed blue-shift of xenon and mercury lines from gas to LAr, [58] applied a blue shift of 7 nm to absorption spectra in the gas phase.

- **Wavelength-integrated** measurements of the intensity at several distances allow to model propagation of LAr VUV scintillation light without depending on absorption spectra. This can be achieved by varying the distance between a scintillation light source and a detector in-situ [59] or by employing multiple photo-detectors at several distances (this work: see chapter 5). Alternatively, since both x and $[\chi]$ appear in the exponent of the Beer-Lambert-Law (eq. 4.4), it is possible to only change the dopant concentration for the same effect [44, 53, 54]. Results of wavelength-integrated measurements of O_2 [44] and CH_4 [54] dopants in LAr are found to be consistent with absorption cross-sections in gas state at room temperature.

4.4 Xenon-doped liquid argon

Xenon alters the optical properties of LAr in more complex ways than most "typical" impurities such as O_2 and N_2. Also, rather than being regarded as a contaminant for which a reduction is strived for, it is frequently studied as a dopant enhancing the performance of future LAr detectors such as DUNE [55]. Especially, LAr doped with Xe profits from a longer attenuation length [48, 60] and enhanced effective light yield due to an improved efficiency of typical wavelength shifters [61]. Additionally, the light

[5] See section 4.4 for more details about the states of xenon-doped LAr.
[6] A collection of cross-sections of various gases can be found here: [57].

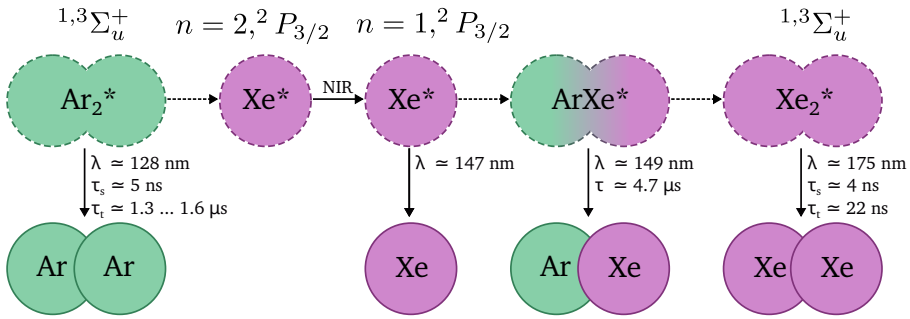

Figure 4.3: Simplified energy transfer scheme from Ar_2^* to Xe_2^*. Radiative transitions are shown with continuous arrows, while non-radiative collisional energy transfer is drawn dashed.

emission happens within a much smaller time window, which worsens PSD properties at low Xe concentration, which gets, however, restored at higher concentrations (starting around 500 µg/g) [62]. Xenon impurities in LAr both quench the Ar_2^* excimers and absorb VUV photons from the LAr scintillation peak. The mechanics are discussed in the following, starting with the excimer quenching, for which a simplified sketch is provided in figure 4.3.

The energy transfer from Ar_2^* excimers[7] to the Wannier-Mott state ($n = 2,^2P_{3/2}$ trapped exciton) was proposed by [49, 63]. The Wannier-Mott state is exclusive to xenon-doped LAr and has no equivalence in the pure xenon gas. The energy level matches the LAr scintillation peak almost exactly, boosting energy transfer [49]. A subsequent radiative transition to the perturbed $^3P_1(n = 1,^2P_{3/2})$ atomic xenon state [64] could explain the near-infrared (NIR) emission found in xenon-doped LAr [49, 65]. Mix states ArXe* are then formed from the Xe*(^{3}P$_1$) states [66]. Those can either decay directly, emitting photons at around 149 nm [63, 66] with a lifetime of around 4.7 µs [55] or form Xe_2^* [67]. Analogous to argon, the Xe_2^* excimers exist in singlet ($^1\Sigma_u^+$) and triplet ($^3\Sigma_u^+$) states, which decay under VUV emission with lifetimes of 4.3 ns and 22 ns, respectively [9]. The emission spectrum peaks at 174 nm, which corresponds to the second excimer continuum of xenon [65].

Additionally, the formation of excited xenon species is possible via absorption of VUV photons previously emitted by Ar_2^* excimers [60]. Broad and strong absorption

[7] For the process of Ar_2^* formation, see section 4.2.1.

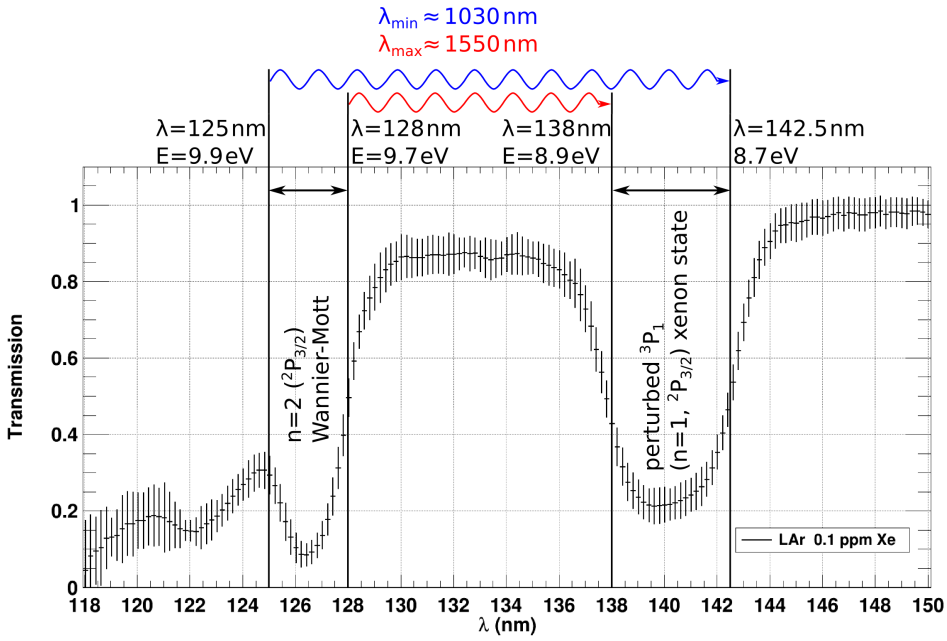

Figure 4.4: Optical transmission of a LAr sample doped with 0.1 ppm of xenon over a path length of 11.6 cm. Two absorption bands from the $n = 2,^2P_{3/2}$ Wannier-Mott impurity state and the perturbed $^3P_1(n = 1,^2P_{3/2})$ atomic xenon state are visible. Taken from [63].

bands of ground state ($^1S_0$) xenon atoms in LAr exist, two of which are shown in figure 4.4. One corresponds to the perturbed $^3P_1(n = 1,^2P_{3/2})$ atomic xenon state and is centered at 140 nm [49]. More important is the $(n = 2,^2P_{3/2})$ Wannier-Mott state, for its position (126.5 nm) almost exactly fits the LAr scintillation peak [49]. Following the energy transfer scheme shown in figure 4.3 from the Wannier-Mott state, eventually Xe_2^* excimers are produced, which decay radiatively. These processes explain the re-emission of the singlet component of LAr scintillation found for xenon concentrations starting from around 600 µg/g by [62]. For that concentration region, the non-radiative excitation transfer rate was shown to be insufficient to fully explain the Xe_2^* formation from the short-lived Ar_2^* state.

Thus, xenon in LAr acts as a diluted wavelength shifter. Even though most light detectors are more sensitive to the emission wavelength region of Xe_2^* than to Ar_2^*, a reduction of the detected light is possible. This is the case for detectors missing photons scattered out of their flight path since the re-emission happens isotropically. The reduction

of the effective light yield with trace amounts of xenon is studied in [68]. Due to the strong wavelength dependence of the absorption cross-section, the intensity over traveled path length deviates from a single exponential function. Increasing the xenon concentration restores the transparency of the mixture as the non-radiative energy transfer channel is enhanced, and the resulting Xe_2^* emission is not attenuated in xenon-doped LAr [63, 68].

For real-world applications, it is essential to understand the effects of other impurities, such as N_2, on the optical properties of xenon-doped LAr. Since energy transfer to xenon dopants competes with the quenching by impurities, xenon doping can mitigate the loss in effective light yield due to contaminants. This mitigation has been shown in calculations by [69] for hypothetical xenon and N_2 concentrations of 1000 ppm and 50 ppm, respectively. Measurements with 1.8 ppm xenon and N_2 levels in the ppm range have been conducted by [55][8], finding that additionally to Ar_2^*, the $ArXe^*$ excimer is subject to quenching by nitrogen, as expected by [68, 69].

4.5 Parameters for modeling liquid argon detectors

As discussed in section 4.3, three key optical properties of LAr (primary light yield, effective triplet lifetime, and attenuation length) are impacted by impurities. Both the primary light yield and the effective triplet lifetime are subject to quenching. Thus, the time structure of the scintillation is altered, while the wavelength spectrum is unchanged. Additionally, optically active impurities absorb part of the emitted light during propagation, leading to a reduced attenuation length. The absorption changes the wavelength spectrum of traveling protons, while the time structure is not affected[9].

These optical parameters are fundamental to model large-volume LAr detectors. The primary light yield affects the energy resolution, trigger threshold, and photon statistics for PSD application [70]. Employing PSD requires knowledge of the time structure of the scintillation and, thus, the effective triplet lifetime. The attenuation length is a crucial parameter to model the location-dependent efficiency, as shown for the GERDA LAr detector in [71].

Many LAr detectors, such as ArDM [58], MicroBooNE [72], GERDA [73] and LEGEND-

[8] Note, that [55] uses “ppm” in terms of mass fraction for xenon concentrations, while using “ppm” in terms of mole fraction for nitrogen concentrations, and lacks any explicit clarification.

[9] This holds as long as no re-emission takes place, which can be caused e.g. by xenon impurities [62].

200 (this work: see sections 6 and 10) face significant impurity levels. This requires obtaining the aforementioned optical parameters corresponding to the present impurity composition.

On the one hand, this can be achieved by comparing simulations with data obtained from physics runs [34, 58, 72] or dedicated calibration campaigns [73]. However, it is challenging to disentangle the light yield, especially the attenuation length and other unknown optical parameters, notably the reflectivities at VUV wavelengths, from each other [58, 72]. Additional mass spectroscopy measurements can support the search for the responsible impurities; hence inductively coupled plasma mass spectrometry (ICPMS) campaigns were conducted for ArDM [58] and MicroBooNE [72, 74]. Though, neither the impurities causing the low attenuation length of 0.5 m in ArDM nor the suspected contamination responsible for the reduced effective light yield in MicroBooNE were found with this technique so far [58, 72].

On the other hand, dedicated measurements can provide and disentangle the optical parameters of LAr. For example, modeling the liquid argon volume of GERDA profits from the attenuation length obtained in a dedicated measurement by LLAMA.

Singular measurements are sufficient only in case the optical properties are stable over the runtime of the experiment, which cannot always be achieved. MicroBooNE observed a drop in effective light yield of around 50 %[10] over the course of two years [72]. In GERDA, the effective triplet lifetime decreased from around 1.00 µs to 0.91 µs for around one month starting at the end of August 2018. This incident is attributed to contamination due to maintenance works on the cryostat [75]. Except for that time frame, the LAr quality was stable over almost four years of GERDA Phase-II data taking.

In conclusion, a model of LAr detectors requires permanent monitoring of key optical properties to account for potential changes in the impurity composition. Thus, LLAMA was developed and deployed into the LEGEND-200 cryostat. The instrument is explained in detail in the next section.

[10] This value corresponds to events close to the cathode; the drop at the anode is about 25 % [72].

References

[1] K. Rielage *et al.*, "Update on the MiniCLEAN Dark Matter Experiment," *Phys. Procedia*, vol. 61, pp. 144–152, 2015. DOI: 10.1016/j.phpro.2014.12.024. arXiv: 1403.4842 [physics.ins-det].

[2] M. Lopes and V. Chepel, "Liquid Rare Gas Detectors: Recent Developments and Applications," *IEEE Trans. Dielectr. Electr. Insul.*, vol. 10, pp. 994–1005, 2004. DOI: 10.1109/TDEI.2003.1255777.

[3] P. Benetti *et al.*, "Measurement of the specific activity of 39Ar in natural argon," *Nucl. Instrum. Meth. A*, vol. 574, no. 1, pp. 83–88, 2007, ISSN: 0168-9002. DOI: 10.1016/j.nima.2007.01.106.

[4] J. Xu *et al.*, "A study of the trace 39Ar content in argon from deep underground sources," *Astropart. Phys.*, vol. 66, pp. 53–60, 2015, ISSN: 0927-6505. DOI: 10.1016/j.astropartphys.2015.01.002.

[5] P. Agnes *et al.*, "Low-Mass Dark Matter Search with the DarkSide-50 Experiment," *Phys. Rev. Lett.*, vol. 121, no. 8, p. 081 307, 2018. DOI: 10.1103/PhysRevLett.121.081307. arXiv: 1802.06994 [astro-ph.HE].

[6] E. Brown, S. Rosendahl, C. Huhmann, C. Weinheimer, and H. Kettling, "In situ measurements of Krypton in Xenon gas with a quadrupole mass spectrometer following a cold-trap at a temporarily reduced pumping speed," *JINST*, vol. 8, P02011, 2013. DOI: 10.1088/1748-0221/8/02/P02011. arXiv: 1212.5136 [physics.ins-det].

[7] E. Aprile *et al.*, "Search for New Physics in Electronic Recoil Data from XENONnT," *Phys. Rev. Lett.*, vol. 129, no. 16, p. 161 805, 2022. DOI: 10.1103/PhysRevLett.129.161805.

[8] J. Aalbers *et al.*, "First Dark Matter Search Results from the LUX-ZEPLIN (LZ) Experiment," 2022. arXiv: 2207.03764 [hep-ex].

[9] A. Hitachi, T. Takahashi, N. Funayama, K. Masuda, J. Kikuchi, and T. Doke, "Effect of ionization density on the time dependence of luminescence from liquid argon and xenon," *Phys. Rev. B*, vol. 27, no. 9, pp. 5279–5285, 1983. DOI: 10.1103/PhysRevB.27.5279.

[10] K. Fujii *et al.*, "High-accuracy measurement of the emission spectrum of liquid xenon in the vacuum ultraviolet region," *Nucl. Instrum. Meth. A*, vol. 795, pp. 293–297, 2015, ISSN: 0168-9002. DOI: 10.1016/j.nima.2015.05.065.

[11] S. Kubota, M. Hishida, M. Suzuki, and J.-z. Ruan, "Liquid and solid argon, krypton and xenon scintillators," *Nucl. Instrum. Meth. Phys. Res.*, vol. 196, no. 1, pp. 101–105, 1982, ISSN: 0167-5087. DOI: 10.1016/0029-554X(82)90623-1.

[12] P. Peiffer, T. Pollmann, S. Schönert, A. Smolnikov, and S. Vasiliev, "Pulse shape analysis of scintillation signals from pure and xenon-doped liquid argon for radioactive background identification," *JINST*, vol. 3, no. 08, P08007–P08007, 2008, ISSN: 1748-0221. DOI: 10.1088/1748-0221/3/08/P08007.

[13] L. Bomben, "The DUNE photon detection system," *Nuovo Cim. C*, vol. 45, no. 5, p. 137, 2022. DOI: 10.1393/ncc/i2022-22137-1.

[14] J. Billard *et al.*, "Direct detection of dark matter—APPEC committee report*," *Rept. Prog. Phys.*, vol. 85, no. 5, p. 056 201, 2022. DOI: 10.1088/1361-6633/ac5754. arXiv: 2104.07634 [hep-ex].

[15] H. Zhang *et al.*, "Dark matter direct search sensitivity of the PandaX-4T experiment," *Sci. China Phys. Mech. Astron.*, vol. 62, no. 3, p. 31 011, 2019. DOI: 10.1007/s11433-018-9259-0. arXiv: 1806.02229 [physics.ins-det].

[16] J. Aalbers *et al.*, "DARWIN: towards the ultimate dark matter detector," *JCAP*, vol. 11, p. 017, 2016. DOI: 10.1088/1475-7516/2016/11/017. arXiv: 1606.07001 [astro-ph.IM].

[17] R. Ajaj *et al.*, "Search for dark matter with a 231-day exposure of liquid argon using DEAP-3600 at SNOLAB," *Phys. Rev. D*, vol. 100, no. 2, p. 022 004, 2019. DOI: 10.1103/PhysRevD.100.022004. arXiv: 1902.04048 [astro-ph.CO].

[18] P. Agnes *et al.*, "DarkSide-50 532-day Dark Matter Search with Low-Radioactivity Argon," *Phys. Rev. D*, vol. 98, no. 10, p. 102 006, 2018. DOI: 10.1103/PhysRevD.98.102006. arXiv: 1802.07198 [astro-ph.CO].

[19] C. E. Aalseth *et al.*, "DarkSide-20k: A 20 tonne two-phase LAr TPC for direct dark matter detection at LNGS," *Eur. Phys. J. Plus*, vol. 133, p. 131, 2018. DOI: 10.1140/epjp/i2018-11973-4. arXiv: 1707.08145 [physics.ins-det].

[20] M. Antonello *et al.*, "A Proposal for a Three Detector Short-Baseline Neutrino Oscillation Program in the Fermilab Booster Neutrino Beam," 2015. arXiv: 1503.01520 [physics.ins-det].

[21] A. Hahn *et al.*, "The LBNE 35 Ton Prototype Cryostat," in *2014 IEEE Nuclear Science Symposium and Medical Imaging Conference and 21st Symposium on Room-Temperature Semiconductor X-ray and Gamma-ray Detectors*, 2016. DOI: 10.1109/NSSMIC.2014.7431158.

[22] A. Abed Abud *et al.*, "Deep Underground Neutrino Experiment (DUNE) Near Detector Conceptual Design Report," *Instruments*, vol. 5, no. 4, p. 31, 2021. DOI: 10.3390/instruments5040031. arXiv: 2103.13910 [physics.ins-det].

[23] G. Anton *et al.*, "Search for Neutrinoless Double-β Decay with the Complete EXO-200 Dataset," *Phys. Rev. Lett.*, vol. 123, no. 16, p. 161 802, 2019. DOI: 10.1103/PhysRevLett.123.161802. arXiv: 1906.02723 [hep-ex].

[24] J. B. Albert *et al.*, "Sensitivity and Discovery Potential of nEXO to Neutrinoless Double Beta Decay," *Phys. Rev. C*, vol. 97, no. 6, p. 065 503, 2018. DOI: 10.1103/PhysRevC.97.065503. arXiv: 1710.05075 [nucl-ex].

[25] M. Agostini *et al.*, "Final Results of GERDA on the Search for Neutrinoless Double-β Decay," *Phys. Rev. Lett.*, vol. 125, no. 25, p. 252 502, 2020. DOI: 10.1103/PhysRevLett.125.252502. arXiv: 2009.06079 [nucl-ex].

[26] N. Abgrall *et al.*, "The Large Enriched Germanium Experiment for Neutrinoless Double Beta Decay (LEGEND)," *AIP Conf. Proc.*, vol. 1894, no. 1, p. 020 027, 2017. DOI: 10.1063/1.5007652. arXiv: 1709.01980 [physics.ins-det].

[27] N. Abgrall *et al.*, "The Large Enriched Germanium Experiment for Neutrinoless $\beta\beta$ Decay: LEGEND-1000 Preconceptual Design Report," 2021. arXiv: 2107.11462 [physics.ins-det].

[28] T. Heindl, "Die Szintillation von flüssigem Argon," Dissertation, Technische Universität München, 2011.

[29] M. A. Hofmann, "Liquid Scintillators and Liquefied Rare Gases for Particle Detectors," Dissertation, Technische Universität München, 2012.

[30] T. Doke, A. Hitachi, J. Kikuchi, K. Masuda, H. Okada, and E. Shibamura, "Absolute Scintillation Yields in Liquid Argon and Xenon for Various Particles," *Jpn. J. Appl. Phys.*, vol. 41, no. 3R, p. 1538, 2002. DOI: 10.1143/JJAP.41.1538.

[31] T. Doke *et al.*, "Let dependence of scintillation yields in liquid argon," *Nucl. Instrum. Meth. A*, vol. 269, no. 1, pp. 291–296, 1988, ISSN: 0168-9002. DOI: 10.1016/0168-9002(88)90892-3.

[32] A. Hitachi, "Exciton kinetics in condensed rare gases," *J. Chem. Phys.*, vol. 80, no. 2, pp. 745–748, 1984. DOI: 10.1063/1.446781.

[33] M. Hofmann *et al.*, "Ion-beam excitation of liquid argon," *Eur. Phys. J. C*, vol. 73, no. 10, p. 2618, 2013. DOI: 10.1140/epjc/s10052-013-2618-0. arXiv: 1511.07721 [physics.ins-det].

[34] P. Adhikari *et al.*, "The liquid-argon scintillation pulseshape in DEAP-3600," *Eur. Phys. J. C*, vol. 80, no. 4, p. 303, 2020. DOI: 10.1140/epjc/s10052-020-7789-x. arXiv: 2001.09855 [physics.ins-det].

[35] W. H. Lippincott *et al.*, "Scintillation time dependence and pulse shape discrimination in liquid argon," *Phys. Rev. C*, vol. 78, no. 3, p. 035 801, 2008. DOI: 10.1103/PhysRevC.78.035801.

[36] D. Lorents, "The physics of electron beam excited rare gases at high densities," *Physica B+C*, vol. 82, no. 1, pp. 19–26, 1976, Proceedings of the Twelfth International Conference on Phenomena in Ionized Gases, ISSN: 0378-4363. DOI: 10.1016/0378-4363(76)90265-5.

[37] P. Adhikari *et al.*, "The liquid-argon scintillation pulseshape in DEAP-3600," *Eur. Phys. J. C*, vol. 80, no. 4, p. 303, 2020, ISSN: 1434-6044. DOI: 10.1140/epjc/s10052-020-7789-x.

[38] R. Acciarri *et al.*, "Effects of Nitrogen contamination in liquid Argon," 2008. DOI: 10.1088/1748-0221/5/06/P06003.

[39] B. Aimard *et al.*, "Study of scintillation light collection, production and propagation in a 4 tonne dual-phase LArTPC," *JINST*, vol. 16, no. 03, P03007, 2021. DOI: 10.1088/1748-0221/16/03/P03007. arXiv: 2010.08370 [physics.ins-det].

[40] D. Whittington, S. Mufson, and B. Howard, "Scintillation Light from Cosmic-Ray Muons in Liquid Argon," *JINST*, vol. 11, no. 05, P05016, 2016. DOI: 10.1088/1748-0221/11/05/P05016. arXiv: 1408.1763 [physics.ins-det].

[41] E. Segreto, "Evidence of delayed light emission of TetraPhenyl Butadiene excited by liquid Argon scintillation light," *Phys. Rev. C*, vol. 91, no. 3, p. 035 503, 2015. DOI: 10.1103/PhysRevC.91.035503. arXiv: 1411.4524 [physics.ins-det].

[42] G. Ribitzki, A. Ulrich, B. Busch, W. Krötz, J. Wieser, and D. E. Murnick, "Electron densities and temperatures in a xenon afterglow with heavy-ion excitation," *Phys. Rev. E*, vol. 50, no. 5, 1994, ISSN: 1063651X. DOI: 10.1103/PhysRevE.50.3973.

[43] R. Luther and A. Nikolopulos, *Z. Phys. Chem.*, vol. 82U, no. 1, pp. 361–384, 1913. DOI: doi:10.1515/zpch-1913-8229.

[44] R. Acciarri *et al.*, "Oxygen contamination in liquid Argon: Combined effects on ionization electron charge and scintillation light," *JINST*, vol. 5, P05003, 2010. DOI: 10.1088/1748-0221/5/05/P05003. arXiv: 0804.1222 [nucl-ex].

[45] A. Neumeier *et al.*, "Attenuation of vacuum ultraviolet light in liquid argon," *Eur. Phys. J. C*, vol. 72, p. 2190, 2012. DOI: 10.1140/epjc/s10052-012-2190-z. arXiv: 1511.07724 [physics.ins-det].

[46] C. E. Barnett, "Some Applications of Wave-length Turbidimetry in the Infrared.," *The Journal of Physical Chemistry*, vol. 46, no. 1, pp. 69–75, 1942. DOI: 10.1021/j150415a009.

[47] G. M. Seidel, R. E. Lanou, and W. Yao, "Rayleigh scattering in rare gas liquids," *Nucl. Instrum. Meth. A*, vol. 489, pp. 189–194, 2002. DOI: 10.1016/S0168-9002(02)00890-2. arXiv: hep-ex/0111054.

[48] N. Ishida *et al.*, "Attenuation length measurements of scintillation light in liquid rare gases and their mixtures using an improved reflection suppresser," *Nucl. Instrum. Meth. A*, vol. 384, no. 2-3, pp. 380–386, 1997, ISSN: 0168-9002. DOI: 10.1016/S0168-9002(96)00740-1.

[49] A. Neumeier *et al.*, "Attenuation of vacuum ultraviolet light in pure and xenon-doped liquid argon —An approach to an assignment of the near-infrared emission from the mixture," *EPL*, vol. 111, no. 1, p. 12 001, 2015. DOI: 10.1209/0295-5075/111/12001. arXiv: 1511.07725 [physics.ins-det].

[50] M. Babicz *et al.*, "A measurement of the group velocity of scintillation light in liquid argon," *JINST*, vol. 15, no. 09, P09009, 2020. DOI: 10.1088/1748-0221/15/09/P09009. arXiv: 2002.09346 [physics.ins-det].

[51] S. Himi, T. Takahashi, J. z. Ruan, and S. Kubota, "Liquid and solid argon, and nitrogen doped liquid and solid argon scintillators," *Nucl. Instrum. Meth.*, vol. 203, pp. 153–157, 1982. DOI: 10.1016/0167-5087(82)90623-8.

[52] R. Acciarri *et al.*, "Effects of Nitrogen contamination in liquid Argon," *JINST*, vol. 5, P06003, 2010. DOI: 10.1088/1748-0221/5/06/P06003. arXiv: 0804.1217 [nucl-ex].

[53] B. J. P. Jones, C. S. Chiu, J. M. Conrad, C. M. Ignarra, T. Katori, and M. Toups, "A Measurement of the Absorption of Liquid Argon Scintillation Light by Dissolved Nitrogen at the Part-Per-Million Level," *JINST*, vol. 8, P07011, 2013, [Erratum: JINST 8, E09001 (2013)]. DOI: 10.1088/1748-0221/8/07/P07011. arXiv: 1306.4605 [physics.ins-det].

[54] B. J. P. Jones *et al.*, "The Effects of Dissolved Methane upon Liquid Argon Scintillation Light," *JINST*, vol. 8, P12015, 2013. DOI: 10.1088/1748-0221/8/12/P12015. arXiv: 1308.3658 [physics.ins-det].

[55] J. Soto-Oton, "Impact of xenon doping in the scintillation light in a large liquid-argon TPC," in *5th International Conference on Technology and Instrumentation in Particle Physics*, 2021. arXiv: 2109.05858 [physics.ins-det].

[56] S. Ogawa and M. Ogawa, "Absorption cross sections of $O_2(a^1\Delta_g)$ and $O_2(X^3\Sigma_g^-)$ in the region from 1087 to 1700 Å," *Can. J. Phys.*, vol. 53, p. 1845, 1975. DOI: 10.1139/p75-236.

[57] H. Keller-Rudek, G. K. Moortgat, R. Sander, and R. Sörensen, "The MPI-Mainz UV/VIS Spectral Atlas of Gaseous Molecules of Atmospheric Interest," *Earth System Science Data*, vol. 5, no. 2, pp. 365–373, 2013. DOI: 10.5194/essd-5-365-2013.

[58] J. Calvo *et al.*, "Measurement of the attenuation length of argon scintillation light in the ArDM LAr TPC," *Astropart. Phys.*, vol. 97, pp. 186–196, 2018. DOI: 10.1016/j.astropartphys.2017.11.009. arXiv: 1611.02481 [astro-ph.IM].

[59] B. Zatschler, "Attenuation of the scintillation light in liquid argon and investigation of the double beta decay of ^{76}Ge into excited states of ^{76}Se in the GERDA experiment," Ph.D. dissertation, Dresden, Tech. U., TU, Dresden (main), 2020.

[60] A. Hitachi, "Photon-mediated and collisional processes in liquid rare gases," *Nucl. Instrum. Meth. A*, vol. 327, no. 1, pp. 11–14, 1993, ISSN: 0168-9002. DOI: 10.1016/0168-9002(93)91398-7.

[61] C. G. Wahl, E. P. Bernard, W. H. Lippincott, J. A. Nikkel, Y. Shin, and D. N. McKinsey, "Pulse-shape discrimination and energy resolution of a liquid-argon scintillator with xenon doping," *JINST*, vol. 9, P06013, 2014. DOI: 10.1088/1748-0221/9/06/P06013. arXiv: 1403.0525 [physics.ins-det].

[62] D. Akimov *et al.*, "Fast component re-emission in Xe-doped liquid argon," *JINST*, vol. 14, no. 09, P09022, 2019. DOI: 10.1088/1748-0221/14/09/P09022. arXiv: 1906.00836 [physics.ins-det].

[63] A. M. Neumeier, "Optical Properties of Liquid Noble Gas Scintillators," Ph.D. dissertation, Munich, Tech. U., 2015.

[64] B. Raz, J. Jortner, and N. F. Mott, "Experimental evidence for trapped exciton states in liquid rare gases," *Proceedings of the Royal Society of London. A. Mathematical and Physical Sciences*, vol. 317, no. 1528, pp. 113–131, 1970. DOI: 10.1098/rspa.1970.0106.

[65] A. Neumeier *et al.*, "Intense vacuum ultraviolet and infrared scintillation of liquid Ar-Xe mixtures," *EPL (Europhysics Letters)*, vol. 109, no. 1, p. 12 001, 2015, ISSN: 0295-5075. DOI: 10.1209/0295-5075/109/12001.

[66] G. Nowak and J. Fricke, "The heteronuclear excimers ArKr*, ArXe* and KrXe*," *J. Phys. B*, vol. 18, no. 7, p. 1355, 1985. DOI: 10.1088/0022-3700/18/7/016.

[67] S. Kubota, M. Hishida, S. Himi, J. Suzuki, and J. Ruan, "The suppression of the slow component in xenon-doped liquid argon scintillation," *Nucl. Instrum. Meth. A*, vol. 327, no. 1, pp. 71–74, 1993, ISSN: 0168-9002. DOI: 10.1016/0168-9002(93)91413-H.

[68] D. Fields, R. Gibbons, M. Gold, N. McFadden, S. Elliott, and R. Massarczyk, "Understanding the enhancement of scintillation light in xenon-doped liquid argon," *Nucl. Instrum. Meth. A*, p. 167 707, 2022, ISSN: 0168-9002. DOI: 10.1016/j.nima.2022.167707.

[69] A. Buzulutskov, "Photon emission and atomic collision processes in two-phase argon doped with xenon and nitrogen," *EPL*, vol. 117, no. 3, p. 39 002, 2017. DOI: 10.1209/0295-5075/117/39002. arXiv: 1702.03612 [physics.ins-det].

[70] P. Agnes *et al.*, "First Results from the DarkSide-50 Dark Matter Experiment at Laboratori Nazionali del Gran Sasso," *Phys. Lett. B*, vol. 743, pp. 456–466, 2015. DOI: 10.1016/j.physletb.2015.03.012. arXiv: 1410.0653 [astro-ph.CO].

[71] L. Pertoldi, "Search for new physics with two-neutrino double-beta decay in Gerda data," Ph.D. dissertation, Università degli Studi di Padova, 2020.

[72] The MicroBooNE Collaboration, "Light Yield Calibration in MicroBooNE," [Online]. Available: https://microboone.fnal.gov/document/microboone-note-1120-tech/.

[73] M. Agostini *et al.*, "Liquid argon light collection and veto modeling in GERDA Phase II," *Eur. Phys. J. C*, vol. 83, no. 4, p. 319, 2023, ISSN: 1434-6052. DOI: 10.1140/epjc/s10052-023-11354-9.

[74] R. Santorelli, "Analysis of the purity of the argon used by the MicroBooNE experiment by ICPMS technique," *LIDINE 2022*, 2022. [Online]. Available: https://events.camk.edu.pl/event/47/contributions/362/attachments/131/286/LIDINE2022_Santorelli.pdf.

[75] C. Wiesinger, "No neutrinos not found," Ph.D. dissertation, Munich, Tech. U., 2020.

Chapter 5

The in-situ measurement device LLAMA

Following the conclusion of the last chapter, i.e. the necessity of a permanent measurement of key optical properties in LAr for modeling the detector performance even in case of varying impurity concentrations, a dedicated device was developed for LEGEND-200. It is referred to as LLAMA and was developed and tested at TUM before it was installed into the LEGEND-200 cryostat. It operates there permanently and in-situ since the cryostat filling operations in Summer 2021. An identical device, referred to as LLAMA-II, remains at TUM for investigating properties of LAr subject to doping with various impurities. For clarification, the instrument now installed in LEGEND-200 is called LLAMA-I.

This chapter reports about the properties of LLAMA itself, from its working principle and setup to the extraction of the optical properties. Details of the operation in the LEGEND-200 cryostat are presented in chapter 6. Results obtained from LLAMA in LEGEND-200 and at TUM are the subject of chapters 7 to 11, while chapter 12 evaluates the performances of LEGEND-200 and LEGEND-1000 based on these findings. A brief description of the topics of this chapter was already published in [1].

The work described here is the result of a collaborative effort. LLAMA was designed in collaboration with P. Krause, L. Papp, and S. Schönert. The copper parts were machined by L. Hein, H. Hess, G. Lerchl, and T. Richter of the chair's mechanical workshop.

Figure 5.1: The LLAMA instrument. A cylindrical copper frame holds 13 SiPMs in distances from 15 cm to 75 cm in steps of 5 cm to a light source, which is mounted on the bottom plate (see fig. 5.2). Individual transversal displacements prevent shadowing, and each SiPM faces the light source directly.

5.1 Instrument and working principle

Figure 5.1 shows a picture of LLAMA. The setup is operated completely immersed in LAr and is made out of copper for radiopurity reasons. Three vertical bars of 85 cm length, twelve copper rings, and plates at both the top and the bottom form a cylindrical frame.

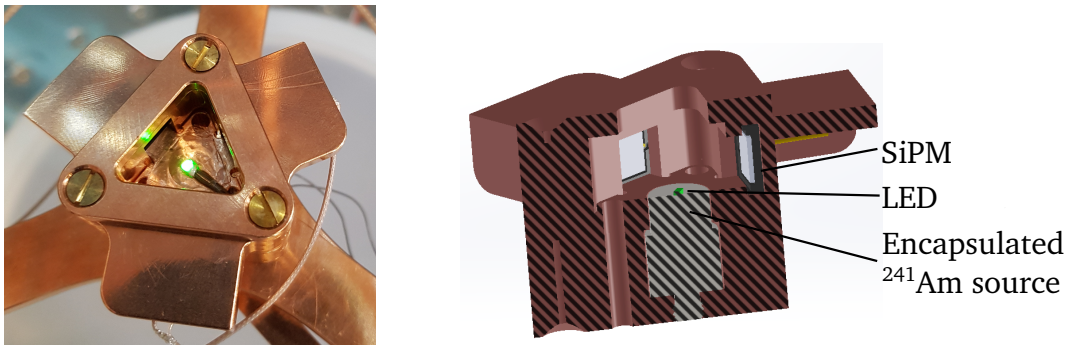

(a) (b)

Figure 5.2: The triggered scintillation light source of LLAMA, shown as a photograph (a) and cut view of a CAD model (b).

5.1.1 Scintillation light source

A triggered scintillation light source is fixed to the bottom plate. Figure 5.2 shows a photograph of the source (a) as well as a cut view of a CAD rendering (b). A triangular copper capsule forms a LAr-filled cavity, with an ^{241}Am source embedded in its bottom part. The ^{241}Am source is welded in a steel mantle, which blocks alpha radiation while allowing a significant fraction of the 60 keV gamma particles to exit. With a mean free path of 6.5 mm [2], most of the gamma particles are stopped in the LAr cavity[1], causing the argon to scintillate.

Three SiPMs, referred to as *source SiPMs*, are embedded in the walls of the cavity and detect these scintillation events. They provide a trigger for the DAQ and allow for obtaining the time and location of the event, as explained in sections 5.3 and 5.4, respectively. VUV photons originating from the scintillation event can leave the capsule through a triangular hole in the top part.

A surface-mounted device (SMD) LED[2] is placed at the bottom of the cavity. It is fixed with BC-600 optical cement and has PTFE foil (Tetratex) glued over its upper surface to attenuate and diffuse the emitted light. Visible light is not subject to scattering or absorption in LAr and is therefore used for estimating geometric effects (such as shadowing) and SiPM efficiency deviations in-situ.

[1] The height of the cavity is 7.8 mm, so around 70 % of the scintillation events happen within its volume.
[2] The type name is LXZ1-PM01-0104, and it emits light in the visible green spectrum [3].

The primary measurement mode uses VUV photons and thus triggers on the source SiPMs, while the LED remains off. Conversely, for calibrating the setup, the LED is pulsed from the outside, and the DAQ triggers on the LED drive pulses.

5.1.2 Peripheral SiPMs

Thirteen *peripheral SiPMs* are placed in distances from 15 cm to 75 cm in steps of 5 cm to the light source. The placement on the transversal plane is such that the direct lines of sight are not obstructed. Furthermore, individual holders make the SiPMs face the light source directly, retaining the full geometric efficiency and minimizing reflections. The lower twelve SiPMs are each mounted to an individual ring, while the topmost SiPM is mounted below the top plate.

VUV photons emitted from the source travel towards the peripheral SiPMs while being subject to attenuation. Thus, the light intensity falls off with increasing distance to the source. The geometric effect of the reduced solid angle of farther SiPMs due to the light source being point-like acts in the same vein. The intensity is then measured by the peripheral SiPMs. Deviations from the expected efficiencies (such as shadowing or different SiPM quantum efficiencies) are detected in dedicated calibration runs with the LED.

All 16 SiPMs employed in the setup are of the VUV4 type of HAMAMATSU[3] [4]. They are directly sensitive to VUV photons from LAr scintillation. The wavelength-resolved efficiency is shown in figure 5.3, reporting a value of around 15 % for 128 nm. This result agrees with a recent independent measurement by [5].

The closest peripheral SiPM of LLAMA-I was fitted out with a suprasil[4] window (see figure 5.4) to detect the amount of wavelength-shifted photons in the setup. The window is opaque to wavelengths at or below 150 nm, while being transparent above around 170 nm [6]. Hence, this SiPM is insensitive for the primary scintillation light of LAr, while re-emission from dissolved e.g. TPB or xenon is detected. This is important since wavelength-shifted photons have a different attenuation length.

[3] The exact model specifier is S13370-6075CN.
[4] Suprasil is a brand name for a high purity synthetic fused silica material by Heraeus.

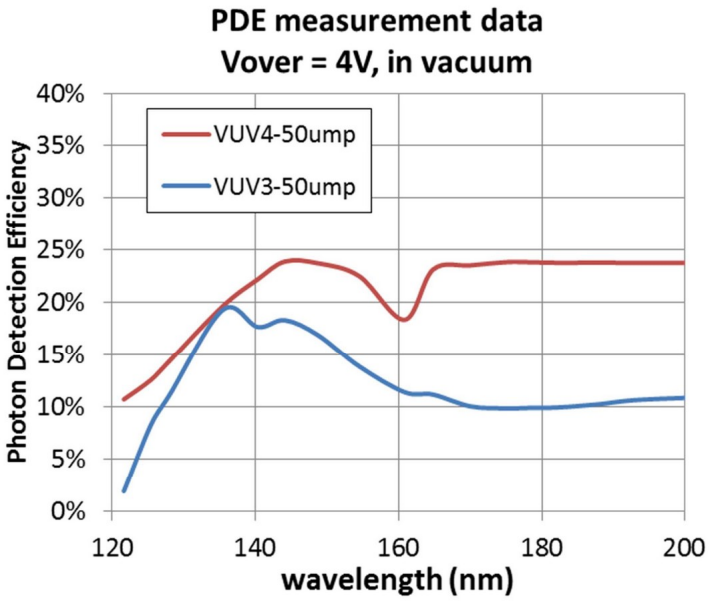

Figure 5.3: Efficiency of HAMAMATSU VUV4 and VUV3 SiPMs for VUV photons, taken from [4]. The LLAMA setup employs 16 SiPMs of the VUV4 type.

5.1.3 Key advantages of LLAMA

The novel design of LLAMA mitigates several systematic biases, which are present in previous experiments measuring optical properties of LAr. This applies especially to the determination of the attenuation length. The key characteristics of LLAMA are listed in the following:

- Due to the usage of state-of-the-art VUV-sensitive SiPMs, the employment of wavelength-shifting materials is entirely avoided. Thus, photons from the primary emission of LAr retain their original wavelength and hence obey the studied attenuation length.
- An ^{241}Am source is used, which produces low-energy gamma particles. Hence, electrons are below the Cherenkov threshold after receiving the gamma particle's energy, which prevents the production of visible photons, which is necessary for the reason stated above.

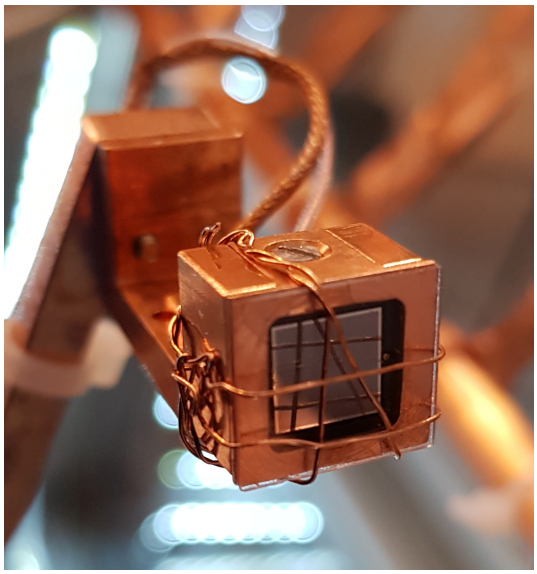

Figure 5.4: Close-up picture of the peripheral SiPM at 15 cm distance to the light source of LLAMA-I before installation in LEGEND-200. A suprasil window is fixed in front of it, which blocks the wavelength region corresponding to the primary emission of LAr; thus, the amount of wavelength-shifting by traces of e.g. TPB or xenon is obtained. The shadowing effect of the holding wires can be estimated from a calibration with the LED, which is part of the LLAMA light source.

- The triggered scintillation light source is a vital component of LLAMA. It allows LLAMA to discriminate light detections not originating from an ^{241}Am-induced event, i.e. other energy depositions in the LAr, such as gamma particles from other sources or muons. Furthermore, the three SiPMs allow discriminating scintillation events by intensity and location. The primary light yield can also be obtained since the close distance renders attenuation negligible.

- The low light intensity in peripheral SiPMs - with expected photon counts per event around or below 2 % - enables the application of counting analysis. This method greatly simplifies the calculation of intensity values and allows the generation of photon emission time spectra devoid of afterpulse effects. Section 5.4.2 provides further details.

5.2 Readout electronics

A circuit diagram of the essential parts of the readout electronics of a single SiPM is shown in figure 5.5. The SiPM is in the LAr volume. A single coaxial cable transports both the bias voltage and the signals; the readout is single-ended. Each channel has an individual power supply, provided by a HAMAMATSU C14156 unit connected to a low-pass pi-filter and a 10 kΩ resistor to reduce noise. The CREMAT CR-111 charge-sensitive amplifier is AC-coupled via a capacity. The amplifier contains a feedback capacity, a bleed resistor, and a resistor at the output stage, shown in the circuit diagram. The charge-sensitive amplifier integrates the SiPM's current signal over time, removing high-frequency noise. Due to the bleed resistor, the signal falls off exponentially with a decay time of 150 µs [7].

A single custom-made power supply and amplification (PSA) box[5] contains the electronics for all 16 channels. Figure 5.6 shows the box's interior and a zoom of a single channel. All parts are attached to a single printed circuit board (PCB) (green). The power supplies are realized as individual PCBs, to which the C14156 unit and the SMD components of the pi-filter are soldered. These modules are operated via control voltages, provided by 12-bit digital-to-analog converter (DAC) units, which are in turn controlled by an Arduino[6] via I2C. Signals are transported via coaxial cables until close to the individual PSA channels to retain a high signal-to-noise ratio, and MCX connectors are used to ease installation and maintenance.

The front panel holds NIM-CAMAC CD/N 549[7] connectors coupling the output stages to the DAQ. The back panel carries BNC connectors for linking to the SiPMs in the cryostat, a DC connector, and a USB socket. The USB interface can be connected to a PC to set the individual voltages via the Arduino and the DAC units. Two DC/DC units transform the 24 V input to the voltages required by the DAC, power supply, and Cremat devices. They have been selected because they are low in noise, and pi-filters are applied for the same reason. The Arduino and the power supplies, DACs and Cremat units, are mounted on sockets to facilitate the exchange in case of failure.

[5] In total three PSA boxes were built (for LLAMA-I, LLAMA-II, and a spare), and the manufacturing was partly done in collaboration with X. Stribl.

[6] To control 16 DACs (MCP4725) with a single Arduino, a multiplexer (TCA9548A) is used. It provides eight separate I2C buses, and one bus can address two DACs.

[7] This kind of connector is more commonly referred to via its brand name "LEMO-00".

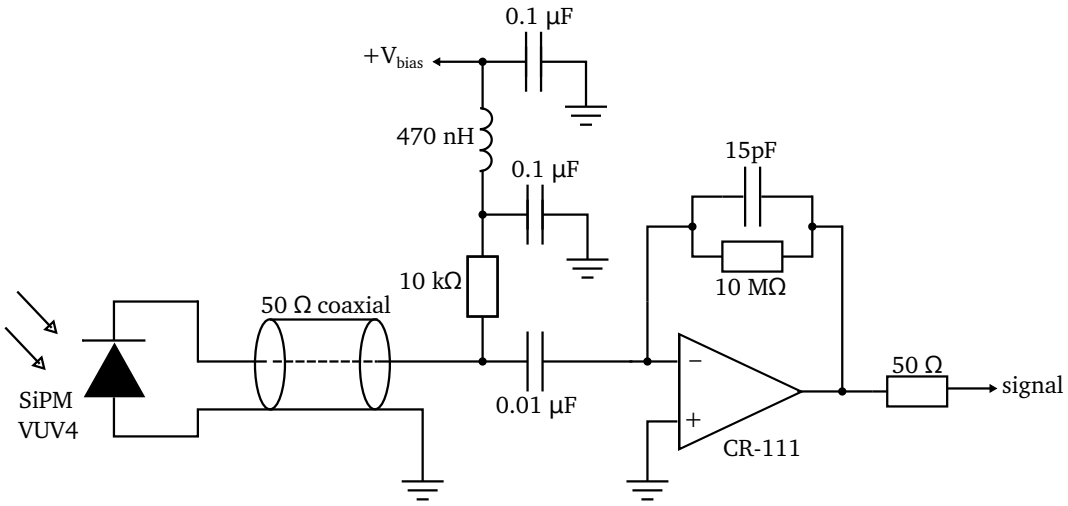

Figure 5.5: Diagram of the readout circuit for a single SiPM. The SiPM itself is operated in LAr, connected to a 50 Ω coaxial cable (single-ended readout). A dedicated custom-made PSA box houses the remaining components (for a picture, see figure 5.6). A C14156 power supply from HAMAMATSU provides the bias voltage [8], while the signals pass a CREMAT CR-111 charge-sensitive amplifier [7].

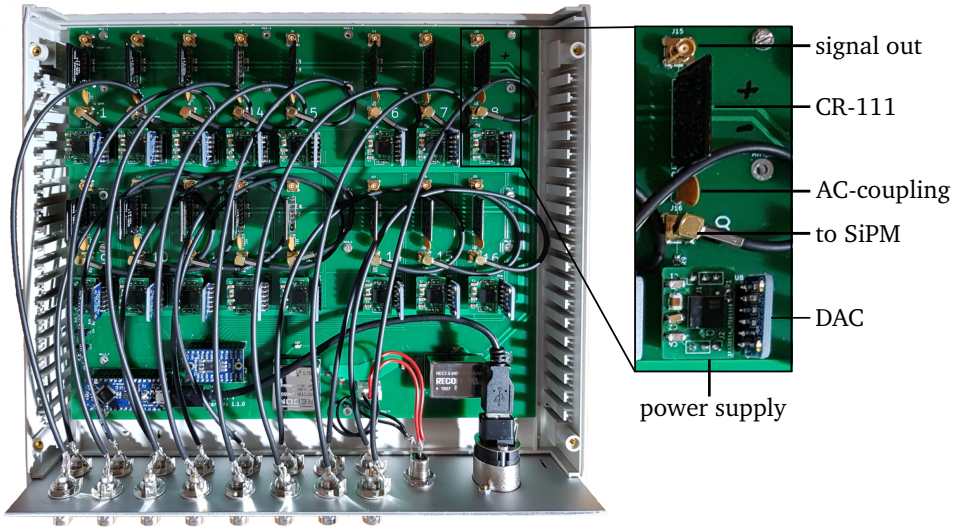

Figure 5.6: Photo of the inside of the PSA box. The front panel and the attached coaxial cables are removed to enhance the visibility of the remaining parts. The zoomed section shows a single channel. The components are explained in the text.

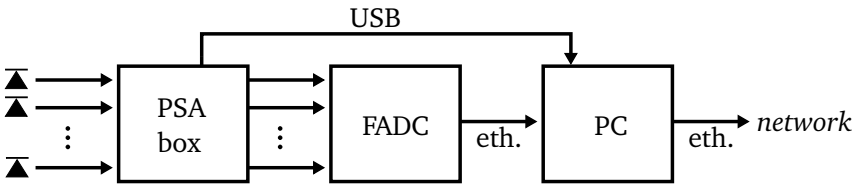

Figure 5.7: The data acquisition scheme of LLAMA. After amplifying and integrating the individual signals from all 16 SiPMs, they are digitalized by the FADC. The data is then transferred via Ethernet to the PC, which stores and processes the waveforms and is reachable via the network. A USB interface is used to control the bias voltages of the SiPMs from the PC and hence remotely via the network.

5.3 Data acquisition and processing

5.3.1 Data acquisition and raw data format

The DAQ scheme is sketched in figure 5.7. As explained in the previous section, signals from all 16 SiPMs are amplified and integrated separately by the PSA box. Then, they are recorded by a Struck SIS3316 flash analog-to-digital converter (FADC), which features a resolution of 14 bit, a maximum clock speed of 250 MHz, and 16 input channels. The data transfer between FADC and a dedicated readout PC is established via a 1 Gbit/s Ethernet interface. The data is then stored and processed offline on the PC. A USB interface connects the PC to the PSA box, which allows for setting the bias voltages for the individual SiPMs from the PC. For the application at LEGEND-200, the PC communicates via a second Ethernet interface with the LNGS network. Thus, the status of the DAQ and processing and the voltages of the SiPMs can be controlled remotely. Additionally, the raw and processed data can be synchronized to remote computing infrastructures.

LLAMA is integrated into the slow control system of LEGEND-200 to harness its full potential as a permanent monitor. The slow control (SC) thus allows observing the optical properties of LAr together with other parameters, which impact the data taken at LEGEND-200. Also, the SC facilitates switching the SiPMs on and off, necessary to avoid damage in case of excessive light in the cryostat, e.g. during calibrations or use of the camera systems. The slow control integration of LLAMA is further discussed in section 6.1.2.

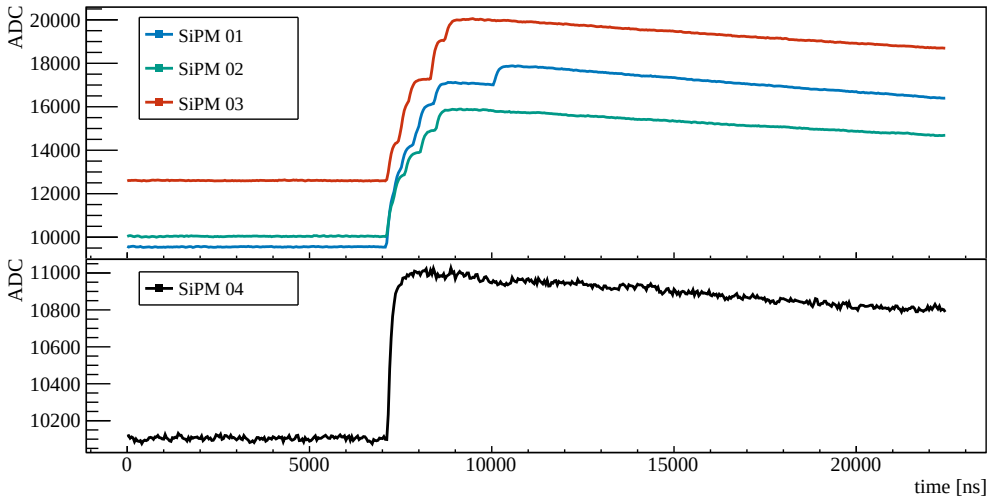

Figure 5.8: Example event recorded by LLAMA. SiPMs 01 to 03 are located within the source and thus see many scintillation photons. In this example, SiPM 04 at 15 cm distance detects a single photon of the scintillation event.

The DAQ records an event upon each triple[8] coincidence between the three source SiPMs. An event contains the waveforms of all 16 SiPMs, acquired simultaneously. Each waveform contains digitalized voltage levels at equidistant points in time. They have a total length of around 22.5 µs, with around 7 µs located in front of the trigger position. The data is recorded originally at a rate of 100 MHz but is down-sampled by a factor of four after transmission to limit the used space on the storage system. Four 14-bit integers are summed up to produce a single 16-bit integer, which is efficiently stored. Thus, 562 samples in steps of 40 ns are stored per channel and event. An example event is shown in figure 5.8.

5.3.2 Digital signal processing

The DAQ and offline data processing take place in multiple stages and are outlined in figure 5.9. The figure compiles programs (diamond shapes), file formats (rectangles), and the configuration meta-information (circles). A dedicated DAQ program referred to as *llamaDAQ* realizes the first stage. It is responsible for communicating with the FADC,

[8] For the period where one of the source SiPMs is not active, the condition was changed to a coincidence between the two remaining SiPMs. See appendix B.

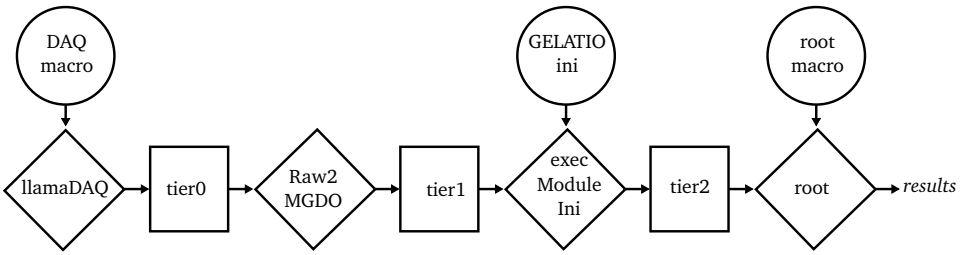

Figure 5.9: Data taking and processing pipeline. Programs are drawn in diamond shapes, files in rectangles, and configuration files in circles. The tier structure up to tier2 corresponds to the processing chain employed in GERDA.

specifically the setup of configuration registers and retrieval of sampled data. Due to its generic implementation, the llamaDAQ program was successfully applied in further projects, most notably MONUMENT, as described further in chapter 15.

Raw data are stored in a file format called *tier0*. This format and the subsequent low-level offline data processing comply with the scheme employed in the GERDA experiment. The necessary tools are part of the GERDA Layout for Input/Output (GELATIO) framework based on MAJORANA-GERDA Data Objects (MGDO) [9]. While the first stage from tier0 to tier1 only involves transforming the waveform information in a TTree-based ROOT format [10], the second stage applies digital signal processing (DSP) algorithms on the waveforms. The second stage generates tier2, which contains information reconstructed from the waveforms, most notably the arrival time of the first pulse in the waveform and the number of PE in a waveform.

The arrival time of the pulse is reconstructed by first deconvolving the exponential decay caused by the preamplifier from the waveform and subsequently applying a leading-edge trigger. The "GEMDFTTrigger" module in GELATIO conducts both steps. The number of PE is reconstructed via a Gaussian shaping algorithm composed of deconvolution and subsequent multiple passes of averaging, both implemented as moving windows. The height of the pseudo-Gaussian shape then corresponds to the number of PE, and the GELATIO module is called "GEMDEnergyGauss". Since the algorithm is independent of the location of the pulse in the waveform, it can reconstruct delayed photons from the triplet emission of LAr without bias.

After the tier2 level, the LLAMA analysis deviates from the one employed in GERDA. In GERDA, data are reprocessed many times, so storing higher tier levels is beneficial since

it saves computation time. Conversely, most data produced by LLAMA are processed only once. Thus, restricting the tier levels saves time spent on storing data and mitigates wearing the hard drives out over several years. However, a tier3 level containing PE-calibrated energy information and relative photon arrival times can be created on-demand for specific tasks.

5.4 Data analysis

The extraction of the optical properties of interest is performed in the high-level analysis. It builds upon the tier2 data level. To achieve sufficient statistical significance, packets of several millions of events are acquired, processed, and analyzed as a whole. For the application in LEGEND-200, each package contains 3 million events, corresponding to an elapsed data-taking and processing time of around 5 hours.

All analysis algorithms are implemented in C++ and use the ROOT framework [10]. The first step involves the fit of the 1 PE-peak with a Gaussian function to calibrate the individual PE spectra. Since robust algorithms are paramount for an automated monitoring device and the 1 PE-peak is of maximum interest for the counting analysis (see section 5.4.2), no further peaks are examined. The calibration functions are thus linear with no offset and are produced for every data package to account for possible gain drifts.

5.4.1 Analysis of source SiPMs and cut conditions

To reconstruct the amount of light emitted within the source, the detected number of photons in all three source SiPMs is summed up on an event-by-event basis. There, the peak corresponding to full energy depositions of 60 keV gamma particles becomes visible, as shown[9] in figure 5.10a. Its position, obtained from the fit with a Gaussian function, is proportional to the primary light yield in LAr due to the spatial proximity of the source SiPMs to the scintillation location, making attenuation negligible.

Additionally, the relative share of detected photons in the three source SiPMs is calculated and displayed as a ternary plot (see figure 5.10b). Using the relative share, one

[9] Figure 5.10a and all the following example plots are obtained from an early run in the LEGEND-200 cryostat.

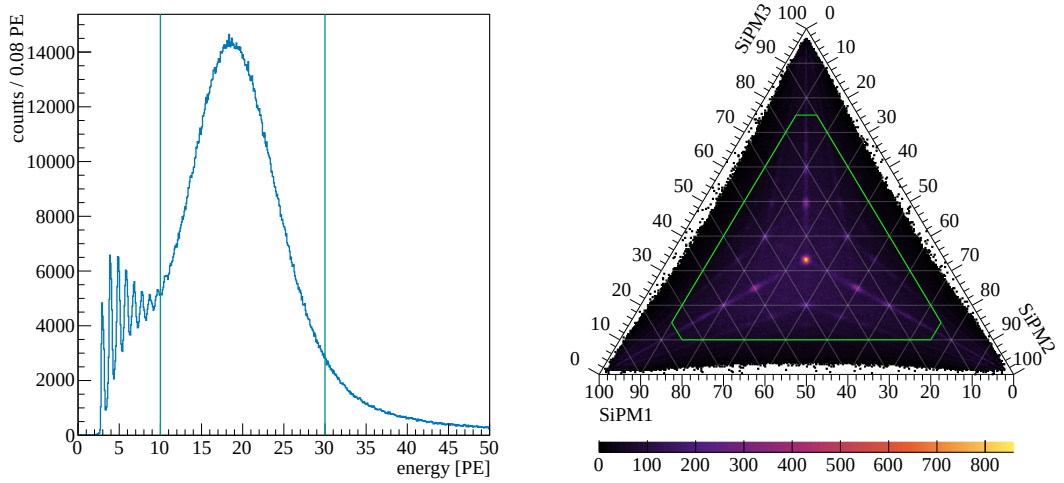

(a) Sum of detected PE in all three source SiPMs. The peak is attributed to full energy depositions of 60 keV gamma particles released from the ^{241}Am source. Events within teal lines are kept for further analysis.

(b) Relative share of photons detected in the three source SiPMs visualized in a ternary plot. Reconstructed photon numbers close to integral values are favored and lead to points of higher statistics. Events within the green boundary are central within the source and thus kept for further analysis.

Figure 5.10

can detect scintillation events that happen off-axis within the source cavity, as the solid angle of the three SiPMs is not identical for those events.

Since a source SiPM detects multiple photons most of the time, the probability of detecting at least one photon of the singlet emission of LAr is high. Thus, the time when the scintillation event happened can be extracted with nanosecond accuracy by determining the location of the first pulse in the waveform. The time positions reconstructed by each of the three source SiPMs are averaged to improve the time resolution.

Cuts are applied based on the analyzed data of the source SiPMs to remove events that might lead to systematic uncertainties. Such events are e.g. caused by scintillation events close to the walls of the cavity or outside, which exhibit distorted geometrical efficiencies for photons reaching the peripheral SiPMs. Both cases can be suppressed by requiring the relative share of detected photons to be sufficiently uniform. This is realized by setting thresholds of the minimum and maximum PE shares of a single SiPM of 0.1 and 0.75, respectively. This region is enclosed in green lines in figure 5.10b.

Both a lower and a higher boundary on the sum of photon hits in the source is placed. Scintillation events outside the source cavity have much smaller geometrical efficiencies for creating hits on the source SiPMs; thus, the energy sum is low. High energies hint to energy depositions from higher energy gamma particles or muons and thus are to be removed. Thus, both a low and high bound on the total number of PE in the source is placed. The bounds in place during the data taking of the example plot (fig. 5.10a) are depicted as teal lines.

An additional cut removes all events for which the scintillation event times reconstructed from individual SiPMs differ strongly. The standard deviation of the individual times t_i quantifies the spread:

$$\sqrt{\frac{1}{3}\sum_{i=1}^{3}(t_i - \bar{t})^2}, \text{ where } \bar{t} = \frac{1}{3}\sum_{i=1}^{3}(t_i). \tag{5.1}$$

High standard deviations can be caused by one or more source SiPMs detecting no singlet photons but only delayed triplet emission. Additionally, accidental coincidences are reduced by demanding a cut on the time difference. Figure 5.11a shows a histogram of the standard deviation values and the upper threshold.

An additional cut is implemented, which removes events with high multiplicity, defined as the number of SiPMs with a reconstructed PE count of at least 0.5 in that event. It is shown in figure 5.11b. The determination encompasses all 16 SiPMs, i.e. both peripheral and source SiPMs, hence the trigger condition prevents[10] events with a multiplicity below 3. Low light intensities in the peripheral SiPMs suppress higher multiplicity values. The cut removes multiplicities exceeding 4, i.e. more than one peripheral SiPM detects a pulse. Those events might be due to muon tracks or other backgrounds creating high-intensity scintillation light outside the source. It is mainly relevant for measurements at the shallow underground laboratory at TUM, which exhibits several orders of magnitude higher muon flux and gamma background than LNGS.

The values of the cut threshold shown above apply to LLAMA data in LEGEND-200 before the failure of one source SiPM in September 2021. Appendix B.4 compiles cut conditions and thresholds after this event.

[10] Events with multiplicities ≤ 2 are caused by false positives in the FADC trigger evaluation or false negatives in the pulse finding in the offline data analysis.

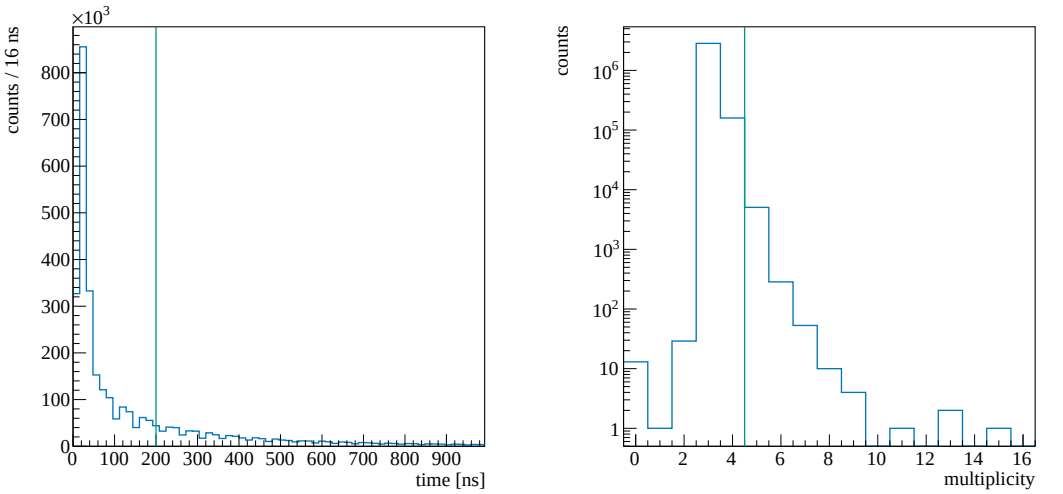

(a) Standard deviation of the scintillation time point, reconstructed individually by the three source SiPMs. Excessively high values above the teal threshold hint to misidentified time positions and are thus removed.

(b) The multiplicity, i.e. the number of SiPMs with a reconstructed number of PE of at least 0.5 in an event. The distribution peaks at 3, corresponding to the three source SiPMs, where a triple coincidence is required to record a given event. Higher PE values get increasingly rare due to the low light intensities in peripheral SiPMs. Multiplicities exceeding 4 are removed as muon events might cause them.

Figure 5.11

5.4.2 Analysis of peripheral SiPMs

The peripheral SiPMs are studied in the data set remaining after cuts. A key feature of LLAMA is the low expectation value of the number of detected photons per event in every peripheral SiPM. The fraction of valid scintillation events, in which a given peripheral SiPM detects one or more photons, is around or below 2 %. Thus, the probability of detecting more than one scintillation photon per event is low as 0.02 % and can be neglected. Hence, counting algorithms are applied, simplifying the light intensity extraction from data. The pulse per trigger (PPT) value is introduced in this context as the number of events exhibiting a 1 PE pulse in a given peripheral SiPM divided by the number of all valid scintillation events. Since the resolution is finite, the 1 PE pulses are counted in the ROI from 0.5 PE to 1.5 PE. Figure 5.12a shows the PE-spectrum of a

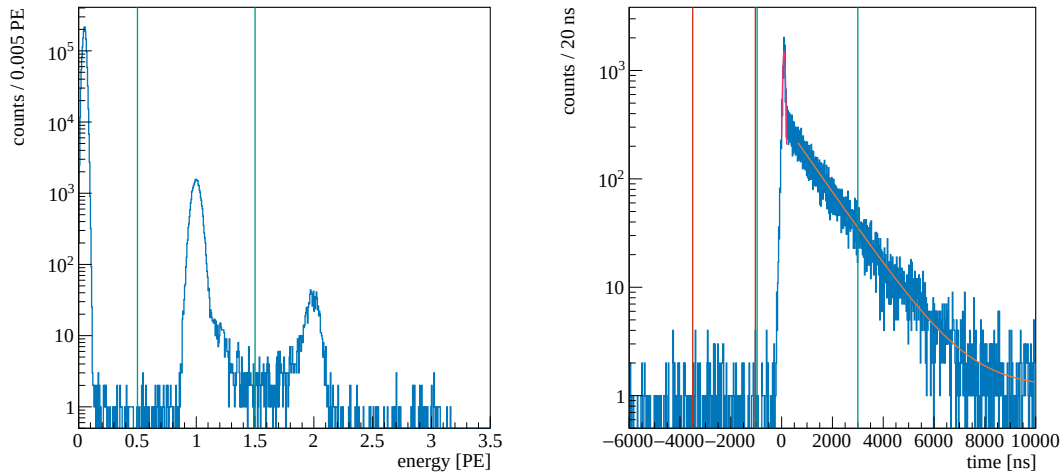

(a) Reconstructed pulse charge distribution after PE-calibration. Due to the expectation value of photon counts being much lower than one, the 2 PE distribution is dominated by optical cross-talk of 1 PE events. 1 PE signals are selected in a region from 0.5 PE to 1.5 PE.

(b) Arrival time of photons in a peripheral SiPM relative to the scintillation event. The position of the singlet peak is fitted with a Gaussian function (magenta) and defines the start and end point of the following fit of the triplet component (orange). Counting windows are placed for the signal (teal) and accidental background (red) to evaluate the intensity.

Figure 5.12

peripheral SiPM together with the ROI.

By dividing the number of 2 PE pulses over the number of 1 PE pulses, the assumption of a negligible contribution of two-photon events is cross-checked. The 1 PE pulses are counted in the range from 0.5 PE to 1.5 PE, while the 2 PE pulses are counted from 1.5 PE to 2.5 PE An example is shown in figure 5.13. All peripheral SiPMs show ratios around 5 %, compatible with the manufacturer's specification of the optical crosstalk probability [4]. Thus, 2 PE pulses are predominantly produced by a single incident photon via crosstalk rather than via two incident photons. Also, the fact that no trend is visible, even though net PPT values range from 1.6 % (SiPM 5) to 0.078 % (SiPM 16), supports the assumption of a crosstalk-dominated 2 PE distribution. The right tail of the 1 PE peak is caused by afterpulses, which are delayed pulses superimposed with the primary pulse and generated by charges trapped in the SiPM's silicon lattice [11]. As visible in figure

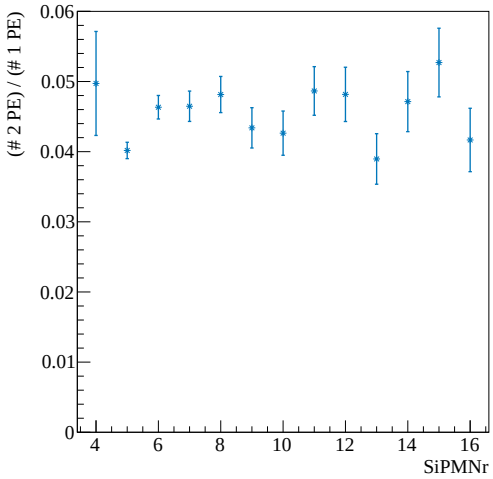

Figure 5.13: Crosstalk probability of different peripheral SiPMs, calculated by dividing the counts in the 2 PE peak by the 1 PE. Values are consistent with each other and with the data sheet value of 5 %. Thus, the 2 PE peak is dominated by crosstalk rather than two incident photons.

5.13, their contribution is minor, and their energy still lies within the ROI.

After selecting all events with 1 PE in a given SiPM, the distribution of the arrival time of this photon relative to the time of the scintillation event, reconstructed from the light source, is studied. An example is shown in figure 5.12b. Since each event exhibits exactly one photon in a given peripheral SiPM, the obtained photon emission time probability density function (PDF) is devoid of systematic biases due to pile-up or SiPM afterpulsing effects. The effective triplet lifetime τ_t' is obtained from the region[11] between 500 ns and 10 000 ns after the reconstructed singlet peak position by a fit with the following function:

$$I(t) = A\exp(-\frac{t}{\tau_t'}) + B \tag{5.2}$$

This simplified formula is chosen to achieve robust automated fits. A more elaborate analysis of the observed time spectrum is performed in a separate study and is presented in chapter 9. The start point of the fit range is chosen such that the influence of the intermediate component is minimal.

Two separate time windows provide PPT values corresponding to the signal and

[11]The values stated here correspond to the analysis of LLAMA data for LEGEND-200.

background (see figure 5.12b). The signal window (teal) contains the singlet and most triplet emissions. The background window (red) is placed ahead of the singlet emission peak. The flat accidental background is subtracted from the signal counts, yielding the *net PPT*, also referred to as *photon count* in this work. It is then corrected according to the individual solid angles:

$$\mathrm{PPT}_{corr,i} = A\, d_i^2\, \mathrm{PPT}_{net,i}, \tag{5.3}$$

with the distance d_i of SiPM i and an arbitrary scale factor A. The PPT_{corr} quantifies the *intensity*, defined via the number of detected photons per solid angle throughout this dissertation. The PPT_{corr} value is devoid of geometrical effects and bears the impact of VUV attenuation in LAr. A thorough study of the attenuation in LEGEND-200 is presented in chapter 8.

The data-taking and analysis scheme of runs with the LED is mainly analogous to a scintillation light run. A pulser drives the LED and coincidently triggers the DAQ. No analysis cuts are applied since all LED pulses are equally valid. The amplitude of the pulses driving the LED is tuned to achieve low light intensities in the peripheral SiPMs necessary for the application of counting analysis.

References

[1] M. Schwarz, P. Krause, A. Leonhardt, *et al.*, "Liquid Argon Instrumentation and Monitoring in LEGEND-200," *EPJ Web Conf.*, vol. 253, p. 11 014, 2021. DOI: 10.1051/epjconf/202125311014.

[2] M. Berger *et al.*, "XCOM: Photon Cross Sections Database," [Online]. Available: https://www.nist.gov/pml/xcom-photon-cross-sections-database.

[3] "LUXEON Z Color Line Product Datasheet," [Online]. Available: https://lumileds.com/wp-content/uploads/files/DS105-LUXEON-Z-Color-Line-datasheet.pdf.

[4] "VUV-MPPC: 4th generation (VUV4)," [Online]. Available: https://hamamatsu.su/files/uploads/pdf/3_mppc/s13370_vuv4-mppc_b_(1).pdf.

[5] T. Pershing *et al.*, "Performance of Hamamatsu VUV4 SiPMs for detecting liquid argon scintillation," *JINST*, vol. 17, no. 04, P04017, 2022. DOI: 10.1088/1748-0221/17/04/P04017. arXiv: 2202.02977 [physics.ins-det].

[6] "Quarzglas für die Optik - Daten und Eigenschaften," [Online]. Available: https://www.heraeus.com/media/media/hca/doc_hca/products_and_solutions_8/optics/Daten_und_Eigenschaften_Quarzglas_fuer_die_Optik_DE.pdf.

[7] "CR-111-R2.1 charge sensitive preamplifier: application guide," [Online]. Available: https://www.cremat.com/CR-111-R2.1.pdf.

[8] "Power supply for MPPC," [Online]. Available: https://www.hamamatsu.com/eu/en/product/optical-sensors/mppc/power-supply_driver-circuit/C14156.html.

[9] M. Agostini, L. Pandola, P. Zavarise, and O. Volynets, "GELATIO: A General framework for modular digital analysis of high-purity Ge detector signals," *JINST*, vol. 6, P08013, 2011. DOI: 10.1088/1748-0221/6/08/P08013. arXiv: 1106.1780 [physics.data-an].

[10] R. Brun and F. Rademakers, "ROOT: An object oriented data analysis framework," *Nucl. Instrum. Meth. A*, vol. 389, pp. 81–86, 1997. DOI: 10.1016/S0168-9002(97)00048-X.

[11] P. Eckert, H.-C. Schultz-Coulon, W. Shen, R. Stamen, and A. Tadday, "Characterisation studies of silicon photomultipliers," *Nucl. Instrum. Meth. A*, vol. 620, no. 2, pp. 217–226, 2010, ISSN: 0168-9002. DOI: 10.1016/j.nima.2010.03.169.

Chapter 6

Monitoring liquid argon in LEGEND-200

The goal of this chapter is to provide details specific to the application of LLAMA as a real-time monitor of optical properties of LAr in LEGEND-200 and to give an overview of the data obtained so far. The first section discusses the hardware setup, the monitoring workflow, and the implementation of LLAMA into the SC of LEGEND-200. Subsequently, an overview of the available data range is shown based on the key optical properties evaluated. The final section gives a detailed description of the LAr cryostat filling campaign, in which LLAMA played an integral role.

The data outlined in this chapter give valuable input to several dedicated studies providing unique insights into different aspects of LAr properties. They are extensive and not strongly interrelated, so they are separated into individual chapters trailing the present one.

6.1 Integration of LLAMA in LEGEND-200

6.1.1 Hardware setup at LNGS

In December 2020, LLAMA-I was successfully mounted on the bottom of the LEGEND-200 cryostat. Figure 6.1 shows both a render of the LEGEND-200 cryostat (a) and a picture of LLAMA (b). LLAMA's location maximizes its distance from the germanium array, rendering its impact on the background index negligible.

Coaxial cables connect LLAMA to an electrical feedthrough at the cryostat's neck (the cables are visible in white at the top of figure 6.1b). In total, 17 cables are used in

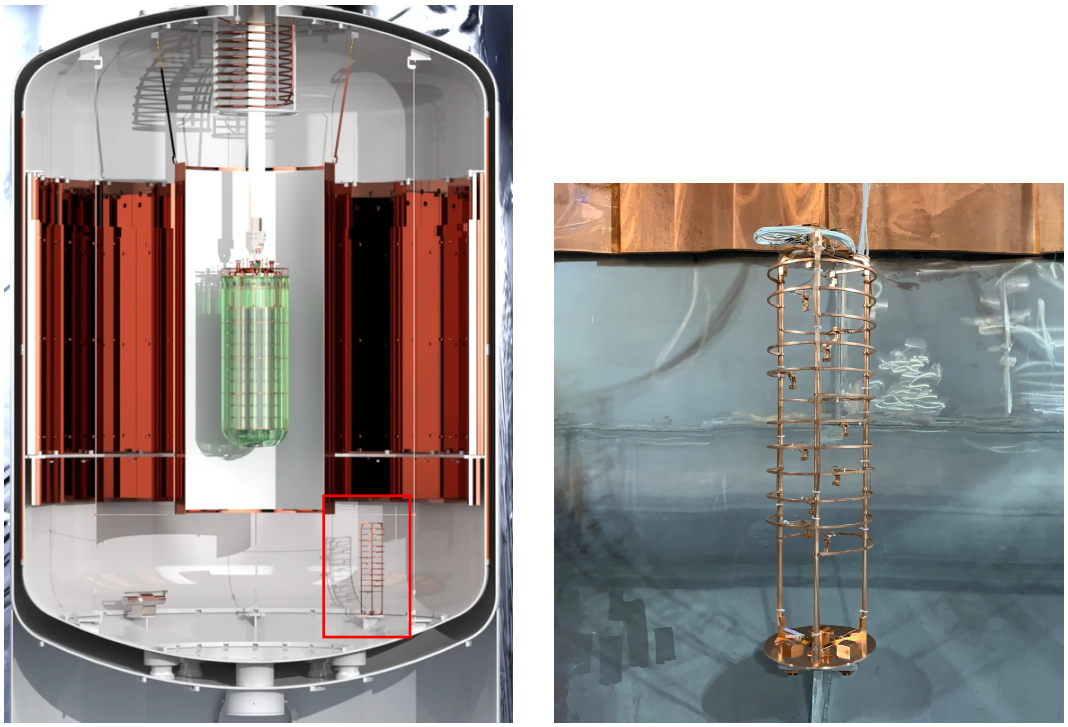

(a) Render of the LEGEND-200 cryostat and deployed components. LLAMA is marked with a red box. Render by P. Krause.

(b) Photo of LLAMA after installation on the cryostat floor. Image courtesy of S. Schönert.

Figure 6.1

parallel: one per SiPM and one for the green LED.

Outside the cryostat, further coaxial cables are routed from the feedthrough connector to the PSA box located in an electronics cabinet in the so-called 6 m-level. The FADC, as well as a dedicated PC, complete the LLAMA setup at LNGS.

6.1.2 Implementation of monitoring routines and integration into LEGEND-200 slow control

LLAMA at LEGEND-200 takes and processes data continuously as long as the SiPMs are biased, and the data taking is not stopped manually. In case of light in the cryostat, which might harm the SiPMs, or operations on the LLAMA electronics, the bias voltage is turned off remotely. The data-taking, processing, and analysis chain is fully automated

and requires manual intervention only in case of rare failures.

The data are segmented in *runs*, each of them containing 3 million events and lasting roughly 5 hours. Since the DAQ splits the run data into 6 packages and each package is processed independently, the data taking and processing happens in parallel, enhancing the duty cycle of LLAMA. Once all packages are recorded and processed, the entire run is analyzed as a whole. Leight-weight histograms and ASCII files are produced, which are stored on the LLAMA PC. They are periodically synchronized to the computing cluster of the Max Planck Institut für Kernphysik (MPIK).

All parts of the monitoring software program on the LLAMA PC are implemented as background tasks (daemons). This way, the operating system can start and maintain the tasks. This enables automated restart of the monitoring in case of a power outage of the PC. The dependencies among the daemons are kept at a minimum and are expressed explicitly. This is key for a stability-focused system since as many tasks as possible keep running once a daemon fails. The monitoring itself, the control of the bias voltages, syncing to the MPIK, and the production of long-term stability plots are all implemented as separate daemons.

LLAMA is integrated into the slow control (SC) of LEGEND-200 to enable supervision of the state of LLAMA and the properties of LAr alongside all other parameters relevant for a stable and secure operation of the entire experiment. A dedicated daemon collects the latest available information (analysis results and power state of the SiPMs) and makes it available to the SC via a web server. Another background task listens to requests from the SC to power the SiPMs collectively on or off.

6.2 Overview of elapsed run time

The first run of LLAMA-I in the LEGEND-200 cryostat was started on July 02 2021 at 05:44:17. The data shown in the following encompass all runs from that date until April 27 2024 at 12:30:28, amounting to 3085 runs. To improve visibility, results from individual runs are averaged in clusters of two days in size, weighted by the statistical uncertainties.

Figure 6.2 (top) shows the evolution of the effective triplet lifetime over the mentioned period. As explained in section 4.3.1, high effective triplet lifetimes correspond to low impurity levels and a high primary light yield. The effective triplet lifetime is a crucial

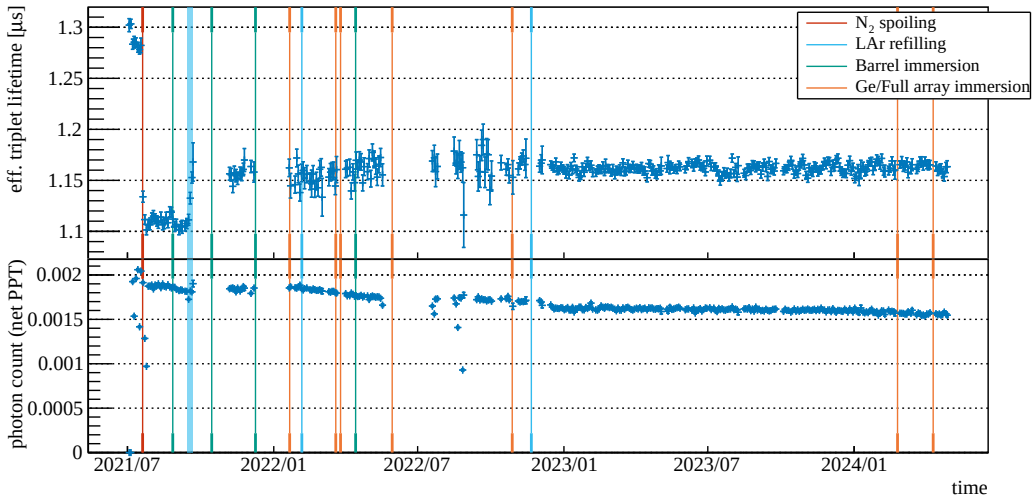

Figure 6.2: Effective triplet lifetime (top) and effective light yield (bottom) of LLAMA in LEGEND-200 from July 02 2021 at 05:44:17 until April 27 2024 at 12:30:28. The effective light yield is obtained from the photon count of the peripheral SiPM at 50 cm distance since it was active for the full range of data taking. Hence, this value is affected not only by a varying primary light yield but also by changes in the attenuation length. Vertical lines indicate important time points; see text.

benchmark for the purity of LAr, since it is intrinsically present in an absolute scale. In contrast, the primary light yield is difficult to quantify in absolute due to knowledge of geometric and SiPM photodetection efficiencies being required. Also, the attenuation length is not an ideal benchmark, as it cannot be expressed in a single value (see chapter 8), and is furthermore challenging to measure (see section 4.5). With an initial effective triplet lifetime of around 1.3 µs, the LAr of the initial filling phase was on a par with the one from [1], which uses an active gas purification system and a small cell. However, during filling, the quality deteriorated to 1.10 µs, which recovered to 1.15 µs by adding LAr in a top-up operation, which has been maintained since then. More details about the filling and the mentioned incident are presented in section 6.3. With an effective triplet lifetime of 1.15 µs, the LAr of LEGEND-200 surpasses the one from GERDA of 1.0 µs (prior its degradation to 0.91 µs) [2].

The photon counts of the peripheral SiPMs allow for obtaining relative changes in the effective light yield, i.e. the primary (possibly quenched) light yield combined with

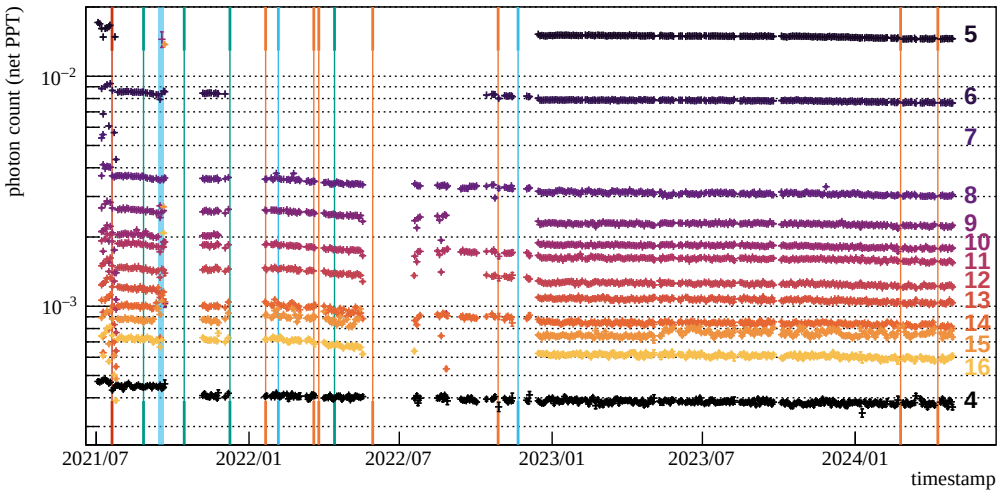

Figure 6.3: Photon counts of the peripheral SiPMs in net PPT. SiPMs are numbered from 4 (closest, at 15 cm) to 16 (farthest, at 75 cm) distance to the light source. The suprasil window in front of SiPM 4 blocks most of the light; hence, it shows the lowest PPT values. Unstable fits lead to rare outlier data points. Vertical lines indicate important time points; see text.

attenuation. The source SiPMs could provide the primary light yield. However, a malfunctioning source SiPM in September 2021 renders that method unusable. Thus, the effective light yield is used here. Figure 6.2 (bottom) shows the photon count of the SiPM at 50 cm distance from the light source, the closest one which shows good performance over the whole run time.

Figure 6.3 shows the photon counts of all peripheral SiPMs. The SiPMs are labeled in increasing order of distance from 4 to 16 (1 to 3 are source SiPMs). Due to attenuation and geometric effects, closer SiPMs detect more light, except for SiPM 4, which is fitted with a suprasil window blocking direct LAr VUV emission.

Both plots include markers (vertical lines) indicating important points in time. The red marker shows the time frame when the spoiling was ongoing (see next section). Refills of LAr are colored in cyan, the first being necessary since the original filling campaign ended prematurely due to the spoiling incident. Later refills compensated small losses in LAr. Immersions of one or both fiber barrels, or parts of it are drawn in teal. If the full array or solely the HPGe detectors are deployed, the marker is colored in orange.

Missing data points, especially in the second half of 2022, are due to SiPM channels failing and being subsequently repaired. The failing and the recovery operations are explained in detail in appendix B.

The photon count of SiPM 4, i.e. the amount of shifted photons is not increasing. Hence, a solution of TPB in LAr during the insertion of the fiber barrels is either very small or does not take place at all.

A slight decrease in photon counts is visible during 2022. This is presumably caused by impurities brought in by hardware operations and is studied in detail in chapter 7. The same chapter also studies the stable phase during 2023.

6.3 Filling campaign and nitrogen spoiling

The filling of the 64 m^3 cryostat with 90 t of purified LAr in Summer 2021 was a milestone in the commissioning of LEGEND-200. It involved 13 people from six institutions, which can be found in the author list of [3]. A simplified sketch of the filling setup is shown in figure 6.4. The parts necessary for the filling process itself are drawn in black. LAr gets delivered with a truck and filled into a storage tank, acting as a buffer. It is then piped through LLArS and filled into the LEGEND-200 cryostat.

LLArS is primarily designed to remove oxygen and water (and, to a limited degree, nitrogen) from LAr and is described in more detail in [3]. Its two columns perform the purification:

- The first column contains a copper catalyst to bind oxygen. To remove the oxygen from the catalyst, the column has to be regenerated by heating it up to 250 °C and flushing it with a mixture of 5 % hydrogen in nitrogen.
- A molecular sieve of 4 Å within the second column removes water and nitrogen from the LAr. It is regenerated by heating the column to 250 °C and pumping it to a high vacuum for several hours.

Due to the large amount of LAr required and the superior quality level necessary for successful operation of the LEGEND-200 LAr instrumentation, a thorough quality assurance of the filled LAr is essential. The involved parts are drawn in red in figure 6.4. Two devices are near the storage tank and LLArS. One of them is the scintillation

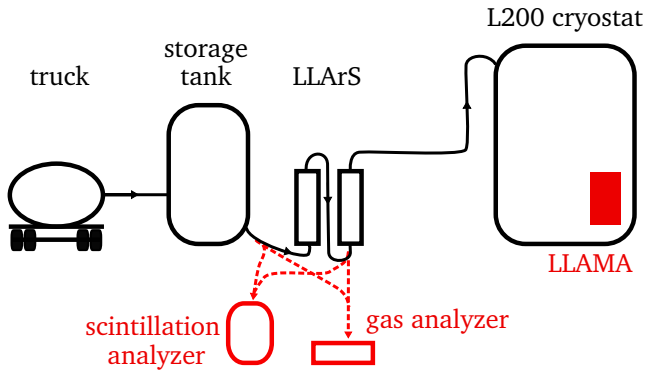

Figure 6.4: Scheme of the setup used to fill the LEGEND-200 cryostat with purified LAr. All parts of the filling process itself are drawn in black: from the LAr delivery truck via the storage tank and LLArS, which performs the purification, until the cryostat. LAr quality control and monitoring systems are drawn with red color. The scintillation analyzer evaluates batches of LAr before or after LLArS, while the gas analyzer measures continuously, primarily after the purifier. LLAMA monitors the LAr in the cryostat after a sufficient filling height is reached.

analyzer, which is composed of a light- and airtight 60 L dewar with two TPB-coated PMTs mounted into it. It can be filled with a LAr sample to measure the effective triplet lifetime using a dedicated DAQ and analysis system. The second device is a gas analyzer[1], which determines the quantity of nitrogen, oxygen, and water at a sub-ppm level[2].

Both devices can evaluate the LAr purity directly after the storage tank or after purification. They provide a necessary cross-check of the purity of the delivered LAr and the performance of LLArS. The gas analyzer monitors the impurity concentration after purification most of the time. Using the results from the scintillation analyzer, it was decided to regenerate the system after 12 t of processed liquid since the effective triplet lifetime dropped from 1.3 µs to 1.1 µs [3].

LLAMA plays a vital role in the quality control of the filled LAr. Its position within the cryostat allows it to probe the LAr at its destination point. Possible contaminations caused by the tubes between LLArS and the cryostat, or the cryostat itself, can thus be probed by LLAMA exclusively. Furthermore, it serves as a permanently active monitor,

[1] Precisely, the gas analyzer measures only the oxygen and nitrogen content, while a dewpoint analyzer measures the water contamination.
[2] The unit “ppm” is defined in terms of mole fraction throughout this work.

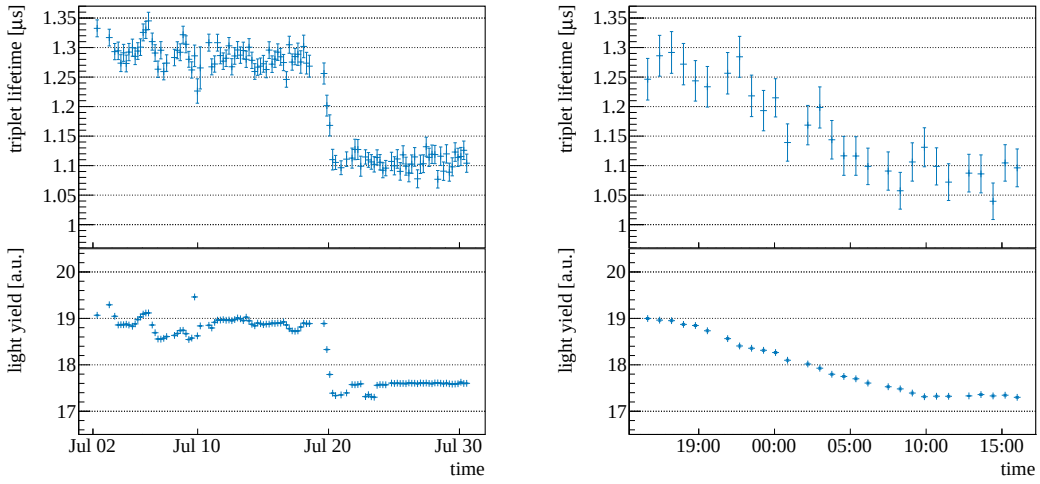

(a) (b)

Figure 6.5: Effective triplet lifetime (top) and primary light yield reconstructed from source SiPMs (bottom). In (a), the time frame from the start of monitoring until the end of July 2021 is shown. A contamination with N_2 deteriorated the LAr from July 19th to 20th. A zoom of this time frame is shown in (b).

in contrast to the scintillation analyzer. The gas analyzer can also be used as a monitor, though limited to the three contaminants mentioned above.

The LAr level within the cryostat reached a sufficient height on July 02, 2021; thus, monitoring with LLAMA started at this time. Initially, only the source SiPMs and the closest two peripheral SiPMs were submerged; thus, only those were biased. At a later stage, all other SiPMs were biased as well, as LLAMA was submerged completely. Fully submerged SiPMs were identified by resistivity measurements.

Figure 6.5a shows the effective triplet lifetime (top) as well as the primary light yield (bottom) during July 2021. In contrast to figure 6.2, the light yield is extracted here from the position of the 60 keV peak of the source SiPMs, since all three SiPMs were active during this early time frame. During the time until the 19th of July, filling with LAr of nominal quality was ongoing. The optical parameters are fluctuating but without a visible trend.

The optical properties deteriorated rapidly from July 19th, 17:30 CEST, until 10:35 the following day. This time frame is shown in figure 6.5b. In that plot, one data point corresponds to 500 000 recorded events (around 45 minutes). A delivery of LAr,

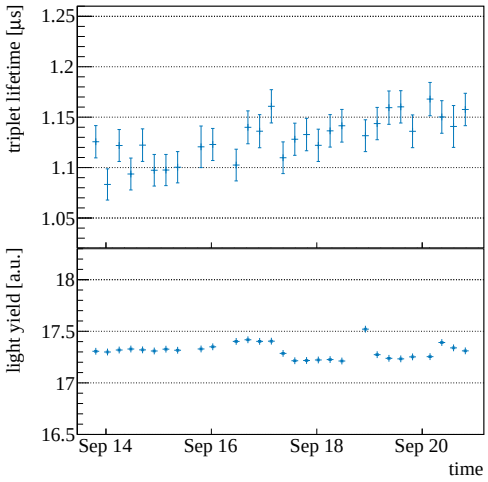

Figure 6.6: Evolution of effective triplet lifetime (top) and primary light yield (bottom) during the final phase of filling the LEGEND-200 cryostat. Nitrogen impurities from the previous spoiling event get diluted, and the effective triplet lifetime recuperates slightly.

contaminated with around 10 ppm of nitrogen, was later identified as the source [4]. LLArS could not effectively reduce the high amount of nitrogen. The filling was halted after the contamination became sufficiently apparent from the monitoring data provided by LLAMA. The LAr storage tank was emptied after the nitrogen content of 10 ppm was discovered by mass spectroscopy measurements [4] and by gas analyzers [5].

Due to the low concentration of nitrogen in the LAr volume in the cryostat, compared to dedicated doping campaigns reported in literature [6, 7], the data recorded by LLAMA around and during the spoiling event were studied in a dedicated analysis. This way, the effect of very low nitrogen concentrations is modeled with unprecedented accuracy, as presented in chapter 10.

Filling with LAr resumed on September 13th and ended on the 20th. The time-resolved evolution of the optical properties is shown in figure 6.6. The added amount of clean LAr diluted the nitrogen contamination; thus, the effective triplet lifetime improved slightly from around 1.10 µs to 1.15 µs. The primary light yield shows instabilities similar to the previous filling operation.

References

[1] T. Heindl *et al.*, "The scintillation of liquid argon," *EPL (Europhysics Letters)*, vol. 91, no. 6, p. 62 002, 2010, ISSN: 0295-5075. DOI: 10.1209/0295-5075/91/62002.

[2] C. Wiesinger, "No neutrinos not found," Ph.D. dissertation, Munich, Tech. U., 2020.

[3] M. Haranczyk *et al.*, "Purification of large volume of liquid argon for LEGEND-200," *PoS*, vol. PANIC2021, p. 102, 2022. DOI: 10.22323/1.380.0102.

[4] C. Vogl, "Liquid Argon: Purification and Xenon-Doping for Legend," *Master's thesis, TUM*, 2021.

[5] S. Schönert and G. Zuzel, "Summary of the LEGEND-Linde Meeting at LNGS," 2021.

[6] B. J. P. Jones, C. S. Chiu, J. M. Conrad, C. M. Ignarra, T. Katori, and M. Toups, "A Measurement of the Absorption of Liquid Argon Scintillation Light by Dissolved Nitrogen at the Part-Per-Million Level," *JINST*, vol. 8, P07011, 2013, [Erratum: JINST 8, E09001 (2013)]. DOI: 10.1088/1748-0221/8/07/P07011. arXiv: 1306.4605 [physics.ins-det].

[7] R. Acciarri *et al.*, "Effects of Nitrogen contamination in liquid Argon," *JINST*, vol. 5, P06003, 2010. DOI: 10.1088/1748-0221/5/06/P06003. arXiv: 0804.1217 [nucl-ex].

Chapter 7

Stability of optical properties of liquid argon in LEGEND-200

Keeping the optical properties of liquid noble gasses stable is critical for detectors building on light readout in this material, which pursue long-term operation. Insight into the behavior of optical properties, acquired over a long time in real-world applications, is thus paramount. Data collected by the in-situ monitor LLAMA[1] offer a unique opportunity to study the optical properties of LAr in LEGEND-200. To date, it encompasses more than two years of runtime, covering crucial activities in LEGEND-200 - from LAr filling, over the commissioning of the HPGe array and LAr instrumentation to physics data taking.

This chapter studies changes in optical properties of LAr over time. It connects to chapter 6, which provides vital knowledge about LLAMA's operation as a monitor in LEGEND-200 as well as hardware activities and external events impacting the LAr. In section 6.3, the spoiling of the LAr with nitrogen during the filling campaign is described.

The nitrogen spoiling constitutes a singular event in which impurity concentration and optical properties varied drastically. Therefore, the impact on the optical properties is analyzed as a single step in section 7.2. The procedure of analyzing the development of the LAr is then applied to the time frame from November 2021 to December 2022, covering most hardware activities affecting the LAr. The last step encompasses the time frame from December 2022 to August 2023, in which the LAr was not affected by any hardware operation.

[1] Details about the operation principle, setup, and data analysis of LLAMA are provided in chapter 5.

7.1 Modeling incremental changes in optical properties

This section develops methods necessary to extract incremental changes in optical properties in specific time steps, which is applied to LLAMA data in the following sections. These methods allow for obtaining effects caused exclusively by impurities introduced during the time frame evaluated, independent of any pre-existing impurities.

Two optical properties are evaluated in this context. One is the primary light yield, i.e. the amount of VUV photons produced per unit of energy deposited, which is affected by impurities quenching excimers before their light emission. Details about processes involved in quenching are presented in section 4.3.1. Secondly, the propagation of emitted VUV light is investigated, precisely the absorption caused by optically active contaminants, as explained in section 4.3.2. Investigating both parameters is paramount due to their direct impact on the performance of the LAr instrumentation of LEGEND-200. Also, both quantities allow for confining or identifying possible contaminants due to their different impact on both values. This technique is further detailed in section 8.4.2.

7.1.1 Combining quenching and absorption

The following formulas assume pre-existing contaminants χ and other substance(s) ξ, which are introduced in addition during the investigated step.

Equation 4.8 calculates the quenched intensity I'_Q based on the intensity in case of pure LAr I, the singlet and triplet fractions (η_s and η_t, respectively), the triplet lifetime of pure LAr τ_t, the rate constant $k_{Q,\chi}$ and the concentration[2] $[\chi]$. For convenience, it is reproduced here, explicitly expressing the dependence of the unquenched emission intensity I on the wavelength λ:

$$I'_Q(\lambda, [\chi]) = I(\lambda)\left(\eta_s + \frac{\eta_t}{1 + \tau_t\, k_{Q,\chi}\, [\chi]}\right). \tag{7.1}$$

Note that while being introduced originally for singular substances, the formula can be easily extended to mixtures of substances χ_i with concentration fractions α_i ($[\chi_i] =$

[2] Concentrations are given in terms of mole fractions in this chapter. See appendix A for details regarding this choice.

$\alpha_i\,[\chi]$) by

$$\sum_i k_{Q,\chi_i}\,[\chi_i] = \sum_i (\alpha_i\, k_{Q,\chi_i})\,[\chi] = k_{Q,\chi}\,[\chi], \tag{7.2}$$

introducing the effective rate constant $k_{Q,\chi}$ of the mixture.

This superposition is used likewise to model the addition of substance ξ:

$$I'_Q(\lambda, [\chi]+[\xi]) = I(\lambda)\left(\eta_s + \frac{\eta_t}{1+\tau_t\,(k_{Q,\chi}\,[\chi]+k_{Q,\xi}\,[\xi])}\right). \tag{7.3}$$

Using the Beer-Lambert-Law [1], the intensity reduction due to traveling a finite distance x in attenuating LAr can be modeled. Here, any potential Rayleigh scattering in pure LAr is accounted for using $\beta(\lambda) = 1/l_{scat}(\lambda)$ (see section 4.2.2). Absorption due to contaminants χ having an absorption coefficient $k_{A,\chi}$ are modeled according to equation 4.10. The intensity after quenching and propagation $I'_{QA}(x, \lambda, [\chi])$ for wavelength λ reads:

$$I'_{QA}(x, \lambda, [\chi]) = I'_Q(\lambda, [\chi])\, e^{-x\,(\beta(\lambda)+k_{A,\chi}(\lambda)[\chi])}. \tag{7.4}$$

In contrast to quenching, attenuation is a potentially wavelength-dependent process.

After adding ξ, the intensity becomes:

$$I'_{QA}(x, \lambda, [\chi]+[\xi]) = I'_Q(\lambda, [\chi]+[\xi])\, e^{-x\,(\beta(\lambda)+k_{A,\chi}(\lambda)[\chi]+k_{A,\xi}(\lambda)[\xi])}. \tag{7.5}$$

7.1.2 Building intensity ratios

By building the ratio between the intensities after and before the introduction of ξ, the propagation term simplifies:

$$\frac{I'_{QA}(x, \lambda, [\chi]+[\xi])}{I'_{QA}(x, \lambda, [\chi])} = \frac{I'_Q(\lambda, [\chi]+[\xi])}{I'_Q(\lambda, [\chi])}\, e^{-x\,k_{A,\xi}(\lambda)[\xi]}. \tag{7.6}$$

Since $\beta(\lambda)$ is no longer present, the following calculations do not require a model for Rayleigh scattering. Furthermore, all potentially impurity-independent instrumental effects that can be absorbed into $\beta(\lambda)$, such as photodetection efficiencies varying across individual SiPMs, are removed. Also, $k_{A,\chi}(\lambda)[\chi]$ disappears, rendering the incremental change in absorption independent of pre-existing contaminants.

Since LLAMA's SiPMs cannot resolve the wavelength of incident photons, the formula

is used wavelength-integrated:

$$\frac{I'_{QA}(x,[\chi]+[\xi])}{I'_{QA}(x,[\chi])} = \frac{I'_{Q}([\chi]+[\xi])}{I'_{Q}([\chi])}\, e^{-x\, k_{A,\xi}\,[\xi]}. \tag{7.7}$$

The ratio of quenched intensities, however, does not show this simplifying behavior and reads as

$$\frac{I'_{Q}([\chi]+[\xi])}{I'_{Q}([\chi])} = \frac{\eta_s + \frac{\eta_t}{1+\Omega_\chi+\tau_t\, k_{Q,\xi}\,[\xi]}}{\eta_s + \frac{\eta_t}{1+\Omega_\chi}}, \tag{7.8}$$

where Ω_χ is defined as

$$\Omega_\chi = \tau_t\, k_{Q,\chi}\,[\chi]. \tag{7.9}$$

For every time frame analyzed, the value Ω_χ has to be supplied by the result from the evaluation of the preceding time frame. The first time frame evaluated (the nitrogen spoiling event) assumes initially pure LAr (i.e. $\Omega_\chi = 0$), which is justified in section 9.3.1.

7.1.3 Application to LLAMA data

LLAMA provides intensities $I'_{QA}(x)$ for travel distances x ranging from[3] 20 cm to 75 cm in steps of 5 cm. In practice, the photon counts are shown and used here since all geometrical effects (including the solid angle) get eliminated by taking the ratios, rendering photon count ratios equal to intensity ratios. Details about evaluating the photon counts are described in section 5.4.2.

As described in section 6.1.2, LLAMA takes and analyzes data granularized in runs, each lasting around 5 hours. Every time frame analyzed in the scope of this chapter defines two time windows spanning multiple runs, which are averaged over, respectively. An overview plot showing the photon counts for all available SiPMs over the total runtime elapsed is available in figure 6.3.

The dedicated algorithm developed for this analysis computes ratios $R(x)$ between the averaged photon counts of the late and early time windows for every travel distance x. The data is modeled using equation 7.7, which can be re-written as

$$R(x) = A e^{-x\,B}, \tag{7.10}$$

[3] The SiPM at distance 15 cm is not usable in this analysis, since it is fitted with a suprasil window blocking the primary scintillation light emission of LAr (see section 5.1.2.)

using the following substitutions:

$$R(x) = \frac{I'_{QA}(x, [\chi] + [\xi])}{I'_{QA}(x, [\chi])}, \quad A = \frac{I'_{Q}([\chi] + [\xi])}{I'_{Q}([\chi])} \quad \text{and} \quad B = k_{A,\xi}\,[\xi]. \tag{7.11}$$

Thus, the fraction of the quenched primary light yield A and the absorption strength B are free parameters and are varied in fits to the data. To make the absorption strength more intuitive, it can be transformed into an absorption length

$$l_{abs,\xi} = 1/(k_{A,\xi}\,[\xi]) = 1/B, \tag{7.12}$$

which would exist in a hypothetical mixture of pure argon and solely the contaminant(s) ξ.

In addition to fits with equation 7.10, the data can also be tested against known or suspected impurities. That requires $k_{Q,\xi}$ and $k_{A,\xi}$ to be obtained from literature. Additionally, η_s, η_t and τ_t of pure LAr have to be assumed, which are taken from a dedicated study of the scintillation emission time profile in chapter 9 and are available in table 9.1.

Then, the concentration $[\xi]$ of the substance (or mixture) remains the sole free fit parameter. Goodness-of-fit parameters are used to indicate the plausibility of assumed contaminants.

7.2 Impact of nitrogen spoiling

The first time frame analyzed is located around the nitrogen spoiling event, which happened in July 2021 during the filling of the LEGEND-200 cryostat and is described in detail in section 6.3. The relevant data in the time range considered for the present analysis of this event is shown in figure 7.1. There, the detected photon counts for individual peripheral SiPMs are plotted over time. Gray shaded areas show the time windows used to average the photon counts before and after the spoiling time range (red area). SiPMs are indexed (right) in increasing order of light travel distance, from 5 (20 cm) to 16 (75 cm). Due to hardware failures[4], SiPMs 5 and 7 are not usable in this time frame. SiPM 8 showed transient instabilities and is likewise excluded.

[4] See appendix B for details.

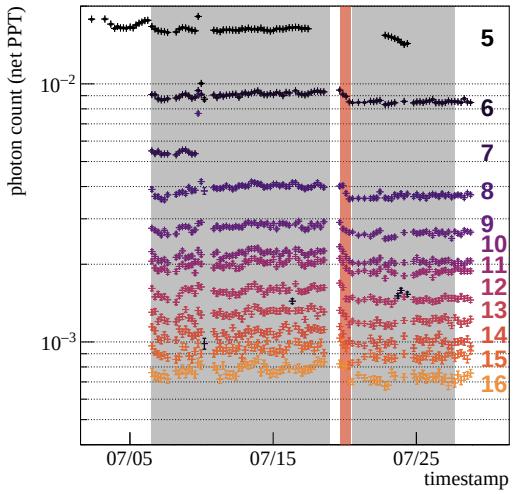

Figure 7.1: Photon counts for different peripheral SiPMs in the time range (July 2021) used to analyze degradation due to the nitrogen spoiling event (red box). Gray-shaded areas depict time windows before and after the event, which are averaged over in the analysis. SiPMs are indexed (right) in increasing order of light travel distance, from 5 (20 cm) to 16 (75 cm), in steps of 5 cm.

As explained previously, intensity ratios are computed, i.e. the relative change in intensity (via photon count) before and after the spoiling event. The resulting data points are drawn in blue in both panels[5] of figure 7.2. Equation 7.10 fits the data independently of any assumed contaminant and is drawn in red. The final fit parameters are:

$$\begin{aligned} \frac{I'_Q([\chi]+[\xi])}{I'_Q([\chi])} &= 0.887 \pm 0.003 \\ k_{A,\xi}[\xi] &= (0.021 \pm 0.009)\,\mathrm{m}^{-1} \\ \rightarrow l_{abs} &= (47 \pm 20)\,\mathrm{m} \end{aligned} \tag{7.13}$$

The reduction in the primary light yield obtained here can be compared to the one observed by the source SiPMs since all of them were active during the currently evaluated time frame. Figure 6.5a (lower panel) shows the light yield measured by the source SiPMs in the relevant time frame. The intensity detected by the source SiPMs directly measures relative changes in the primary light yield due to the proximity of these SiPMs

[5]Two panels are used to show the red final fit function, as it coincides mainly with the teal one.

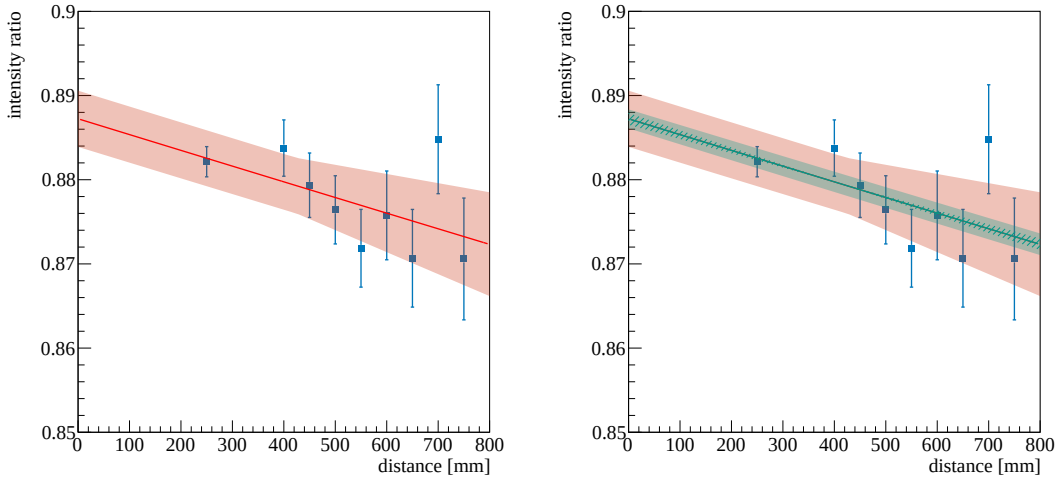

(a) (b)

Figure 7.2: Relative change of light intensities detected in different travel distances around the nitrogen spoiling event. Equation 7.10 is fit to the data (red). In (b), literature values of quenching and absorption coefficients of nitrogen are used to extract its concentration. Shaded areas show statistical uncertainties, while systematic uncertainties are drawn hatched.

to the scintillation location. By using the already defined time windows for integrating these values before and after the nitrogen spoiling, the following result is obtained:

$$\left(\frac{I'_Q([\chi]+[\xi])}{I'_Q([\chi])}\right)_{source} = 0.931 \pm 0.010 \tag{7.14}$$

The quoted uncertainty is the standard deviation of the data points averaged over. A tension exists between both measures of the reduction in the primary light yield, which can not be fully explained. The instabilities during LAr filling, which manifest as distortions in the mentioned plot, hint at effects distorting the light yield evaluation by the source SiPMs.

Overall, the results show weak absorption, barely able to be resolved by LLAMA, while the quenching is comparably strong. This is compatible with nitrogen, the substance introduced during the spoiling event. Since both k_{Q,N_2} and k_{A,N_2} are available in literature ([2] and [3], respectively), they are used to make the model only dependent on $[N_2]$. The final fit function is shown in 7.2b in teal. The shaded (hatched) area displays the

statistical (systematic) uncertainty. The extracted concentration is:

$$[N_2] = 1.40 \pm 0.02\,(\text{stat})\,^{+0.13}_{-0.11}\,(\text{sys})\ \text{ppm} \tag{7.15}$$

This value deviates from the nitrogen concentration of around 0.9 ppm computed by M. Harańczyk [4]. As explained in section 10.2.2, the latter calculation is based on a mass spectroscopic measurement of the filled LAr as well as the quantities of already present and added spoiled LAr in the cryostat. The deviation might hint at underestimated systematic effects, potentially connected to temporary instabilities of SiPM efficiencies during and shortly after the filling operations, and is not considered critical. The model using the parameters of the nitrogen contaminant fits the data well (the p-value is 0.62). Nitrogen was already previously identified as the substance introduced in the spoiling event. Thus, the presented analysis confirms the validity of the method.

7.3 Degradation during hardware operations

In the scope of the LEGEND-200 commissioning, payloads were immersed into the LAr-filled cryostat on several occasions. This can introduce impurities deteriorating optical properties of LAr. Figure 7.3 displays the time frame analyzed in this context, which contains most of the immersions. Those are marked with teal vertical lines if they only contain the fiber barrels and in orange, if they additionally or exclusively employ HPGe detectors. Furthermore, cyan lines indicate LAr top-up operations, which compensated for a slow loss in fill level happening in this time frame. The top-ups use certified LEGEND-200-quality LAr and employ LLArS, i.e. no significant introduction of impurities is expected. Instead, they presumably lead to a dilution of pre-existing contaminants. Analogous to before, two time windows are defined (shaded in gray), located before and after the hardware operations.

Several SiPMs started to fail within this time frame, which were recovered at the beginning of December 2022, as described in appendix B. The second time window defined here is located after the recovery operations, maximizing the number of usable SiPMs in this analysis.

Already in figure 7.3, a reduction in detected photon counts is visible, which happens gradually rather than step-like. All panels in figure 7.4 show the relative changes in

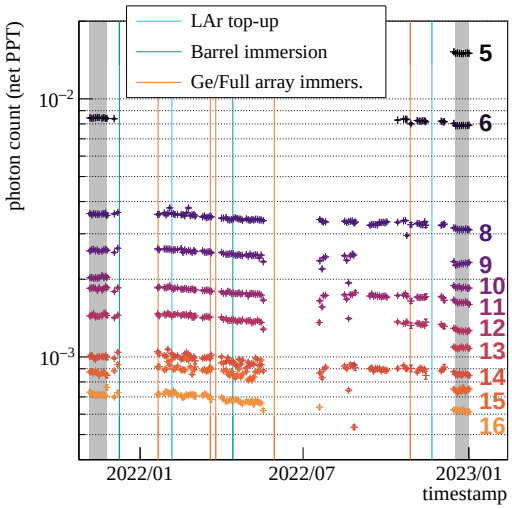

Figure 7.3: Photon counts for different peripheral SiPMs in the time range containing most payload immersions in the scope of the LEGEND-200 commissioning. Vertical lines show time points of such immersions: payloads only using the fiber barrels (teal) and ones including HPGe detectors (orange). LAr op-up operations are drawn in cyan. Gray-shaded areas depict time windows bordering the time frame and are used to extract the photon counts for further analysis (see text). SiPMs are indexed (right) in increasing order of light travel distance, from 5 (20 cm) to 16 (75 cm), in steps of 5 cm.

detected intensities for all available light travel distances (blue). The panels share the same fit to the data (red) using the model equation 7.10, i.e. without assuming a particular impurity. The final fit parameters are:

$$\begin{aligned} \frac{I'_Q([\chi]+[\xi])}{I'_Q([\chi])} &= 0.97 \pm 0.03, \\ k_{A,\xi}[\xi] &= (0.19 \pm 0.07)\,\mathrm{m}^{-1}, \\ \rightarrow l_{abs} &= (5.2 \pm 1.8)\,\mathrm{m}. \end{aligned} \tag{7.16}$$

The resulting absorption coefficient indicates the addition of an optically active impurity. Compared with the results obtained from the nitrogen spoiling time frame, the present results suggest a contamination characterized by a stronger absorption of LAr scintillation light and much weaker or even vanishing quenching of the primary light yield

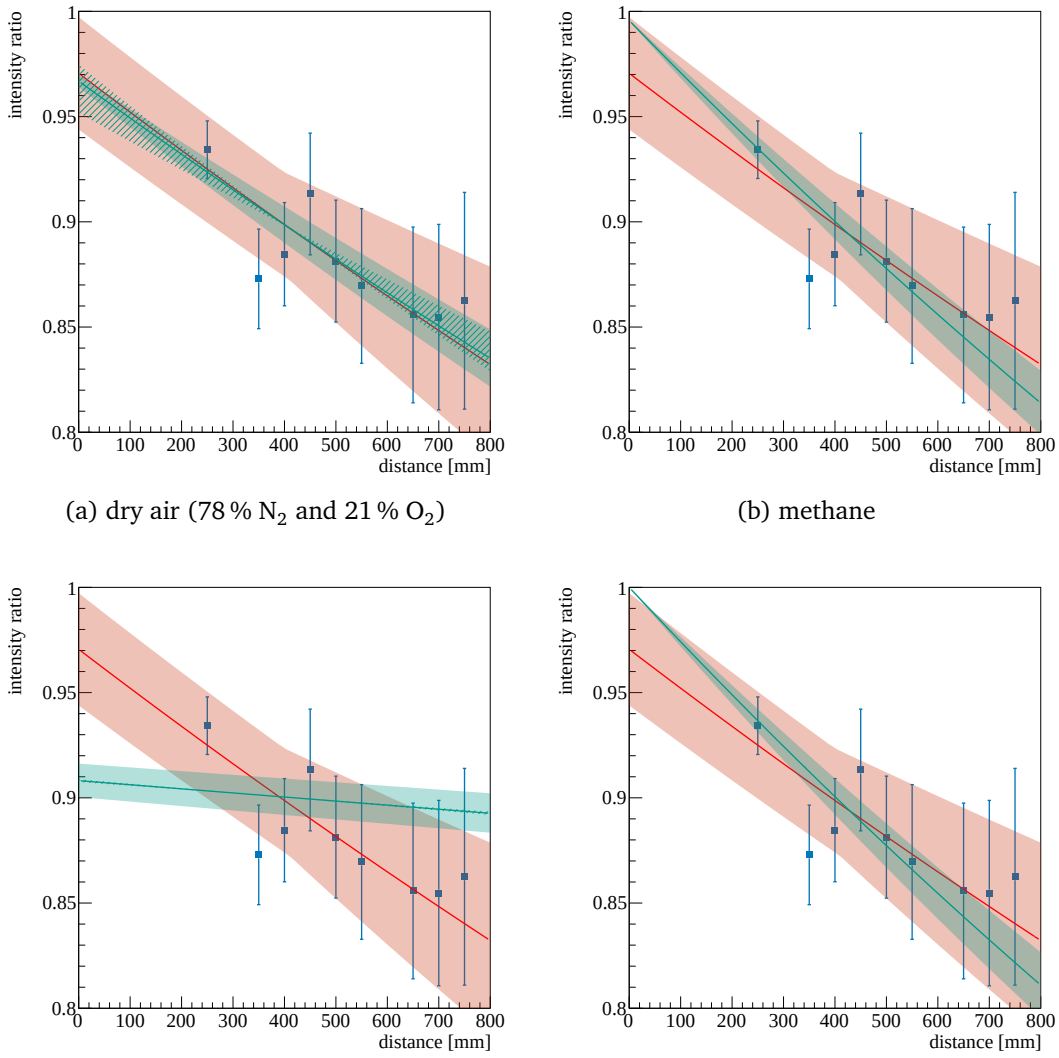

(a) dry air (78 % N_2 and 21 % O_2)

(b) methane

(c) nitrogen

(d) water

Figure 7.4: Relative change of light intensities detected in different travel distances from November 2021 to December 2022. All plots feature a fit with equation 7.10 to the data (red). Additionally, models assuming certain impurities are fit using parameters obtained from literature (teal; see sub-captions for the substances used). Shaded areas show statistical uncertainties, while systematic uncertainties are drawn hatched. The result for water lacks important inputs and thus serves as a rough estimate only (see text for details).

Table 7.1: Resulting concentrations of suspected contaminants ξ, obtained by modeling the decrease in detected light intensity during a time frame containing most hardware activities of the LEGEND-200 commissioning. As consistently done throughout this chapter, concentrations are given in terms of mole fractions. The result for water lacks necessary inputs (including k_{Q,H_2O}) and thus serves as a rough estimate only (see text for details).

ξ	$[\xi]$ in ppm	p-value	k_Q and k_A sources
dry air	$0.26 \pm 0.02\,(\text{stat})\,^{+0.13}_{-0.06}\,(\text{sys})$	0.88	k_{Q,N_2}: [2], k_{A,N_2}: [3], k_{Q,O_2} & k_{A,O_2}: [5]
methane	$0.0084 \pm 0.0008\,(\text{stat})\,^{+0.000009}_{-0.000008}\,(\text{sys})$	0.80	k_{Q,CH_4} & k_{A,CH_4}: [6]
nitrogen	$1.43 \pm 0.14\,(\text{stat})\,^{+0.13}_{-0.11}\,(\text{sys})$	0.25	k_{Q,N_2}: [2], k_{A,N_2}: [3]
water	$0.028 \pm 0.003\,(\text{stat})\,^{+0.086}_{-0.012}\,(\text{sys})$	0.76	k_{A,H_2O}: [7]

(quenching $< 4\,\%$ at $90\,\%$ C.L.). Since the responsible impurity or mixture is unknown, several candidates are explored using k_Q and k_A obtained from literature. As before, the parameters are inserted into the model to make it depend only on $[\xi]$. The final fit functions for individual contaminants are drawn in teal in separate panels of figure 7.4. Shaded areas show statistical uncertainties, while systematic uncertainties are drawn hatched.

Table 7.1 compiles the concentrations obtained for individual contaminants, as well as the p-values and literature sources of k_Q and k_A used. Both dry air (modeled as a mixture of 78 % nitrogen and 21 % oxygen) and methane are in good agreement with the data. The oxygen component of dry air is responsible for the absorption of the VUV scintillation light. Methane can be regarded as a proxy for other hydrocarbons, for which k_Q or k_A are unavailable. Nitrogen does not fit the data well and can thus be presumably excluded, at least as the sole contaminant in question.

Several shortcomings in modeling a pure water contamination render its resulting concentration a rough estimate. Even a thorough literature search produced no work yielding experimental results on k_Q or k_A of water-doped LAr. Thus, $k_{Q,H_2O} = 0$ had to be assumed, and k_{A,H_2O} is based solely on the VUV absorption of gaseous pure water, as derived by [7]. Non-zero values of k_{Q,H_2O} can lead to a worse matching of data and model and a reduction in the resulting concentration. Thus, the result of $[H_2O] \approx 30\,\text{ppb}$

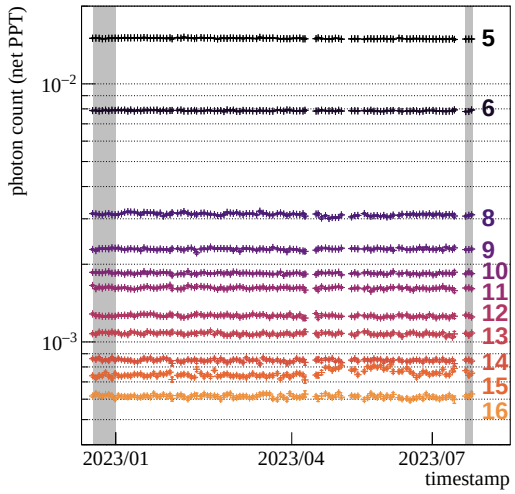

Figure 7.5: Photon counts for different peripheral SiPMs in the time range past all hardware operations, i.e. with stable LAr conditions. Gray-shaded areas depict time windows bordering the time frame and are used to extract the photon counts for further analysis (see text). SiPMs are indexed (right) in increasing order of light travel distance, from 5 (20 cm) to 16 (75 cm), in steps of 5 cm.

serves as a rough upper limit for the real concentration.

Modeling of the LAr scintillation quenching by water is hampered further because water does not dissolve in cryogenic liquids but is present in undissolved aggregates [8]. Furthermore, water is known to strongly attach to walls within LAr vessels [9, 10], which presumably includes the front surfaces of SiPMs. Thus, the VUV absorption by water films can lead to an overall reduction in the detected intensity, mimicking the quenching of the primary light yield. These effects make water contamination in LAr difficult to study and model.

7.4 Stable conditions after hardware operations

7.4.1 Analysis of relative changes in detected light intensity

The last time frame analyzed spans from December 2022 until the middle of August 2023[6]. This time frame is devoid of any hardware interaction affecting the LAr volume and thus

[6]The present analysis was conducted in August 2023, hence the position of the second time window.

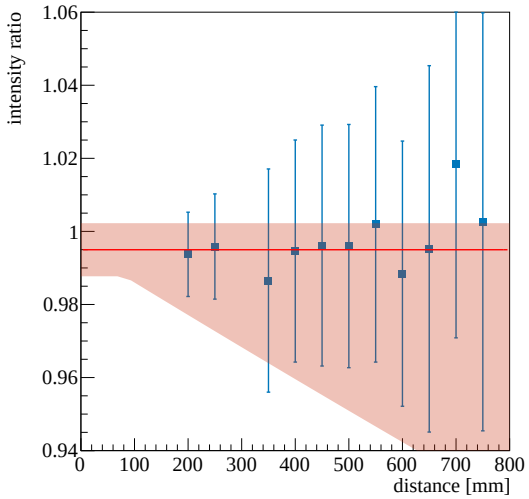

Figure 7.6: Relative change of light intensities detected in different travel distances from December 2022 to August 2023. This time range is devoid of hardware operations affecting the LAr, and all values are compatible with a vanishing deterioration. The plot features a fit with equation 7.10 to the data (red). The shaded area shows statistical uncertainties.

benchmarks the evolution of LAr properties in the stable data-taking mode of LEGEND-200. Figure 7.5 shows the development of photon counts for all available peripheral SiPMs. It is visible that both the optical properties of LAr and LLAMA's performance are stable.

The intensity ratios shown in figure 7.6 also reflect this stability, as all values are compatible with 1, i.e. a vanishing degradation. A fit with equation 7.10 (red) to the data quantifies this. Both final fit parameters, i.e. the change in primary light yield and the absorption strength, are compatible with no change within one standard deviation.

Analogous to previous time ranges, known properties of several potential impurities are injected into the model. This way, upper limits (90 % C.L.) on concentration increases are derived. The results are given in terms of rate, as potential changes are regarded to appear gradually rather than being point-like in time. They are compiled in table 7.2. These values stress the capability of the LEGEND-200 cryostat and its contents to keep the LAr in a pure state, especially when compared to the amount of contaminants introduced during the insertion of payloads.

Table 7.2: Upper limits (90 % C.L.) on the concentration increases of individual contaminants ξ during the time frame without payload insertions. The limit for water is presumably overestimated, as it lacks necessary inputs (including k_{Q,H_2O}).

ξ	upper limit on $\Delta[\xi]/\Delta t$ in ppb/yr
dry air	64
nitrogen	300
methane	1.8
water	11

7.4.2 Stability of detected intensity after maximum travel distance

The stability of the effectively observable light output in LEGEND-200 is studied in an alternative approach. Here, the photon count Φ of the most remote SiPM (75 cm of light travel path) is analyzed time-resolved. This yields the combined evolution of the primary light yield and the absorption due to the travel path, which are both crucial for the performance of the LEGEND-200 LAr instrumentation. Figure 7.7 shows the relevant data. The photon counts refer to the net PPT, defined in section 5.4.2. An affine function is fit to the data, and the final fit parameters are[7]:

$$\begin{aligned} \Phi_{16}(0) &= (0.6181 \pm 0.0016) \cdot 10^{-3}, \\ \Delta\Phi_{16}/\Delta t &= -(0.009 \pm 0.004) \cdot 10^{-3}/\text{yr}. \end{aligned} \tag{7.17}$$

A non-zero slope is borderline significant and is transformed into a limit: $\Delta\Phi_{16}/\Delta t > -0.015 \cdot 10^{-3}$/yr (90 % C.L.). Using the constant[8] $\Phi_{16}(0)$, the limit in terms of the relative change is calculated. Since the dependence on the geometrical efficiency is lost, the result equals the temporal change in intensity:

$$\frac{\Delta I_{16}/\Delta t}{I_{16}(0)} > -2.4\,\%/\text{yr}. \tag{7.18}$$

Thus, the intensity detected in 75 cm distance decreases by less than 10 % throughout 4 years of stable conditions.

[7] This SiPM is indexed with number 16; hence, the labels applied.
[8] The value corresponds to December 2022.

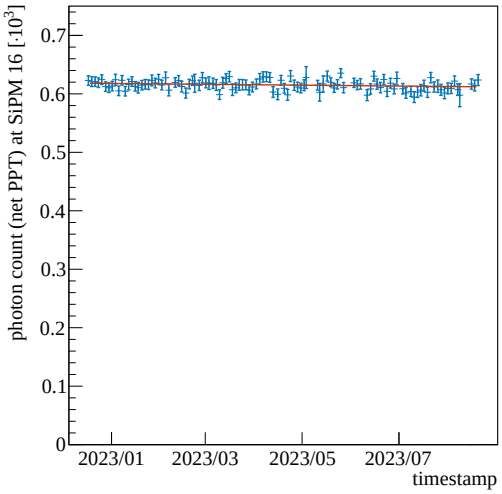

Figure 7.7: Time-resolved photon count in 75 cm distance from the scintillation light source of LLAMA. No hardware activities affecting the LAr were conducted in the used time frame. An affine function is fit to the data (red).

7.4.3 Evolution of the triplet lifetime

In section 4.3.1, the direct connection between the effective triplet lifetime τ_t' and the primary light yield is explained. Both parameters are reduced by contaminants, which quench argon excimers. Thus, the following study of the temporal stability of τ_t' complements and concludes the study of the LAr stability of LEGEND-200.

Figure 7.8 shows the time-resolved evolution of τ_t' measured by LLAMA. An affine function (red) is used to model the change over time, from November 2021 until August 2023, skipping the time range of unstable operation (gray). The final fit parameters are:

$$\begin{aligned} \tau_t'(0) &= (1.1564 \pm 0.0011)\,\mu\text{s}, \\ \Delta\tau_t'/\Delta t &= (0.0037 \pm 0.0009)\,\mu\text{s/yr}. \end{aligned} \tag{7.19}$$

The change in τ_t' is small but positive. This hints at a slight reduction in the concentration of quenching contaminants. As shown earlier, two top-up operations with high-quality and purified LAr occurred during this time frame. Those diluted pre-existing impurities.

Additionally, a second analysis of τ_t' uses only the time frame of stable LAr without

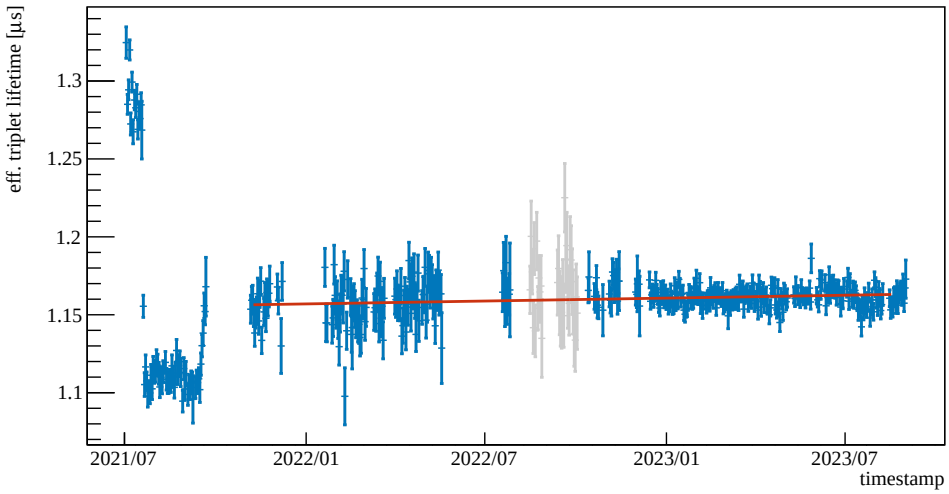

Figure 7.8: Time-resolved evolution of the effective triplet lifetime in LEGEND-200. A fit with an affine function (red) is performed, ranging from the first available data once the cryostat was filled completely, until August 2023. Part of the data is not used for the fit (gray), since several peripheral SiPMs failed during that period.

hardware interactions. The final fit parameters for this data set are:

$$\begin{aligned} \tau_t'(0) &= (1.1619 \pm 0.0007)\,\mu\text{s} \\ \Delta\tau_t'/\Delta t &= -(0.0014 \pm 0.0019)\,\mu\text{s/yr} \end{aligned} \tag{7.20}$$

Note that the initial effective triplet lifetime $\tau_t'(0)$ always corresponds to the beginning of the fit range, i.e. November 2021 for the long and December 2022 for the short range. No significant change in τ_t' is obtained in the shorter time range, compatible with the previous explanation, since the time frame is devoid of LAr top-ups. A limit on the annual decrease of τ_t' of $\Delta\tau_t'/\Delta t > -0.0039\,\mu\text{s/yr}$ (90 % C.L.) is derived, which constitutes another validation of the superior LAr stability during this time frame.

7.5 Conclusions and outlook

7.5.1 Discussion and lessons learned from LEGEND-200

The results of this chapter provide valuable input for understanding detectors employing liquid noble gases on large scales. Also, knowledge on the long-term stability of LLAMA in in-situ conditions is gained.

The analysis of the nitrogen spoiling event validates the method used, which is based on the relative changes in detected light intensities at different distances. Further evaluation of this event provides details about LAr doped with small quantities of nitrogen rather than contributing to a complete picture of the long-term stability of LAr. Thus, the detailed analysis of this event is covered in chapter 10.

The analysis of the time frame encompassing most hardware operations, in which payloads enter the LAr, shows deterioration of optical properties due to introduced impurities. The impurities could enter due to an insufficient vacuum pumping of the lock or via outgassing payloads. Since a nitrogen contamination is unlikely according to the presented results, the initial gas content of the lock cannot contribute[9]. However, air could enter the lock while it is being pumped and thus below ambient pressure; a dry air impurity matches the data well. Payloads can also lead to air contamination due to outgassing.

Furthermore, organic solvents like isopropyl alcohol and methanol, used to rinse HPGe detectors and components, can potentially enter the cryostat with the payload. Those substances cannot be modeled directly due to missing input from literature, but methane can be used as a proxy for organic molecules. Methane agrees with the data virtually as well as dry air. This comparison also applies to oils used when machining parts employed in the payloads, which can remain in small quantities if cleaning is insufficient. Thorough cleaning and vacuum pumping procedures applied in the LEGEND-200 commissioning are expected to keep those impurities low. However, according to the model, relevant methane concentrations would be as low as single-digit ppb.

Water is a potential further candidate for causing deterioration in liquid noble gas detectors. However, neither its distribution inside a cryostat nor its impact on the optical properties of LAr are sufficiently known to date. It is known from measurements in pure

[9]The lock is surrounded by a glove box, which is flushed with nitrogen gas while mounting the detectors. After closing the lock, the glove box is always vented with air.

warm gas state that water absorbs VUV light, which is critical since water can adsorb to surfaces of optical instrumentation. Water can remain on parts of the payload after insufficient vacuum pumping or can enter through air leaks.

Concluding, air, organic molecules, or a mixture thereof are plausible candidates for the degradation observed. The properties of water are too less known for making a decisive statement about its potential influence.

In the analysis of the last time frame, in which the LAr was unaffected by hardware operations, all results univocally indicate the stable optical properties of LAr. Limits on the increase of several impurity concentrations in the range of ppb per year are derived. More importantly, the evolution of the detectable VUV light intensity, as a combination of the primary light yield and the absorption over a path length of 75 cm, is studied. This value is critical due to its direct impact on the performance of the LAr instrumentation. The limit obtained translates to a less than 10 % reduction throughout 4 years of stable conditions.

7.5.2 Outlook to LEGEND-1000

Requirements for achieving long-term stability for large-scale liquid noble gas detectors can be derived from the presented results. Precisely, the planned procedures for LEGEND-1000 are based on them.

The conclusions from the phase of frequent payload immersions suggest that thorough cleaning of the parts and exhaustive vacuum pumping of the lock is paramount for maintaining pure LAr conditions. In this regard, the multi-lock[10] scheme proposed for LEGEND-1000 would be advantageous since it would allow for longer pumping and flushing cycles. This is especially important since due to the use of the UAr vessel, the ratio of inserted materials (such as HPGes, WLS fibers and electronics) to the LAr they come in contact with, is much higher (roughly a factor three to four) compared to LEGEND-200 [11].

Conversely, the feasibility of a long-term stable operation of LAr in a full-fledged detector system without re-purification is demonstrated for stable data-taking conditions. Hence, LEGEND-1000 can presumably operate without permanent LAr re-purification. Instead, on-demand re-purification is proposed, conducted as required, e.g. after insertion

[10] See section 3.3.2 for details.

of detector strings. The employment of LLAMA or a similar in-situ monitor in the UAr volume of LEGEND-1000 will identify LAr degradation calling for re-purification.

References

[1] R. Luther and A. Nikolopulos, *Z. Phys. Chem.*, vol. 82U, no. 1, pp. 361–384, 1913. DOI: doi:10.1515/zpch-1913-8229.

[2] R. Acciarri *et al.*, "Effects of Nitrogen contamination in liquid Argon," *JINST*, vol. 5, P06003, 2010. DOI: 10.1088/1748-0221/5/06/P06003. arXiv: 0804.1217 [nucl-ex].

[3] B. J. P. Jones, C. S. Chiu, J. M. Conrad, C. M. Ignarra, T. Katori, and M. Toups, "A Measurement of the Absorption of Liquid Argon Scintillation Light by Dissolved Nitrogen at the Part-Per-Million Level," *JINST*, vol. 8, P07011, 2013, [Erratum: JINST 8, E09001 (2013)]. DOI: 10.1088/1748-0221/8/07/P07011. arXiv: 1306.4605 [physics.ins-det].

[4] M. Harańczyk, "private communications," 2022.

[5] R. Acciarri *et al.*, "Oxygen contamination in liquid Argon: Combined effects on ionization electron charge and scintillation light," *JINST*, vol. 5, P05003, 2010. DOI: 10.1088/1748-0221/5/05/P05003. arXiv: 0804.1222 [nucl-ex].

[6] B. J. P. Jones *et al.*, "The Effects of Dissolved Methane upon Liquid Argon Scintillation Light," *JINST*, vol. 8, P12015, 2013. DOI: 10.1088/1748-0221/8/12/P12015. arXiv: 1308.3658 [physics.ins-det].

[7] J. Calvo *et al.*, "Measurement of the attenuation length of argon scintillation light in the ArDM LAr TPC," *Astropart. Phys.*, vol. 97, pp. 186–196, 2018. DOI: 10.1016/j.astropartphys.2017.11.009. arXiv: 1611.02481 [astro-ph.IM].

[8] A. J. Rest, R. G. Scurlock, and M. Wu, "The solubilities of nitrous oxide, carbon dioxide, Aliphatic ethers and alcohols, and water in cryogenic liquids," *The Chemical Engineering Journal*, vol. 43, no. 1, pp. 25–31, 1990, ISSN: 0300-9467. DOI: 10.1016/0300-9467(90)80041-A.

[9] M. Adamowski *et al.*, "The Liquid Argon Purity Demonstrator," *JINST*, vol. 9, no. 07, P07005, 2014. DOI: 10.1088/1748-0221/9/07/P07005.

[10] A. Zhang *et al.*, "Modeling impurity concentrations in liquid argon detectors," *Nucl. Instrum. Meth. A*, vol. 1010, p. 165 491, 2021, ISSN: 0168-9002. DOI: 10.1016/j.nima.2021.165491.

[11] S. Schönert, "LEGEND-1000 internal presentation," 2023.

Chapter 8

Attenuation length analysis

8.1 Measured attenuation curves in LEGEND-200

LLAMA provides light intensities at different distances from its triggered VUV light source. A detailed description of LLAMA is the subject of chapter 5. Specifically, the determination of the light intensities measured by the peripheral SiPMs is explained in section 5.4.2. In summary, the fraction of valid light emission events exhibiting a detected photon in a given peripheral SiPM is computed and referred to as pulse per trigger (PPT). Since PPT values in the peripheral SiPMs are below 2 %, multiple photon hits in the same SiPM can be neglected, making the PPT value proportional to the light intensity at the SiPM's location.

For studying the attenuation of LAr to its own scintillation light, VUV light emissions from the 60 keV gamma source are used. Valid events trigger the light source and pass all quality cuts. The light intensity over distance traveled, in the following referred to as *attenuation curve*, is shown in figure 8.1a for two of such runs of LLAMA in the LEGEND-200 cryostat. There, the two attenuation curves correspond to runs before (blue) and after (red) the contamination[1] of the LAr with around 0.9 ppm of nitrogen. Both are normalized to the light intensity at 25 cm distance, which was chosen since the closer peripheral SiPMs feature either a suprasil window (at 15 cm) or malfunction around and shortly after the contamination (at 20 cm).

The Beer-Lambert-Law describes the light curve within an attenuating medium, as explained in section 4.2.2. When assuming a wavelength-independent attenuation

[1]The contamination took place during the filling of LEGEND-200 with LAr and is described in section 6.3.

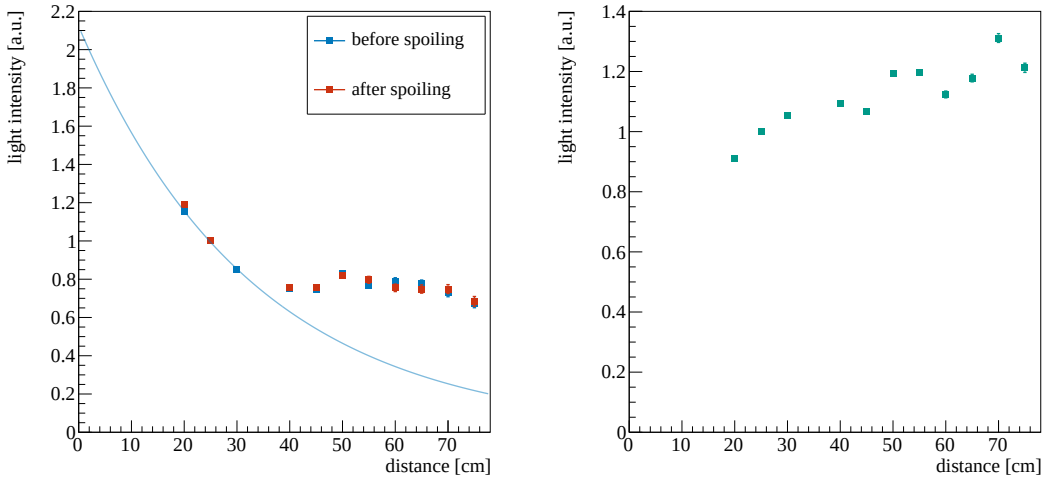

(a) (b)

Figure 8.1: Light intensities measured by peripheral SiPMs, normalized to the SiPM at 25 cm distance. (a): VUV scintillation light is used, and results are shown before (blue) and after (red) nitrogen spoiling. A fit with an exponential function to close distances of the data set before spoiling (light blue) shows that a single attenuation length can explain the data only for $x \lesssim 30\,\text{cm}$. (b): visible photons from the LED are used in a dedicated run; LAr does not attenuate visible photons.

cross-section, equation 4.4 simplifies to:

$$I'_A(x) = I\, e^{-\frac{x}{l_{att}}}. \tag{8.1}$$

A fit to data before the spoiling with nitrogen, for distances up to 30 cm (light blue) yields $l_{att} = (33.0 \pm 1.3)\,\text{cm}$. As the plot shows, the data deviates strongly from the model starting around 40 cm. While a wavelength-dependent cross-section causing deviations from a single exponential function is expected in the presence of impurities (see section 4.3.2 and [1]), the present case seems extreme. Virtually no attenuation is present for distances around and exceeding 40 cm. Attributing this effect to wavelength-dependent attenuation induced by impurities appears challenging and is the subject of section 8.4.

By using the data at hand, at least the attenuation caused by nitrogen impurities is identified to be negligible, as the introduction of 0.9 ppm during the spoiling does not change the attenuation curve significantly. This can be seen by comparing both

attenuation curves in figure 8.1a and is also studied in section 10.3.3.

Apart from intrinsic LAr features, also instrumental effects might explain the shape of the measured attenuation curve. Those are e.g. reflections on the LLAMA setup itself or the inner walls of the cryostat, or inequalities among the photodetection efficiencies of the peripheral SiPMs. Studying this effect is the primary goal of the LED calibration run. During this dedicated measurement campaign conducted on July 08th, 2021, i.e. very early during the filling campaign of LEGEND-200, the LED was active, and data taking was triggered by the signals driving the LED. Thus, this measurement run uses visible green photons, which exhibit negligible attenuation in LAr. The resulting attenuation curve is shown in figure 8.1b. Without any instrumental effect, the intensity is expected to be constant with respect to the travel distance. The visible trend of increasing intensity with distance can be explained with reflections. The intensity increase due to reflections is around 30 %, which is expected to be reduced by a factor of 3 when studying VUV photons and thus cannot explain the strong deviations in those attenuation curves by itself.

8.2 Implementation of a dedicated optical simulation

A dedicated Monte Carlo simulation of LLAMA in the LEGEND-200 cryostat was implemented using the Geant4 framework [2–4]. Its main purpose is the study of reflections on the LLAMA setup and the inner cryostat wall, as well as their interplay with scattering within the LAr. The geometry is implemented[2] in source code using geometry primitives provided by Geant4 to limit the computing resources required. The program includes only the necessary parts of the setup, which are shown in figure 8.2. The render displays the copper rings and bars of LLAMA (red), as well as its copper light source and peripheral SiPMs (black). Cryostat walls are displayed in shades of green. A segmentation of its bottom part was necessary since the curvature radius varies. The simulated setup omits the inner copper lining of the cryostat as well as the WLSR, as those end in positions above LLAMA[3].

[2] The implementation of parts of the LLAMA setup was done by X. Stribl.

[3] The WLSR (inner copper lining) ends around 13 cm (21 cm) above the front surface of LLAMA's topmost SiPM [5]. Since LLAMA's peripheral SiPMs are facing downwards, scattering from locations above LLAMA can be neglected.

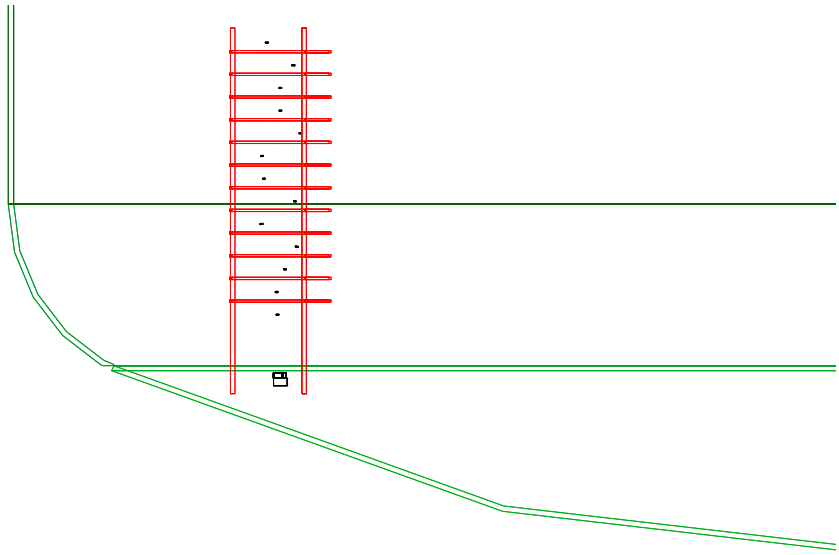

Figure 8.2: A rendering of the geometry implemented in a dedicated Monte Carlo simulation studying light propagation for LLAMA in LEGEND-200. Components of LLAMA are drawn in red (vertical bars, rings) and black (light source and SiPMs). The cryostat walls are drawn in shades of green.

The wavelength-dependent Rayleigh scattering length of LAr implemented[4] is calculated from the dielectric constant measured by [6]. In the mentioned publication, the scattering length at 128 nm amounts to (99.1 ± 2.3) cm. A slight correction is applied for the LAr in LEGEND-200, since the temperature there is around 88.8 K [7], rather than 90 K used by [6]. Thus, the implemented scattering length at 128 nm is around 100.4 cm.

Reflectivities of the cryostat's inner wall are modeled based on results of dedicated reflectivity measurements of steel from the visible region to 120 nm by [8]. The total reflectivity of 0.2 in the VUV region is chosen following these results. However, the specular to total reflectivity ratio is set to 0.2 rather than the 0.4 provided by the aforementioned measurement using polished steel samples, because the cryostat wall is not polished.

The reflectivity of the copper parts of LLAMA were set to 0.2 for VUV photons, approx-

[4]The implementation follows the "legend-geom-optics" project by L. Pertoldi and M. Huber: `https://github.com/legend-exp/legend-geom-optics`

imating the reflectivity of copper parts implemented in the MAJORANA-GERDA (MaGe) simulation package [9]. In turn, the value is obtained from an extrapolation of results from a dedicated measurement by [10]. A specular to total reflectivity ratio of 0.2 is assumed here since most of LLAMA's surfaces are not polished either.

Emissions of single photons from the center of the source cavity with random momentum directions and polarizations are simulated. The energies are sampled according to the LAr scintillation wavelength distribution measured by [11].

Individual photons are tracked until they are absorbed at any surface. If the absorption occurs at the optically active surface of a peripheral SiPM, the photon's energy, total travel distance, and the respective SiPM index are recorded. These data allow postponing the application of absorption effects to the post-processing of the Monte Carlo output. Thus, absorption spectra from different impurities at different concentrations can be investigated without re-running the time and resource-intensive simulation chain.

8.3 Study of instrumental effects

Several effects can impact the measured light curve, which are connected to the setup itself, i.e. LLAMA and the LEGEND-200 cryostat, rather than being caused by LAr or its impurities. Reflections on LLAMA or the cryostat walls can lead to an excess in detected photons in some peripheral SiPMs. The experimental approach using a pulsed green LED shown earlier suffers from reflectivities in the visible range vastly exceeding the ones in the VUV. Thus, the optical Monte Carlo simulation outcome is used here instead of relying on the LED calibration measurements. Light curves were produced for reflectivities at their default values and for vanishing reflectivities on all surfaces. No LAr absorption is assumed in both cases. The result, shown in figures 8.3, shows negligible impact of reflectivities on the simulated light curves.

Additionally, non-equalities in the photodetection efficiencies of the peripheral SiPMs can contribute to systematic biases in the measured attenuation curves. To estimate their impact, the LED run was reproduced in simulation using the aforementioned Monte Carlo implementation. To this end, photons of 530 nm wavelength were tracked, and the reflectivities of the cryostat and the copper parts of LLAMA were set to 0.65 [8] and 0.5 [10], respectively. The ratio of specular to diffuse reflectivity was assumed to be 1:1. The resulting attenuation curve is shown in figure 8.4 (red) and compared to the

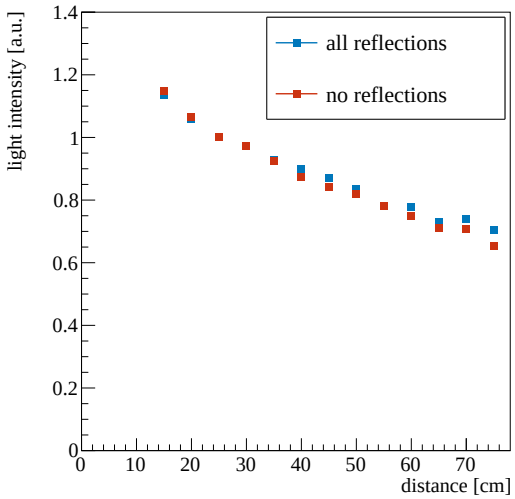

Figure 8.3: Simulated light intensities at different distances from the light source using LAr scintillation photons. The simulation includes Rayleigh scattering and reflections on the cryostat wall and the LLAMA setup. Disabling reflections entirely leads to minor effects.

measurement (teal). Individual light intensities differ, which can be partly attributed to difficulties in reproducing the geometry to a level required for exact photon tracking in the presence of specular reflections on small surfaces, i.e. the rings of LLAMA. However, the overall behavior is reproduced, limiting a possible bias spanning several consecutive SiPMs.

8.4 Liquid argon properties

With instrumental effects presumably having a subdominant effect on the light curve measured by LLAMA, the dominant features of the light curve are tentatively explained by properties intrinsic to LAr and any diluted impurities. This section requires inputs from the Monte Carlo simulation of the LLAMA setup in LEGEND-200, which was explained earlier.

The simulation output is treated with post-processing algorithms applying the Beer-Lambert-Law using arbitrary absorption spectra. Additionally, the wavelength-dependent efficiencies of the VUV4 SiPMs obtained from vendor information (see figure 5.3) are

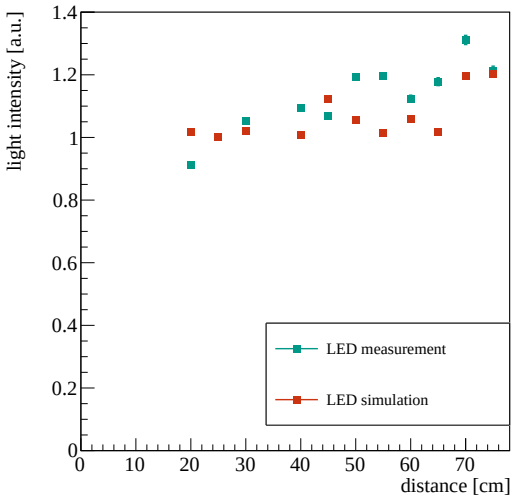

Figure 8.4: Comparison of the measured LED run to a Monte Carlo simulation.

used to weight the spectra. Different properties impacting light propagation in LAr are discussed in the following.

8.4.1 Rayleigh scattering

Rayleigh scattering is investigated first, as it is a universal property of LAr, independent of impurity compositions. Since the measurement of the group velocity of VUV photons in LAr by [6], both the refractive index and the Rayleigh scattering length are known with unprecedented precision. As mentioned, Rayleigh scattering based on those findings is implemented into the Monte Carlo simulation of LLAMA. Accounting for wavelength-dependent parameters is a crucial concept of this study since the refractive index and, thus, the scattering length changes strongly within the LAr scintillation wavelength region due to its vicinity to a resonance line at 106.6 nm [6].

The simulated light curve without absorption or wavelength shifting, i.e. only using scattering and reflections, is shown in figure 8.5 (teal). The measured data is drawn in blue. A χ^2 minimization was used to fix the arbitrary scale of the simulated curve. Apart from the wavelength-dependent efficiencies of the VUV4 SiPMs used here, the result corresponds to the “all reflections” curve in figure 8.3.

It becomes clear that the model shown does not reproduce the measurement over the

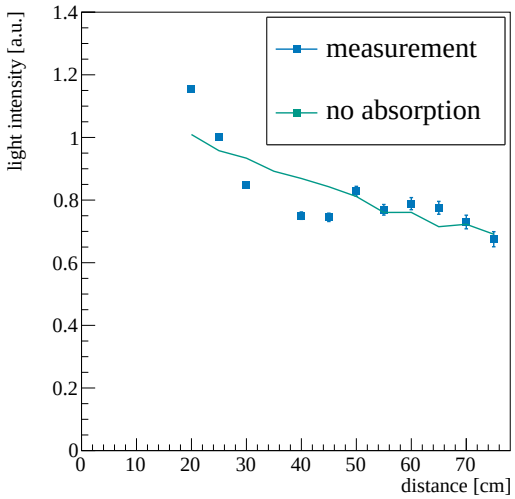

Figure 8.5: Comparison of a measured and a simulated light curve. The latter uses no absorbing or wavelength-shifting species, i.e. only reflections and Rayleigh scattering is applied. The normalization of the simulated curve is obtained by minimizing the chi2 to the data points.

entire distance range studied. Note that the scaling is arbitrary. Thus, the simulation might not match the data for $x \geq 50\,\text{cm}$, as one might infer from the plot. The steep falling slope for $x \leq 30\,\text{cm}$ in measurement data is not reproduced by the scattering-only assumption. Since the model of a completely clean LAr solely featuring Rayleigh scattering is not reproducing the data at hand, the presence of absorbing contaminants is considered in the following.

8.4.2 Optically absorbing contaminants

Deriving concentrations for individual contaminants

Several VUV-absorbing contaminants are studied in their possible impact on the measured light curve. To this end, the output of the Monte Carlo simulation of LLAMA is used and treated with the post-processing algorithm explained earlier to simulate wavelength-dependent absorption. The post-processing allows fitting the simulated light curves to measurement data, varying the concentration[5] of the individual contaminants. The

[5] Concentrations quoted in the following are defined in terms of mole fraction.

normalization of the whole resulting curve constitutes another free parameter.

The procedure of investigating several individual contaminants' abilities to cause the attenuation measured is adopted from [12]. There, the contaminant(s) causing the attenuation length of 50 cm in the ArDM detector were searched for. Required impurity concentrations are computed from doped LAr measurements for nitrogen and xenon, while pure, warm gas state measurements are used for all other contaminants. With constraints from triplet lifetime quenching and mass spectroscopy analysis, several molecules could be excluded for causing the attenuation, while the relevant contaminants could not be identified [12].

In the present analysis, the procedure yielding the concentrations of the absorbing contaminants deviates from [12] in treating wavelength-dependent effects. The wavelength-dependent absorption cross-section is used to retain effects causing non single-exponential attenuation curves and to study the interplay with Rayleigh scattering, which is by itself strongly wavelength-dependent. Conversely, in [12], the cross-sections are averaged over the LAr emission spectrum to obtain effective cross-sections.

The absorption of xenon-doped LAr is taken from the transmission measurement by [13], using the spectrum obtained from a xenon concentration of 0.1 ppm. Since no other wavelength-resolved absorption spectra of impurity-doped LAr were available in literature, spectra obtained from absorption measurements done in the warm gas were used[6], as explained in section 4.3.2. Figure 8.6 shows some simulated attenuation curves and measured data (blue). In figure 8.6a, the minimization considers the entire range. The resulting curves do not deviate significantly from the "no absorption" curve (teal), and thus resulting concentrations are not considered in the following. Instead, the analysis uses a restricted range up to and including 30 cm, where a clear attenuation behavior is visible (see figure 8.6b).

The results from fits in this window are presented in the second column of table 8.1. For computing values in the third column, the same absorption spectra are shifted by 7 nm towards shorter wavelengths ("blue shift"). This procedure was motivated and performed by [12], after discovering a blue shift of around 7 nm for xenon and mercury

[6]The relevant cross-section spectra were obtained from [14], which provides a list of measured and digitized absorption spectra from the gas state compiled from several publications. The ones used in this work are: O_2: [15], N_2: [16], CH_4: [17], H_2O: [18], NO_2: [19], SO_2: [20], C_2H_2: [21], NH_3: [22], CO_2: [23] and NO: [24].

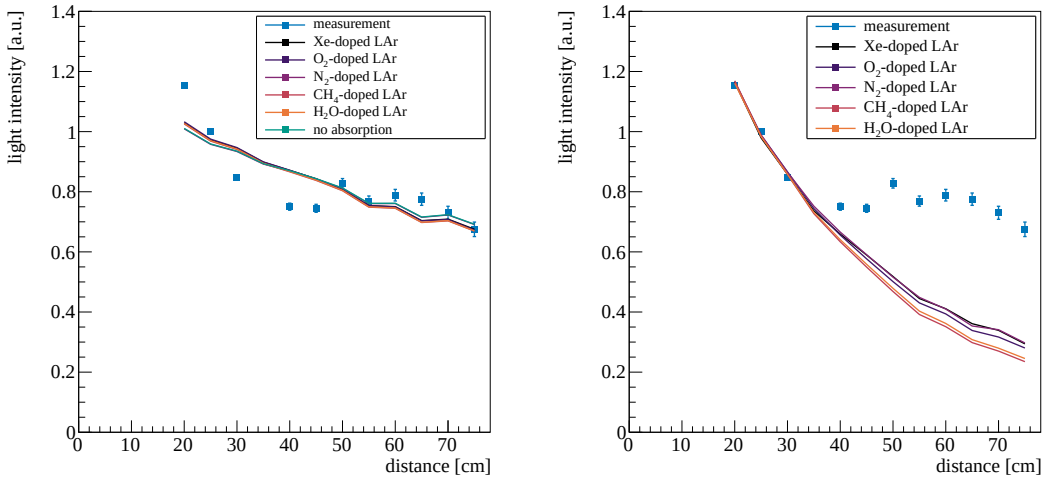

(a) (b)

Figure 8.6: Simulated attenuation curves with included absorption by singular contaminants. Concentrations are obtained by a χ^2 minimization to measured data points (blue) over the full range (a) and using only data points $x \leq 30\,\text{cm}$ (b). (a) also includes a curve simulated without an absorbing contaminant. See table 8.1 for a list of final concentrations and sources of used spectra.

when transitioning from the gas state to the LAr medium. Additionally, cross-sections obtained from wavelength-integrated measurements in doped LAr are used[7] and provide concentrations listed in the fourth column. For comparison, the last column lists the results computed by [12] for explaining the 50 cm attenuation length found by ArDM. All concentration values are defined in terms of mole fraction, as specified in appendix A.

The nitrogen concentrations obtained from spectra in the gas state compared to values computed from the doped LAr are in tension. This is attributed to differences in the absorption cross-sections used, which are shown and discussed in section 10.3.3. Since an increase in cross-section by the transition from the gas state to the LAr environment for nitrogen is speculated there, concentrations derived from measurements in doped LAr are preferably used in the following.

Differences between concentrations obtained from LLAMA and results for ArDM can be attributed to different attenuation lengths and divergences in treating wavelength-dependent effects, as discussed earlier.

[7] The values are taken from: O_2: [25], N_2: [26] and CH_4: [27].

Table 8.1: Concentrations (in mole fraction) of individual contaminants matching the measured absorption in LAr. The LLAMA results were obtained by matching the simulated attenuation curves to measurement data in the range $x \leq 30\,\text{cm}$. ArDM results are taken from [12], which match the 50 cm attenuation length present there. For LLAMA, both wavelength-resolved spectra and λ-integrated measurements yield absorption cross-sections used.
Notes: ^{l} Cross-sections obtained from measurements in doped LAr (others: pure warm gas).
* [12] uses the oxygen spectrum of the metastable state $a^1\Delta g$, while for LLAMA the ground state $X^3\Sigma g^-$ is used.

Contaminant	LLAMA results for LEGEND-200 [ppm]			ArDM results [ppm]
	spectrum	blue shifted sp.	λ-integrated	
Xe	0.11^{l}			0.027^{l}
O_2	2.4	0.34	0.64^{l}	0.170^{*}
N_2	6349	5098	143^{l}	135^{l}
CH_4	0.064	0.18	0.072^{l}	0.097
H_2O	0.16	0.37		0.22
NO_2	0.052	0.098		
SO_2	0.043	0.22		0.099
C_2H_2	0.13	0.30		0.023
NH_3	0.12	0.15		0.094
CO_2	2.5	1.5		1.5
NO	0.45	0.29		0.38

Limits on contaminant concentrations

Upper limits on individual contaminant concentrations are derived to exclude or find contaminants responsible for the attenuation measured by LLAMA in LEGEND-200. A given impurity is excluded for being solely responsible for the observed attenuation in case its concentration required for explaining the attenuation features exceeds those limits. This procedure is performed in analogy to [12].

Since all contaminants affect the effective triplet lifetime via quenching[8], the measured τ_t' is used to generate limits on the individual concentrations. Here, $\tau_t' = (1.315 \pm$

[8] See section 4.3.1 for a description of the quenching process in LAr.

Table 8.2: Quenching rate constants k_Q of several contaminants measured in LAr. They are used for generating limits on contaminant concentrations compiled in table 8.3. Note that the value quoted by [28] is converted by changing the concentration definition from mass to volume fraction.

Contaminant	Quenching rate constant [$\mu s^{-1}\,ppm^{-1}$]	Reference
Xe	0.289	[28]
	0.169	[29]
	0.338	[30]
O_2	0.54 ± 0.03	[25]
N_2	0.11 ± 0.01	[31]
CH_4	0.76	[27]

0.037) µs is taken from a fit with the full LAr time profile of light emission model in section 9.3. Additionally, the triplet lifetime of pure LAr has to be assumed. The value from the DEAP-3600 pulse shape model of $\tau_t = 1.445\,\mu s$ is used. Though it might be affected by delayed TPB emission and thus overestimates the actual value, it provides a conservative upper limit.

Quenching rate constants k_Q are obtained from literature and compiled in table 8.2. All entries are measured in LAr doped with the respective contaminants.

The equation

$$[\chi]_{max} = (1/\tau_t' - 1/\tau_t)/k_Q \tag{8.2}$$

yields concentration limits for every available quenching rate constant listed in the third column of table 8.3. Limits derived from the triplet lifetime are paramount, as they hold even in case of potential contamination after delivery and purification of the LAr.

Additionally, concentration limits are provided by the "LEGEND-200 quality" specification of delivered LAr, according to [32]. This specification is based on Ar of 5.0 purity[9], but imposes stricter limits on oxygen, nitrogen and water of 1 ppm. The limits on hydrocarbons, here CH_4 and C_2H_2 are 0.2 ppm. Other values are bound by the requirement of the sum of all contaminants not exceeding 10 ppm. For xenon, a limit of ≈ 0.008 ppm is

[9] Purity of industrial gases are usually denoted in the notation, where an integer preceding the decimal dot corresponds to the number of "9" digits, while the digit trailing the decimal dot equals the first digit not being "9". For example, argon 5.0 contains at least 99.999 % argon atoms.

Table 8.3: Comparison of concentrations (mole fractions) required to explain the attenuation measured by LLAMA with single contaminants to their respective limits. Part of the limits are obtained from the quenching of the effective triplet lifetime from $\tau_t = 1.445\,\mu s$ to $\tau_t' = (1.315 \pm 0.037)\,\mu s$ using the quenching rate constants compiled in table 8.2. Additionally, limits are extracted from the "LEGEND-200 specification" of the ordered LAr [32], except for xenon, for which [33] provides the limits. ^{ga} denotes limits from the gas analyzer after purification. Required concentrations are taken from table 8.1 using measurements in the LAr (^{l}) or blue-shifted spectra (no label).

Contaminant	Required conc. [ppm]	Conc. limits [ppm]	
		using τ_t'	LAr specification
Xe	0.11^{l}	0.24 ± 0.07	≈ 0.008, 0.1
		0.41 ± 0.13	
		0.20 ± 0.06	
O_2	0.64^{l}	0.13 ± 0.04	$1, 0.1^{ga}$
N_2	143^{l}	0.62 ± 0.20	1
CH_4	0.072^{l}	0.09 ± 0.03	0.2
H_2O	0.37		$1, 0.1^{ga}$
NO_2	0.098		10
SO_2	0.22		10
C_2H_2	0.30		0.2
NH_3	0.15		10
CO_2	1.5		10
NO	0.29		10

obtained from information provided by LINDE [33]. This is derived using the ratio of xenon to krypton in the atmosphere of 1:13, together with LINDE's detection limit of krypton of ≈ 0.1 ppm. However, ICPMS measurements by [12] on ALPHAGAZ-1 and -2 from AirLiquide Spain with purity levels of 5.0 and 6.0, respectively, show xenon contents exceeding krypton by around one order of magnitude. Thus, the more conservative limit of 0.1 ppm according to [33] is quoted additionally. For oxygen and water, limits from the gas analyzer after purification (see section 6.3) are provided and marked with ^{ga} [34].

The limits are compared to the required concentrations of individual impurities. The

latter correspond to the values in table 8.1, preferably using results based on measurements in doped LAr (marked with ^{l}) and otherwise from the gas phase with applied blue shift.

By comparing required concentrations and limits, several contaminants can be tentatively excluded in solely causing the attenuation measured by LLAMA: nitrogen, oxygen, and water. Providing a statement about xenon is challenging. The limit of ≈ 0.008 ppm would exclude it, but might not hold as discussed previously. Thus, only the presumed contamination in the "lower ppb or even ppt" range by [33] can limit the influence of xenon. Other contaminants cannot be excluded using the data at hand.

Additionally, mixtures of contaminants can also be responsible for the attenuation measured by LLAMA and are more challenging to investigate. However, a contamination with dry air only is excluded because the triplet lifetime yields limits on nitrogen and oxygen, forcing the dry air content below 1 ppm. Thus, nitrogen and oxygen are insufficient, and other components of dry air are below 1 ppb and hence negligible.

In conclusion, a singular contaminant responsible for the attenuation length measured by LLAMA for distances up to 30 cm could not be identified. This was also the case for [12]. In that publication, CH_4 was emphasized since its significant abundance in LAr is possible "due to its abundance in the atmosphere and a similar boiling point" [12]. There, the required CH_4 concentration was identified borderline compatible with the triplet lifetime quenching. This situation reproduces here.

While xenon was excluded in [12] according to ICPMS measurements, the situation is less clear here. Xenon shows strong absorption bands for LAr scintillation and is thus attributed a "critical impurity in pure liquid argon scintillation detectors" [13]. Commercial LAr can have xenon contents around 0.1 ppm and above [13], e.g. ICPMS by [12] found a xenon content of around 0.05 ppm in ALPHAGAZ-1 (5.0 quality) from AirLiquide Spain.

Mass spectroscopy can be used to identify the impurity composition responsible for the attenuation measured by LLAMA, but sensitivities of $\mathcal{O}(0.1)$ ppm or below are required. Alternatively, spectroscopic measurements of the absorption cross-section of LEGEND-200's LAr can lead to an identification.

8.4.3 Extraction of absorption spectrum from measurement

In the first part of section 8.4.2, known absorption spectra of impurities were matched to the measured attenuation curve by varying the contaminants' concentrations. However, no contaminant could explain the entire attenuation curve measured. Thus, an alternative approach is pursued, in which an arbitrary absorption spectrum whose parameters are varied freely is used. Analogous to the previous section, the output of the dedicated optical Monte Carlo simulation of LLAMA in the LEGEND-200 cryostat is used; thus, e.g. Rayleigh scattering is accounted for. Since the impurity concentration is unknown, absorption strengths are used in the following, defined as $K_A(\lambda) = 1/l_{abs}(\lambda) = k_{A,\chi}(\lambda)[\chi]$ (see also equation 4.9).

A step function is used to minimize the degeneracies of the modeled absorption spectrum. It features two domains of constant absorption strengths, delimited by a threshold wavelength λ_{ths}, i.e. has three free parameters. In accordance with absorption spectra of typical contaminants, the domain at a shorter wavelength is assigned the shorter absorption length $l_{abs,s}$. The longer absorption length is denoted with $l_{abs,l}$.

Figure 8.7a shows the measurement (blue) together with the best-matching attenuation curve simulated (teal, also used in all following plots in this section). The obtained absorption spectrum is shown in figure 8.7b, featuring the following parameters:

$$l_{abs,s} = 5.6\,\text{cm},\ l_{abs,l} = 1000\,\text{cm},\ \lambda_{ths} = 133\,\text{nm}. \tag{8.3}$$

To estimate the validity of the "best fit", each free parameter is varied with the remaining ones fixed at the found optimum. Attenuation curves are produced, which are drawn against the measurement data using individually optimized scalings. Figures 8.8 (a) and (b) show the effect of changing the absorption lengths $l_{abs,l}$ and $l_{abs,s}$, respectively. The result of varying the threshold wavelength is shown in figure 8.9. The long absorption length matches the data at its optimal value and equally well for arbitrarily larger values. Apart from this degeneracy, deviating from the "best fit" leads to the inability to describe the data in the whole domain.

To compare the obtained absorption spectrum to spectra measured for contaminants, the attenuation strengths are converted[10] to cross-sections assuming a plausible concen-

[10] See equation 4.11 for calculating the conversion.

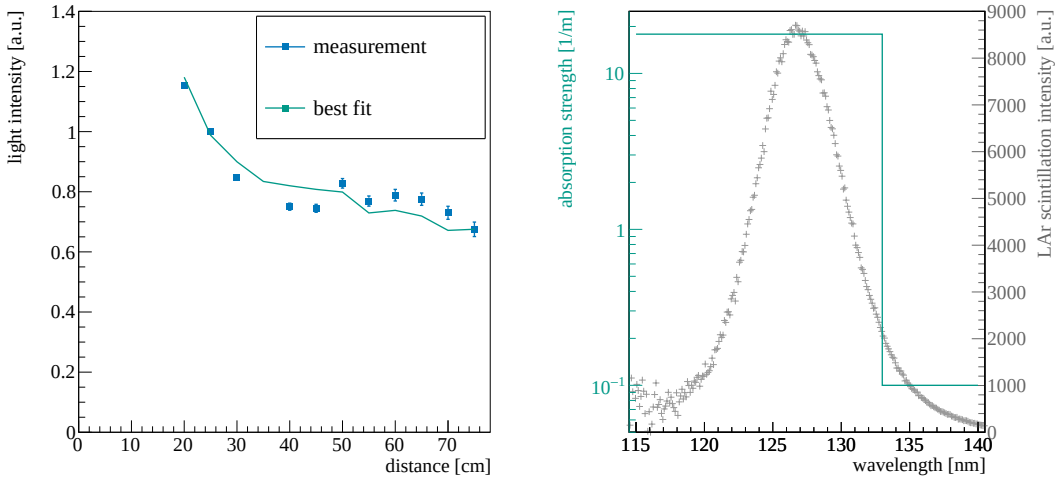

(a) (b)

Figure 8.7: A simulated attenuation curve matching data (a) was obtained by varying parameters of a step function (b) modeling the absorption spectrum. The latter plot also shows the LAr emission spectrum from [11], demonstrating the small fraction of the weak absorption strength component.

tration of 0.1 ppm:

$$\sigma_s = 8.5 \times 10^{-17}\,\mathrm{cm}^2 = 85\,\mathrm{Mbarn}, \text{ and } \sigma_l = 4.7 \times 10^{-19}\,\mathrm{cm}^2 = 0.47\,\mathrm{Mbarn}. \quad (8.4)$$

On the one hand, the values themselves and the difference amounting to two orders of magnitude are typically found in measured absorption spectra in the relevant wavelength region. For example, the spectrum of oxygen shows peaks exceeding $1 \times 10^{-17}\,\mathrm{cm}^2$ and valleys as low or lower than $1 \times 10^{-19}\,\mathrm{cm}^2$ (see figure 4.2). On the other hand, the absorption spectrum is modeled in an arbitrary and simple way. It is impossible to infer the absorbing impurity by matching the absorption spectra.

Concluding, the absorption spectrum generated demonstrates that the measured attenuation curve can potentially be explained by an unknown contaminant absorbing VUV photons. The obtained absorption spectrum can be used as a starting point for modeling the optical photon propagation in the LEGEND-200 cryostat. However, due to the arbitrary model used, the wavelength composition of tracked photons will presumably not match reality. Thus, results must be taken with a grain of salt once the contribution

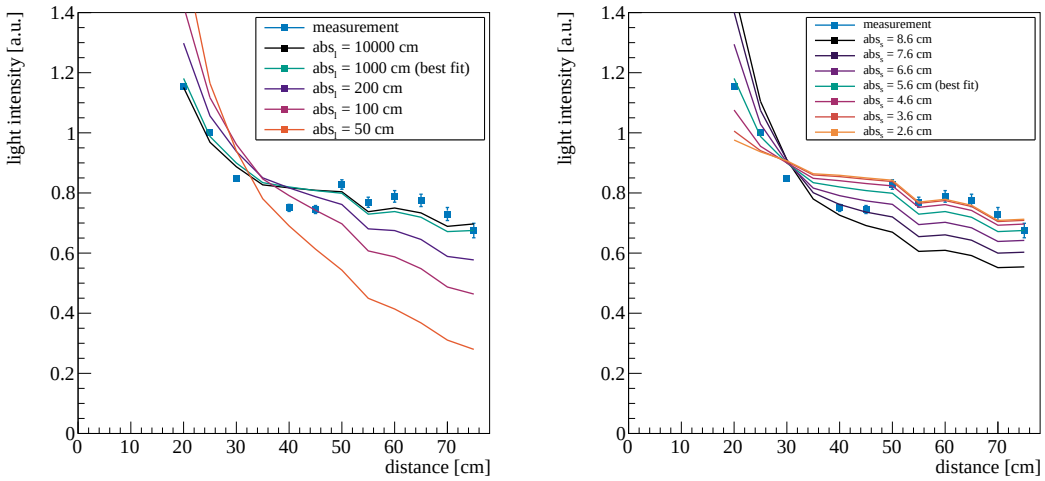

(a) (b)

Figure 8.8: Simulated attenuation curves using varied absorption lengths of the absorption spectrum model shown in 8.7b. Both the longer (a) and shorter (b) absorption lengths are varied. The "best fit" is drawn in teal.

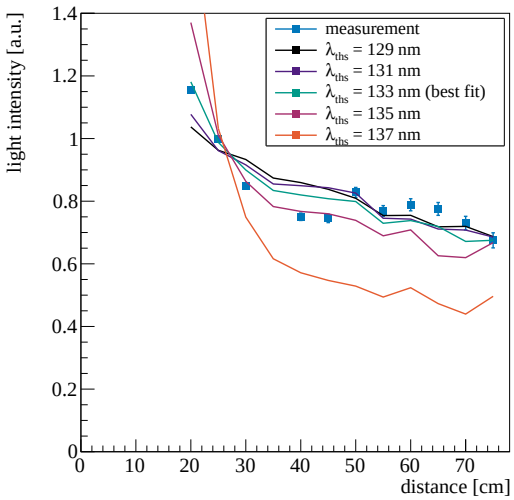

Figure 8.9: Simulated attenuation curves obtained by varying the threshold wavelength between both absorption length domains of the model shown in 8.7b. The "best fit" is drawn in teal.

of other wavelength-dependent effects is studied, e.g. reflectivities or efficiencies of wavelength-shifting parts of the setup.

8.4.4 Wavelength-shifting contaminants

Contaminants in the argon volume, shifting the wavelength of traveling photons to higher values can also impact the attenuation curve measured by LLAMA. Motivated by this possibility, the closest peripheral SiPM at 15 cm distance of LLAMA-I is fitted with a suprasil window (see section 5.1.2). It blocks photons of wavelengths below 150 nm, i.e. primary LAr scintillation, while being transparent above around 170 nm [35]. This region contains the 175 nm emission line of the decay of Xe_2^* excimers, as well as visible photons from e.g. TPB flourescence. Section 9.3.4 calculates that photons with wavelengths able to pass the suprasil window contribute only around 1.5 % to the number of photons detected by LLAMA. This result limits potential influences of volume-distributed wavelength-shifting contaminants (e.g. diluted TPB) on the measured attenuation curve to negligible fractions.

A caveat remains, however, since suprasil is opaque below 150 nm [35]. Thus, contributions of wavelength-shifted photons in this range cannot be estimated and might show a longer attenuation length [11]. The $ArXe^*$ excimer is a potential candidate since it decays with emitting photons with a peak wavelength of around 149 nm [36, 37]. As explained in section 4.4, it can be formed by Xe^*, excited by LAr scintillation photons.

However, the xenon content must be low enough, such that the collisional energy transfer from $ArXe^*$ to Xe_2^* is negligible to match the limit the windowed SiPM provides. Thus, the radiative decay rate of $ArXe^*$ of $R_{ArXe} = 0.21\,\mu s^{-1}$ [38] would have to surpass the transfer rate from $ArXe^*$ to Xe_2^* given by [28] as[11]

$$R_{trans} = 0.85\,\mu s^{-1}([Xe]/ppm)^{0.7}. \tag{8.5}$$

For a simple estimate, the intensity of $ArXe^*$ is assumed to be at least a factor of 10 higher than the emission from Xe_2^*. This yields a lower limit on the xenon concentration of 0.005 ppm, too low to effectively absorb LAr scintillation photons, according to the result presented in table 8.1.

[11] The quantity was adapted to use concentrations defined as mole fraction (originally, it is given in terms of mass fraction).

In conclusion, significant wavelength shifting can be excluded for target wavelengths above 170 nm. This indirectly limits also the direct emission from $ArXe^*$. Other contaminants could also shift wavelengths to regions blocked by the suprasil window, but a proper study is rendered impossible due to insufficient knowledge about impurity concentrations.

8.5 Conclusions

Understanding the LAr of LEGEND-200 in attenuating its own scintillation light is a key input for simulations involving optical photon tracking in the cryostat, and can give insights into the actual impurity composition. Thus, the attenuation curve measured by LLAMA was analyzed in detail. While a deviation from a single exponential function was expected due to wavelength-dependent effects, the measured attenuation curve (figure 8.1a) proves difficult to explain. A dedicated Monte Carlo simulation with photon tracking was developed to aid in explaining the data at hand. By using the simulation and the outcome of the calibration measurement with the green LED, instrumental effects can be presumably excluded from having a significant impact.

This leaves only the LAr medium itself for explaining the unexpected attenuation curve measured. Absorbing contaminants are a natural candidate. A “reverse-engineering” approach deriving an arbitrarily shaped absorption spectrum from the measured attenuation curve succeeded, demonstrating the possibility of describing the entire attenuation curve by absorption. However, it proved impossible to infer an existing sole impurity from that result or a dedicated campaign producing attenuation curves using measured absorption spectra. Additionally, a preliminary analysis presented in appendix C, in which absorption spectra are benchmarked against data measured in LEGEND-200, disfavors the reverse-engineered absorption curve while supporting a single absorption length.

Nevertheless, several contaminants were excluded or limited by constraints from LAr vendor specifications and foremost from the measured effective triplet lifetime. With nitrogen, oxygen, and even the mixture dry air, key candidates are excluded. In conclusion, experimental results on the contents of absorbing impurities have to act in synergy with the obtained attenuation length to step from measuring to understanding this data. This is necessary to extrapolate the attenuation curve and simulate the proper wavelength dependence in photon propagation.

In the analysis, two contaminants were identified as being of special interest:

- **Xenon** has a strong absorption band within the LAr scintillation region, and its suspected presence in commercial argon makes it a critical impurity, as pointed out by [1, 13, 39]. Its wavelength-shifting capabilities enhance its potential influence while allowing to put constraints on its concentration in LEGEND-200. Its presence in LEGEND-200 is yet unclear.
- The analysis of the attenuation in ArDM yields **methane** as a possible contaminant able to explain the attenuation length measured there [12]. Also, CH_4 can plausibly explain the first 30 cm of the attenuation curve for LEGEND-200. Furthermore, CH_4 can proxy for other hydrocarbons with unknown properties as impurities in LAr.

This result indicates the demand for a focus shift from the classic LAr contaminants oxygen, nitrogen, and water to xenon, methane, other hydrocarbons, and more unexpected trace substances. The necessity arises from both the need to characterize the LAr, but also from contemporary means of purification currently targeting primarily oxygen and water (see section 6.3 and [40]) and was already pointed out by the ArDM group [12]. Mass spectroscopy measurements sensitive to 0.1 ppm or below can discover impurities to be targeted with dedicated means of purification.

References

[1] A. Neumeier *et al.*, "Attenuation of vacuum ultraviolet light in liquid argon," *Eur. Phys. J. C*, vol. 72, p. 2190, 2012. DOI: 10.1140/epjc/s10052-012-2190-z. arXiv: 1511.07724 [physics.ins-det].

[2] S. Agostinelli *et al.*, "Geant4—a simulation toolkit," *Nucl. Instrum. Meth. A*, vol. 506, no. 3, pp. 250–303, 2003, ISSN: 0168-9002. DOI: 10.1016/S0168-9002(03)01368-8.

[3] J. Allison *et al.*, "Geant4 developments and applications," *IEEE Transactions on Nuclear Science*, vol. 53, no. 1, pp. 270–278, 2006. DOI: 10.1109/TNS.2006.869826.

[4] J. Allison *et al.*, "Recent developments in Geant4," *Nucl. Instrum. Meth. A*, vol. 835, pp. 186–225, 2016, ISSN: 0168-9002. DOI: 10.1016/j.nima.2016.06.125.

[5] P. Krause, "private communications," 2024.

[6] M. Babicz *et al.*, "A measurement of the group velocity of scintillation light in liquid argon," *JINST*, vol. 15, no. 09, P09009, 2020. DOI: 10.1088/1748-0221/15/09/P09009. arXiv: 2002.09346 [physics.ins-det].

[7] K. T. Knöpfle and B. Schwingenheuer, "Design and performance of the GERDA low-background cryostat for operation in water," *JINST*, vol. 17, no. 02, P02038, 2022. DOI: 10.1088/1748-0221/17/02/P02038. arXiv: 2202.03847 [physics.ins-det].

[8] B. Zatschler, "Attenuation of the scintillation light in liquid argon and investigation of the double beta decay of ^{76}Ge into excited states of ^{76}Se in the GERDA experiment," Ph.D. dissertation, Dresden, Tech. U., TU, Dresden (main), 2020.

[9] M. Boswell *et al.*, "MaGe-a Geant4-Based Monte Carlo Application Framework for Low-Background Germanium Experiments," *IEEE Transactions on Nuclear Science*, vol. 58, no. 3, pp. 1212–1220, 2011. DOI: 10.1109/TNS.2011.2144619.

[10] A. C. Wegmann, "Characterization of the liquid argon veto of the GERDA experiment and its application for the measurement of the ^{76}Ge half-life," Ph.D. dissertation, U. Heidelberg, 2017. DOI: 10.11588/heidok.00022568.

[11] T. Heindl *et al.*, "The scintillation of liquid argon," *EPL (Europhysics Letters)*, vol. 91, no. 6, p. 62 002, 2010, ISSN: 0295-5075. DOI: 10.1209/0295-5075/91/62002.

[12] J. Calvo *et al.*, "Measurement of the attenuation length of argon scintillation light in the ArDM LAr TPC," *Astropart. Phys.*, vol. 97, pp. 186–196, 2018. DOI: 10.1016/j.astropartphys.2017.11.009. arXiv: 1611.02481 [astro-ph.IM].

[13] A. Neumeier *et al.*, "Attenuation of vacuum ultraviolet light in pure and xenon-doped liquid argon —An approach to an assignment of the near-infrared emission from the mixture," *EPL*, vol. 111, no. 1, p. 12 001, 2015. DOI: 10.1209/0295-5075/111/12001. arXiv: 1511.07725 [physics.ins-det].

[14] H. Keller-Rudek, G. K. Moortgat, R. Sander, and R. Sörensen, "The MPI-Mainz UV/VIS Spectral Atlas of Gaseous Molecules of Atmospheric Interest," *Earth System Science Data*, vol. 5, no. 2, pp. 365–373, 2013. DOI: 10.5194/essd-5-365-2013.

[15] S. Ogawa and M. Ogawa, "Absorption cross sections of $O_2(a^1\Delta_g)$ and $O_2(X^3\Sigma_g^-)$ in the region from 1087 to 1700 Å," *Can. J. Phys.*, vol. 53, p. 1845, 1975. DOI: 10.1139/p75-236.

[16] R. Babcock, I. Liberman, and W. Partlow, "Volume ultraviolet preionization from bare sparks," *IEEE Journal of Quantum Electronics*, vol. 12, no. 1, pp. 29–34, 1976. DOI: 10.1109/JQE.1976.1069027.

[17] F. Chen and C. Wu, "Temperature-dependent photoabsorption cross sections in the VUV-UV region. I. Methane and ethane," *Journal of Quantitative Spectroscopy and Radiative Transfer*, vol. 85, no. 2, pp. 195–209, 2004, ISSN: 0022-4073. DOI: 10.1016/S0022-4073(03)00225-5.

[18] R. Mota *et al.*, "Water VUV electronic state spectroscopy by synchrotron radiation," *Chemical Physics Letters*, vol. 416, no. 1, pp. 152–159, 2005, ISSN: 0009-2614. DOI: 10.1016/j.cplett.2005.09.073.

[19] T. Nakayama, M. Y. Kitamura, and K. Watanabe, "Ionization Potential and Absorption Coefficients of Nitrogen Dioxide," *J. Chem. Phys.*, vol. 30, no. 5, pp. 1180–1186, 1959. DOI: 10.1063/1.1730152.

[20] S. L. Manatt and A. L. Lane, "A compilation of the absorption cross-sections of SO2 from 106 to 403 nm," *Journal of Quantitative Spectroscopy and Radiative Transfer*, vol. 50, no. 3, pp. 267–276, 1993, ISSN: 0022-4073. DOI: 10.1016/0022-4073(93)90077-U.

[21] B.-M. Cheng *et al.*, "Absorption cross section of gaseous acetylene at 85 K in the wavelength range 110-155 nm," *The Astrophysical Journal Supplement Series*, vol. 196, no. 1, p. 3, 2011, ISSN: 0067-0049. DOI: 10.1088/0067-0049/196/1/3.

[22] Y.-J. Wu, H.-C. Lu, H.-K. Chen, B.-M. Cheng, Y.-P. Lee, and L. C. Lee, "Photoabsorption cross sections of NH3, NH2D, NHD2, and ND3 in the spectral range 110–144nm," *J. Chem. Phys.*, vol. 127, no. 15, p. 154 311, 2007. DOI: 10.1063/1.2790440.

[23] E. C. Y. Inn, K. Watanabe, and M. Zelikoff, "Absorption Coefficients of Gases in the Vacuum Ultraviolet. Part III. CO2," *J. Chem. Phys.*, vol. 21, no. 10, pp. 1648–1650, 1953. DOI: 10.1063/1.1698637.

[24] K. Watanabe, F. M. Matsunaga, and H. Sakai, "Absorption Coefficient and Photoionization Yield of NO in the Region 580–1350 Å," *Appl. Opt.*, vol. 6, no. 3, pp. 391–396, 1967. DOI: 10.1364/AO.6.000391.

[25] R. Acciarri *et al.*, "Oxygen contamination in liquid Argon: Combined effects on ionization electron charge and scintillation light," *JINST*, vol. 5, P05003, 2010. DOI: 10.1088/1748-0221/5/05/P05003. arXiv: 0804.1222 [nucl-ex].

[26] B. J. P. Jones, C. S. Chiu, J. M. Conrad, C. M. Ignarra, T. Katori, and M. Toups, "A Measurement of the Absorption of Liquid Argon Scintillation Light by Dissolved Nitrogen at the Part-Per-Million Level," *JINST*, vol. 8, P07011, 2013, [Erratum: JINST 8, E09001 (2013)]. DOI: 10.1088/1748-0221/8/07/P07011. arXiv: 1306.4605 [physics.ins-det].

[27] B. J. P. Jones *et al.*, "The Effects of Dissolved Methane upon Liquid Argon Scintillation Light," *JINST*, vol. 8, P12015, 2013. DOI: 10.1088/1748-0221/8/12/P12015. arXiv: 1308.3658 [physics.ins-det].

[28] C. G. Wahl, E. P. Bernard, W. H. Lippincott, J. A. Nikkel, Y. Shin, and D. N. McKinsey, "Pulse-shape discrimination and energy resolution of a liquid-argon scintillator with xenon doping," *JINST*, vol. 9, P06013, 2014. DOI: 10.1088/1748-0221/9/06/P06013. arXiv: 1403.0525 [physics.ins-det].

[29] A. Hitachi, "Photon-mediated and collisional processes in liquid rare gases," *Nucl. Instrum. Meth. A*, vol. 327, no. 1, pp. 11–14, 1993, ISSN: 0168-9002. DOI: 10.1016/0168-9002(93)91398-7.

[30] S. Kubota, M. Hishida, S. Himi, J. Suzuki, and J. Ruan, "The suppression of the slow component in xenon-doped liquid argon scintillation," *Nucl. Instrum. Meth. A*, vol. 327, no. 1, pp. 71–74, 1993, ISSN: 0168-9002. DOI: 10.1016/0168-9002(93)91413-H.

[31] R. Acciarri *et al.*, "Effects of Nitrogen contamination in liquid Argon," *JINST*, vol. 5, P06003, 2010. DOI: 10.1088/1748-0221/5/06/P06003. arXiv: 0804.1217 [nucl-ex].

[32] G. Zuzel, "LAr for L200; internal presentation," 2019.

[33] S. Waldleitner, "Linde GmbH, Private communications,"

[34] M. Harańczyk *et al.*, "LEGEND-200 filling and purification logbook,"

[35] "Quarzglas für die Optik - Daten und Eigenschaften," [Online]. Available: https://www.heraeus.com/media/media/hca/doc_hca/products_and_solutions_8/optics/Daten_und_Eigenschaften_Quarzglas_fuer_die_Optik_DE.pdf.

[36] G. Nowak and J. Fricke, "The heteronuclear excimers ArKr*, ArXe* and KrXe*," *J. Phys. B*, vol. 18, no. 7, p. 1355, 1985. DOI: 10.1088/0022-3700/18/7/016.

[37] A. M. Neumeier, "Optical Properties of Liquid Noble Gas Scintillators," Ph.D. dissertation, Munich, Tech. U., 2015.

[38] J. Soto-Oton, "Impact of xenon doping in the scintillation light in a large liquid-argon TPC," in *5th International Conference on Technology and Instrumentation in Particle Physics*, 2021. arXiv: 2109.05858 [physics.ins-det].

[39] D. Fields, R. Gibbons, M. Gold, N. McFadden, S. Elliott, and R. Massarczyk, "Understanding the enhancement of scintillation light in xenon-doped liquid argon," *Nucl. Instrum. Meth. A*, p. 167 707, 2022, ISSN: 0168-9002. DOI: 10.1016/j.nima.2022.167707.

[40] M. Haranczyk *et al.*, "Purification of large volume of liquid argon for LEGEND-200," *PoS*, vol. PANIC2021, p. 102, 2022. DOI: 10.22323/1.380.0102.

Chapter 9

Photon emission time distribution of purified liquid argon

During the filling campaign of the LEGEND-200 cryostat, LLAMA recorded optical properties in freshly purified LAr with high statistics. This data is harnessed to develop a model for the photon emission time spectrum of LAr with low impurity levels. The data was recorded from July 2nd until the 18th, just before the nitrogen spoiling happened; see section 6.3 for more details. In total, 211 million scintillation events are used.

9.1 Model

As described in section 4.2.1, the model of the photon emission time spectrum of liquid argon is dominated by the decay of singlet ($^1\Sigma_u^+$) and triplet ($^3\Sigma_u^+$) excimers. Since one cannot exclude impurities causing non-negligible quenching, an effective triplet lifetime τ_t' as described in section 4.3.1 is used. However, a negligible influence on the singlet lifetime τ_s is expected.

According to section 4.2.1, the existence of an additional intermediate component in the time spectra of pure LAr is actively discussed in literature. It is included in this model as it matches the data (see later).

Two Gaussian functions are summed up and folded with the emission part of the time spectrum to model the apparatus's time resolution. They share the same mean μ, while the σ are independent (denoted σ_a and σ_b). A constant I_{acc} accounts for accidental background. The full model reads:

$$
\begin{aligned}
I'(t) = &\left(\frac{I_s}{\tau_s} e^{-t/\tau_s} + \frac{I'_t}{\tau'_t} e^{-t/\tau'_t} + \frac{I_i}{\tau_{rec}} \frac{1}{(1 + t/\tau_{rec})^2} \right) \\
&\otimes (\text{Gauss}(t, \mu, \sigma_a) + \text{Gauss}(t, \mu, \sigma_b)) \\
&+ I_{acc}.
\end{aligned}
\tag{9.1}
$$

Comparing this model to other models used in literature shows that the lack of detector-effected components makes this analysis outstanding. Conversely, modeling the photon arrival times in DEAP-3600 introduced terms accounting for delayed emission of the used wavelength shifter and PMT afterpulsing, which led to difficulties in the fit. Several experiments employ wavelength shifters and record waveforms containing multiple PE per scintillation event. Hence, they have to cope with delayed emission and afterpulsing [1–5].

Avoiding the application of wavelength shifters and measuring single photons averts taking these additional terms into account. Apart from LLAMA, this is also implemented in [6], where the scintillation due to excitation with an ion beam is studied. Thus, the model of the photon arrival times there matches equation 9.1, except for the detector resolution, which is modeled as a single Gaussian there.

9.2 Implementation and performance of the fit routine

Data processing, analysis, and quality cuts applied to the recorded data follow the procedures explained in sections 5.3 and 5.4. The only exception is extracting the onset time of a PE pulse in the waveform. Since this analysis requires a good time resolution, the waveform is linearly interpolated before a leading-edge trigger is used. The default processing estimates the trigger position only at discrete time points defined by the sample interval of 40 ns.

As explained in section 5.4.2, the time profile of detected photons for a given peripheral SiPM is generated by computing the time difference between the scintillation event and the reconstructed photon arrival time in an event-by-event basis. The time of the scintillation event is obtained from the triggered light source, and the reconstruction of the onset of the singlet component profits from a high number of detected photons.

Conversely, the probability of detecting photons in a peripheral SiPM is very low, allowing to perform single-photon analysis, which eliminates any influence from SiPM afterpulsing. One photon time spectrum is generated for each of the 13 peripheral SiPMs and stored as a one-dimensional histogram.

In advance of performing the fit, the spectra are treated with a Bayesian Blocks algorithm[1] [7] to reduce the number of bins used while keeping the essential features. This algorithm detects statistically significant variations and segments the data into variable-sized bins while retaining those variations. A reduced number of bins greatly enhances the computational performance of the fit.

The RooFit [8] toolkit is used for performing the fits. It is known that RooFit exhibits a bias in its calculation of the distance of the PDF to data [9]. This is because it only considers the value of the PDF at the respective bin's center. Strongly curved models over broad bins thus lead to biases. The implementation in [9] mitigates this by providing an algorithm for transforming a continuous PDF into a binned one by integrating it over the full bin width. It is included in ROOT 6.25 [10] and used in this work.

The entire analysis window has a width of 13.5 µs, from which around 3 µs are located ahead of the singlet peak. The region from 3 µs to 1 µs before the singlet peak is used to obtain the accidental background level in order to fix I_{acc}. Also, the singlet lifetime is fixed since its derivation from a global fit is rendered impossible due to insufficient time resolution. It is fixed to 8.2 ns, as found by [11]. A binned maximum likelihood fit over the window of 13.5 µs width is performed subsequently, with all remaining parameters of equation 9.1 being free.

Fits are performed on each of the 13 peripheral SiPMs' time spectra individually and independently. This is done to estimate the impact of systematic uncertainties since the different spectra show varying properties. Most importantly, the ratio between signal and accidental background decreases for farther SiPMs. The SiPM at 15 cm distance is of particular interest since its suprasil window blocks primary LAr VUV scintillation while allowing shifted light (e.g. by xenon or TPB) to pass (see section 5.1.2).

The measured time spectrum and the model curve resulting from the mentioned fit routine for the SiPM at 20 cm distance are shown in figure 9.1 (top). The complete model is drawn with a continuous line, while the subcomponents are drawn in dashed.

[1] The implementation used in this work is implemented by L. Pertoldi and is available at `https://github.com/gipert/bayesian-blocks`

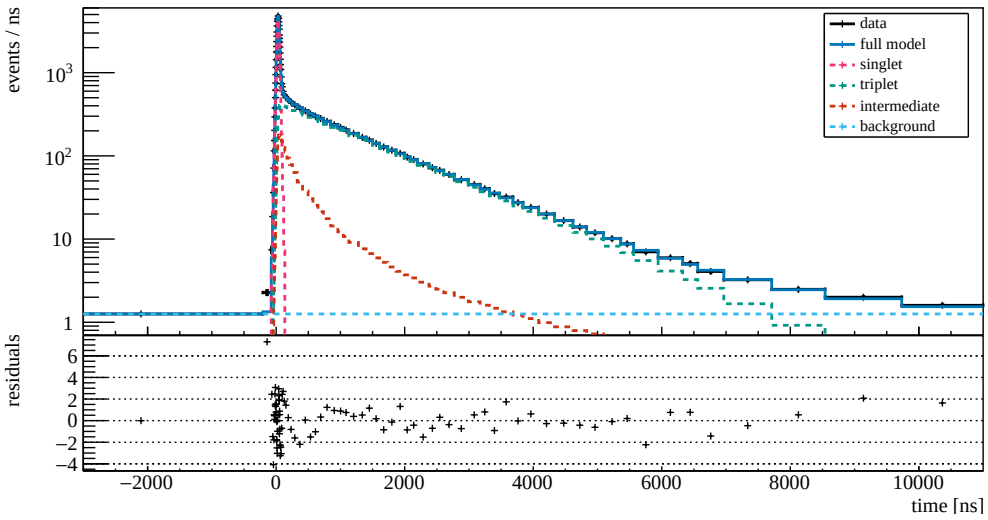

Figure 9.1: Photon arrival time spectrum for the SiPM at 20 cm distance during the period of optimal LAr quality and fit with equation 9.1 (top). Fit parameter I_{acc} is obtained solely from the area before the singlet peak, and τ_s is fixed to 8.2 ns [5]. All other parameters are free in a fit over the entire time range shown. Components of equation 9.1 are drawn in dashed after applying the resolution model. Residuals in sigma are shown in the lower panel.

They refer to the summands in the first bracket of the function, which are drawn after convolution with the detector resolution model. The accidental background component is drawn additionally. Residuals are computed and normalized to the bins' statistical uncertainties and are shown in the bottom panel.

Figure 9.2a shows the same for a more narrow region around the singlet peak. It can be compared to the result from the farthest SiPM at 75 cm distance in figure 9.2b. Both spectra show almost the same accidental background rate, which leads to the conclusion that accidental backgrounds are not predominantly produced in the light source.

Additionally, all fits are performed using the model without the intermediate component (i.e. forcing I_i to zero). In figure 9.3, the result of the full model (a) is compared to the one lacking an intermediate component (b). It is visible that the intermediate component is required to explain the spectrum in the region from around 50 ns to 250 ns.

The spectrum recorded with the SiPM at 15 cm distance, which has a suprasil window, is shown in figure 9.4 together with the fit using the complete model. As explained earlier, the spectrum is composed exclusively of photons with a wavelength exceeding the one

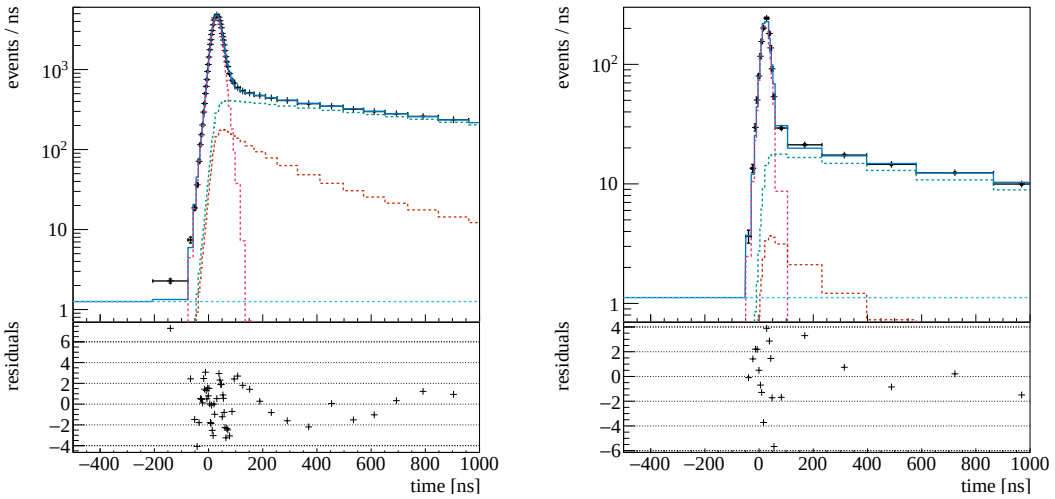

(a) (b)

Figure 9.2: Photon arrival time spectra for SiPMs at 20 cm (a) and 75 cm (b) distance. See the caption of figure 9.1 for more information.

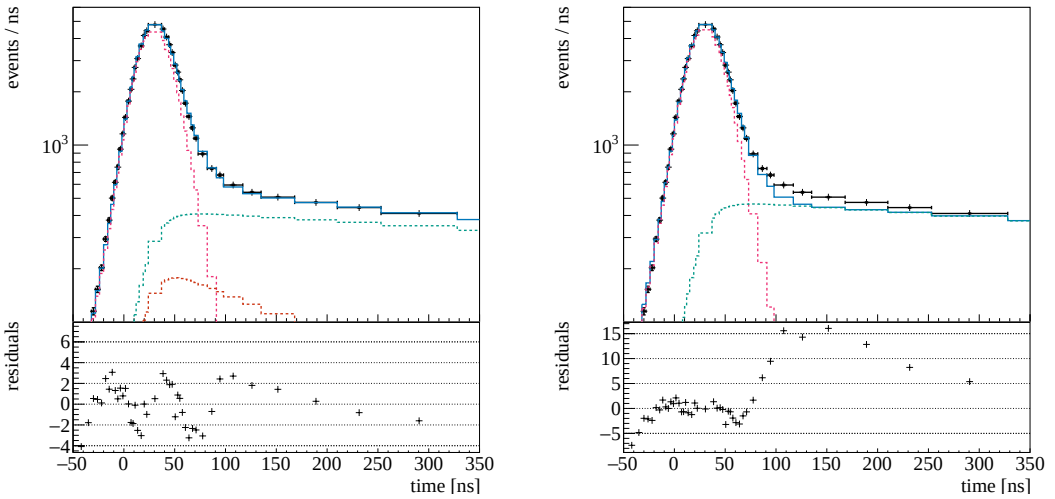

(a) (b)

Figure 9.3: Photon arrival time spectra for SiPMs at 20 cm distance, using the full model (equation 9.1) (a) and idem without the intermediate component (b). Both fits are performed independently. See the caption of figure 9.1 for more information.

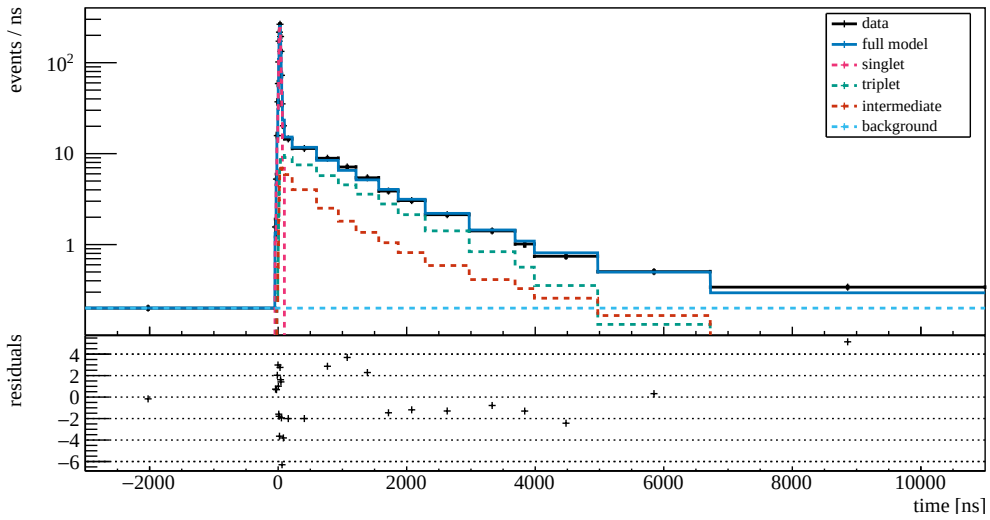

Figure 9.4: Photon arrival time spectrum for the SiPM at 15 cm distance with a fit using equation 9.1. This SiPM features a suprasil window, blocking primary LAr scintillation light while allowing shifted photons (e.g. from xenon or TPB impurities) to pass. A comparably high fraction of delayed photons pull I_i and τ_{rec} and might be attributed to delayed emission from e.g. TPB [12]. However, the low number of events makes an analysis challenging. See the caption of figure 9.1 for more information.

from the primary LAr emission. The spectrum shows hints for an additional component, which decays slower than the LAr triplet. This is expected since the wavelength-shifting process, which all photons detected in this SiPM have to undergo, can introduce an additional delayed component. See section 9.3.4 for a further discussion.

9.3 Results and discussion

9.3.1 Overview of final fit parameters and discussion of triplet lifetime

Table 9.1 shows the most important final fit parameters of the SiPM at 20 cm distance. This SiPM is chosen since it features the maximum photon count. While the statistical uncertainty is extracted from the fit, the systematic uncertainty is obtained from variations

Table 9.1: Final fit parameters obtained from the SiPM at 20 cm distance. Statistical uncertainties are extracted from the fit, while systematic uncertainties are obtained from variations across the 10 other suitable peripheral SiPMs. For simplicity, the intensity of all signal components (singlet, triplet, and intermediate) is denoted with I_{sig}, i.e. $I_{sig} = I_s + I'_t + I_i$. Results from the pulse shape model of DEAP-3600 [5] are compiled in comparison.

Parameter	LLAMA results			DEAP results [5]
	Value	Stat. unc.	Syst. unc.	
τ_s	8.2 ns	-	-	8.2 ns
τ'_t	1315 ns	2 ns	35 ns	1445 ns
τ_{rec}	293 ns	16 ns	121 ns	75.5 ns
I_i/I_{sig}	0.078	0.003	0.025	0.06
$(I_s + I_i)/I_t$	0.494	0.005	0.032	0.41
$(I_s + I_i)/I_{sig}$	0.331	0.003	0.014	0.29

across the 10 well-perfoming[2] windowless peripheral SiPMs. Values from the pulse shape model of DEAP-3600 are shown in comparison.

The effective triplet lifetime τ'_t is significantly smaller than in DEAP. Potentially, this could be explained by a higher impurity concentration in LEGEND-200. However, the DEAP result is likely affected by the emission time profile of TPB. They compute a variation of the effective triplet lifetime from 1387 ns to 1544 ns when varying the delayed TPB emission parameters within their uncertainties [5]. A different experiment, which avoids the use of wavelength shifters, finds a value of (1300 ± 60) ns [13], which is compatible with our result. This renders the assumption of negligible contamination in the pure LAr data set in LLAMA data credible, which is required for several analyses within this work.

[2]The SiPM at 35 cm distance shows an increased noise level and is therefore excluded from this analysis. Additionally, the SiPM at 30 cm distance stopped working soon after LLAMA's data taking commenced (see appendix B).

Table 9.2: Recombination time τ_{rec} and relative intensity I_i/I_{sig} of the intermediate component of LAr scintillation obtained in this work are compared to literature results.

Experiment	exciting particle	τ_{rec}	I_i/I_{sig}
LLAMA (this work)	γ	(293 ± 137) ns	0.078 ± 0.028
DEAP-3600 [5]	e^-	75.5 ns	0.06
Heindl et al [14]	e^-	175 ns	0.07
Kubota et al [15]	e^-	(0.8 ± 0.2) ns	-
Hofmann et al [6]	S^{9+}	(37.4 ± 0.2) ns	-
Hofmann et al [6]	p^+	(7.7 ± 0.1) ns	-

9.3.2 Intermediate component and recombination time

As shown earlier, the fits favor the model, which includes an intermediate component, over the one without.

The recombination time τ_{rec} obtained in this work differs from the value used in the DEAP-3600 pulse shape model. Tensions exist among these and further literature values for τ_{rec}, compiled in table 9.2. Note, that τ_{rec} depends on the LET via the initial electron density $n_{e,t=0}$ [16]

$$\tau_{rec} = \frac{1}{c_{rec}\, n_{e,t=0}}, \tag{9.2}$$

thus, the recombination time values obtained from proton and sulfur beams are expected to be smaller than the ones from incident gammas or electrons. The so-called recombination rate constant c_{rec} depends on material and temperature only [16] and is thus constant for all measurements. Hence, the results from the ion beam excitation measurements are not in conflict with the LLAMA results. Conversely, the (0.8 ± 0.2) ns measured by [15] are not compatible with the results from this work but also not with the ones from [6]. The tension was already identified by [6], and the necessity of future dedicated measurements was concluded for solving it.

The intensity fraction of the intermediate component I_i with respect to the total LAr emission intensity $I_{sig} = I_s + I_t' + I_i$ found here is compatible with the result from DEAP-3600 and Heindl et al.

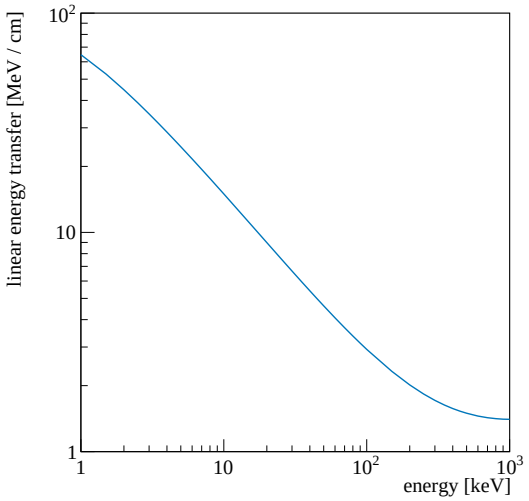

Figure 9.5: LET of electrons in LAr with data taken from [17]. The value decreases with increasing electron energy below around 1 MeV.

9.3.3 Singlet-to-triplet ratio

For computing the singlet-to-triplet ratio, the intensity of the intermediate component is considered part of the singlet emission. This follows the argumentation by [6, 14]. They state that photons from singlet excimers formed by delayed recombination follow the recombination time function since the singlet emission happens fast. Conversely, due to the lifetime of the triplet excimer vastly exceeding the recombination time, light from triplet excimers formed by delayed recombination is still dominated by the effective triplet lifetime. It is thus not distinguished from triplet excimers formed directly. Hence, the singlet-to-triplet ratio is computed as $(I_s + I_i)/I_t$ and is reported together with the singlet fraction $(I_s + I_i)/I_{sig}$ in table 9.1.

As explained in section 4.2.1, the singlet-to-triplet ratio increases with higher LET. This effect is due to the higher electron densities facilitating the energy transition from triplet to singlet states via the process shown in equation 4.1. Though predominantly applying to e.g. ion beams, also an experiment with a 10 keV electron beam observes an increased singlet-to-triplet ratio, which is explained by the mentioned transition [14]. Since the LET decreases with increasing incident electron energies below around 1 MeV (see figure 9.5), the singlet-to-triplet ratio observed using electron or gamma interactions

in this range can be expected to decrease accordingly. This effect must be considered when comparing singlet-to-triplet ratios of different experiments. The comparably high singlet-to-triplet ratio of [14] of 0.56 can thus be explained by the low electron energy of 10 keV. For comparison, the value found in this work is 0.49 ± 0.04 for an electron energy[3] of 60 keV. The difference can be attributed to different LET. The singlet-to-triplet ratio reconstructed by DEAP-3600 is 0.41, for electron energies between 13 keV and 40 keV [5]. This result is in slight tension to the LLAMA result but might be attributed to strong correlations between the delayed TPB emission and the LAr triplet component in the DEAP-3600 pulse shape model [5].

9.3.4 Wavelength-shifted photons

As explained in section 9.2, spectra showing wavelength-shifted photons exclusively[4] are obtained from the peripheral SiPM at 15 cm distance, which has a suprasil window. The window's cutoff wavelength allows photons from the emission of xenon excimers to pass, but also optical photons produced e.g. by TPB. The resulting time spectrum and the model curve after the fit are shown in figure 9.4. Table 9.3 lists the corresponding final fit parameters.

The accidental background level visible in the spectrum is around a factor of five lower than for the other SiPMs. Integrating all counts above the accidental background level and dividing that by the number of triggers passing the quality cuts yields the net PPT value (see section 5.4.2). This value is proportional to the light intensity at the SiPM's position. The SiPM with the suprasil window has a net PPT value of $(0.493 \pm 0.003) \cdot 10^{-3}$, while the one at 20 cm distance shows $(17.91 \pm 0.02) \cdot 10^{-3}$. After calculating the ratio and accounting for the difference in solid angle, one obtains that only around 1.5 % of all correlated photons pass the window, i.e. were subject to wavelength shifting.

Comparing the spectrum in figure 9.4 to the one showing the primary LAr emission (figure 9.1), one observes an increased contribution of very late photons. As a result, the intermediate component of the model shows increased values of I_i and τ_{rec}, while the reconstructed triplet lifetime is still compatible with the results from windowless SiPMs.

[3] For gamma energies of 60 keV, energy deposition via the photoelectric effect is dominating [18].

[4] In principle, also photons emitted initially by other sources, such as LEDs can be detected by this SiPM. However, they are unlikely to cause triple coincidences among the source SiPMs and are also reduced by quality cuts. Thus, they are expected to primarily contribute to accidental background.

Table 9.3: Final fit parameters obtained from the SiPM at 15 cm distance, which has a suprasil window and thus only detects wavelength-shifted photons. Compared to a windowless SiPM (see table 9.1), the intermediate component is much more prominent, and the recombination time is much longer. This might hint at a delayed emission component of the wavelength shifter, which is not accounted for in the model (see text).

Parameter	Results for SiPM with suprasil window	
	Value	Stat. unc.
τ_s	8.2 ns	-
τ'_t	1325 ns	19 ns
τ_{rec}	1000 ns	6 ns
I_i/I_{sig}	0.24	0.02
$(I_i + I_s)/I_{sig}$	0.64	0.02

A delayed emission by an unknown wavelength shifter can cause this component. For example, in the case of TPB which might be dissolved in the LAr, a slow component with a lifetime of around 3.5 µs and a relative intensity of (8 ± 1) % was found by [12]. Since the spectra of the windowless SiPMs have a contribution of wavelength-shifted photons of only around 1.5 %, no additional model component accounting for time delays due to wavelength-shifting processes was included in the complete model.

References

[1] R. Acciarri *et al.*, "Effects of Nitrogen contamination in liquid Argon," *JINST*, vol. 5, P06003, 2010. DOI: 10.1088/1748-0221/5/06/P06003. arXiv: 0804.1217 [nucl-ex].

[2] W. H. Lippincott *et al.*, "Scintillation time dependence and pulse shape discrimination in liquid argon," *Phys. Rev. C*, vol. 78, no. 3, p. 035 801, 2008. DOI: 10.1103/PhysRevC.78.035801.

[3] P. Peiffer, T. Pollmann, S. Schönert, A. Smolnikov, and S. Vasiliev, "Pulse shape analysis of scintillation signals from pure and xenon-doped liquid argon for radioactive background identification," *JINST*, vol. 3, no. 08, P08007–P08007, 2008, ISSN: 1748-0221. DOI: 10.1088/1748-0221/3/08/P08007.

[4] N. McFadden *et al.*, "Large-scale, precision xenon doping of liquid argon," *Nucl. Instrum. Meth. A*, vol. 1011, p. 165 575, 2021. DOI: 10.1016/j.nima.2021.165575. arXiv: 2006.09780 [physics.ins-det].

[5] P. Adhikari *et al.*, "The liquid-argon scintillation pulseshape in DEAP-3600," *Eur. Phys. J. C*, vol. 80, no. 4, p. 303, 2020. DOI: 10.1140/epjc/s10052-020-7789-x. arXiv: 2001.09855 [physics.ins-det].

[6] M. Hofmann *et al.*, "Ion-beam excitation of liquid argon," *Eur. Phys. J. C*, vol. 73, no. 10, p. 2618, 2013. DOI: 10.1140/epjc/s10052-013-2618-0. arXiv: 1511.07721 [physics.ins-det].

[7] J. D. Scargle, J. P. Norris, B. Jackson, and J. Chiang, "STUDIES IN ASTRONOMICAL TIME SERIES ANALYSIS. VI. BAYESIAN BLOCK REPRESENTATIONS," *The Astrophysical Journal*, vol. 764, no. 2, p. 167, 2013, ISSN: 0004-637X. DOI: 10.1088/0004-637X/764/2/167.

[8] W. Verkerke and D. P. Kirkby, "The RooFit toolkit for data modeling," *eConf*, vol. C0303241, MOLT007, 2003. arXiv: physics/0306116.

[9] V. Gligorov, S. Hageboeck, T. Nanut, A. Sciandra, and D. Tou, "Avoiding biases in binned fits," *JINST*, vol. 16, no. 08, T08004, 2021, ISSN: 1748-0221. DOI: 10.1088/1748-0221/16/08/T08004.

[10] I. Antcheva *et al.*, "ROOT — A C++ framework for petabyte data storage, statistical analysis and visualization," *Computer Physics Communications*, vol. 180, no. 12, pp. 2499–2512, 2009, ISSN: 0010-4655. DOI: 10.1016/j.cpc.2009.08.005.

[11] P. Adhikari *et al.*, "The liquid-argon scintillation pulseshape in DEAP-3600," *Eur. Phys. J. C*, vol. 80, no. 4, p. 303, 2020, ISSN: 1434-6044. DOI: 10.1140/epjc/s10052-020-7789-x.

[12] E. Segreto, "Evidence of delayed light emission of TetraPhenyl Butadiene excited by liquid Argon scintillation light," *Phys. Rev. C*, vol. 91, no. 3, p. 035 503, 2015. DOI: 10.1103/PhysRevC.91.035503. arXiv: 1411.4524 [physics.ins-det].

[13] T. Heindl *et al.*, "The scintillation of liquid argon," *EPL (Europhysics Letters)*, vol. 91, no. 6, p. 62 002, 2010, ISSN: 0295-5075. DOI: 10.1209/0295-5075/91/62002.

[14] T. Heindl, "Die Szintillation von flüssigem Argon," Dissertation, Technische Universität München, 2011.

[15] S. Kubota, M. Hishida, M. Suzuki, and J.-z. Ruan(Gen), "Dynamical behavior of free electrons in the recombination process in liquid argon, krypton, and xenon," *Phys. Rev. B*, vol. 20, no. 8, pp. 3486–3496, 1979. DOI: 10.1103/PhysRevB.20.3486.

[16] G. Ribitzki, A. Ulrich, B. Busch, W. Krötz, J. Wieser, and D. E. Murnick, "Electron densities and temperatures in a xenon afterglow with heavy-ion excitation," *Phys. Rev. E*, vol. 50, no. 5, 1994, ISSN: 1063651X. DOI: 10.1103/PhysRevE.50.3973.

[17] M. Z. M.J. Berger J.S. Coursey and J. Chang, "NIST Standard Reference Database 124," 2017. DOI: 10.18434/T4NC7P.

[18] M. Berger *et al.*, "XCOM: Photon Cross Sections Database," [Online]. Available: https://www.nist.gov/pml/xcom-photon-cross-sections-database.

Chapter 10

Properties of nitrogen-doped liquid argon

While slightly impairing the performance of the LAr instrumentation of LEGEND-200, the incident resulting in a contamination of the LAr with around 0.9 ppm of nitrogen provides data perfectly suitable for studying the effect of low nitrogen levels in LAr. The data are obtained by LLAMA, described in chapter 5. It is a permanent in-situ monitor of optical properties in LEGEND-200's LAr volume, of which the primary light yield and the effective triplet lifetime are of paramount interest for the analysis presented in this chapter. The aforementioned contamination with nitrogen, hereinafter referred to as *doping*, took place during the filling campaign of the LEGEND-200 cryostat with purified LAr and is the subject of section 6.3.

The available data provide unique insight into the properties of LAr with low nitrogen concentration. High-statistics data from clean and freshly purified LAr are available from the first part of the LAr filling campaign. The subsequent doping happened over 17 hours, thus generating a slowly and continuously rising nitrogen concentration. After the filling was halted, the LAr properties are stable again, and LLAMA provides optical properties with high statistics.

Concluding, the data can be analyzed in two ways: by comparing the optical properties in clean LAr to LAr with around 0.9 ppm of added nitrogen, as well as by studying the evolution of the parameters during doping. The main advantage lies in the low nitrogen concentrations, which were not extensively studied in previous doping campaigns. Those primarily target concentrations on the ppm level or beyond and evaluate only a few sub-ppm values at most [1–3]. However, recent detectors define limits on the nitrogen

content around or below 1 ppm, such as MicroBooNE ($\leq$ 2 ppm [3]) or LEGEND-200 ($\leq$ 1 ppm [4]), making this range more attractive for dedicated measurements of optical properties.

This work profits from the profound understanding of the time distribution of photon emission in liquid argon scintillation gained by analyzing LLAMA data in purified LAr. Chapter 9 presents the model, the data treatment, and the fit routine, which are reused here.

The change of the effective triplet lifetime and primary scintillation light yield evaluated in the following impacts the performance of the LAr instrumentation and thus affects the physics performance of LEGEND-200. This is evaluated further in section 12.1.

10.1 Modeling nitrogen-induced quenching

Nitrogen in LAr quenches LAr excimers without re-emission [1]; the impact of such a contaminant on the optical properties of LAr is explained in section 4.3.1. Due to the longer lifetime, excimers in the triplet state are affected mainly, while the impact on the singlet states can be neglected in the concentration range studied [1]. The effective triplet lifetime is introduced in section 4.3.1 and its concentration dependence is expressed following equation 4.6:

$$\frac{1}{\tau_t'} = \frac{1}{\tau_t} + k_{Q,\mathrm{N_2}}[\mathrm{N_2}], \tag{10.1}$$

where k_{Q,N_2} is the quenching rate constant of nitrogen. Following the convention used in this work, the nitrogen concentration $[\mathrm{N_2}]$ is defined in terms of mole fraction (see appendix A).

As explained, the singlet lifetime τ_s is not expected to change. Since only quenching of excimers is assumed, the lifetime of Ar^+ ions and free electrons are assumed unchanged, and thus, the properties of the intermediate component are constant. The intensity of the intermediate component is considered part of the singlet emission, following the argumentation in section 9.3.3.

Thus, the integral intensity I_Q' follows equation 4.8, which is reproduced here for completeness:

$$I_Q'([\mathrm{N_2}]) = I\left(\eta_s + \frac{\eta_t}{1+\tau_t\, k_{Q,\mathrm{N_2}}[\mathrm{N_2}]}\right). \tag{10.2}$$

Here, η_s and η_t are constants denoting the intensity fractions of the singlet and triplet component in pure LAr, respectively, and $\eta_s + \eta_t = 1$.

At the low concentrations studied, nitrogen is not expected to cause significant absorption of LAr scintillation light [2]. Thus, the detected light intensity should follow only the change in primary light yield, regardless of the light path length. Nevertheless, since LLAMA provides intensity information at distances up to 75 cm (top peripheral SiPM), the absorption increase due to the additional nitrogen content is studied in this work. The results are shown in section 10.3.3 and confirm the absorption being subdominant to quenching.

10.2 Data sets and derivation of optical parameters

As explained in the introduction of this chapter, the analysis of separate time windows provides two ways to obtain parameters necessary to describe quenching by nitrogen. While the use of the stable periods before and after the doping yields high-statistics data at two concentration points, the data obtained during doping are used to analyze multiple nitrogen concentrations with the drawback of high statistical uncertainties. Both analyses are performed independently yet largely analogously.

The extraction of parameters describing the photon emission time spectrum is performed in the same way as described in section 9.2; in a nutshell: A time spectrum is obtained individually for every peripheral SiPM and then treated with a Bayesian Blocks algorithm to speed up the following fit routines by reducing the number of bins [5]. Then, the model equation 9.1 is fit to the spectra using binned maximum likelihood. All parameters, except for the singlet lifetime (fixed at 8.2 ns [6]) and the intensity of accidental coincidences I_{acc} (obtained via a separate algorithm) are free in the fit over a time range of 13.5 µs.

Additionally, the primary light yield is computed. Since all three SiPMs in the source are active during all time frames studied here, the primary light yield is extracted from the light source, as explained in detail in section 5.4.1. In short, the number of photons in the source SiPMs are summed up on an event-by-event basis and a fit with a Gaussian function to the resulting peak, corresponding to full energy depositions of 60 keV gammas, provides the primary light yield.

10.2.1 Stable time periods

The stable periods around the doping are separated into two data sets:

- The *pure* data set begins on July 2nd 2021 and ends on the 18th of the same month. It encompasses around 200 million LAr scintillation events.
- The *doped* data set begins on July 20th, around 2 hours after the doping finished, and lasts until the 26th[1] of the same month, containing around 80 million events.

The final fit parameters obtained from the 1st data set are presented and discussed in chapter 9. For the 2nd data set, all procedures are replicated. Since the SiPM at 20 cm distance failed shortly before the doping, it is not used in the analysis of the 2nd data set. Comparisons of both data sets are made using the SiPM at 25 cm distance for that reason.

Figure 10.1 shows the comparison of the final model PDFs after fits to either the pure (blue) or doped (red) data sets. Analogous to section 9.2, both the full model and subcomponents (after application of the time resolution model of the system) are shown. Here, the full model is drawn with a continuous line, while broken lines are used for the subcomponents.

Table 10.1 lists the corresponding final fit parameters, i.e. using the SiPM at 25 cm distance in both cases. Thus, the results for the pure data set slightly deviate from the values in table 9.1, which uses the SiPM at 20 cm distance. The first uncertainty quoted for each quantity is statistical and extracted from the individual fit, while the second uncertainty is systematical and equals the standard deviation across all well-performing peripheral SiPMs.

As expected, the most notable difference is the lifetime of the triplet component (dashed line in the plot), which is reduced by the doping. Effects on the intermediate component (dotted line) are not significant. The uncertainties involved with the intermediate component are large, because it varies strongly across different SiPMs, presumably since this component is not dominating the spectrum in any time range.

[1]The data period stops here due to an unidentified event causing the time resolution to worsen slightly.

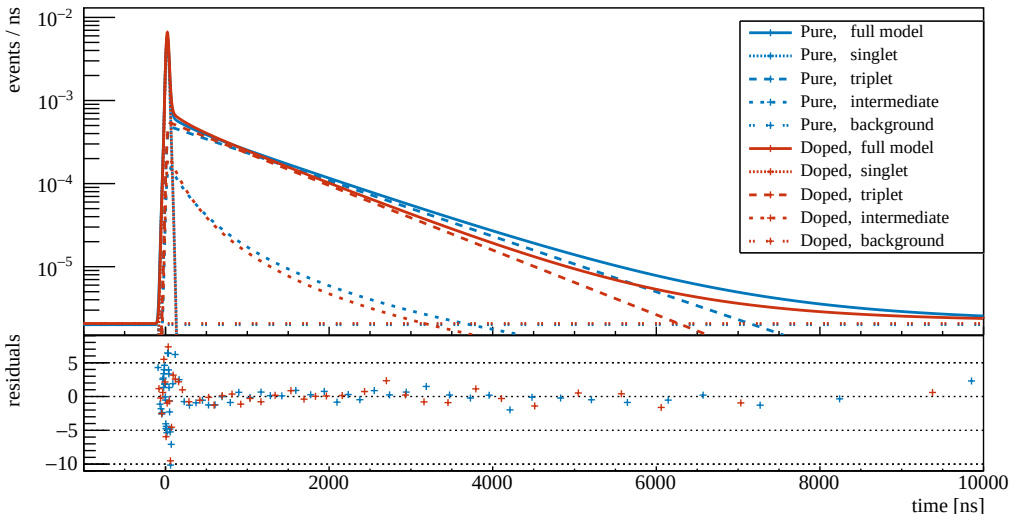

Figure 10.1: Model PDFs of the measured photon time spectrum (equation 9.1) after fit with either the pure (blue) or doped (red) data sets. The continuous line shows the full model, and the subcomponents are drawn dashed (triplet), dotted (intermediate), fine dotted (singlet), and double-dotted (accidental background). Residuals are given in sigma in the lower panel.

Table 10.1: Final parameters of fits of model equation 9.1 to both data periods. The first uncertainty quoted is statistical, while the second one is systematic. Here, the parameter values and the statistical uncertainties are taken from the SiPM at 25 cm distance, in contrast to table 9.1. The systematic uncertainties are computed as the standard deviation of the final fit parameters across the spectra from all well-performing peripheral SiPMs.

Data set	τ_t'/ns	τ_{rec}/ns	$(I_s + I_i)/I_{sig}$
pure	$1299 \pm 4 \pm 22$	$422 \pm 27 \pm 93$	$0.337 \pm 0.004 \pm 0.018$
doped	$1117 \pm 5 \pm 33$	$307 \pm 26 \pm 194$	$0.359 \pm 0.005 \pm 0.041$

10.2.2 Doping in progress

The data set recorded during doping is segmented into 11 slices of 1 million events each, corresponding to around one and a half hours of run time per slice. Since the number of events is relatively low, the time spectra obtained from the five closest, well-performing

SiPMs are summed up[2]. Thus, only one photon arrival time spectrum is analyzed per slice. The fits of these spectra with the model and the extraction of the primary light yield follow the procedure explained previously.

Additionally, the nitrogen concentration is computed for the time positions of the slices, which follows the formula derived by M. Harańczyk [7]. It uses the filling rate, which was obtained by monitoring the filling height in the LEGEND-200 storage tank at regular intervals. It was observed, that the rate was around $400\,\mathrm{kg\,h^{-1}}$ from 17:30 to 03:30 (July 19th and 20th 2021) and around $300\,\mathrm{kg\,h^{-1}}$ from 03:30 until 10:30 (July 20th), amounting to 6100 kg of LAr. The calculation assumes a negligible capacity of LLArS (see section 6.3) for removing nitrogen [7]. While the system has been shown to remove nitrogen, it was presumably close to saturation at the beginning of the doping, for it had processed around 8 t of LAr with default quality at this point. When processing the LAr with around 10 ppm of nitrogen, which is a factor of 10 above the maximum LEGEND-200 specification and a factor of 50 above the default quality [8], saturation was presumably reached very fast. The LAr level in the cryostat after the filling was halted was measured[3] to be 68 t. Thus, the nitrogen concentration after doping is 0.9 ppm.

Figure 10.2 shows the effective triplet lifetime (top), primary light yield (middle), and increase in nitrogen content (bottom) over the timestamp. While the effective triplet lifetime has high statistical uncertainties connected to the low number of events, the primary light yield extracted from the light source shows negligible statistical uncertainties. Both values are decreasing with increasing nitrogen concentration, as expected.

10.3 Results and discussion

10.3.1 Quenching of primary light yield

The change of the primary light yield due to an increase in nitrogen concentration is studied using data taken during doping. The validity of the model, shown in equation 10.2, is investigated. Assuming values of η_s, η_t and τ_t, i.e. the singlet-to-triplet ratio and the triplet lifetime of pure LAr, respectively, the quenching rate constant of nitrogen

[2] These are the SiPMs at distances of 25 cm, 40 cm, 50 cm, 55 cm and 60 cm. Other SiPMs have a suprasil window, a high noise level, failed before the doping or are too far away from the source to make a significant contribution.

[3] The measurements were conducted by P. Krause and S. Schönert.

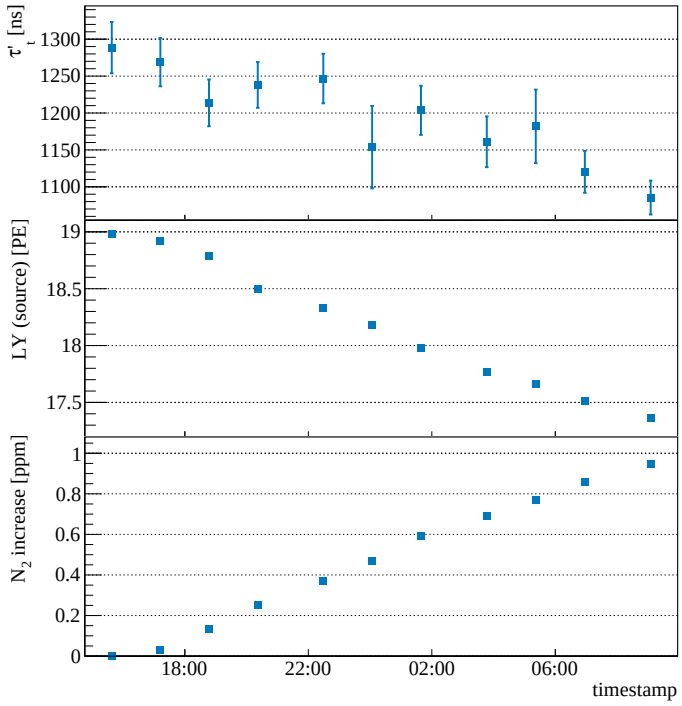

Figure 10.2: Evolution of the effective triplet lifetime (top), primary light yield (middle), and increase in nitrogen content in the LEGEND-200 LAr during the nitrogen doping from July 19th to 20th 2021.

k_{Q,N_2} can be computed. Here, the LAr before the doping is assumed to expose negligible contamination, i.e. $[N_2] = 0$, and thus the required properties can be taken from table 10.1. Explicitly, $\tau_t = \tau'_t(pure)$, $\eta_s = ((I_s + I_i)/I_{sig})(pure)$ and $\eta_t = 1 - \eta_s$.

Figure 10.3 shows the primary light yield of the time slices obtained from the light source over the calculated nitrogen content. Using equation 10.2, the dependence of the primary light yield on the nitrogen concentration is modeled. A χ^2 fit is performed, where I and k_{Q,N_2} are free. The final result of the quenching rate parameter is

$$k_{Q,N_2} = (0.120 \pm 0.001\,(\text{stat}) \pm 0.006\,(\text{sys}))\ \mu\text{s}^{-1}\,\text{ppm}^{-1},$$

with the statistical and systematical uncertainties of the model's LAr properties propagated into the result.

The value can be compared to an early study in literature, reporting $3.8 \times 10^{-12}\,\text{cm}^3\,\text{s}^{-1}$,

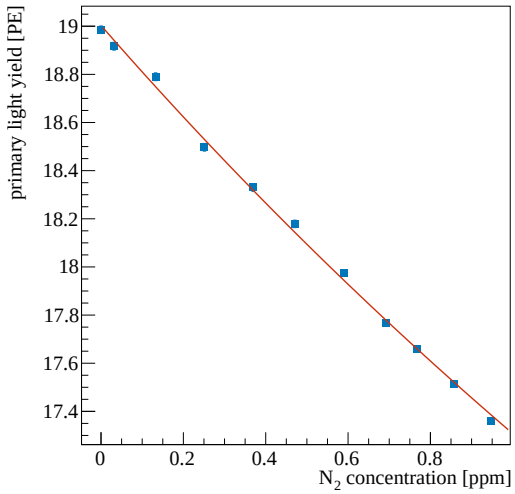

Figure 10.3: Primary light yield reconstructed by LLAMA's light source over the calculated amount of nitrogen in the LEGEND-200 cryostat. Here, the initial LAr is assumed to be devoid of nitrogen. The red line is the result of a fit with equation 10.2 with I and k_{Q,N_2} varied, while the other parameters are taken from table 10.1 (pure).

which is equivalent[4] to around $0.08\,\mathrm{ppm}^{-1}\,\mu\mathrm{s}^{-1}$ [1]. The result presented here is compatible with a recent work, which finds $k_{Q,\mathrm{N}_2} = (0.11 \pm 0.01)\,\mathrm{ppm}^{-1}\,\mu\mathrm{s}^{-1}$ [2]. This shows that both model and rate parameter measured for added nitrogen concentrations between 1 ppm to 3000 ppm [2] and 5 ppm to 20 ppm [1] are valid also in the sub-ppm range.

10.3.2 Correlation between primary light yield and effective triplet lifetime

Following the argumentation in section 10.1, the doping quenches the light output from triplet excimers, but not significantly from singlet excimers, in the concentration region investigated. Combining formulas 10.1 and 10.2, the dependence of the quenched light

[4]The value in units of $\mathrm{cm}^3\,\mathrm{s}^{-1}$ is multiplied by $10^{-12}\,\rho_{LAr}\,A_{Ar}^{-1}\,N_A\,\mathrm{s}/\mu\mathrm{s} \approx 2.11 \times 10^{10}\,\mathrm{cm}^{-3}\,\mathrm{ppm}^{-1}\,\mathrm{s}/\mu\mathrm{s}$, where ρ_{LAr} is the mass density of LAr at the boiling point, A_{Ar} is the molar mass of argon and N_A is Avogadro's constant.

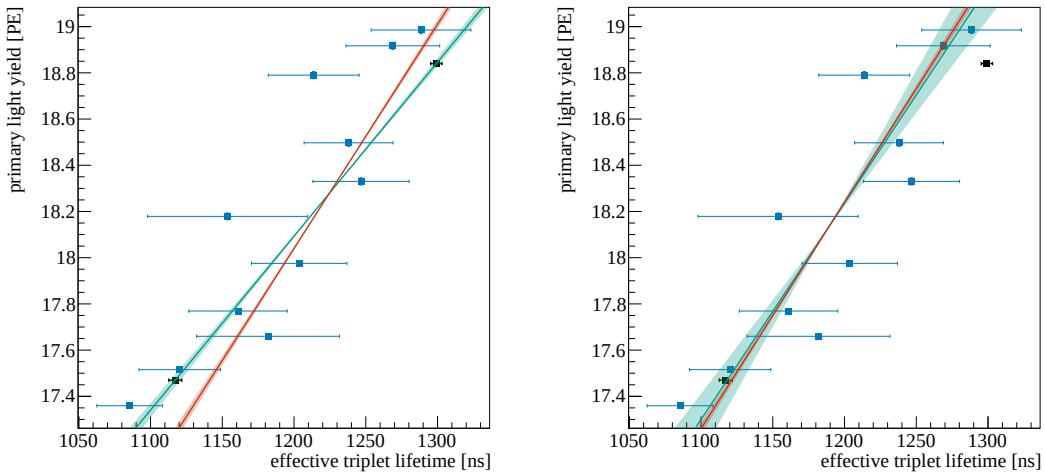

(a) (b)

Figure 10.4: The primary light yield extracted from the light source over effective triplet lifetime. The results from both stable data frames are shown in black, while the values obtained during doping are shown in blue. The lines and 1σ regions correspond to realizations of the model (equation 10.4). The best fit for stable data frames is drawn in teal, while the expectation using LAr properties from table 10.1 are shown in red. The fits are performed both on stable data frames (a) and during spoiling (b).

yield on the effective triplet lifetime can be expressed as

$$I'_Q(\tau'_t) = I\left(\eta_s + \frac{\eta_t}{\tau_t}\tau'_t\right). \tag{10.3}$$

This equation is valid for any combination of contaminants quenching triplet excimers non-radiatively, i.e. it does not exclusively apply to nitrogen. For using it to model the dependency of the primary light yield on the effective triplet lifetime using the data at hand, the formula is reshaped into

$$I'_Q(\tau'_t) = \frac{I\,\eta_t}{\tau_t}\left(\frac{\eta_s}{\eta_t}\,\tau_t + \tau'_t\right), \tag{10.4}$$

which is effectively an affine function with both $\frac{I\,\eta_t}{\tau_t}$ and $\frac{\eta_s}{\eta_t}\,\tau_t$ acting as independent parameters.

The data and representations of the model are shown in figure 10.4. The plot combines data points from stable data frames (black) and during doping (blue).

For fits of the model to the data, either the stable data frames (figure 10.4a) or the ones during doping (figure 10.4b) are used, since the stable data frames would dominate in a fit to the combined data sets due to their much smaller uncertainties. Model parameters η_s, η_t, and τ_t can be fixed to the values obtained for the pure data set (table 10.1), assuming negligible quenching before doping:

$$\tau_t = (1299 \pm 4\,(\text{stat}) \pm 22\,(\text{sys}))\ \text{ns} \quad \text{and} \quad \frac{\eta_s}{\eta_t} = 0.51 \pm 0.01\,(\text{stat}) \pm 0.04\,(\text{sys}).$$

This way, only the arbitrary scaling $\frac{I\,\eta_t}{\tau_t}$ is obtained by a fit to the data. The resulting best fit is shown in red together with the 1σ region evaluated by propagating statistical and systematical uncertainties of η_s, η_t, and τ_t.

Additionally, a fit with both $\frac{I\,\eta_t}{\tau_t}$ and $\frac{\eta_s}{\eta_t}\,\tau_t$ varied is performed and drawn in teal. Its 1σ region represents the statistical uncertainty extracted from the fit. Assuming a triplet lifetime of pure LAr, the singlet-to-triplet ratio can be obtained from $\frac{\eta_s}{\eta_t}\,\tau_t$ (and vice versa). Using τ_t from table 10.1, the singlet-to-triplet ratio in pure LAr can be calculated for the fit to the stable data frames:

$$\frac{\eta_s}{\eta_t} = 0.94 \pm 0.06\,(\text{stat}) \pm 0.02\,(\text{sys}).$$

The deviation of the result from the value presented in table 10.1 becomes also apparent in incompatible model curves in figure 10.4a. The primary light yield value of the pure data range might be affected by the instabilities present during the filling operations (see section 6.3). Hence, this systematic effect would affect the slope of the model function and, thus, the reconstructed singlet-to-triplet ratio.

In contrast, the fit to the data during spoiling matches the expectation more closely, as visible in figure 10.4b. The singlet-to-triplet ratio in pure LAr obtained from this fit is

$$\frac{\eta_s}{\eta_t} = 0.58 \pm 0.23\,(\text{stat}) \pm 0.01\,(\text{sys}),$$

which is more in agreement with the singlet-to-triplet ratio obtained from the fit to the pure data set but shows a higher statistical uncertainty.

10.3.3 Attenuation cross-section of nitrogen

Though assumed to be small in magnitude [2], the increase in absorption caused by 0.9 ppm in nitrogen can be well studied by LLAMA, as it measures the light intensity over a range up to 75 cm. Section 7.2 obtained the absorption strength of the additional nitrogen $k_{A,N_2}\,[N_2]$ from the change in photon counts in the peripheral SiPMs before and after the doping using the Beer-Lambert-Law (4.10).

Using the nitrogen concentration of 0.9 ppm, the absorption strength calculates as

$$k_{A,N_2} = (0.023 \pm 0.010)\,\mathrm{m}^{-1}\,\mathrm{ppm}^{-1}.$$

The absorption length l_{abs} is

$$l_{abs} = (47 \pm 20)\,\mathrm{m}.$$

The high uncertainty reflects the difficulty of LLAMA to reconstruct an attenuation length of $\mathcal{O}(10)$ m using a maximum light path of 75 cm.

Using equation 4.11, the absorption cross-section of nitrogen can be computed from the absorption coefficient:

$$\sigma_{A,N_2} = k_{A,N_2}\,10^6\,\frac{A_{Ar}}{N_A\,\rho_{LAr}}, \tag{10.5}$$

with ρ_{LAr} being the mass density of LAr, A_{Ar} is its molar mass and N_A denotes Avogadro's number.

With the absorption coefficient quoted above, this formula yields

$$\sigma_{A,N_2} = (1.1 \pm 0.5) \times 10^{-20}\,\mathrm{cm}^{-2}$$

This value can be compared to a study of the absorption cross-section of LAr doped up to around 40 ppm in nitrogen for LAr scintillation light [3]. The result derived there, $\sigma_{A,N_2} = (4.99 \pm 0.51) \times 10^{-21}\,\mathrm{cm}^{-2}$, is compatible within 2σ with the result of this work.

Both values are plotted in figure 10.5. The wavelength-resolved absorption cross-section of pure gaseous nitrogen is also shown (blue, taken from [9]). The mean of the wavelength-resolved spectrum is computed to facilitate comparison, using the emission intensity of LAr taken from [10] as weight. The result is shown in magenta and amounts to $8.5 \times 10^{-22}\,\mathrm{cm}^{-2}$. Position and x-errorbars of the wavelength-integrated data points

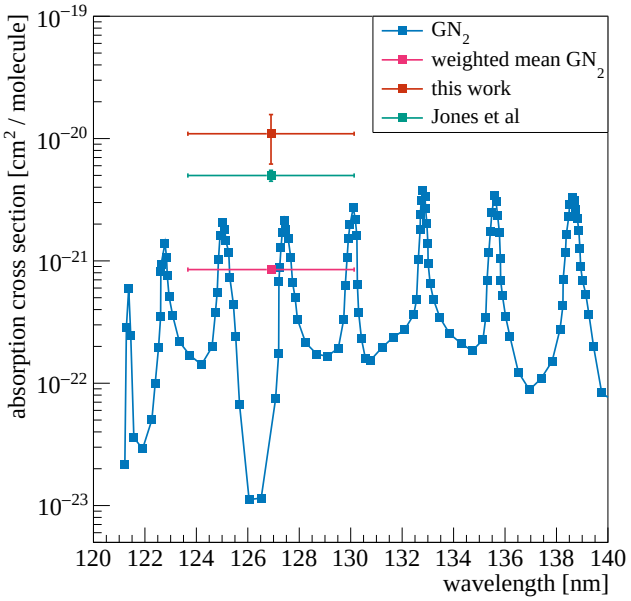

Figure 10.5: Comparison of absorption cross-sections obtained from LLAMA (red, this work) to literature values. The result from [3] (teal) is also obtained using nitrogen-doped LAr. The absorption cross-spectrum from gaseous nitrogen from [9] is shown in blue, and its mean value weighted by the LAr emission intensity in magenta. Uncertainties in wavelength display the width of the LAr scintillation peak (1σ) [10].

correspond to the LAr emission peak (mean and σ).

Both measurements in LAr show consistently higher absorption cross-sections than expected from pure nitrogen gas. This might hint at an increase in the cross-section of nitrogen when transitioning from the warm gas state to the cold liquid. The comparison would profit from further measurements, e.g. wavelength-resolved in nitrogen-doped LAr.

References

[1] S. Himi, T. Takahashi, J. z. Ruan, and S. Kubota, "Liquid and solid argon, and nitrogen doped liquid and solid argon scintillators," *Nucl. Instrum. Meth.*, vol. 203, pp. 153–157, 1982. DOI: 10.1016/0167-5087(82)90623-8.

[2] R. Acciarri *et al.*, "Effects of Nitrogen contamination in liquid Argon," *JINST*, vol. 5, P06003, 2010. DOI: 10.1088/1748-0221/5/06/P06003. arXiv: 0804.1217 [nucl-ex].

[3] B. J. P. Jones, C. S. Chiu, J. M. Conrad, C. M. Ignarra, T. Katori, and M. Toups, "A Measurement of the Absorption of Liquid Argon Scintillation Light by Dissolved Nitrogen at the Part-Per-Million Level," *JINST*, vol. 8, P07011, 2013, [Erratum: JINST 8, E09001 (2013)]. DOI: 10.1088/1748-0221/8/07/P07011. arXiv: 1306.4605 [physics.ins-det].

[4] G. Zuzel, "LAr for L200; internal presentation," 2019.

[5] J. D. Scargle, J. P. Norris, B. Jackson, and J. Chiang, "STUDIES IN ASTRONOMICAL TIME SERIES ANALYSIS. VI. BAYESIAN BLOCK REPRESENTATIONS," *The Astrophysical Journal*, vol. 764, no. 2, p. 167, 2013, ISSN: 0004-637X. DOI: 10.1088/0004-637X/764/2/167.

[6] P. Adhikari *et al.*, "The liquid-argon scintillation pulseshape in DEAP-3600," *Eur. Phys. J. C*, vol. 80, no. 4, p. 303, 2020. DOI: 10.1140/epjc/s10052-020-7789-x. arXiv: 2001.09855 [physics.ins-det].

[7] M. Harańczyk, "private communications," 2022.

[8] M. Haranczyk *et al.*, "Purification of large volume of liquid argon for LEGEND-200," *PoS*, vol. PANIC2021, p. 102, 2022. DOI: 10.22323/1.380.0102.

[9] R. Babcock, I. Liberman, and W. Partlow, "Volume ultraviolet preionization from bare sparks," *IEEE Journal of Quantum Electronics*, vol. 12, no. 1, pp. 29–34, 1976. DOI: 10.1109/JQE.1976.1069027.

[10] T. Heindl *et al.*, "The scintillation of liquid argon," *EPL (Europhysics Letters)*, vol. 91, no. 6, p. 62 002, 2010, ISSN: 0295-5075. DOI: 10.1209/0295-5075/91/62002.

Chapter 11

Measurements in xenon-doped liquid argon

This chapter discusses the xenon doping campaign, for which the measurement was conducted in 2021 from May 26 until June 14 at TUM. This work does not consider the piloting campaign in the Summer of 2020, as the setup was less mature and the performance less elaborate. Nevertheless, valuable experience was gained from this operation, which aided the following experiment.

This chapter begins with a motivation about xenon doping in LAr. In section 11.2, the whole setup is explained: from the cryogenic infrastructure, over the doping and mass spectroscopy instrument until the measurement of optical parameters with LLAMA-II. The experiment and especially the setup result from a collaborative effort, with the doping and mass spectroscopy being implemented, maintained, and operated by Christoph Vogl, Johanna Grießing, and Xaver Stribl. This setup part is explained in detail in Christoph Vogl's Master's thesis [1]. The doping measurement procedure and data analysis are explained in section 11.3. The obtained evolution of the optical properties with xenon concentration is the subject of section 11.4. A large part of this chapter's contents is summarized in a dedicated publication [2].

Before continuing the subject of xenon doping, the notation used for concentrations requires clarification. As explained in detail in appendix A, the usage of "parts-per" notation (e.g. ppm) is largely ambiguous in literature concerning xenon doping in LAr. While some use it to express mole fractions (e.g. [3, 4]), others express mass fractions (e.g. [2, 5–7]). Especially older works miss an explicit clarification (e.g. [3, 4]), further

hampering comparisons.

Consequently, this chapter follows the guideline by [8] in using SI units instead, even though it is not yet adopted in the field. Thus, molar fractions are expressed by µmol/mol equalling ppm by mole or ppm by volume in literature. Analogously, mass fractions are expressed by µg/g equalling ppm by mass in other publications. Both definitions are quoted in some places to facilitate comparison with literature using either notation.

Conversely, all other chapters in this dissertation use the "parts-per" notation, exclusively denoting mole fraction. This is done since in literature LAr impurity studies save xenon doping consistently use the "parts-per" notation in this definition.

11.1 Motivation

In section 4.4, the physics of xenon-doped argon is explained, including the advantages over pure LAr. In summary, several optical properties are enhanced with respect to the performance in large-scale LAr detectors with scintillation light readout. Xenon shifts the photon wavelength from the LAr primary emission wavelength peaking at 128 nm to 175 nm. Since typical wavelength shifters such as TPB are more efficient for this region, the effective light yield, i.e. the number of detected PE per unit of energy deposited, increases [5]. The energy resolution benefits indirectly from this fact. Also, the attenuation length increases [9, 10]. Furthermore, the effective triplet lifetime of LAr gets reduced, narrowing the time window of photon emission at sufficient xenon concentration. Hence, LAr detectors reduce dead times. Especially, LAr detectors working in conjunction with detectors faster than the LAr triplet lifetime, such as HPGe arrays, profit, as coincidence windows can be reduced. This reduces the influence of backgrounds such as ^{39}Ar and increases the overall performance of the combined detector, as discussed in section 12.3.

These properties render xenon-doped LAr superior to pure LAr in many, especially large-scale applications, while largely retaining the inexpensiveness and availability of argon compared to xenon. Detectors gain in spacial uniformity and are less susceptible to impurities [11]. For example, its application is considered for DUNE [11]. Furthermore, an application in the atmospheric argon volume of LEGEND-1000 is foreseen, and even the possibility of doping the underground argon is considered.

Several experiments have already studied xenon-doped LAr. However, the presented

campaign stands out in several aspects. First, the measurements were conducted on a large scale, using a 1 t LAr cryostat, only recently surpassed by the ProtoDUNE 750 t Dual-Phase LAr TPC [11]. Second, a dedicated mass spectrometer system sensitive to the single µmol/mol level of xenon evaluated the dopant concentration in the gas and liquid phases. Repeated cross-checks of the actual impurity concentration in the mixture are key, since freezeout and losses of xenon through overpressure valves are a concern. Last, LLAMA is perfectly tailored for measuring the change of the effective light yield, photon emission time spectrum, and attenuation length in the parameter regions reached by xenon-doped LAr. Its monitoring capabilities are paramount for studying the evolution during mixing and validating the stability. Remarkably, the distance-resolved measurement of light intensity and photon arrival times are outstanding features of LLAMA in this field. Previous studies of xenon-doped LAr mostly lack distance-resolved information entirely [5, 6, 12, 13] or require detector modeling and track reconstruction [11]. Only [9] provides distance-resolved intensities for xenon-doped LAr, however, only for a comparably high xenon concentration of 3 %. Thus, LLAMA is paramount in developing a comprehensive picture of xenon-doped LAr, encompassing photon emission and propagation.

11.2 Doping and mass spectroscopy setup at TUM

The measurements were conducted in SCARF in the shallow underground laboratory at TUM. SCARF is a 1 t research cryostat with an automated passive cooling by liquid nitrogen and is described in detail in [14]. Its lock allows for the easy immersion of custom payloads without introducing impurities. LLAMA-II, described in detail in chapter 5, was submerged before the campaign and kept stable for the entire duration.

The mixing setup consists of an argon 6.0 and a xenon 5.0 bottle, connected to an empty 10 L vessel hosting the final mixture. A turbo-molecular pump evacuates the vessel with the piping, and a pressure gauge is used to estimate the amount of dopant.

The mixing setup shares a connection to SCARF with the mass spectrometer setup Impurity DEtector For Investigation of Xenon (IDEFIX), which is described in detail in [1]. IDEFIX is designed and extensively optimized to detect trace gases in an argon carrier gas, apart from xenon, also for e.g. nitrogen and oxygen. Its core component is a Prisma 200 quadrupole mass spectrometer by Pfeiffer Vacuum. It is connected to an ultra-high

Table 11.1: Detection limits on the 3σ level for the mass spectrometer setup IDEFIX. Taken from [1].

Molecule	Detection limit [µmol/mol]
N_2	38
O_2	0.44
CO_2	6.74
Xe	0.77

vacuum chamber, evacuated by a turbo-molecular pump. A leakage valve allows injecting sample gas in a very controlled way, reaching a pressure in the chamber in the range of 1×10^{-6} mbar. Apart from SCARF or custom containers, the sample gas can also be taken from an argon 6.0 and a calibration gas bottle using static and leak-tested piping. Thus, the system can be calibrated, and detection limits are derived and compiled in table 11.1.

11.3 Measurement procedure and data taking

Doping is performed in several incremental stages. The target concentrations of each stage are listed in table 11.2. Before each injection, the mixing vessel was evacuated and subsequently filled with xenon. The amount was regulated by reading the pressure in this vessel, and the final xenon content expected from the pressure measurement is listed in the third column of table 11.2. The two last stages are regulated to achieve a slight excess in expected concentration to counteract previously detected losses in xenon due to mass spectroscopy measurements in continuous mode [1].

Subsequently, the mixing vessel is filled with argon gas up to a pressure of around 34.4 bar. This way, argon acts as a carrier gas, avoiding potential freeze-out of xenon at the inlet section [12]. With SCARF's liquid-nitrogen-powered cooling active, the mixture is condensed into the LAr volume, avoiding overpressure to trigger the security relief valves. After around one hour, each injection was completed with a pressure equilibrium between the mixing bottle and the cryostat.

Mass spectrometry measurements of SCARF's content were conducted at every doping

Table 11.2: Xenon concentrations of the doping stages of the measurement campaign. The table lists the values aimed for (target), expected from the xenon pressure in the mixing vessel before injection (expected), and from mass spectroscopy measurements. The latter are done from both the bottom outlet, accessing the liquid, and the cryostat's lock probing the ullage. Taken from [1].

target		expected [µg/g]	bottom outlet		lock [µg/g]
[µg/g]	[µmol/mol]		mode	result [µg/g]	
0	0	-	batch	0.07 ± 0.86	0.13 ± 0.89
3	0.91	3.0 ± 0.5	batch	1.3 ± 1.1	1.6 ± 1.2
10	3.0	10.3 ± 0.7	cont.	9.1 ± 2.7	-
50	15.2	50.1 ± 2.8	forced	37.9 ± 7.9	37.3 ± 7.6
100	30.4	110 ± 4	forced	87.8 ± 8.9	18.5 ± 2.7
300	91.2	314 ± 10	forced	360 ± 59	133 ± 22

stage and before the campaign commenced. The xenon content in the ullage was measured for all stages except for 10 µg/g, since IDEFIX measured from the bottom outlet continuously at that stage. Via the cryostat's bottom outlet, the mixture from the liquid phase is drawn, thus allowing for a more accurate assessment of the liquid's composition. Apart from a continuous measurement at the 10 µg/g stage, measurements from the bottom outlet were conducted in batches. Before the aforementioned stage, the batches were evaporated slowly and during their flow through the pipes. This might bias the results due to xenon freezing on the pipes' walls and Henry's Law [15] causing differences in composition in gas and liquid phases in equilibrium [1]. Thus, from 50 µg/g on, measurements from the bottom outlet were conducted using forced evaporation, where a pump was pumping the liquid in the bottom outlet directly. This causes fast, non-equilibrium evaporation; thus, measured impurity concentrations are expected to represent the condition in the liquid phase [1]. Measured xenon concentrations in the ullage and through the bottom outlet are listed in table 11.2, along with the mode used for measuring the liquid's composition.

LLAMA-II is fully submerged and active during the entire campaign. Its setup, operation principle, and data analysis are described in detail in chapter 5. Hence, only relevant aspects are summarized in the following, along with properties particular to this campaign.

Three of its 13 peripheral SiPMs were not used, as vacuum feedthroughs were missing or connections were too noisy. LLAMA's time-resolved results allowed to confirm stable conditions in advance of any subsequent injection. Since the high amount of PE detected for late doping stages saturated the CR-111 preamplifiers of the source SiPMs, they were replaced by CR-112 with a 10-fold lower gain during the 100 µg/g stage.

11.4 Evolution of optical properties with xenon concentration

11.4.1 Time-resolved analysis

Figure 11.1 shows the evolution of the optical parameters over the campaign's entire duration. The photon time spectrum is reconstructed by taking the time difference between the beginning of the scintillation event in the source and a photon detection in the closest peripheral SiPM on an event-by-event basis. A fit to the right-hand tail from 200 ns to 8000 ns after the singlet peak with $I(t) = I_0 \exp(-t/\tau_t') + I_{acc}$ yields the effective triplet lifetime τ_t'. This value is shown in the top panel.

The effective[1] light yield is reconstructed by summing up the PE detected by all three source SiPMs in an event-by-event basis. The resulting spectrum is dominated by a peak corresponding to 60 keV energy depositions by gamma particles. The peak's position is taken as a measure of the effective light yield and is shown in the middle panel of figure 11.1. It also shows when the preamplifiers were exchanged (red).

The light intensity at different distances is used to reconstruct the attenuation length via a fit with a single exponential function, $I(x) = I_0 \exp(-x/l_{att})$. Its development is shown in the bottom panel.

From the figure, one can infer that it takes up to 60 h until stable conditions are reached. Overall, the data match the general expectation of an increased effective light yield and attenuation length, and a reduced effective triplet lifetime. However, the situation is inverted when going from 0 µg/g to 3 µg/g for both effective triplet lifetime and light yield. This effect is addressed later in this section.

The last stage is measured for around five days, verifying the long-term stability of the mixture according to figure 11.1.

[1] The light yield is referred to as effective here since detection efficiencies vary with wavelengths.

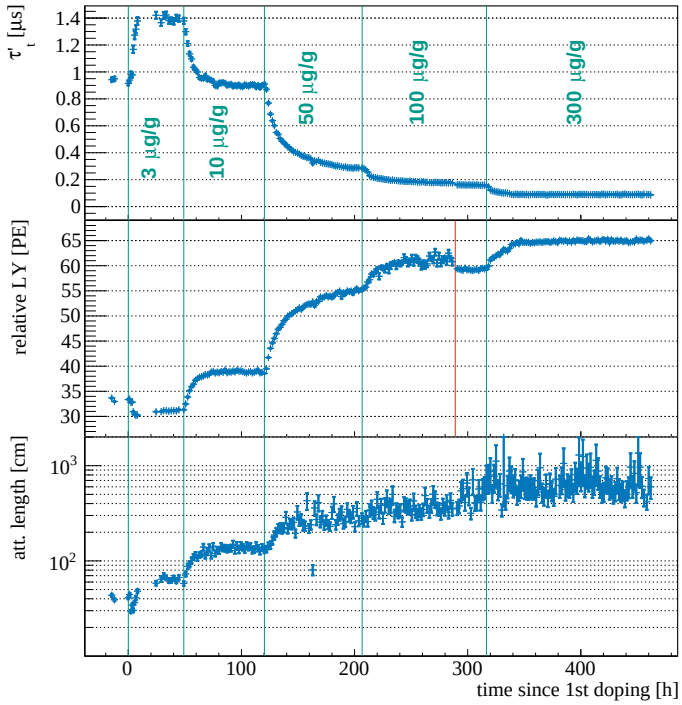

Figure 11.1: Effective triplet lifetime (top), effective light yield (middle), and attenuation length (bottom) measured by LLAMA-II during the xenon doping campaign in 2021. Lines in teal mark the start of each doping injection; total target concentrations are written in the same color. The red line marks the change of preamplifiers required for properly reconstructing the light yield for $[\mathrm{Xe}] \gtrsim 50\,\mu\mathrm{g/g}$ (see text). The time on the x-axis is aligned to the beginning of the 1st injection.

11.4.2 Photon emission time profile

The stable time frames from each doping stage are utilized to study the optical properties of each step in more detail. For the $100\,\mu\mathrm{g/g}$ stage, the region used is located after exchanging the preamplifiers. These regions are analyzed analogously to the monitoring data, and the final parameters are compiled in table 11.3.

The effective triplet lifetime prior doping is only 941 ns, which indicates substantial quenching by contaminants (see section 4.3.1). SCARF was contaminated with air earlier since the pressure inside shortly decreased below ambient pressure. On the one hand, this renders modeling the effect of xenon doping more difficult since oxygen and nitrogen

Table 11.3: Optical properties extracted for stable periods within each doping step, including the time frame before the first injection.

target conc.		eff. triplet lifetime	eff. light yield	att. length
[µg/g]	[µmol/mol]	[ns]	[PE]	[cm]
0	0	941	33.63 ± 0.05	41.6 ± 0.9
3	0.91	1395	31.10 ± 0.03	64.1 ± 1.1
10	3.0	883	39.15 ± 0.03	139.0 ± 2.1
50	15.2	405	54.51 ± 0.05	288 ± 8
100	30.4	159	59.33 ± 0.06	498 ± 26
300	91.2	89	64.99 ± 0.04	653 ± 22

compete in quenching argon excimers and can reduce the lifetime of $ArXe^*$ states. On the other hand, it aids in understanding the mitigation of quenching impurities by xenon. Using the effective quenching rate constant of dry air[2] of $0.20\,\mu s^{-1}(\mu mol/mol)^{-1}$, the amount of air results in around 1.5 µmol/mol, corresponding to 1.2 µmol/mol nitrogen and 0.32 µmol/mol oxygen.

The photon time spectra for all doping stages are shown in figure 11.2, obtained using the SiPM in 15 cm distance. It clearly shows the development of a broad, late peak, which is in literature commonly referred to as "hump". For increasing xenon content, the peak gains intensity, gets shifted to earlier time frames, and merges with the singlet peak of LAr scintillation. This behavior is already found e.g. by [4, 5]. It is attributed to a concentration-dependent energy transfer from Ar_2^* via $ArXe^*$ to Xe_2^* proposed by [4] and modeled by [5]. It furthermore yields a tentative explanation for the increasing effective triplet lifetime from 0 µg/g to 3 µg/g: The lifetime of $ArXe^*$ is $(4.7 \pm 0.1)\,\mu s$ [11] and the induced quenching by xenon atoms is $8.8 \times 10^{-2}\,(\mu g/g)^{-1}\mu s^{-1}$ [5]. Thus, the effective lifetime of $ArXe^*$ at $[Xe] = 3\,\mu g/g$ is around 2.1 µs, exceeding the one from pure LAr and hence increasing the observed effective triplet lifetime. Above around $[Xe] = 6\,\mu g/g$ the effect vanishes, since the effective lifetime of $ArXe^*$ becomes smaller than the triplet lifetime of pure LAr.

[2] Due to its volatile concentration in air and potential freezeout effects, water is neglected here. The effective quenching rate constant of dry air is derived using the values of nitrogen [16] and oxygen [17], and their respective atmospheric abundances.

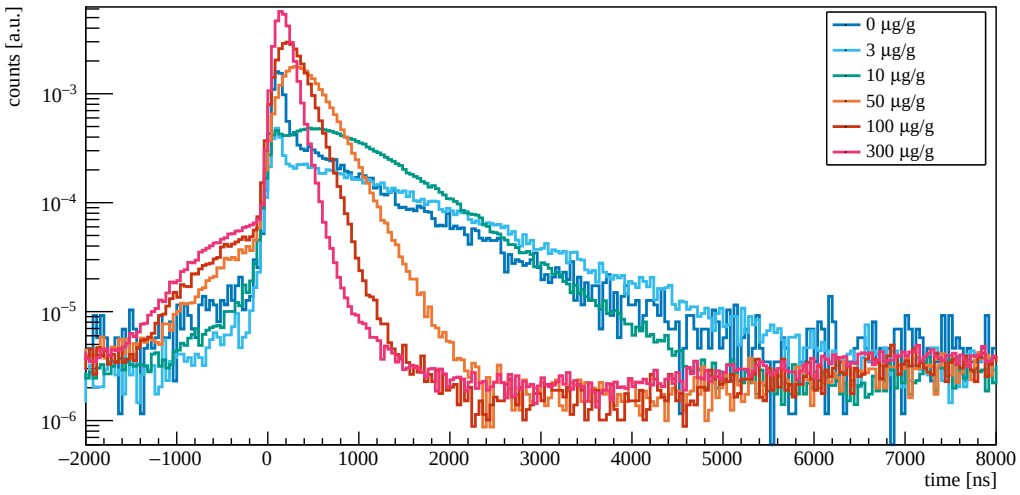

Figure 11.2: Photon emission time profiles for different xenon doping stages. The development of a "hump" structure at around 10 µg/g and its subsequent merge with the LAr singlet peak matches literature [4, 5]. The spectra are obtained at a distance of 20 cm from the light source.

11.4.3 Light yield

The spectra in figure 11.3a show the total amount of light detected in all three source SiPMs evaluated on an event-by-event basis. They feature a clear peak originating from full energy depositions of 60 keV gamma particles, and their shift corresponds to the observed increase in primary light yield. The artifact at around 60 PE for concentrations up to 50 µg/g is caused by the preamplifiers reaching the end of their dynamic range.

The increase in effective light yield is in accordance with literature [5, 12]. In [5, 12], this effect is attributed to increasing efficiency of TPB for shifted light. LLAMA does not use TPB, however the VUV4 SiPMs used are more efficient at 175 nm compared to 128 nm (see figure 5.3). The dependency is modeled using emission spectra from [3] (0.1 µmol/mol, 1 µmol/mol, 10 µmol/mol, 100 µmol/mol and 1000 µmol/mol) and [18] (pure LAr) to study the impact of the wavelength-dependent detection efficiency on the effective light yield. Here, an ideal wavelength-shifting process is assumed, i.e. all emission spectra are normalized before projecting on the efficiency spectrum.

Figure 11.3b shows effective light yields both measured and modeled, respectively normalized to 0 µg/g. One can infer that an increased efficiency of the SiPMs for shifted

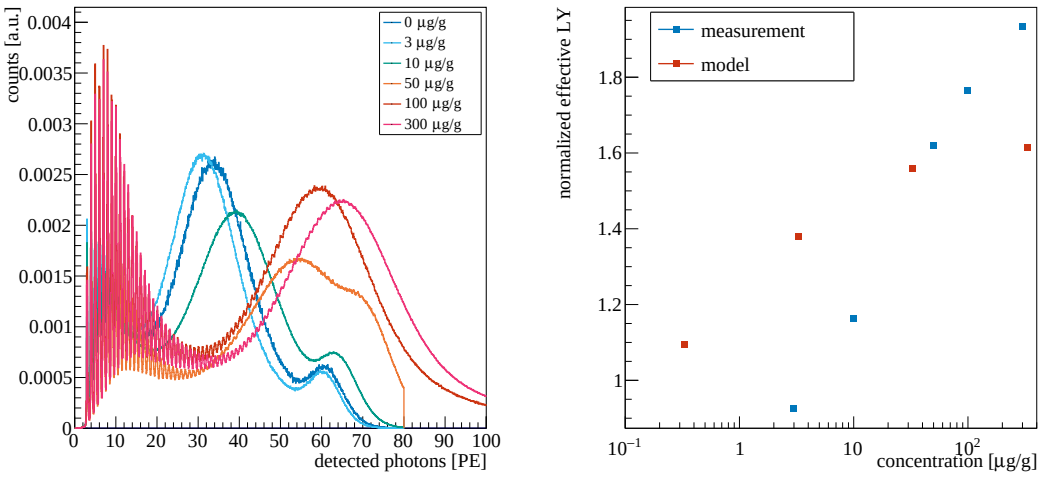

(a) (b)

Figure 11.3: (a): Evolution of the number of PE detected by the source SiPMs. The prominent peak consists of 60 keV energy deposition in the source. The effective light yield is reconstructed from its position.
(b): Effective light yield extracted from (a), normalized to 0 µg/g (blue). Its behavior can be partially explained by the increased efficiency of VUV4 SiPMs for detecting shifted photons (red).

light can only partly explain the measured dependency.

The measured values are lower than the model expectations at low but non-zero concentrations. The model developed by [13] also yields a minimum in effective light yield for low but non-zero xenon concentrations (around 0.1 µmol/mol). There, this behavior is explained by a combination of absorption by xenon and increased quenching of the ArXe* state with a long lifetime. The distance of the source SiPMs to the center of LLAMA's cavity is 8.5 mm, and thus, absorption is expected to be subdominant. However, the substantial dry air contamination presumably quenches a significant fraction of the long-lived ArXe* state, reducing the effective light yield for low xenon concentrations.

At high concentrations, the measured values surpass the expectations, tentatively explained by mitigating quenching effects caused by non-radiative impurities. This effect is studied in detail in [19] using a hypothetical mixture of 50 µmol/mol nitrogen and 1000 µmol/mol xenon in LAr. That work obtains that xenon successfully competes with nitrogen in quenching argon excimers. This result can be transferred to the present data.

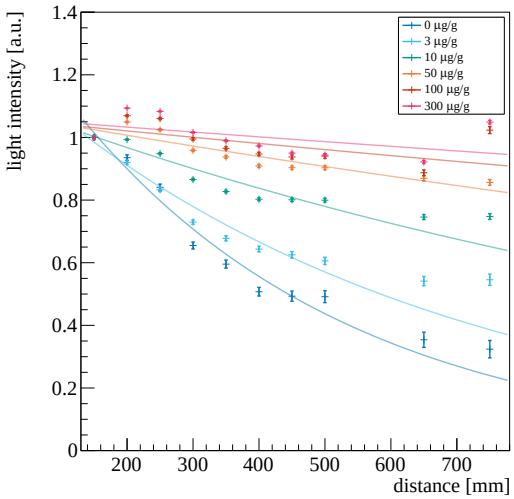

Figure 11.4: Evolution of the attenuation length for xenon-doped LAr for all concentrations used. Light intensities are normalized to 15 cm.

11.4.4 Photon propagation

LLAMA provides distance-resolved intensity and photon arrival time information. Data is available for distances from 15 cm to 75 cm in steps of 5 cm, save 55 cm, 60 cm and 70 cm due to missing vacuum feedthroughs or excessive noise conditions. Figure 11.4 shows light intensities for all doping stages at these points. Fits with functions of the form $I(x) = I_0 \exp(-x/l_{att})$ yield attenuation length values, listed in table 11.3. An increasing attenuation length is visible and matches literature results [9]. In [9], the effect is attributed to longer Rayleigh scattering lengths[3] for photons shifted to the longer wavelength. Additionally, the absorption due to xenon impurities is negligible for the Xe_2^* emission wavelength region while substantial for the Ar_2^* emission peak [3]. Thus, xenon's wavelength-shifting properties mitigate the absorption caused by itself.

Figure 11.5a shows the time spectrum of photons detected at 15 cm, 40 cm and 75 cm distance for the 3 µg/g stage. The singlet peak and the early part of the second "hump" are decreasing for farther distances. This effect is tentatively attributed to the absorption of the primary LAr scintillation peak by xenon. The property of xenon to absorb the emission from Ar_2^* excimers with high efficiency was measured by [3]. At 1 µmol/mol = 3.29 µg/g,

[3]The Rayleigh scattering length is proportional to λ^4 [20].

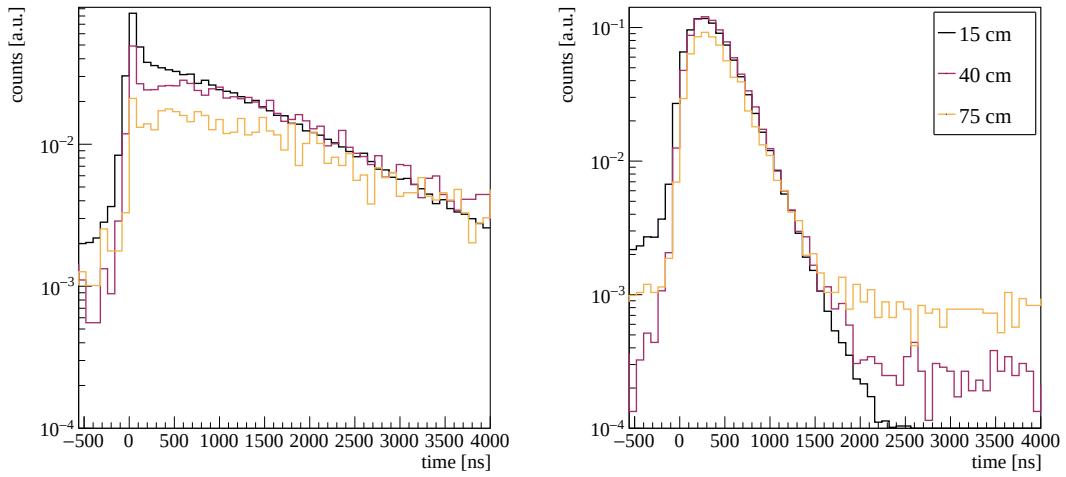

(a) (b)

Figure 11.5: Photon arrival time spectra for different distances, measured for xenon concentrations of 3 µg/g (a) and 50 µg/g (b). While absorption of primary LAr emission dominating the early spectrum is strong for 3 µg/g, a negligible effect is visible for 50 µg/g, indicating a dominance of wavelength-shifted photons. Spectra are normalized to their integral within −2 µs to 10 µs.

a large part of the scintillation peak is strongly absorbed. Since the singlet peak and the early part of the second "hump" are dominated by photons around 128 nm, as measured by [5] for e.g. 9 µg/g, those time regions are mainly susceptible to absorption. The late part of the second "hump" is dominated by 175 nm photons and thus not affected.

For higher concentrations, e.g. 50 µg/g, transfer and absorption processes eliminate the 128 nm photons prior reaching the 15 cm SiPM. Thus, the spectra shown in figure 11.5b become almost identical.

11.5 Conclusions

The doping campaign discussed in this chapter addresses multiple essential topics in the field of xenon-doped LAr. On the one hand, these encompass well-established properties such as the increase of both effective light yield and attenuation length or the evolution of the photon emission time spectrum.

On the other hand, the setup composed of the large-volume SCARF cryostat, the

dedicated mass-spectroscopy and doping system, and the novel instrument LLAMA yield unprecedented results. The mitigation of quenching is studied and confirmed in the quaternary mixture of xenon, oxygen, and nitrogen in LAr. In state-of-the-art literature, the mitigation of quenching is studied for ternary mixtures of xenon and nitrogen in LAr, once in a model-only study [19] and once in measurement [11]. However, both consider a single xenon concentration only, in contrast to the five stages investigated in the presented work.

The absorption of the primary emission from LAr scintillation by xenon, speculated by [6], was observed using distance-resolved time spectra. Though LLAMA-II does not provide wavelength-resolved spectra, the property of primary LAr scintillation light to dominate the early time region observed by [5] was used and confirmed. According to section 4.4 based on the measurements by [3, 6, 21], re-emission of photons absorbed by xenon is possible. Since re-emission happens in all directions, photons are effectively scattered and not expected to reach peripheral SiPMs with high probability.

Overall, LLAMA provides input to model emission and propagation of VUV photons in distance and time dimensions. However, providing a full model exceeds the scope of this work, because the presence of a quaternary mixture introduces additional absorption and quenching effects, potentially impacting all excited species involved. A third xenon doping campaign using LLAMA-II and the same cryogenic infrastructure, planned for 2024, will employ LAr of much higher purity. Thus, the obtained data will allow for improved models of xenon-doped LAr.

The present work yields promising results in view of the application of xenon-doped LAr in large-scale detectors. Increases in both effective light yield and attenuation length enhance uniformity and energy resolution, respectively. Regarding dead-time reduction when employed in combination with HPGe detectors in LEGEND, xenon-doped LAr highlights by reducing the response time of the LAr detector. These properties render xenon-doped LAr a highly attractive choice for the AAr volume in LEGEND-1000, potentially also its UAr volume, as well as other large-scale particle detectors based on LAr. The application of xenon-doped LAr in LEGEND-1000 is studied further in section 12.3 in the upcoming chapter.

References

[1] C. Vogl, "Liquid Argon: Purification and Xenon-Doping for Legend," *Master's thesis, TUM*, 2021.

[2] C. Vogl, M. Schwarz, X. Stribl, J. Grießing, P. Krause, and S. Schönert, "Scintillation and optical properties of xenon-doped liquid argon," *JINST*, vol. 17, no. 01, p. C01031, 2022. DOI: 10.1088/1748-0221/17/01/C01031.

[3] A. Neumeier *et al.*, "Attenuation of vacuum ultraviolet light in pure and xenon-doped liquid argon —An approach to an assignment of the near-infrared emission from the mixture," *EPL*, vol. 111, no. 1, p. 12 001, 2015. DOI: 10.1209/0295-5075/111/12001. arXiv: 1511.07725 [physics.ins-det].

[4] S. Kubota, M. Hishida, S. Himi, J. Suzuki, and J. Ruan, "The suppression of the slow component in xenon-doped liquid argon scintillation," *Nucl. Instrum. Meth. A*, vol. 327, no. 1, pp. 71–74, 1993, ISSN: 0168-9002. DOI: 10.1016/0168-9002(93)91413-H.

[5] C. G. Wahl, E. P. Bernard, W. H. Lippincott, J. A. Nikkel, Y. Shin, and D. N. McKinsey, "Pulse-shape discrimination and energy resolution of a liquid-argon scintillator with xenon doping," *JINST*, vol. 9, P06013, 2014. DOI: 10.1088/1748-0221/9/06/P06013. arXiv: 1403.0525 [physics.ins-det].

[6] D. Akimov *et al.*, "Fast component re-emission in Xe-doped liquid argon," *JINST*, vol. 14, no. 09, P09022, 2019. DOI: 10.1088/1748-0221/14/09/P09022. arXiv: 1906.00836 [physics.ins-det].

[7] E. Segreto, "Properties of liquid argon scintillation light emission," *Phys. Rev. D*, vol. 103, no. 4, p. 043 001, 2021. DOI: 10.1103/PhysRevD.103.043001.

[8] S. E. Schwartz and P. Warneck, *Pure and Applied Chemistry*, vol. 67, no. 8-9, pp. 1377–1406, 1995. DOI: doi:10.1351/pac199567081377.

[9] N. Ishida *et al.*, "Attenuation length measurements of scintillation light in liquid rare gases and their mixtures using an improved reflection suppresser," *Nucl. Instrum. Meth. A*, vol. 384, no. 2-3, pp. 380–386, 1997, ISSN: 0168-9002. DOI: 10.1016/S0168-9002(96)00740-1.

[10] A. Hitachi, "Photon-mediated and collisional processes in liquid rare gases," *Nucl. Instrum. Meth. A*, vol. 327, no. 1, pp. 11–14, 1993, ISSN: 0168-9002. DOI: 10.1016/0168-9002(93)91398-7.

[11] J. Soto-Oton, "Impact of xenon doping in the scintillation light in a large liquid-argon TPC," in *5th International Conference on Technology and Instrumentation in Particle Physics*, 2021. arXiv: 2109.05858 [physics.ins-det].

[12] P. Peiffer, T. Pollmann, S. Schönert, A. Smolnikov, and S. Vasiliev, "Pulse shape analysis of scintillation signals from pure and xenon-doped liquid argon for radioactive background identification," *JINST*, vol. 3, no. 08, P08007–P08007, 2008, ISSN: 1748-0221. DOI: 10.1088/1748-0221/3/08/P08007.

[13] D. Fields, R. Gibbons, M. Gold, N. McFadden, S. Elliott, and R. Massarczyk, "Understanding the enhancement of scintillation light in xenon-doped liquid argon," *Nucl. Instrum. Meth. A*, p. 167 707, 2022, ISSN: 0168-9002. DOI: 10.1016/j.nima.2022.167707.

[14] C. Wiesinger, "The TUM Liquid Argon Test Stand: Commissioning and Characterization of a Low Background Test Stand for Background Suppression Studies in the Frame of the GERDA ($0\nu\beta\beta$)-Experiment," *Master's thesis, TUM*, 2014.

[15] W. Henry and J. Banks, "III. Experiments on the quantity of gases absorbed by water, at different temperatures, and under different pressures," *Philosophical Transactions of the Royal Society of London*, vol. 93, pp. 29–274, 1803. DOI: 10.1098/rstl.1803.0004.

[16] R. Acciarri *et al.*, "Effects of Nitrogen contamination in liquid Argon," *JINST*, vol. 5, P06003, 2010. DOI: 10.1088/1748-0221/5/06/P06003. arXiv: 0804.1217 [nucl-ex].

[17] R. Acciarri *et al.*, "Oxygen contamination in liquid Argon: Combined effects on ionization electron charge and scintillation light," *JINST*, vol. 5, P05003, 2010. DOI: 10.1088/1748-0221/5/05/P05003. arXiv: 0804.1222 [nucl-ex].

[18] T. Heindl *et al.*, "The scintillation of liquid argon," *EPL (Europhysics Letters)*, vol. 91, no. 6, p. 62 002, 2010, ISSN: 0295-5075. DOI: 10.1209/0295-5075/91/62002.

[19] A. Buzulutskov, "Photon emission and atomic collision processes in two-phase argon doped with xenon and nitrogen," *EPL*, vol. 117, no. 3, p. 39 002, 2017. DOI: 10.1209/0295-5075/117/39002. arXiv: 1702.03612 [physics.ins-det].

[20] M. Babicz *et al.*, "A measurement of the group velocity of scintillation light in liquid argon," *JINST*, vol. 15, no. 09, P09009, 2020. DOI: 10.1088/1748-0221/15/09/P09009. arXiv: 2002.09346 [physics.ins-det].

[21] A. Neumeier *et al.*, "Intense vacuum ultraviolet and infrared scintillation of liquid Ar-Xe mixtures," *EPL (Europhysics Letters)*, vol. 109, no. 1, p. 12 001, 2015, ISSN: 0295-5075. DOI: 10.1209/0295-5075/109/12001.

Chapter 12

Implications on the physics performances of LEGEND-200 and LEGEND-1000

So far, the liquid argon part of this dissertation focused on LLAMA and the data obtained from it both in LEGEND-200 and in SCARF. This chapter leaves this path as it uses results previously obtained to draw conclusions on the physics performance of LEGEND-200 and LEGEND-1000. Precisely, the performance of the LAr instrumentation is investigated based on the acquired knowledge of the optical properties of LAr by LLAMA. As described in section 3.2.3, the LAr instrumentation is a core component of LEGEND, and sufficient performance is obligatory for reaching the background levels required.

As this topic is under heavy development, the results should be regarded as a snapshot rather than as carved in stone. Also, apart from the first section, the chapter summarizes work done by other LEGEND members rather than providing new results.

12.1 Performance impact of the spoiling event

During filling of the LEGEND-200 cryostat, the LAr was contaminated with around 0.9 ppm of nitrogen. Details about the incident are presented in section 6.3. Using LLAMA data, the effect on the optical properties of LAr was studied in detail, and the results are shown in chapter 10. In conclusion, the light yield decreased, while the effect on the absorption length was marginal.

Here, the goal is to study the effect of the changing light yield on the performance of

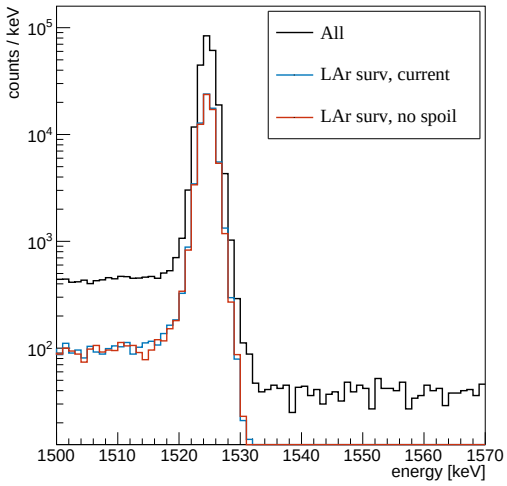

Figure 12.1: Spectrum of simulated energy depositions in all HPGe detectors in the LEGEND-200 setup, focussing the ^{42}K decay gamma line at 1525 keV. ^{42}K decays are simulated in the LAr volume surrounding the detectors. The black spectrum is before cuts, while the other two display the situation after LAr anti-coincidence, either using the current LAr quality (blue) or assuming no N_2 spoiling (red).

LEGEND-200. To this end, the MaGe simulation package [1] is used, which simulates ^{42}K decays in different parts of the setup. The current light yield implemented in MaGe is used as a baseline, while a light yield increased by a factor of 1.089 simulates the case of un-spoiled LAr.

The suppression of the 1525 keV gamma line of the decay of ^{42}K is investigated here. The decay has a Q-value of around 3525 keV, and the emitted beta particle allows suppressing the gamma line by LAr anti-coincidence, providing a good performance benchmark.

Figure 12.1 shows the 1525 keV gamma line before (black) and after LAr anti-coincidence, the latter using either LAr quality implemented: with (blue) and without (red) spoiling. For this plot, ^{42}K decays are simulated in a cylinder of 1 m radius and 1.2 m height covering the entire array. It is visible that the performance of the LAr system is only marginally affected by the nitrogen contamination.

Survival fractions are calculated by taking the ratio of the intensities before and after the cut using either LAr quality, and the results are compiled in table 12.1. The last

Table 12.1: Survival fractions for LAr anti-coincidence obtained from the 1525 keV gamma line of ^{42}K simulated in different parts of the LEGEND-200 setup. The LAr instrumentation performance assumes two LAr qualities: the current one and without N_2 spoiling, with the last column showing the ratio. See the text for details and definitions of the simulated locations.

Location	survival fraction with LAr anti-coincidence		
	current quality	no N_2 spoiling	relative change
cylinder	0.287 ± 0.001	0.281 ± 0.001	0.977 ± 0.005
inside MS	0.078 ± 0.001	0.075 ± 0.001	0.97 ± 0.02
outside MS	0.339 ± 0.001	0.331 ± 0.001	0.977 ± 0.006
MS surface	0.0374 ± 0.0002	0.0359 ± 0.0002	0.962 ± 0.008
HPGe surface	0.319 ± 0.002	0.311 ± 0.002	0.975 ± 0.007

column lists the relative changes in the survival fractions when transitioning from the current quality to the quality before spoiling. The rows show the effects of using different locations of ^{42}K, with the first using the cylinder defined before. The cylinder is further separated into volumes outside and inside the MSs, and their surfaces are also sampled. Additionally, ^{42}K decays on the surface of the HPGe detectors are simulated.

In conclusion, nitrogen spoiling affects the performance of the LEGEND-200 LAr instrumentation only marginally. Survival fractions would decrease by a few percent, if the LAr was not spoiled during filling. This stresses the performance of LLAMA as a warning system during filling, as it signaled the halt of the filling operations before the LAr quality deteriorated strongly.

12.2 With observed photon emission time spectra towards a likelihood-based anti-coincidence classifier

LLAMA yields valuable information about the scintillation time structure of the LAr currently situated in the LEGEND-200 cryostat. This data provides a base for improving the anti-coincidence condition of the LAr instrumentation in LEGEND-200.

Currently, the anti-coincidence condition in LEGEND-200 tags all events as background-like, which exhibit at least 4 PE in a single channel or at least a majority of 4, i.e. 4 SiPM channels with at least 0.5 PE each [2]. The PE are counted within a window from $-1\,\mu s$ to $5\,\mu s$ with respect to the trigger of a HPGe detector[1]. This condition has an acceptance for $\beta\beta$-like test pulser events of around 95 %.

In GERDA, a $\beta\beta$ decay acceptance of around 98 % was achieved using low thresholds of less than 1 PE on any channel, i.e. a simple light/no light condition [3]. However, this is impossible in LEGEND-200 , since the test pulser acceptance would be too low because both the light collection efficiency and the instrumented volume are much larger in LEGEND-200 [2]. This "luxury problem" opens up the possibility to implement more elaborate and fine-tuned anti-coincidence conditions in LEGEND-200.

A promising approach uses the LAr scintillation time profile to build a test statistic, which weights individual incoming photons of an event [2]:

$$T = \sum_{i}^{n} \frac{f(t_i)}{n} \tag{12.1}$$

The weighting function $f(t)$ uses the singlet-to-triplet ratio and the current triplet lifetime from LLAMA. However, the singlet part is driven by the detector resolution, which has to be obtained directly from LEGEND-200 data.

At the time of writing, the work on the test statistic is still heavily in progress, and hence, no results are presented here. Several people contribute to this effort, including E. Bossio, R. Deckert, N. Doll, P. Krause, and L. Pertoldi.

12.3 Advantages from xenon doping

Correlation of photons detected by the LAr instrumentation to pulses in HPGe detectors suffers from the long triplet lifetime of LAr scintillation. The random coincidence rate faced in LEGEND-200 forces a compromise between $0\nu\beta\beta$ decay acceptance and background rejection, as described in the previous section.

Doping LAr with xenon shortens the effective triplet lifetime and hence confines the photon arrival times much more to the onset of the HPGe detector pulse, mitigating the

[1] This accounts both for possible long drift times of the HPGe detectors and late photon arrivals from the tail of the LAr triplet emission. [2]

Table 12.2: Survival fractions of simulated scintillation events correlated to HPGe triggers in LAr doped with different xenon concentrations. Different events are simulated: either with a fixed number of PE or using the PE distribution of ^{42}K events in LEGEND-200 data (60 kg phase). Thresholds are tuned to keep the acceptance of random coincidences at 95 %. Taken from [2].

[Xe] in µg/g	τ_t' [ns]	survival fractions [%]				
		1 PE	2 PE	3 PE	4 PE	^{42}K
0	1100	39.2	28.4	19.5	13.3	13.3
10	883	35.2	24.0	15.9	10.5	12.7
50	300	10.0	2.0	0.5	0.1	10.0
100	156	1.7	0.1	< 0.1	< 0.1	9.4
300	89	0.1	< 0.1	< 0.1	< 0.1	9.4

influence of random coincidences. In a study by P. Krause [2], the effect was simulated using the LAr test statistic described in the previous section. The results of the xenon doping campaign at TUM[2] in 2021 are used as input for both the test statistic and for generating simulated scintillation events. The effective triplet lifetimes from table 11.3 are used. The decay time of the singlet emission is kept at 6 ns and the singlet fraction $I_s = 1/3$ is used following the result for pure LAr in table 9.1. No intermediate component is included.

Events coincident with a HPGe detector pulse and random coincidences with an arbitrary time difference are simulated. Thresholds are tuned to maintain a survival fraction of 95 % for random coincidences.

The resulting survival fractions taken from [2] are summarized in table[3] 12.2. Events with a fixed number of PE in the range from 1 to 4 are simulated, as well as events following the PE distribution of ^{42}K events in LEGEND-200 data (60 kg phase). It is visible that xenon concentrations starting from around 50 µg/g strongly boost the performance of the LAr instrumentation. Some ^{42}K events remain, because the used PE distribution contains a 0 PE contribution.

[2]The doping campaign is described in detail in chapter 11.

[3]Note, that τ_t' for [Xe] = 50 µg/g is assumed to be 300 ns rather than 405 ns. This is due to a slightly different fit procedure used in [4], from which the values are adopted by [2].

It has to be noted, however, that the results are produced assuming an infinite temporal detector resolution, which is not realistic. Application of a proper smearing using the currently achievable time resolution is in progress at the moment.

Further, the change in the photon emission time distribution is the only aspect studied here. Results from section 11.4.2 further show that the attenuating length is strongly increased by adding xenon, and the efficiency of light detection systems changes due to the different wavelengths. These will strongly affect the performance of the LAr instrumentation, as the efficiency to detect both true and random coincident energy depositions, especially in far regions of the LAr volume, is strongly enhanced. This mandates a careful evaluation of random coincidences, as currently unproblematic far-away scintillation events e.g. in the cryostat's neck can become much more prominent.

12.4 Conclusions and outlook

Performance impacts to the LAr instrumentation of LEGEND-200 and LEGEND-1000 are studied with a focus on optical properties of LAr. The deterioration due to the nitrogen spoiling during the filling of the LEGEND-200 cryostat is marginal, i.e. no substantial performance benefit is expected for the removal of nitrogen.

Nevertheless, it is vital to maintain a good LAr quality, especially regarding contaminants with much higher quenching or absorption strength, such as oxygen or hydrocarbons. This refers to the degradation of the LAr observed during LEGEND-200 commissioning and analyzed in section 7.3. However, it is caused mainly by a decrease in absorption length, which is not studied here since a final model for the absorption in LEGEND-200 LAr is still pending (see chapter 8).

Furthermore, the use of a likelihood-based anti-coincidence classifier is promising for boosting the LAr instrumentation's performance when random coincidences become a limiting factor. As already explained, this is the case for LEGEND-200, and presumably also the large AAr volume of LEGEND-1000. Especially in case UAr is not be available for LEGEND-1000, the inner LAr volume would face a high luminosity from ^{39}Ar, necessitating an elaborate classifier.

To further enhance the performance of the anti-coincidence classifier, the LAr can be doped with trace amounts of xenon, which severely compresses the time spectrum of photon emission. Dedicated simulations based on measured scintillation time spectra

yield substantial performance benefits starting from 50 µg/g to 100 µg/g. Thus, doping of the LAr volumes of LEGEND-1000 is proposed. Future doping of the LAr in LEGEND-200 is planned to provide a credible large-scale benchmark.

References

[1] M. Boswell *et al.*, "MaGe-a Geant4-Based Monte Carlo Application Framework for Low-Background Germanium Experiments," *IEEE Transactions on Nuclear Science*, vol. 58, no. 3, pp. 1212–1220, 2011. DOI: 10.1109/TNS.2011.2144619.

[2] P. Krause, "Shining Light on Backgrounds," Ph.D. dissertation, Technische Universität München, 2023.

[3] C. Wiesinger, "No neutrinos not found," Ph.D. dissertation, Munich, Tech. U., 2020.

[4] C. Vogl, "Liquid Argon: Purification and Xenon-Doping for Legend," *Master's thesis, TUM*, 2021.

Part IV

Ordinary muon capture for $0\nu\beta\beta$ decay nuclear matrix elements

Chapter 13

Benchmarking nuclear structure calculations with OMC

As explained in section 1.2, next-generation $0\nu\beta\beta$ decay experiments target discovery. The allowed parameter space is aimed to be completely covered in case of the inverted ordering, while a large part is probed in case of the normal ordering. Achieving this ambitious goal requires pushing the discovery sensitivity on the effective Majorana mass to regions as low as $m_{\beta\beta} \approx 10\,\text{meV}$. Vast amounts of material and unprecedented background limits are the consequence, rendering these experiments complex and expensive. Currently, insufficient knowledge of nuclear properties, which are needed for translating between the directly measured half-live and $m_{\beta\beta}$, hamper an estimation of the required performance.

Precisely, NMEs carry uncertainties of factors between two or three, and the processes leading to an apparent quenching of the axial vector coupling g_A are still under investigation. Unique properties of $0\nu\beta\beta$ decay prevent direct measurements of the NMEs, which thus have to be calculated. Experimental benchmarks address associated uncertainties, amongst which OMC provides an exceptional opportunity due to its underlying nuclear physics closely related to $0\nu\beta\beta$ decay.

This chapter contains two sections, respectively discussing the connection between $0\nu\beta\beta$ decay and nuclear structure calculations, and between these calculations and OMC. Chapter 14 covers experimental aspects by describing MONUMENT, a current OMC experiment.

13.1 Nuclear structure theory for $0\nu\beta\beta$ decay

The requirement of nuclear structure theory input for calculating the $0\nu\beta\beta$ decay half-life was already mentioned in section 1.2. The following formula connects experimental observables ($0\nu\beta\beta$ decay rate $\Gamma^{0\nu}$ or half-life $T^{0\nu}_{1/2}$) with the effective Majorana mass $m_{\beta\beta}$ for the light neutrino exchange mechanism:

$$\frac{\Gamma^{0\nu}}{\ln(2)} = \frac{1}{T^{0\nu}_{1/2}} = \mathcal{G}^{0\nu}\, g_A^4\, |\mathcal{M}^{0\nu}|^2\, \frac{m^2_{\beta\beta}}{m^2_e}. \tag{13.1}$$

While the phase-space factor $\mathcal{G}^{0\nu}$ can be calculated with sufficient precision, both the NME $|\mathcal{M}^{0\nu}|$ and potentially the axial vector coupling g_A carry large uncertainties.

Several nuclear structure models predict NME values differing by a factor of two or three [1]. This becomes a severe issue for designing next-generation $0\nu\beta\beta$ experiments, as it translates to almost[1] an order of magnitude uncertainty in the exposure necessary for achieving a given discovery sensitivity on $m_{\beta\beta}$.

The so-called g_A problem constitutes another potential issue for connecting $T^{0\nu}_{1/2}$ with $m_{\beta\beta}$. In the past, beta and $2\nu\beta\beta$ decay rates did not match theoretical predictions, motivating phenomenological correction sometimes referred to as *quenching* of g_A [1]. An effective value g_A^{eff} is introduced, which is around 70 % of g_A, and the factor depends on the mass number of the decaying nucleus. Since the $0\nu\beta\beta$ decay rate depends on g_A to the fourth power, a strong suppression is possible, depending on the actual mechanism [1].

However, recent ab initio calculations suggest omitted nuclear processes, precisely two-body currents and missing many-body correlations [3], to be responsible for the apparent quenching [3–5]. Thus, assigning the quenching to overpredicted NMEs may be more appropriate than to g_A. OMC, together with neutrino-nucleus scattering, provide a way to test for overpredictions of NMEs [6].

[1] In case of quasi background-free experiments. Background-limited experiments suffer from even higher uncertainties [2].

13.2 Ordinary muon capture for $0\nu\beta\beta$ decay

Benchmarking nuclear structure calculations is required to tackle both the NME uncertainties and the g_A problem for $0\nu\beta\beta$ decay. It turns out that $2\nu\beta\beta$ decays do not provide good benchmarks for the $0\nu\beta\beta$ decay due to the different momentum and energy scales involved [1]. In $2\nu\beta\beta$ decays, neutrinos emerge, and momentum and energy transfer are constrained by the transition's Q-value, i.e. on the order of 1 MeV. Conversely, the neutrinos stay virtual in $0\nu\beta\beta$ decay, and the scale is confined by the average distance between both decaying neutrons, resulting in around 100 MeV.

This impacts the selection of states of the intermediate nucleus reached via virtual transitions in $\beta\beta$ decays. Only 0^+ and 1^+ states are accessible by $2\nu\beta\beta$ decay due to the limited momentum transfer, while, in principle, all J^π multipoles take part in $0\nu\beta\beta$ decay [1, 7]. Furthermore, beta decays only probe the lowest-lying state [7].

Thus, a proper probe of all intermediate states involved in $0\nu\beta\beta$ decay requires momentum and energy transfers at a comparable scale. This is given for OMC due to the muon's sufficient rest mass. OMC as a benchmark for $0\nu\beta\beta$ decay was first proposed by [8] and is based on the following semi-leptonic reaction [9]:

$$\mu^- + p \rightarrow n + \nu_\mu. \tag{13.2}$$

Typically, the proton is part of a target nucleus, which captures the muon. Before the nuclear capture, the muon is captured in the atomic shells, producing muonic X-rays by transitioning down to the K shell.

Figure 13.1 compares $0\nu\beta\beta$ decay with OMC, demonstrating that OMC probes the right virtual transition of $0\nu\beta\beta$ decay. In the scheme, the $\beta\beta$ decaying isotope ${}^AX_Z$ decays to ${}^AY_{Z+2}$ via the intermediate isotope ${}^AW_{Z+1}$. OMC uses the isotope ${}^AY_{Z+2}$ as a target in order to probe isomers of ${}^AW_{Z+1}$, populating different J^π states including highly excited ones [7].

The excited states of ${}^AW_{Z+1}$ decay via gamma emission, frequently accompanied by proton and neutron emission [9]. The measurement and analysis of the gamma radiation, together with an identification of the nuclear levels, allow for obtaining partial and total capture rates. While partial capture rates correspond to the rates of directly populating individual excited states of ${}^AW_{Z+1}$, total capture rates integrate all final isomers of ${}^AW_{Z+1}$

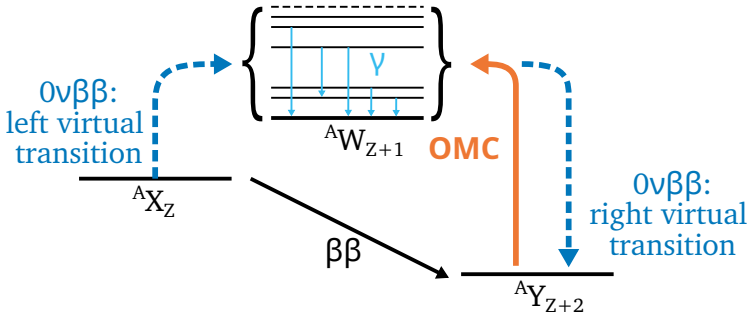

Figure 13.1: $0\nu\beta\beta$ decay scheme involving virtual transitions via excited states of the intermediate (odd, odd) nucleus. OMC on the daughter isotope probes the right virtual transition of $0\nu\beta\beta$ at similar energy scales and leads to gamma cascades in the intermediate nucleus. Adapted from [10].

including the ground state [10]. Both provide the actual experimental input for the nuclear theory calculations [8, 10].

The following chapter provides an overview of OMC experimental aspects and introduces MONUMENT, an OMC experiment benchmarking $0\nu\beta\beta$ nuclear theories at the Paul Scherrer Institut (PSI).

References

[1] J. Engel and J. Menéndez, "Status and future of nuclear matrix elements for neutrinoless double-beta decay: a review," *Reports on Progress in Physics*, vol. 80, no. 4, p. 046 301, 2017. DOI: 10.1088/1361-6633/aa5bc5.

[2] J. Gómez-Cadenas *et al.*, "Sense and sensitivity of double beta decay experiments," *Journal of Cosmology and Astropart. Phys.*, vol. 2011, no. 06, p. 007, 2011. DOI: 10.1088/1475-7516/2011/06/007.

[3] A. Belley, T. Miyagi, S. R. Stroberg, and J. D. Holt, "Ab initio calculations of neutrinoless $\beta\beta$ decay refine neutrino mass limits," 2023. arXiv: 2307.15156 [nucl-th].

[4] M. Agostini, G. Benato, J. A. Detwiler, J. Menéndez, and F. Vissani, "Toward the discovery of matter creation with neutrinoless $\beta\beta$ decay," *Rev. Mod. Phys.*, vol. 95, no. 2, p. 025 002, 2023. DOI: 10.1103/RevModPhys.95.025002. arXiv: 2202.01787 [hep-ex].

[5] P. Gysbers *et al.*, "Discrepancy between experimental and theoretical β-decay rates resolved from first principles," *Nature Phys.*, vol. 15, no. 5, pp. 428–431, 2019. DOI: 10.1038/s41567-019-0450-7. arXiv: 1903.00047 [nucl-th].

[6] A. C. Hayes, P. Navratil, and J. P. Vary, "Neutrino C-12 scattering in the ab initio shell model with a realistic three body interaction," *Phys. Rev. Lett.*, vol. 91, p. 012 502, 2003. DOI: 10.1103/PhysRevLett.91.012502. arXiv: nucl-th/0305072.

[7] M. Kortelainen and J. Suhonen, "Microscopic study of muon-capture transitions in nuclei involved in double-beta-decay processes," *Nuclear Physics A*, vol. 713, no. 3, pp. 501–521, 2003, ISSN: 0375-9474. DOI: 10.1016/S0375-9474(02)01303-9.

[8] M. Kortelainen and J. Suhonen, "Ordinary muon capture as a probe of virtual transitions of $\beta\beta$ decay," *Europhysics Letters*, vol. 58, no. 5, p. 666, 2002. DOI: 10.1209/epl/i2002-00401-5.

[9] D. Measday, "The nuclear physics of muon capture," *Physics Reports*, vol. 354, no. 4, pp. 243–409, 2001, ISSN: 0370-1573. DOI: 10.1016/S0370-1573(01)00012-6.

[10] D. Zinatulina *et al.*, "Ordinary muon capture studies for the matrix elements in $\beta\beta$ decay," *Physical Review C*, vol. 99, no. 2, p. 024 327, 2019, ISSN: 2469-9985. DOI: 10.1103/PhysRevC.99.024327.

Chapter 14

The MONUMENT experiment

OMC experiments provide observables crucial for benchmarking nuclear structure calculations, especially in the realm of $0\nu\beta\beta$ decay. The theoretical background is addressed in the previous chapter, while the current one comprehends the experimental approach, focused on MONUMENT.

While the three measurement campaigns initially foreseen already finished successfully at the time of writing, the analysis work is in full swing. Thus, the current work compiles the setups and experience from these measurement campaigns while providing a snapshot of the analysis in progress.

The actual work in the scope of this dissertation comprises the implementation, benchmarking, and performance evaluation of ALPACA - one of the two DAQ systems employed in two of MONUMENT's campaigns. Thus, the current chapter contains limited details, while in-depth information about ALPACA is given in two consecutive chapters. The implementation and unique features of ALPACA are presented in chapter 15, while its performance is evaluated in chapter 16.

14.1 Overview

MONUMENT (Muon Ordinary capture for the NUclear Matrix elemENTs) conducts OMC on various isotopes. It profits from the experiences of precious OMC experiments [1–3], which were conducted at the Paul Scherrer Institut (PSI) in Switzerland, in common with MONUMENT. The site features the world's most intense muon beam and is thus perfectly suited to host the experiment.

The MONUMENT collaboration was formed in 2020 and includes 30 members from

13 institutions. Initially, three campaigns were foreseen, with measurements performed in 2021, 2022 and 2023. Each campaign used unique sets of target isotopes, covering topics of $0\nu\beta\beta$ decay and astrophysical applications.

The first measurement campaign was conducted in October and November 2021 and used two enriched targets: ^{76}Se and ^{136}Ba. They are the daughter isotopes of the $0\nu\beta\beta$ decay candidates ^{76}Ge and ^{136}Xe and thus benchmark nuclear theories for those decays [4]. As mentioned in chapter 2, both isotopes will be used in the leading next-generation $0\nu\beta\beta$ decay experiments LEGEND and nEXO, respectively.

The second campaign was held in September and October 2022 [5]. The target isotope ^{100}Mo is motivated by nuclear reactions involving astrophysical neutrinos [6, 7].

In October 2023, the third campaign took place featuring a ^{48}Ti target. It was chosen as it is the daughter isotope of the lightest $\beta\beta$ decaying isotope ^{48}Ca. Nuclear theory is most advanced on this $0\nu\beta\beta$ decay isotope, which is studied e.g. with three different ab initio methods so far [8–10], facilitating cross-benchmarks [11].

14.2 Measurement principle and fundamental setup

14.2.1 Experimental access to partial and total capture rates

As explained in the previous chapter, partial and total capture rates constitute the primary experimental observables informing nuclear theory calculations for $0\nu\beta\beta$ decay. Partial capture rates refer to the population of the individual excited states of the $^{A}W_{Z+1}$ nucleus directly via OMC on $^{A}Y_{Z+2}$. They become experimentally accessible by measuring the decay gamma radiation of $^{A}W_{Z+1}$, with the following mechanism: [3]

The sum of the rates populating a given isomeric state, either directly via OMC or via gamma transition from a higher-lying state equals the rate of de-population of the same state via (further) gamma decay. Thus, the extraction of partial capture rates relies on well-measured intensities of gamma lines. In order to inform theoretical calculations, it is enough to derive relative intensities of captures to certain excited states [3]. Nonetheless, muonic X-rays of the K-series can be used to extract the number of muon stops in the target and thus to normalize gamma line intensities [3].

OMC competes with the decay of the muon bound in the atomic shell. The rate of the

latter can be calculated[1]. Thus, the total capture rate (i.e. capture by the nucleus) can be derived from the total rate of muon disappearance, which manifests in the time structure of gamma emissions. The gamma emissions follow a falling exponential distribution after the time point when the muon stops in the target. Distortions to the distribution are caused by non-zero lifetimes of the gamma lines and a limited detector time resolution. Since the time structures of all gamma lines of ${}^{A}W_{Z+1}$ obey the same muon disappearance rate, the results can be averaged, yielding uncertainty estimations in the process [3].

In conclusion, identification and intensity determination of gamma lines emitted from the target is paramount to achieve the physics goals of OMC measurements informing $0\nu\beta\beta$ decay theories. Further, the detector system must determine the arrival time of both gammas and muons with an accuracy sufficient to resolve the muon's lifetime.

14.2.2 Design principles of the MONUMENT setup

A schematic view of the MONUMENT setup is shown in figure 14.1. MONUMENT uses HPGe detectors to measure the target's gamma emissions. They offer a superior energy resolution, crucial for identifying gamma lines. They surround the target in close proximity ($\approx 15\,\mathrm{cm}$ [13]), boosting geometrical efficiency. Since muonic X-rays are similar in energy to the gamma lines studied, the HPGe detectors also record those. Past campaigns produced a catalog[2] of muonic X-rays for elements from $Z = 9$ to $Z = 90$ as a by-product, which can aid experiments in the realm of muon captures [14].

Each target used in the past MONUMENT campaigns is solid and has a mass of around $2\,\mathrm{g}$. Targets with high isotopic enrichment are used since small quantities of unwanted isotopes can spoil the measurement, as after OMC and neutron emission, they can produce the same excited states of ${}^{A}W_{Z+1}$.

The target in use is housed in a light-tight cell filled with ambient air. The cell contains four counters: plastic scintillators read out by PMTs, registering muons traveling in specific parts of the cell.

Two counters (C_1 and C_2) contain thin scintillator sheets and are located in the path of the incoming muon beam. They provide a time signal in case of muon arrival to correlate

[1] The decay rate of the muon in the atomic K-shell is the product of the free muon decay rate and the Huff factor [12].

[2] The catalog can be accessed at the following URL: `https://muxrays.jinr.ru/`

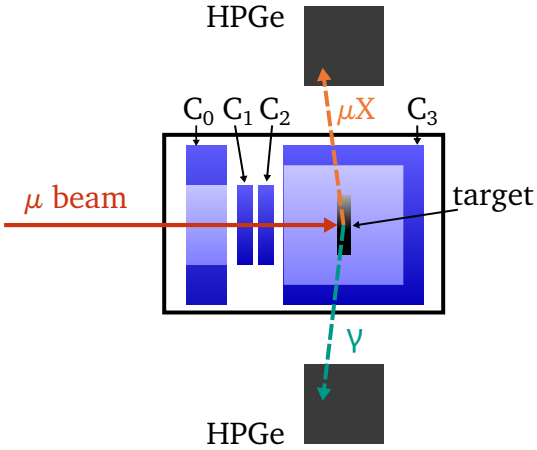

Figure 14.1: Schematic view of the experimental setup used by MONUMENT. The muon beam passes into the target cell (black outline). Muons stopping inside the target pass two veto counters: the ring-shaped C_0 and the cup-shaped C_3, while being detected in the sheet-like counters C_1 and C_2. After the stopping, muonic X-rays (μX) and gammas are produced and potentially detected in high-purity germanium (HPGe) detectors surrounding the cell. For the 2023 campaign, C_3 was replaced by a disk-shaped counter behind the target.

gamma events in time proximity to muon stops, and to provide a start signal for the evaluation of the time structure of gamma emission following the muon stop.

Additionally, a ring-shaped counter (C_0) surrounds the entry window, providing a veto against muons missing the target, which may be captured in other parts of the setup[3]. Another counter (C_3) is installed for the same reason. In the first two measurement campaigns, C_3 had a cup-like shape surrounding the target, while it was replaced by a disc behind the target for the last campaign.

A typical condition for selecting muons stopped in the target thus reads:

$$\mu_{stop} = \overline{C_0} \wedge C_1 \wedge C_2 \wedge \overline{C_3}. \tag{14.1}$$

[3]Furthermore, the veto scintillators take an essential role when tuning and steering the muon beam.

14.2.3 Measurement schedule

Each measurement campaign is separated into several data takings. Several calibrations with radioactive sources are performed in beam-off mode to calibrate gamma line positions, efficiency, and energy resolution. Since no gamma sources are available for the high-energy part of the spectrum (reaching up to around 8 MeV), calibrations with natural lead targets in beam-on mode are used to complement the calibrations there. Additionally, each enriched target has a "twin" of the same element in natural abundance, used for beam tuning (including the beam momentum) and steering in advance of a run with the enriched target.

The superior stability of the PSI accelerator allows to measure the enriched target for several consecutive days with only rare short-term interruptions. These interruptions and a day-long beam-off phase immediately following the irradiation are used to measure gamma lines of metastable states. Beam-off measurements continue off-site for several weeks to obtain spectra of long-lived isotopes produced.

14.3 Data taking and processing

This section summarizes data-taking routines and ALPACA-specific offline analysis procedures. Since the selection and tuning of digital signal processing algorithms and the consecutive higher-level analysis is content of the dissertation works of E. Bossio [15] and E. Mondragon [16], only a brief description is presented here. At the time of writing, the analysis works are focused on providing final results for the 2021 campaign. Thus, all offline processing and higher-level analysis presented here apply only to this campaign.

14.3.1 DAQ systems

For all on-site measurements of the first two campaigns, two DAQ systems were employed. The analog signals of all HPGe detectors and all counters are split just before reaching the DAQ. While the MIDAS-based system was used already in pre-MONUMENT campaigns, the new ALPACA system was first integrated in 2021. Both systems' detailed description and comparison are available in chapter 15, followed by an analysis of ALPACA's performance in chapter 16. Thus, only a brief overview is given in the following.

MIDAS triggers all channels independently and evaluates energy and time information online. Conversely, ALPACA triggers on pulses in HPGe detectors and reads out counters in coincidence with HPGe pulses. Waveforms are stored for offline analysis, allowing tuning energy and time reconstruction after the measurement campaign's end and preventing missing single PMT pulses in case of pile-ups.

Processing and analysis of data obtained with either DAQ system are kept separate to facilitate cross-checks at several stages, up to comparisons of the partial and total capture rates obtained.

The last campaign used only the MIDAS-based system due to the observation of critically high dead-time values in ALPACA, which could not be mitigated in time for the 2023 campaign.

14.3.2 ALPACA: Multi-level data structure and digital signal processing

ALPACA's raw output contains waveforms, from which all observables are extracted using digital signal processing. All waveforms of coincidently triggered channels are combined into one event at the DAQ level. Details about the waveform configuration are presented in section 15.2.3.

Raw data (tier0) constitutes the lowermost level of the hierarchical multi-tier structure defined in the analysis scheme of ALPACA. Higher tiers store event information of consecutive analysis steps. This way of data treatment is analogous to the implementation by GERDA [17]. Tier0 is almost identical to the format used by GERDA, with only a small custom modification: Timestamps are stored per-waveform rather than per-event since the DAQ hardware of MONUMENT was observed to start recording separate channels with small offsets.

The software stack used to transform tier0 into higher levels is based on ROOT [18], MGDO [19] and GELATIO [17] and all tiers higher than tier0 use the ROOT file format. Tier1 contains raw traces in a ROOT-based format, while tier2 compiles the immediate output of digital signal processing algorithms acting on the raw traces.

The energy of HPGe pulses is determined using a trapezoidal filter, implemented as the consecutive application of moving-window deconvolution and moving-window average. The uncalibrated energy is obtained by taking the amplitude of the filtered waveform at

a fixed position within the flat top region. Both moving windows' sizes are optimized using ^{60}Co calibration data and physics data [16]. The optimized window size used for deconvolving is limited by the trace length, stressing the importance of long traces for superior energy resolution. Leading-edge triggers are used for estimating the arrival time of pulses, both for HPGe and PMT traces. They act on traces before and after applying a fast trapezoidal filter, the latter being necessary to resolve multiple pulses within the same trace. Further observables aid the selection of events by quality cuts. They include the rise time of pulses and the spread within the baseline, i.e. the part of the waveform preceding the pulse.

HPGe and PMT data are processed in separate chains at the tier2 level. Tier3 recombines both data streams and takes external input obtained from the tier2 level, such as energy calibration functions. Tier3 provides event-based data crucial for any higher-level analysis [15]: It contains the time difference between HPGe and coincident PMT pulses, used e.g. to derive the total capture rate of muons. It further provides calibrated energies for HPGe pulses necessary for gamma line identification. The multiplicity, defined as the number of coincidently triggering HPGe channels, and boolean flags indicating problematic events are provided.

Currently, tier4 presents the highest stage of the data structure. Events are classified according to the time correlation between gamma arrival and muon stop (see section 14.4.5).

14.3.3 MIDAS: online tuning and data structure

MIDAS makes use of the versatile online processing capabilities of the FADC hardware. It offers trapezoidal filtering implemented as moving windows, which can be configured before data taking [20]. Separate trapezoidal filters are used for energy and arrival time determination. The amplitude at a constant location within the flat-top region is used for energy reconstruction, analogous to ALPACA's offline processing scheme. The shaping parameters are tuned on-site during dedicated calibration measurements using gamma sources. Additionally, boolean flags indicate e.g. pile-ups or excessive pulse heights. Small traces (1.4 µs length) are exclusively stored for HPGe events to enable improving time resolution in offline processing.

Raw data stored by the MIDAS DAQ is converted into a ROOT-based file structure

in advance of higher-level analysis [13]. This step does not involve event selection or processing.

14.4 Analysis of 2021 campaign data: current status

Most of the contents in this section are present in the recent Conceptual Paper [13], partly in more detail.

14.4.1 Germanium detector setup

In the 2021 measurement campaign, eight HPGe detectors were used, labeled from Ge 1 to Ge 8. From those, Ge 2 and Ge 6 are of BEGe type, while the remaining ones are semi-coaxial. While providing less efficiency, BEGe detectors offer superior energy resolution.

14.4.2 Data cleaning

The data cleaning step excludes problematic time regions from further analysis and is conducted individually for the MIDAS and ALPACA analyses. Instabilities in the muon beam, HPGe detectors, electronics including the test pulser, or the DAQ lead to unusable data. Their identification primarily uses logs written during the measurement campaign. Further data cleaning is retroactively applied in case instabilities emerge during offline analysis.

14.4.3 Quality cuts

While data cleaning acts on full chunks of data, quality cuts target individual events. The goal is to exclude unphysical or otherwise unusable events from further analysis.

Most of the excluded events are pile-ups, i.e. two pulses appearing too close in time within the same channel, such that pulses overlap. Pile-ups in HPGe channels are rejected since energy and arrival time resolution are severely hampered for those events. In practice, two classes of pile-ups can be distinguished, based on which of two close pulses trigger the DAQ. *In-trace* pile-ups are triggered on the first pulse, i.e. the second pulse appears within the time window dedicated for sampling or processing the first

pulse. Conversely, *pre-trace* pile-ups are triggered on the second pulse, which thus is distorted by the superimposed tail of the first pulse.

MIDAS analysis utilizes pile-up flags generated by the FADC. Both classes of pile-ups are recognized separately, using the window size required for energy reconstruction [20].

For the ALPACA analysis, quality cuts are based on information provided by the tier2 level [16]. They use e.g. the number of recognized pulses per trace or the spread of the baseline to identify pile-ups and are tuned using the ^{40}K background line. Overall, quality cuts show survival fractions of 75 % to 95 %.

14.4.4 Energy and efficiency calibration and line intensities

Energy end efficiency calibrations are performed individually per detector and analysis branch. Gamma lines from calibration sources and muonic X-rays are used for energy calibration, and calibration functions are either linear or quadratic, depending on the performance.

Relative efficiencies are obtained from gamma lines of ^{152}Eu and mounic X-rays of a $^{\text{nat}}$Pb target probing the spectrum's low and high energy parts, respectively. For HPGe detector data in ALPACA, the following polynomial model is used, which is based on [21]:

$$\epsilon(E) = \frac{1}{E} \cdot \sum_i C_i \ln(E)^i \tag{14.2}$$

The order of the polynomial is chosen to minimize the χ^2 over degrees of freedom, individually for each detector [13].

The intensities of spectral lines are obtained using the peak model described in [22]. The peak is modeled as the sum of a Gaussian function and a tail towards lower energies. The background is accounted for by both a polynomial and a step function (if required).

14.4.5 Event classification

Events are classified according to the time correlation between the gamma detection and any muon stop signal, reconstructed by the counters [3, 13]. In the case of *correlated* events, the separation between muon stop and gamma arrival is less than a few microseconds, while other events are referred to as *uncorrelated*. Correlated events are further subdivided into *prompt* and *delayed* events. Prompt events show a separation lower

than the detectors' time resolution and are dominated by muonic X-rays. Delayed events exhibit a longer time separation and contain mostly gamma radiation following OMC. Thus, they are of primary interest since total and partial capture rates are extracted from their distribution.

14.4.6 Performance parameters

Several performance parameters are crucial for MONUMENT to achieve its physics goals. They are evaluated in dedicated studies, presented in [13] and compiled in the following.

Sufficient energy resolution of the HPGe detectors is required for resolving and identifying spectral lines. The resolution of several lines was studied, separated by the detector, DAQ system, and target. The results are shown in table 16.1 in section 16.1, which elaborates on the advantage in energy resolution gained by ALPACA. In short, BEGe detectors show better energy resolution than semi-coaxial detectors, and ALPACA's energy resolution surpasses the one of MIDAS.

Sufficient time resolution is required to reconstruct the lifetime of captured muons. Energy-dependent time resolution is observed, with lower-energy events having worse time resolution, as shown in figure 16.1. Furthermore, this effect changes between detector types. Thus, analyzing total capture rates requires obtaining the time resolution separately per energy region and detector [13].

It is further essential to estimate the time stability of reconstructed gamma lines. Multiple effects can influence the position of gamma lines, such as instabilities of the HPGe detectors, the electronics, or the DAQ. Stable conditions are verified by investigating several high-intensity gamma lines, with the 511 keV one being of particular interest since it exists for both enriched targets used [13].

An elaborate study of the livetime of the ALPACA system was done to characterize this new DAQ system. Details of this study are presented in section 16.3. A high dead time was observed, which lowered the livetime of measurements with enriched targets to around 20 %.

Another study analyzed the trigger rates of the four counters, both individually and in different coincidence setups [13]. It is observed that the baseline muon-stop condition $\overline{C_0} \wedge C_1 \wedge C_2 \wedge \overline{C_3}$ removes an unfeasibly high amount of data. A high number of counts in C_3 is responsible, hence, the current analysis uses a reduced condition: $\overline{C_0} \wedge C_1 \wedge C_2$.

This trigger condition leads to a fraction of random coincidences of $< 1\,\%$ [13]. Since the number of random coincidences can be lowered to around $\approx 0.5\,\%$ by using $\overline{C_0} \wedge C_1 \wedge C_2 \wedge \overline{C_3}$, it remains important to render this condition usable. This requires investigating the spectrum of C_3, which is not fully understood yet and motivated the change of the scintillator used for C_3 in the last campaign.

References

[1] V. Egorov *et al.*, "μCR42β: Muon capture rates for double-beta decay," *Czechoslovak Journal of Physics*, vol. 56, no. 5, pp. 453–457, 2006, ISSN: 0011-4626. DOI: 10.1007/s10582-006-0108-4.

[2] D. Zinatulina, V. Brudanin, V. Egorov, M. Shirchenko, and N. Rumyantseva, "Ordinary muon capture (OMC) studies by means of γ-spectroscopy," *AIP Conference Proceedings*, vol. 1894, no. 1, p. 020 028, 2017, ISSN: 0094-243X. DOI: 10.1063/1.5007653.

[3] D. Zinatulina *et al.*, "Ordinary muon capture studies for the matrix elements in $\beta\beta$ decay," *Physical Review C*, vol. 99, no. 2, p. 024 327, 2019, ISSN: 2469-9985. DOI: 10.1103/PhysRevC.99.024327.

[4] G. R. Araujo *et al.*, "OMC4DBD: ordinary muon capture as a probe of properties of double-beta decay processes," *BVR 53: Progress Report R-20-01.1*, 2022.

[5] G. R. Araujo *et al.*, "OMC4DBD: ordinary muon capture as a probe of properties of double-beta decay processes," *BVR 54: Progress Report R-20-01.1*, 2023.

[6] H. Ejiri, "Nuclear spin isospin responses for low-energy neutrinos," *Physics Reports*, vol. 338, no. 3, pp. 265–351, 2000, ISSN: 0370-1573. DOI: 10.1016/S0370-1573(00)00044-2.

[7] L. Jokiniemi, J. Suhonen, H. Ejiri, and I. Hashim, "Pinning down the strength function for ordinary muon capture on 100Mo," *Physics Letters B*, vol. 794, pp. 143–147, 2019, ISSN: 0370-2693. DOI: 10.1016/j.physletb.2019.05.037.

[8] J. M. Yao, B. Bally, J. Engel, R. Wirth, T. R. Rodríguez, and H. Hergert, "*AbInitio* Treatment of Collective Correlations and the Neutrinoless Double Beta Decay of ^{48}Ca," *Phys. Rev. Lett.*, vol. 124, no. 23, p. 232 501, 2020. DOI: 10.1103/PhysRevLett.124.232501. arXiv: 1908.05424 [nucl-th].

[9] A. Belley, C. G. Payne, S. R. Stroberg, T. Miyagi, and J. D. Holt, "*AbInitio* Neutrinoless Double-Beta Decay Matrix Elements for ^{48}Ca , ^{76}Ge , and ^{82}Se," *Phys. Rev. Lett.*, vol. 126, no. 4, p. 042 502, 2021. DOI: 10.1103/PhysRevLett.126.042502. arXiv: 2008.06588 [nucl-th].

[10] S. Novario *et al.*, "Coupled-Cluster Calculations of Neutrinoless Double-β Decay in ^{48}Ca," *Phys. Rev. Lett.*, vol. 126, no. 18, p. 182 502, 2021. DOI: 10.1103/PhysRevLett.126.182502. arXiv: 2008.09696 [nucl-th].

[11] A. Belley *et al.*, "Ab initio uncertainty quantification of neutrinoless double-beta decay in ^{76}Ge," 2023. arXiv: 2308.15634 [nucl-th].

[12] R. W. Huff, "Decay rate of bound muons," *Annals of Physics*, vol. 16, no. 2, pp. 288–317, 1961, ISSN: 0003-4916. DOI: 10.1016/0003-4916(61)90039-2.

[13] G. R. Araujo *et al.*, "The MONUMENT Experiment: Ordinary Muon Capture studies for $0\nu\beta\beta$ decay," 2024. arXiv: 2404.12686 [nucl-ex].

[14] Zinatulina, Daniya *et al.*, "Electronic catalogue of muonic X-rays," *EPJ Web Conf.*, vol. 177, p. 03 006, 2018. DOI: 10.1051/epjconf/201817703006.

[15] E. Bossio, "Beyond the Standard Model physics searches with double-beta decays," Ph.D. dissertation, Munich, Tech. U., 2022.

[16] E. Mondragon, "thesis in preparation," Ph.D. dissertation, Munich, Tech. U.

[17] M. Agostini, L. Pandola, P. Zavarise, and O. Volynets, "GELATIO: A General framework for modular digital analysis of high-purity Ge detector signals," *JINST*, vol. 6, P08013, 2011. DOI: 10.1088/1748-0221/6/08/P08013. arXiv: 1106.1780 [physics.data-an].

[18] R. Brun and F. Rademakers, "ROOT: An object oriented data analysis framework," *Nucl. Instrum. Meth. A*, vol. 389, pp. 81–86, 1997. DOI: 10.1016/S0168-9002(97)00048-X.

[19] M. Agostini *et al.*, "The MGDO software library for data analysis in Ge neutrinoless double-beta decay experiments," *J. Phys. Conf. Ser.*, vol. 375, p. 042 027, 2012. DOI: 10.1088/1742-6596/375/1/042027. arXiv: 1111.7260 [physics.data-an].

[20] Struck Innovative Systeme GmbH, "SIS3316 16 Channel VME Digitizer: User Manual," 2018.

[21] I. A. Alnour, H. Wagiran, N. Ibrahim, S. Hamzah, W. B. Siong, and M. S. Elias, "New approach for calibration the efficiency of HpGe detectors," *AIP Conference Proceedings*, vol. 1584, no. 1, pp. 38–44, 2014. DOI: 10.1063/1.4866101. eprint: https://pubs.aip.org/aip/acp/article-pdf/1584/1/38/11739317/38_1_online.pdf.

[22] M. Agostini *et al.*, "Calibration of the Gerda experiment," *Eur. Phys. J. C*, vol. 81, no. 8, p. 682, 2021. DOI: 10.1140/epjc/s10052-021-09403-2. arXiv: 2103.13777 [physics.ins-det].

Chapter 15

ALPACA: The new DAQ system for MONUMENT

MONUMENT is an OMC experiment, and its primary goal is giving input to nuclear theory of $0\nu\beta\beta$ decay. A description of the entire experiment is given in the previous chapter, introducing two DAQ systems working mainly in parallel: While MIDAS was already used in predecessors of MONUMENT and represents the state of the art, the novel ALPACA system was applied for the first time. Since the design, implementation, and application of ALPACA is part of this dissertation work, it is described in detail and compared to MIDAS in the present chapter. The following chapter works out the performance and challenges of ALPACA.

15.1 Contemporary MIDAS DAQ system

MIDAS (Maximum Integrated Data Acquisition System) is a DAQ system developed at PSI and TRIUMF [1]. It is applied in numerous experiments, including DEAP-3600 [2] and MONUMENT [3]. Its flexible implementation and support for many data acquisition systems via all standard data transfer interfaces enable various applications.

MIDAS was already successfully used by predecessor experiments of MONUMENT at PSI and hence chosen to be used in MONUMENT as well. There, MIDAS reads out several systems in parallel and provides primary physics data together with a context of monitoring information.

The main data stream originates from SIS3316-250 FADC cards[1], where the signals

[1]This FADC variant has a maximum sampling frequency of 250 MHz and a resolution of 14 bits.

from the HPGe detectors and counters arrive. The FADCs are configured to trigger on pulses individually for each channel. Energy and arrival time are computed by online processing filters and algorithms, which are implemented on field-programmable gate arrays (FPGAs) on the FADC cards. Raw waveforms are not stored, except for small traces at the onset of HPGe pulses, which can be used to enhance the time resolution offline.

While offline tuning of most observables is impossible in this approach, data throughput and disk space usage are heavily reduced. Furthermore, online processing provides observables immediately, which is crucial for monitoring the experiment, especially during beam-tuning operations.

15.2 Motivation and readout scheme

15.2.1 Advantages from a second DAQ system

While the unique features of MIDAS obligate its application in MONUMENT, the addition of another DAQ system was decided for. It is referred to as ALPACA (Adapted LLAMA Program for Accelerator Applications), since it is based on the DAQ system of LLAMA and continues its development further. ALPACA receives signals from the main detectors (i.e. HPGe detectors and counters) in parallel to MIDAS.

Two main aspects motivate the introduction of ALPACA:

- The use of offline processing allows fine-tuning the energy and arrival time reconstruction, as well as other algorithms, after the measurement campaign. This avoids the strong time constraints during the campaign and allows tuning and benchmarking the data processing with plenty of acquired data.
- ALPACA's trigger scheme records counter pulses appearing in arbitrary proximity within the same channel. This helps to prevent systematic biases when correlating HPGe pulses to counter pulses.

It is important to stress the synergy between both DAQ systems. MIDAS is crucial for providing both online monitoring and live information for beam tuning. It incorporates vital systems and stores slow-control information important for data cleaning. ALPACA's higher energy resolution can aid in resolving and identifying close spectral lines. Having

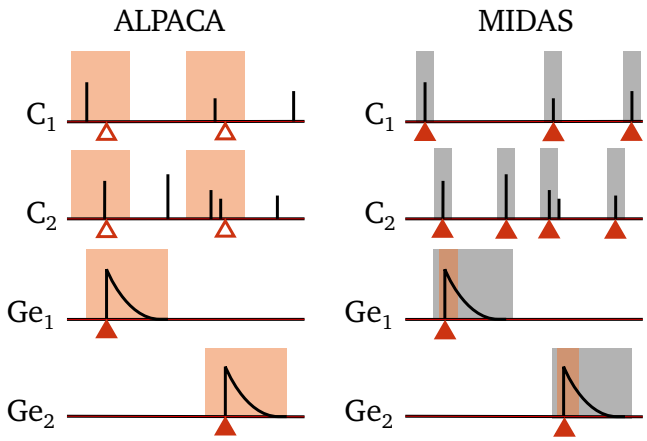

Figure 15.1: Comparison of the trigger schemes used by the ALPACA and MIDAS DAQ systems. Example traces are shown for two counters ($C_{1,2}$) and two HPGe detectors ($Ge_{1,2}$). Filled triangles denote primary triggers, while empty ones represent induced triggers. Orange shaded areas are stored to disk (offline analysis), while gray areas are used for online processing. See text for details.

two DAQ systems target the core detectors greatly boosts the experiment's reliability. The further processing and analysis chains are kept independent, with separate infrastructure, teams, and software. This facilitates cross-checks on all levels of the analysis.

Further, ALPACA's offline analysis and trigger scheme follows the approach used in GERDA, i.e. are developed for a low-rate environment. Its usage in a beam experiment with high trigger rates in all channels constitutes a novel field of application; hence, it is regarded as experimental. Thus, the MONUMENT campaigns provide useful information about ALPACA's stability and performance. This is paramount for future applications of ALPACA or similar systems, which become increasingly feasible due to recent hardware developments. Higher data transfer speeds and more storage capacities render DAQ systems with offline analysis much more practical.

15.2.2 Trigger scheme

Figure 15.1 compares the trigger and readout schemes of ALPACA and MIDAS. Two example waveforms for counters ($C_{1,2}$) and HPGe detectors ($Ge_{1,2}$) are presented each. ALPACA triggers on individual pulses arriving from HPGe detectors (primary triggers,

filled triangles). The pulses are then stored for later offline analysis in shape of waveforms (orange shaded boxes). Additionally, all[2] counter channels are triggered simultaneously (induced trigger, empty triangles), and waveforms are also recorded for them.

Conversely, MIDAS triggers on all individual pulses, both for counters and for HPGe detectors. Triggering pulses are processed online, using waveform regions marked with gray shaded boxes in the figure. The sketch shows that single triggers are missed if they are too close within the same channel. Orange shaded boxes denote the part of the HPGe detectors' waveforms stored to disk, which encompasses the leading edge only.

ALPACA defers counter pulse finding to offline analysis, offering more comprehensive and fine-tuned tools to identify close pulses and pile-ups. This helps to reduce biases caused by mismatching a potential muon signal with an HPGe hit. However, this comes at the cost of recording full waveforms for all counters upon any HPGe pulse. Additionally, ALPACA requires long HPGe waveforms to enable offline energy reconstruction. Both effects result in the amount of data generated by the ALPACA FADC vastly surpassing the one of MIDAS.

15.2.3 Waveform setup

Elaborate tuning of the recorded waveforms allows for reducing the data load created by ALPACA. Since certain waveform parts require different sampling rates, two traces are recorded per waveform, analogous to the approach used by GERDA [4]. The *low-frequency trace* covers the waveform's entire duration and contains averaged samples, i.e. its sample frequency is a tunable fraction of the clock frequency. Conversely, the *high-frequency* trace covers only part of the waveform but uses the total clock frequency.

Length, location (relative to the trigger), and sampling frequencies of all traces were tuned individually for HPGe detectors and counters before the first MONUMENT campaign. The waveform setup is illustrated by an example event shown in figure 15.2. The low-frequency trace of an HPGe channel (blue dashed) spans around 20 µs and has a sampling rate of approximately 15 MHz, optimized for energy resolution in a dedicated study [5]. An additional high-frequency trace of 2 µs and 125 MHz (blue continuous) is centered around the pulse's onset to boost the time resolution.

Counter channels feature a 2 µs and 125 MHz high-frequency trace. It mostly precedes

[2] While MONUMENT features four counters, only two are shown in the example for simplicity.

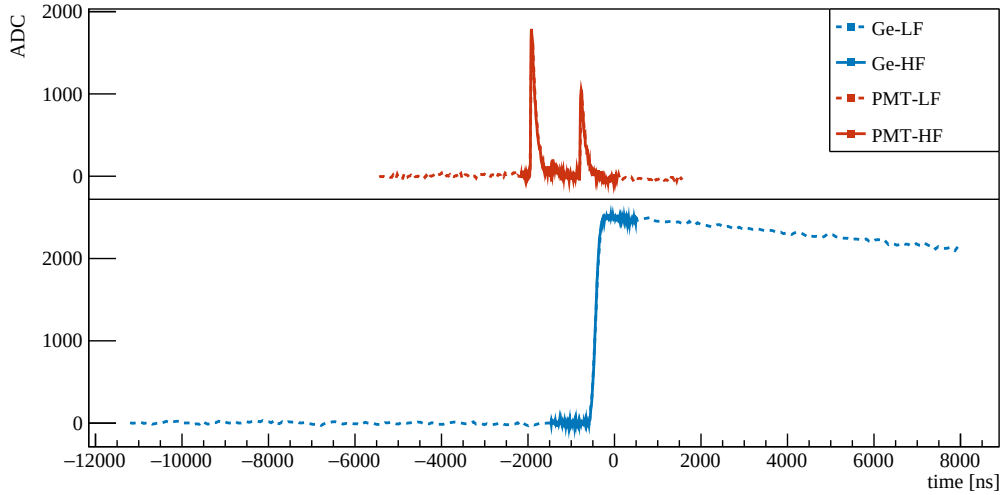

Figure 15.2: Waveforms of one HPGe (blue) and one counter (PMT, red) channel of an example event taken during MONUMENT's 2021 campaign. Both waveforms are composed of two traces: low-frequency (dashed) and high-frequency (continuous), which provide different sampling rates and extents, offering a good compromise between size and physics performance. The FADC's trigger is located at time = 0. See text for details.

the location of the HPGe pulse's onset since the counters detect traveling muons before muonic x-rays or gammas are released. While most correlated muon signals are expected to be within this window, an additional 7 µs and 31 MHz low-frequency trace is recorded to extend the available range. The example shows the recorded waveform for C_1 for the same event (red).

15.3 Hardware components

The choice of two-trace waveforms requires the 125-MHz variant of the SIS3316 FADC, which provides those by performing on-board down-sampling. This feature is unavailable for the 250-MHz variant used by MIDAS. However, it is crucial for ALPACA since it reduces the data throughput already before it passes the Ethernet interface between the FADC and the readout server. The data throughput of the Ethernet interface was measured to maximally reach 600 Mbit/s.

The high expected data rates and the computationally demanding offline analysis

require a dedicated server to perform readout and processing. The server provides multiple Ethernet interfaces, of which one is exclusively used to establish a point-to-point connection to the FADC, maximizing stability and transfer speed. Hard drives in RAID-6 configuration[3] provide fast and fail-safe storage with a total size of 160 TB. The size was chosen to sustain three weeks of constant data-taking with the maximum Ethernet interface throughput.

15.4 Software implementation

15.4.1 ALPACA's core: llamaDAQ - overview and applications

The core of the ALPACA DAQ software system is an executable program referred to as *llamaDAQ*. It is originally developed as part of the LLAMA system, hence the name. llamaDAQ is dedicated to SIS3316 FADCs and can access almost all its features. Its flexible interface and multiple available output file formats enable its application in several experiments using the mentioned FADC. Apart from LLAMA and MONUMENT, it is also used in test setups of CRESST [6] and NUCLEUS [7] at TUM.

15.4.2 Implementation and features of llamaDAQ

llamaDAQ is written in C++, and its object-oriented and modular design facilitates adaptions and enhancements. This programming language was chosen since execution speed is paramount. Low-level classes for accessing the Ethernet interface and controlling the actual data transfer are provided by Struck Innovative Systeme[4], while the majority of the software is written in the scope of this dissertation work. The latter encompasses the following features:

- Several mechanisms are implemented to improve stability, including automated restarts of the Ethernet interface on both the server and FADC side.
- Soft-termination mechanisms are implemented, which write the remaining buffer and close the current file upon an external interrupt, necessary for stopping runs

[3] RAID (redundant array of independent disks) combines individual hard drives to improve access speed and fail-safety. RAID-6 provides sufficient read and write performance while being able to sustain the failure of two disks without data loss.

[4] Struck Innovative Systeme GmbH is the manufacturer of SIS3316 FADCs.

by hand.

- A command-line interface provides interactive control over configuration and readout of the FADC and enables macros to automate entire data-taking runs.
- llamaDAQ supports event-building for output file formats, which require the combination of all simultaneously triggering channels into events. The FADC transfers data clustered by channels, making event-building necessary for those output formats, including MGDO.

15.4.3 Necessary enhancements for application in ALPACA

ALPACA's application in a beam experiment made several enhancements of llamaDAQ necessary. Since the data taking is more unstable and characterized by voluntary and involuntary interruptions, the soft-termination feature is implemented to facilitate immediate stops and fast re-starts of the DAQ. Further, the event building is improved, as the trigger scheme is a hybrid between a fully synchronous (all channels trigger jointly) and a fully asynchronous scheme. This requires the software to build events containing only a subset of recorded waveforms for each channel. Additionally, llamaDAQ faces high data throughput, heavily exceeding the traffic experienced in LLAMA. Thus, the throughput was enhanced by using large buffers at the input and output stage because large data chunks boost the performance of both Ethernet and hard disks.

For the 2021 measurement campaign, a simple Python wrapper was used, which detects a crashing or stalling program and re-starts llamaDAQ in those cases. Based on the experiences gained in this campaign, an improved Python program was implemented by D. Berger and used for the measurement campaign in 2022. It is composed of both a client and a server executable, which allow monitoring and controlling the DAQ via a graphical user interface installed on workstations in the beam hall's control room. This facilitates the shifting duties on-site regarding ALPACA[5].

15.4.4 Further developments

The performance of ALPACA during the 2021 campaign is evaluated in the upcoming chapter and has impacts on further developments. While the energy and time resolution

[5] MIDAS features an independent web-browser-based user-interface system.

of the system meet the requirements, the unexpectedly high deadtime discovered needs to be addressed. An important measure among the mitigation strategies, described in section 16.4, is the online evaluation of the current deadtime. Permanent knowledge of the deadtime is essential for taking immediate measures during the measurement campaign and limiting the data rate. To this end, algorithms can be implemented into the event building stage of llamaDAQ, which identify missing or incomplete events, as explained in the following chapter.

References

[1] S. Ritt, P. Amaudruz, and K. Olchanski, "The MIDAS data acquisition system," in *Proc. IEEE 10th Real Time Conf.*, 1997, pp. 309–312.

[2] T. Lindner and for DEAP-3600 collaboration, "DEAP-3600 Data Acquisition System," *Journal of Physics: Conference Series*, vol. 664, no. 8, p. 082 026, 2015. DOI: 10.1088/1742-6596/664/8/082026.

[3] G. R. Araujo *et al.*, "The MONUMENT Experiment: Ordinary Muon Capture studies for $0\nu\beta\beta$ decay," 2024. arXiv: 2404.12686 [nucl-ex].

[4] M. Agostini, L. Pandola, and P. Zavarise, "Off-line data processing and analysis for the GERDA experiment," *J. Phys. Conf. Ser.*, vol. 368, p. 012 047, 2012. DOI: 10.1088/1742-6596/368/1/012047. arXiv: 1111.3582 [physics.data-an].

[5] E. Bossio, "Beyond the Standard Model physics searches with double-beta decays," Ph.D. dissertation, Munich, Tech. U., 2022.

[6] A. K. H. Langenkämper, "Characterisation of the Muon-Induced Neutron Background with a LiF Cryogenic Detector," Ph.D. dissertation, Technische Universität München, 2023, p. 178.

[7] A. Erhart, V. Wagner, A. Wex, C. Goupy, D. Lhuillier, *et al.*, "A Plastic Scintillation Muon Veto for Sub-Kelvin Temperatures,"

Chapter 16

Physics performance and challenges of ALPACA

ALPACA is a DAQ system employed in MONUMENT, and its working principle, hardware, and software components are explained in chapter 15. The trigger and readout scheme of ALPACA follows the one of GERDA, which was a low-background and low-rate experiment. The application of this system in an OMC experiment is regarded as experimental, and an analysis of its performance is crucial for assessing its maturity and usability.

This chapter evaluates ALPACA's main performance parameters by compiling results of energy and time resolution presented in [1], and further details on the analysis of the livetime reduction faced by ALPACA during the 2021 campaign. This chapter concludes the MONUMENT part of this dissertation and contains an outlook regarding possible enhancements of ALPACA for future campaigns.

16.1 Energy resolution

Sufficient energy resolution is crucial for identifying and separating spectral lines and thus directly affects MONUMENT's physics performance. ALPACA offers the possibility to tune the energy reconstruction offline and hence is expected to surpass the energy resolution achieved by the MIDAS analysis branch.

This advantage is verified in a dedicated study, in which the energy resolution is determined per detector for both analysis branches using the ^{40}K background peak. Table 16.1 shows examples of FWHM values for data takings of both enriched targets, separated

by HPGe[1] detector and DAQ system. The table is taken from [1], and the values are provided by D. Bajpai. The BEGe detector Ge 2 exhibits superior energy resolution compared to the semi-coaxial detector Ge 4. Concerning DAQ systems, it confirms that ALPACA's energy resolution surpasses the one of MIDAS.

Table 16.1: Energy resolution (FWHM in keV) of the ^{40}K-line for two example detectors using both MIDAS and ALPACA data for both enriched targets of the 2021 campaign. The BEGe's energy resolution is superior to the semi-coaxial detector. Also, ALPACA shows a better resolution than MIDAS, attributed to offline energy reconstruction. Taken from [1] with data provided by D. Bajpai.

	Ge 2 (BEGe)		Ge 4 (semi-coaxial)	
Runs	MIDAS	ALPACA	MIDAS	ALPACA
^{136}Ba	2.35 ± 0.02	2.31 ± 0.02	4.12 ± 0.02	3.62 ± 0.01
^{76}Se	2.29 ± 0.02	2.15 ± 0.03	3.87 ± 0.02	3.40 ± 0.02

16.2 Time resolution

The time resolution of MONUMENT needs to be sufficient to resolve the lifetime of stopped muons, which is $\mathcal{O}(100)$ ns for ^{76}Se [2] and ^{136}Ba [3]. The calculation uses the arrival time of a muon t_μ as a start signal and the arrival time of a decay gamma t_γ as a stop signal, obtained from the counters and HPGe detectors, respectively. The lifetime is then extracted via $t_\gamma - t_\mu$.

Muonic x-rays provide a perfect benchmark for the system's time resolution because they are also detected by HPGe detectors, share the same energy region as gamma lines, and are emitted virtually immediately after the muon stop ($\mathcal{O}(1)$ ps [4]). The time resolution of ALPACA was studied separately for each HPGe detector and using several muonic x-ray lines of selenium by E. Bossio [1]. Figure 16.1 shows time difference spectra for a semi-coaxial detector using different muonic x-ray lines. The resolution deteriorates for lower energies, which can be attributed to the worse performance of algorithms finding the onset of low-energy HPGe pulses. This effect is presumably caused

[1] The labeling of HPGe detectors was introduced in section 14.4.1.

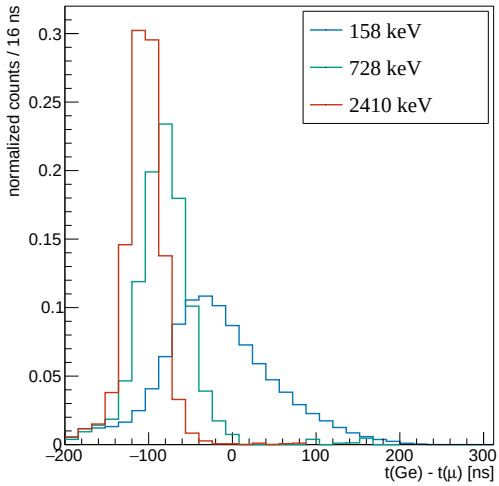

Figure 16.1: Time difference spectra $t_{Ge} - t_{\mu}$ for different muonic x-ray lines for Ge 4 (semi-coaxial). At lower energies, the time resolution deteriorates, demonstrating the HPGe detector's dominating influence on the time resolution. Drawn according to [1] with data provided by E. Bossio.

by intrinsic properties of the HPGe detectors and electronic noise. Thus, ALPACA's time resolution needs no improvement since it has no leading effect on the time resolution of the experiment.

16.3 DAQ livetime

The livetime of ALPACA constitutes one of its essential performance parameters due to its direct influence on the efficiency of the entire experiment and, thus, on the statistical uncertainties of the final results. Commonly, the livetime of a DAQ system is defined as the share of the entire runtime, in which valid triggers lead to successful processing or recording of signals. Conversely, no triggers are processed during deadtime of the DAQ. The amount of remaining livetime per elapsed runtime is referred to as *livetime fraction* in the following.

This section evaluates different effects causing a reduction of ALPACA's livetime during the 2021 measurement campaign. It concludes with time-resolved results on the livetime reduction of the entire system.

The data taking used two targets (^{136}Ba and ^{76}Se) and is separated into three phases: A first measurement with the ^{136}Ba target (^{136}Ba-I), followed one with the ^{76}Se target, and then another ^{136}Ba phase (^{136}Ba-II). Livetime results are evaluated in the context of these phases since the target material itself and the adjustments of detectors or electronics happening in conjunction with the exchanges are expected to impact the results.

16.3.1 Prolonged gaps in the DAQ livetime

Hardware features causing gaps

In recorded data, several extended periods were observed in which the livetime fraction equals zero, i.e. no events were recorded at all. They are called *gaps* in the following and arise from features of the DAQ hardware components explained here.

As described in section 15.3, ALPACA contains a Struck SIS3316-125 FADC, connected via Ethernet to a dedicated readout server. Digitized data is first sampled from the analog signals in the shape of waveforms by the FADC, and then stored in its memory. The llamaDAQ program executed on the server simultaneously demands the transfer of sampled data from the FADC to a random-access memory (RAM) buffer on the server. The contents of the server's buffer are periodically stored in consecutive files.

In more detail, the FADC's memory is separated into two banks. Based on that, the firmware of the FADC's FPGAs and llamaDAQ implement a two-buffer scheme. One bank receives sampled data and is called *active*, while the content of the other (*passive*) bank is concurrently transmitted to the server. Each bank allocates 16 buffers sized 64 MB, each dedicated to a single input channel. These channel buffers are filled individually with digitized waveforms. A *bank swap* changes the roles of active and passive banks, and is issued by llamaDAQ once at least a small amount of sampled data is accumulated and the transfer from the passive bank is complete. All channel buffers are affected by a bank swap at the same time. Data transmission from the new passive bank commences immediately after the bank swap.

An issue exists if data is acquired with a rate surpassing the maximum throughput of the Ethernet interface, measured as roughly 600 Mbit/s. Then, the saturation of some channel buffers happens before all data from the passive bank is transferred. Those channels show deadtime until the completed transmission triggers the next bank swap.

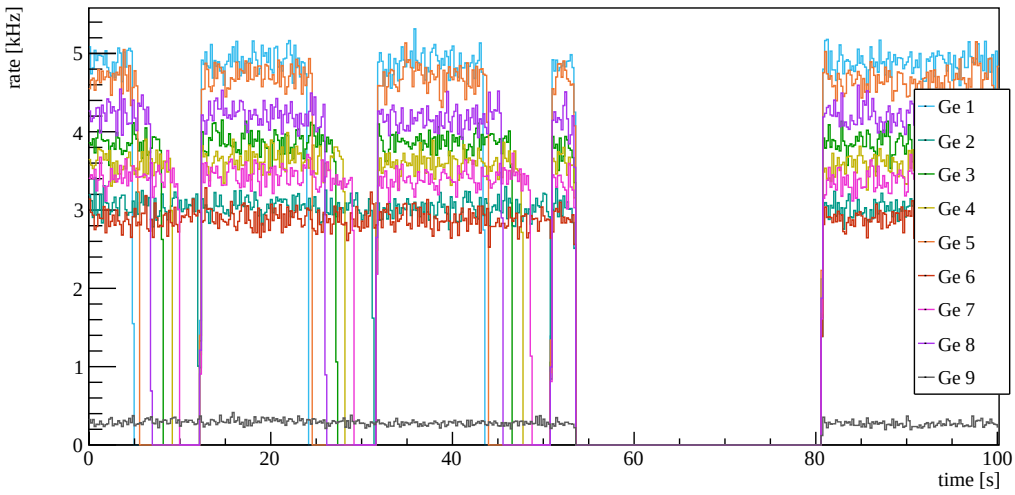

Figure 16.2: Time-dependent rate of triggered events per HPGe channel. Ge 1 to Ge 8 surround the target cell, while Ge 9 is situated further away. Three smaller gaps are visible in the left part, where the DAQ memory buffers of individual channels filled up before they were reset for all channels simultaneously by a bank swap. While these three gaps are within one file, the big gap is located between two files, presumably caused by the operating system finishing writing to the file before closing it.

Intrafile and interfile gaps in MONUMENT data

To give an illustrative example, figure 16.2 shows the rate of recorded events per HPGe channel for a part of the ^{76}Se data taking. Three small gaps are visible in the first part of the plot, which are caused by the deadtime-producing process mentioned previously. Detectors showing a higher rate (e.g. Ge 1 and Ge 4) fill up their dedicated buffers faster than lower-rate detectors (e.g. Ge 7). HPGe detectors showing even lower rates (e.g. Ge 6) do not exhibit gaps in this example, as their channel buffers never get consumed entirely. This is especially true for Ge 9, which is not part of the array surrounding the target cell but is placed around one meter away[2].

Additionally, a large gap appears in the plot, which spans from the end of one file to the beginning of the succeeding file. Presumably, the server finishes storing the preceding file on the hard drive during this time frame, thus suspending the program. As the program

[2]The purpose of Ge 9 is to estimate random background in medium proximity to the beam line. It was applied in the 2021 campaign only.

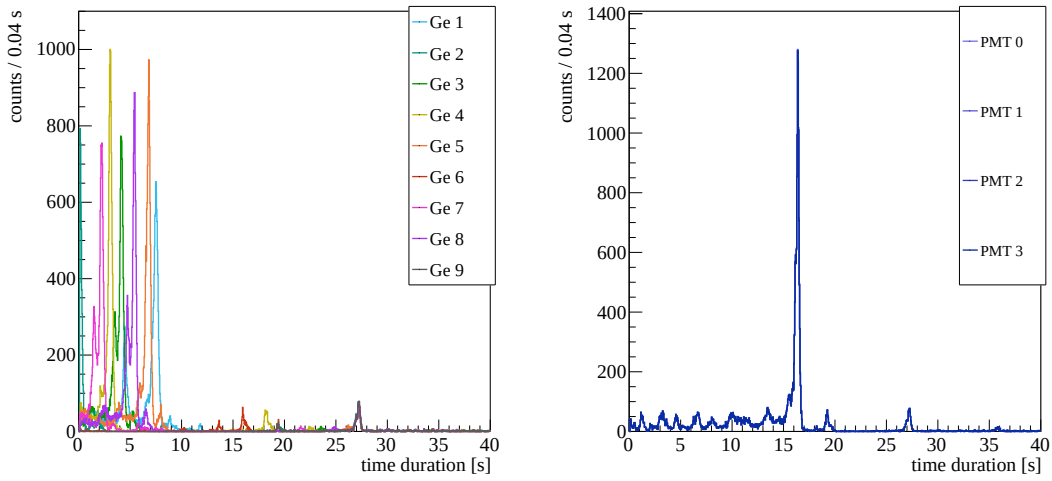

(a) (b)

Figure 16.3: Gap sizes present in ^{76}Se data for (a) HPGe and (b) counter channels. Smaller-sized gaps within files are most frequent, while rarer gaps between files are common to all channels and are around 27 s wide.

waits for the creation of a new file to continue data taking, all channels show identical gaps in this case. To distinguish both types of gaps, the ones present within individual files are called *intrafile* gaps, while the ones between two consecutive files are called *interfile* gaps.

A dedicated algorithm was developed[3], which calculates the livetime reduction due to both types of gaps time-resolved and for every detector channel. The implementation investigates differences in timestamps of consecutive events and stores them for further analysis in case a threshold of 100 ms is exceeded[4]. Time differences above 60 s are rejected since manual interruptions of the data taking usually cause them. Figure 16.3 shows histograms of gap sizes present in ^{76}Se data for all HPGe channels (a) and counters (b). The most frequent gap sizes correspond to the intrafile type, which differ among HPGe channels while being the same size for counters. Intrafile gaps of counters are larger than of HPGes detectors since the counters' trigger rates are higher, and thus, exhaustion of their buffers takes place earlier, (see section 16.3.4). Interfile gaps, spanning around 27 s, appear equally sized in all channels (both HPGe detectors and counters).

[3]The algorithm operates on the tier2 level; see section 14.3.2.
[4]Since gaps are typically in the timescale of seconds, this condition holds for almost all of them.

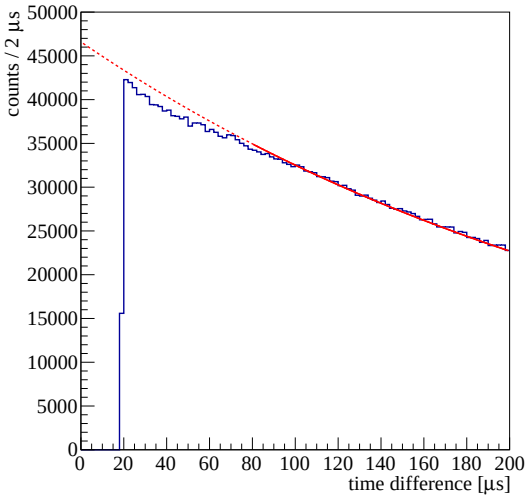

Figure 16.4: Histogram of time differences between each test pulser signal and the closest arbitrary pulse preceding it in the same HPGe channel. For time differences exceeding around 20 µs, the distribution is exponential (red curve), corresponding to a vanishing correlation between both signals. Smaller time differences are not recorded, as the second pulse would fall within the event window of the first (see text).

16.3.2 In-trace pileup

In-trace pileups also cause deadtime in the data taking of ALPACA. While the FADC processes a signal, it blocks any potential trigger in the same channel. Each processed signal thus creates deadtime to an extent defined by the *event window*. Its size is determined by the duration of the most time-consuming process: online processing or sampling. For ALPACA, the event windows are driven by the sizes of the low-frequency traces, which are sized 19.2 µs and 7.04 µs for HPGe channels and counters, respectively.

This behavior becomes apparent when observing histograms of the time differences of consecutive pulses recorded in the same channel[5]. Figure 16.4 shows this plot for ^{76}Se data using Ge 1. Only event pairs are selected, in which the second event originates from the test pulser. The test pulser is a hardware device injecting pulses into HPGe channels, using a fixed frequency of 30 Hz. This condition renders both pulses in a pair fully independent of each other[6]. Thus, the conditions of a homogeneous Poisson point

[5]This analysis is performed on the tier3 level

[6]This holds as long for time differences smaller than the time difference between two consecutive test

process are met. Hence, distances between both pulses in these pairs are exponential random variables [5]. The plot shows a fit with an exponential function in the range from 80 µs to 1000 µs (continuous) and extrapolated to 0 (dashed).

No pairs are recorded with a difference below around 20 µs, due to the event window of the first trigger blocking the ability to trigger on the second pulse. The livetime reduction caused by in-trace pileups is calculated as the difference between the integrals of the fit function and the histogram.

16.3.3 Single channel livetimes

Livetimes observed in individual ALPACA channels result from gaps and deadtimes introduced by in-trace pileups. The livetimes of each effect can be derived separately using the methods described earlier. Effective livetimes of single channels can be obtained by multiplying the livetimes from both effects. This approach is called *gap analysis* in the following.

However, an alternative approach using test pulser events is preferred due to being less model dependent[7]. There, the number of recorded test pulses per channel and file is counted and divided by the calculated number of test pulses generated within each file's duration[8]. The livetime reduction due to in-trace pileups and intrafile gaps is included intrinsically. Additionally, the evaluation of the livetime reduction due to interfile gaps is implemented into this analysis using the files' initial timestamps and durations[9]. This method is named *test pulser analysis*.

Figure 16.5a shows time-resolved livetime fractions for HPGe channels during ^{136}Ba-II, taking only gaps into account. Ge 1 shows a reduced livetime compared to other channels, explained by a strongly increased trigger rate. Small time frames showing enhanced livetime fractions appear as spikes and are attributed to a temporarily weaker or vanishing muon beam. When additionally taking livetime reduction due to in-trace pileups into account, livetime fractions get reduced slightly, as shown in figure 16.5b.

Both results originate from two independent analysis procedures: the first is from the gap analysis, while the latter is derived using the test pulser analysis. A comparison yields

pulser events, which is around 33 ms

[7] This analysis is performed on the tier3 level

[8] Using the constant test pulser frequency of 30 Hz

[9] Analogous to the gap analysis, interfile gaps exceeding 60 s are neglected.

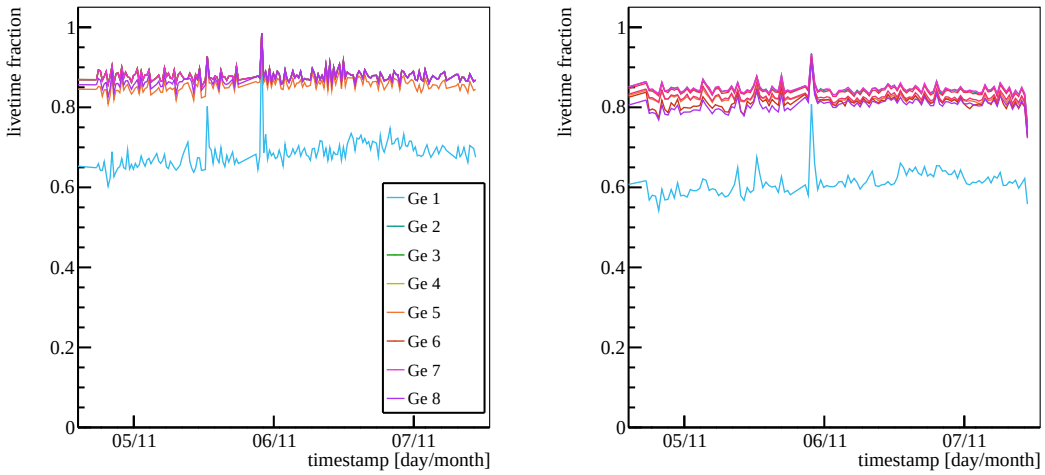

Figure 16.5: Time-resolved livetime fractions for ^{136}Ba-II including only gaps (a) and including also deadtimes introduced by in-trace pileups (b). Spikes in the livetime fractions correspond to a weaker or vanishing muon beam, reducing trigger rates in all DAQ channels and thus reducing deadtimes.

a valuable cross-check, validating both methods. Since in-trace pileups are intrinsically accounted for only in the test pulser analysis, results cannot be compared immediately. To solve this, the livetime reduction due to gaps only is calculated from the test pulser analysis result. The required livetime reduction due to in-trace pileups is obtained from the procedure described in section 16.3.2.

Figure 16.6 displays the livetime fractions only caused by gaps for individual HPGe channels. Results of the gap analysis are drawn in blue, while results of test pulser analysis (combined with in-trace pileup evaluation) are drawn in red. Both results agree, thus validating both branches of analysis.

16.3.4 Combined livetimes

The previous section described the livetime evaluation of single HPGe channels independent of the remaining system. However, the measurement principle of MONUMENT requires multiple channels to work in combination. Regarding ALPACA, the full performance of any HPGe channel depends on its ability to record its own waveform and to

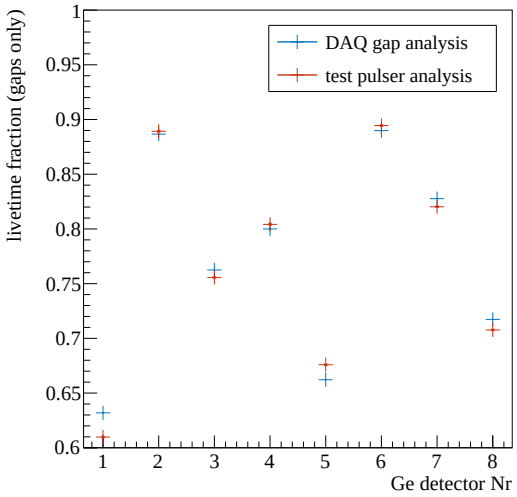

Figure 16.6: Comparison of livetime fractions caused by gaps in the DAQ livetime reconstructed using two different algorithms for part of the ^{76}Se data taking. The values calculated by the gap analysis are drawn in blue. Additionally, red data points denote values generated by the test pulser analysis. Since the latter intrinsically includes deadtimes caused by in-trace pileups, they are being corrected for using the in-trace pileup evaluation described in section 16.3.2.

successfully trigger all four counters once a valid trigger arrives. The term *combined livetime* is introduced in this context as the time, in which a given HPGe channel can process its own valid triggers and simultaneously record all four counters. By construction, it is always smaller or equal to the livetime of the single HPGe channel.

Combined livetimes are obtained from the test pulser analysis by additionally requiring the existence of waveforms of all four counters in recorded data. However, for both ^{136}Ba-I and the early part of the ^{76}Se data takings, the test pulser was not available for all channels, rendering this method unusable for these time frames.

Thus, an alternative approach is pursued in those cases. This analysis is based on the gap analysis, which does not depend on the test pulser. Livetime reduction due to in-trace pileups on the single HPGe channel is accounted for using the evaluation described in section 16.3.2, which is validated in the previous section[10]. Additionally, livetime losses

[10]Note that the in-trace pileup analysis shown previously demands the 2nd pulse to originate from the test pulser to ensure statistical independence of two consecutive pulses. This requirement has to be

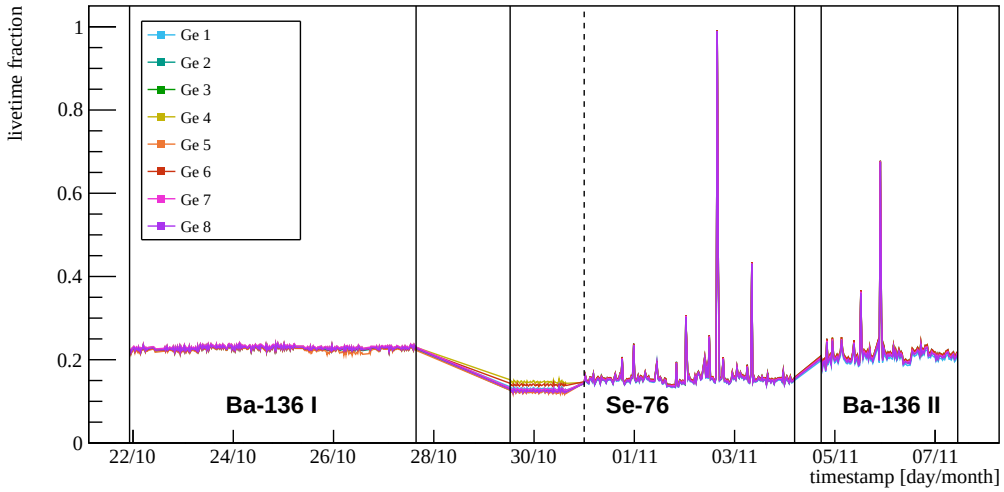

Figure 16.7: Time-resolved combined livetime fraction for all HPGe channels during the entire data-taking period employing enriched targets. The combined livetime fraction measures the performance of ALPACA, encompassing the livetime of single HPGe channels and the availability of all counters. The dashed line marks the time when the test pulser becomes fully operational. Results on either side are obtained with different analysis procedures, which are either dependent on (right) or independent of (left) the test pulser (see text).

caused by failing to record at least one counter waveform for a successfully triggered and processed HPGe pulse are calculated and included. Thus, combined livetimes can be obtained even for time frames lacking a fully functioning test pulser, extending the evaluated region to cover all runs using enriched targets[11].

Figure 16.7 shows time-resolved combined livetime fractions for each HPGe detector for the mentioned time frames. Vertical continuous lines mark borders of data-taking campaigns, while the dashed line indicates the first time point after which the test pulser becomes fully operational, and thus different analysis procedures are applied. Vertical spikes towards higher livetime fractions can be explained by irregular, short interruptions of the muon beam, greatly reducing the data rate and thus improving the livetime. No

dropped for time frames lacking a functioning test pulser, causing slight but inevitable distortions due to correlated events.

[11] Evaluation of combined livetimes for data takings using natural targets, lead targets, calibrations or background measurements are possible, but less important and thus not performed so far.

spikes are visible in the gap analysis part (preceding the dashed line) since the required in-trace pileup evaluation uses cumulative spectra, limiting the time resolution.

Overall, data takings with enriched targets show similar combined livetimes, which are substantially lower than the respective single detector livetimes. This stresses the dominant impact of the counter channels' deatime on ALPACA's overall performance. The trigger scheme provides an explanation: Every trigger signal generated by individual HPGe channels is routed to the counter channels. Thus, any counter channel accumulates the trigger rates of all HPGe channels, thus exceeding the trigger rate any single HPGe channel exhibits.

Table 16.2 compiles the livetimes in cumulative stages from gaps-only to combined performance, separated by data taking (^{76}Se, ^{136}Ba-I and ^{136}Ba-II). Combined livetime fractions for individual detectors during the same data taking are very similar and amount to around 16 % for ^{76}Se, 23 % for ^{136}Ba-I, and 22 % for ^{136}Ba-II.

16.4 Conclusions and outlook

ALPACA's performance during the first MONUMENT campaign in 2021 was evaluated. On the one hand, the data quality, especially the energy and time resolution capabilities, proved to be sufficient. The offline tuning possibilities render its energy resolution superior to the MIDAS DAQ system employed in parallel.

On the other hand, the unexpectedly low livetime fraction experienced constitutes a major challenge, limiting the statistical significance of the results. It is caused by an excessive trigger rate on all HPGe channels, leading to a massive data rate exceeding the throughput of the Ethernet interface between the FADC and the server. ALPACA's livetime fraction during the 2021 campaign was around 20 % for the complete system.

Mitigation is mandatory for further applications of this system. However, this proves challenging since a change of the trigger scheme or a departure from offline analysis would touch ALPACA's core operation principles. In the following, several approaches are compiled:

- A thorough testing campaign needs to reproduce the deadtime and provide the basis for further developments or mitigation strategies.
- Online tools have to be implemented into llamaDAQ, which detect and report high

deadtimes during runtime, allowing for last-minute adjustments during measurement campaigns.

- Re-evaluation of recorded waveform parameters can help to reduce the data throughput. Reducing the trace length of counter channels is possible but requires sample-specific tuning due to varying muon lifetimes.
- A possible introduction of a second FADC effectively splits the traffic between two Ethernet interfaces, doubling the available bandwidth.
- As a last resort, ALPACA might be set up to record only a subset of the available HPGe detectors.

While another application of ALPACA requires considerable efforts, it nonetheless keeps being an essential building block of new beam experiments due to the reasons explained in section 15.2.1. Though the livetime loss during the 2021 campaign is evaluated, its influence on the final analysis is yet unclear. It is now on the current analysis efforts to provide quantitative results on the remaining statistical power of the MONUMENT campaigns featuring ALPACA. In any case, ALPACA data allows valuable cross-checks, which profit the current analysis.

References

[1] G. R. Araujo *et al.*, "The MONUMENT Experiment: Ordinary Muon Capture studies for $0\nu\beta\beta$ decay," 2024. arXiv: 2404.12686 [nucl-ex].

[2] E. Bossio, "Determination of the total capture rate of ^{76}Se with ALPACA data," 2023, MONUMENT-internal draft.

[3] G. R. Araujo, "Advancing Neutrinoless Double Beta Decay Search with LEGEND and MONUMENT, and Exploring Passive Neutrino Detectors with PALEOCCENE," Ph.D. dissertation, Universität Zürich, 2023.

[4] D. Zinatulina *et al.*, "Ordinary muon capture studies for the matrix elements in $\beta\beta$ decay," *Physical Review C*, vol. 99, no. 2, p. 024 327, 2019, ISSN: 2469-9985. DOI: 10.1103/PhysRevC.99.024327.

[5] S. Ross, *Stochastic Processes* (Wiley series in probability and mathematical statistics). Wiley, 1996, ISBN: 9780471120629. [Online]. Available: https://books.google.de/books?id=ImUPAQAAMAAJ.

Table 16.2: Livetime of ALPACA during the individual data takings with enriched targets. "gaps" denotes livetime reduction due to gaps in the DAQ livetime only, "single" additionally accounts for in-trace pileups and "combined" measures the entire performance, also requiring the counters to successfully record waveforms (see text for details).

^{76}Se			
detector	gaps	single	combined
Ge 1	0.632	0.579	0.158
Ge 2	0.887	0.855	0.164
Ge 3	0.762	0.715	0.161
Ge 4	0.800	0.765	0.163
Ge 5	0.662	0.622	0.162
Ge 6	0.890	0.859	0.164
Ge 7	0.828	0.783	0.162
Ge 8	0.717	0.667	0.160

^{136}Ba-I			
detector	gaps	single	combined
Ge 1	0.879	0.806	0.227
Ge 2	0.879	0.825	0.226
Ge 3	0.880	0.810	0.229
Ge 4	0.880	0.816	0.230
Ge 5	0.875	0.784	0.224
Ge 6	0.880	0.823	0.227
Ge 7	0.880	0.819	0.231
Ge 8	0.880	0.807	0.228

^{136}Ba-II			
detector	gaps	single	combined
Ge 1	0.685	0.609	0.207
Ge 2	0.880	0.844	0.219
Ge 3	0.880	0.822	0.214
Ge 4	0.880	0.841	0.219
Ge 5	0.858	0.812	0.218
Ge 6	0.880	0.846	0.219
Ge 7	0.880	0.826	0.215
Ge 8	0.874	0.805	0.212

Part V

Synopsis

Chapter 17

Conclusions and outlook

The discovery of $0\nu\beta\beta$ decay - an unambiguous observation of lepton number non-conservation - would prove the Majorana nature of neutrinos, with far-reaching consequences for fundamental particle physics. LEGEND pursues the search for $0\nu\beta\beta$ decay using HPGe detectors enriched in ^{76}Ge. The detectors are deployed in scintillating LAr. This medium is transformed into a full-fledged detector using a light readout instrumentation, vital for pursuing the low-background search. The requirement to understand and model the performance of this detector demands continuous knowledge of optical properties of LAr with a potentially time-varying impurity content.

In LEGEND-200, this is realized by LLAMA, an in-situ monitor of the light yield, effective triplet lifetime, and attenuation length at the LAr emission wavelength. LLAMA constitutes the main part of this dissertation work, which covers its lifecycle from the design phase up to the current stable operation in LEGEND-200. This also includes custom electronics, the DAQ, and the analysis of data acquired in LEGEND-200 and beyond. A technical overview of the design and functionality of LLAMA was already published in [1].

The first task of LLAMA in LEGEND-200 consisted of supervising the filling campaign, serving as the only quality monitor for the LAr at its final destination. Its discovery of a degrading LAr quality due to the filling of a nitrogen-contaminated LAr delivery caused the premature stop of the filling operations, preventing further contamination. On the plus side, the data taken around and during the nitrogen spoiling allowed modeling of the quenching effect of nitrogen in the sub-ppm range with unprecedented precision. This work extended the validity of current nitrogen quenching models to sub-ppm levels and provided a precise quenching rate constant of $k_{Q,\mathrm{N}_2} = (0.120 \pm 0.007)\ \mu\mathrm{s}^{-1}\,\mathrm{ppm}^{-1}$.

Further, a model for the time structure of the scintillation of very pure LAr was created based on data in LAr purified by LLArS before the spoiling. The data strongly favors the existence of an intermediate-lifetime component, whose presence and origin are currently debated in literature. LLAMA is the second experiment to measure this component while entirely avoiding critical instrumental effects potentially mimicking this component, thus strongly pointing towards a LAr effect. Separate publications on both the time structure of purified LAr scintillation and the impact of nitrogen contaminants are foreseen.

During the phase of frequent payload insertions in the scope of the LEGEND-200 commissioning, LLAMA data yields a slight degradation of the optical performance of LAr. Light yield quenching and absorption length reduction could be disentangled, which allowed spotlighting dry air, methane, and other hydrocarbons as possible causes while disfavoring pure nitrogen. Since December 2022, the LAr has been left undisturbed, which reflects in stable optical properties measured by LLAMA. The data allowed to constrain the concentration increases of several individual impurities (dry air, nitrogen, methane, water) in the ppb/yr level or below. A limit on the combined effect of the decrease in primary light yield and the absorption increase over a path length of 75 cm amounting to less than 10 % over 4 yr was placed. A planned publication will encompass both the impact of operations and the long-term stability of undisturbed LAr.

Apart from its application in the LEGEND-200 cryostat, LLAMA was used to conduct measurements in SCARF at TUM. During the xenon doping campaign in 2022, LLAMA measured the compression of the photon emission time spectrum and the large increase in attenuation length for increasing xenon concentration and confirmed the stability of the mixture. These properties are key for achieving a fast, uniform, and stable large-volume LAr-based detector. Part of the presented work was already published in [2].

In conclusion, LAr detectors profit from LLAMA (i) directly when employing it as a real-time monitor and warning system, and (ii) indirectly from the comprehensive knowledge gained about the behavior of LAr in various conditions. Notwithstanding the general applicability of LLAMA and its results, most of the work is done in view of LEGEND-1000.

The planned use of xenon-doped LAr in the outer LAr volume of LEGEND-1000 will boost the uniformity and general efficiency of the light collection. For the inner LAr volume, xenon doping is under consideration, and would improve the performance of the

LAr instrumentation, especially in conjunction with a likelihood-based anti-coincidence classifier. This can serve as a viable fallback if the anticipated UAr is unavailable.

The stable LAr quality of LEGEND-200 during data taking supports an on-demand purification strategy, in which LAr is purified in loop mode if optical properties deteriorate critically. Apart from its monitoring task during the filling and operation phases, LLAMA in LEGEND-1000 will indicate the demand for a re-purification. The experience in LEGEND-200 calls for retrievability of LLAMA, which can be achieved for the inner volume by integrating LLAMA into a dedicated string, while for the outer volume, this presumably requires a dedicated lock system.

To broaden the view on the topic of $0\nu\beta\beta$ decay, this dissertation contains a part about MONUMENT, which performs OMC to inform nuclear theory regarding $0\nu\beta\beta$ decay NMEs. ALPACA is one of both DAQ systems of MONUMENT, and its design, implementation, and operation are performed within the scope of this dissertation work. The offline processing approach and HPGe-driven trigger scheme contrast the current MIDAS-based system. While the energy resolution achieved with ALPACA is superior to the one with MIDAS and the time resolution proved sufficient, the high data rate strongly reducing ALPACA's livetime constitutes a major challenge. Nonetheless, ALPACA can be a valuable building block for future beam experiments, and possible actions tackling the livetime issue were discussed. A summary of the livetime analysis is part of the recently submitted MONUMENT Conceptual Paper [3].

References

[1] M. Schwarz, P. Krause, A. Leonhardt, *et al.*, "Liquid Argon Instrumentation and Monitoring in LEGEND-200," *EPJ Web Conf.*, vol. 253, p. 11 014, 2021. DOI: 10.1051/epjconf/202125311014.

[2] C. Vogl, M. Schwarz, X. Stribl, J. Grießing, P. Krause, and S. Schönert, "Scintillation and optical properties of xenon-doped liquid argon," *JINST*, vol. 17, no. 01, p. C01031, 2022. DOI: 10.1088/1748-0221/17/01/C01031. arXiv: 2112.07427 [physics.ins-det].

[3] G. R. Araujo *et al.*, "The MONUMENT Experiment: Ordinary Muon Capture studies for $0\nu\beta\beta$ decay," 2024. arXiv: 2404.12686 [nucl-ex].

Abbreviations

Particle physics, nuclear models and optics

$0\nu\beta\beta$	neutrinoless double beta
$2\nu\beta\beta$	two-neutrino double beta
$\beta\beta$	double beta
BSM	beyond-Standard-Model
CC	coupled-cluster
EDF	energy-density functional
IBM	interacting boson model
IM-GCM	in-medium generator coordinate method
NIR	near-infrared
NME	nuclear matrix element
NSM	nuclear shell model
OMC	ordinary muon capture
PE	photoelectron
PMNS	Pontecorvo–Maki–Nakagawa–Sakata
PPT	pulse per trigger
QRPA	quasiparticle random phase approximation
VS-IMSRG	valence-space formulation of the in-medium similarity renormalization group
VUV	vacuum-ultraviolet
WLS	wavelength-shifting

Experiments, devices, and detectors

BEGe	broad energy germanium
DAQ	data acquisition
HPGe	high-purity germanium

IC inverted coaxial

IDEFIX Impurity DEtector For Investigation of Xenon

LEGEND Large Enriched Germanium Experiment for Neutrinoless $\beta\beta$ Decay

LLAMA LEGEND Liquid Argon Monitoring Apparatus

LLArS LEGEND Liquid Argon purification System

LZ LUX-ZEPLIN

MONUMENT Muon Ordinary capture for the NUclear Matrix elemENTs

MS mini-shroud

PMT photomultiplier tube

PPC p-type point contact

SC slow control

SCARF Subterranean Cryogenic Argon Research Facility

SiPM silicon photomultiplier

TPC time-projection chamber

WLSR wavelength-shifting reflector

Electronics

DAC digital-to-analog converter

FADC flash analog-to-digital converter

FPGA field-programmable gate array

PCB printed circuit board

PSA power supply and amplification

RAM random-access memory

SMD surface-mounted device

Materials

AAr atmospheric argon

LAr liquid argon

LXe liquid xenon

PEN polyethylene naphthalate

PMMA poly(methyl methacrylate)

TPB tetraphenyl butadiene
UAr underground argon

Laboratories and institutions

LNGS Laboratori Nazionali del Gran Sasso
MPIK Max Planck Institut für Kernphysik
PSI Paul Scherrer Institut
SNOLAB Sudbury Neutrino Observatory Laboratory
TUM Technical University of Munich

Software and algorithms

ALPACA Adapted LLAMA Program for Accelerator Applications
DSP digital signal processing
GELATIO GERDA Layout for Input/Output
MaGe MAJORANA-GERDA
MGDO MAJORANA-GERDA Data Objects
MIDAS Maximum Integrated Data Acquisition System
PSD pulse-shape discrimination

Miscellaneous

C.L. confidence level
FWHM full width at half maximum
ICPMS inductively coupled plasma mass spectrometry
LET linear energy transfer
m.w.e. meter water equivalent
PDF probability density function
ROI region of interest

Appendix A

Notation of concentration quantities

A.1 Inconsistent and ambiguous notation of concentration in literature

Any study of trace amounts of substances diluted in LAr, either brought in via doping or contamination, requires a notation system for concentrations. Some past and current publications in this field are found to lack an unambiguous unit system, hampering comparisons.

Precisely, issues arise from the usage of the "parts-per" notation, e.g. ppm, ppb and ppt. They refer to the ratio between the amount of a trace substance and the total amount of the mixture. The central ambiguity refers to the dimension of the amount, for which typical choices are the number of molecules (mole) or the mass. By itself, the "parts-per" notation does not reveal the underlying choice of the dimension in use. In the case of e.g. xenon in argon, the values resulting from the by-mole and by-mass definition differ by more than a factor of three.

The unit is sometimes annotated with the used dimension to tackle this issue. For example, a "v" denotes volume fraction, and "m" usually denotes mass fraction. However, the letter "m" still leaves room for ambiguity because it is rarely used for mole fractions as well [1]. Also, using the volume fraction is inferior to the mole fraction, as the latter also stays meaningful in condensed phases [1]. Further, the appendage of labels to units is disfavored [1].

An additional minor ambiguity of the "parts-per" notation lies in the fact that the meaning of the terms billion and trillion deviate between Northern American and some European countries [1].

Literature in the field of LAr impurities and xenon doping use the "parts-per" notation predominantly and are thus often prone to creating ambiguities mentioned above. Only rarely and recently have publications started to be explicit about the used dimension of the amount of substance. In other cases, the dimension in use either remains unclear or has to be reverse-engineered, e.g. by studying the use of concentration in formulas (see formula (5.1) in [2]) or the equivalence of concentration and column density (see figure 3 in [3]).

Table A.1 compiles publications, separated by their definition of the amount of substance. Only some publications make their choice explicit (marked with ^{e}). The table shows that xenon doping studies (indicated with ^{x}) use either definition, while investigated works targeting other impurities use the per-mole definition only. Not included in the table is [4], since it uses the unit ppm both for mole fractions for quantities related to nitrogen impurities and for mass fractions for quantities of xenon impurities[1].

Table A.1: Literature about impurities in LAr, separated by their choice of the dimension (mole or mass) used to construct the impurity fraction quoted. Only publications marked with ^{e} explicitly clarify their choice. Additionally, works focusing on xenon doping are marked with ^{x}. *: [5] refers to results from [6], assuming that the latter quotes values using mass fraction. However, comparing the quenching rate published by [6] to the quoted triplet lifetime reduction yields that concentrations are presumably defined in mole fraction in [6].

mole fraction used	mass fraction used
[2]	[5]^{e,x,*}
[3]^{x}	[7]^{e,x}
[8]^{x}	[9]^{e,x}
[10]^{e}	[11]^{e,x}
[12]^{e}	
[13]^{x}	
[14]^{e}	
[6]^{x}	
[15]^{x}	

[1]The work misses a clear definition of the dimensions used, which have to be inferred from the ppmv / ppmm unit labels visible in the legend of only one plot.

A.2 Notation used in this work

This work uses the "parts-per" notation defined via the mole fraction. Explicitly, the units used here are expressed in terms of SI units as follows:

$$\text{ppm} = \mu\text{mol/mol} \quad \text{and} \quad \text{ppb} = \text{nmol/mol}. \tag{A.1}$$

This choice avoids the verbosity of the alternative SI units and benefits from the widespread prevalence of the "parts-per" notation in the field. Possible ambiguities are counteracted by explicit clarifications of the choice of the dimension in the introductions of relevant chapters.

The only exception to this practice is the quotation of xenon concentrations in chapter 11, for which SI units are used exclusively. This convention is due to the literature using either mass fraction or mole fraction in xenon doping while being restricted to mole fraction for all other trace contaminants. Xenon concentrations are frequently quoted both ways to facilitate comparisons to publications using either dimension. Mass fractions quoted in SI units then read e.g. μg/g and ng/g.

References

[1] S. E. Schwartz and P. Warneck, *Pure and Applied Chemistry*, vol. 67, no. 8-9, pp. 1377–1406, 1995. DOI: doi:10.1351/pac199567081377.

[2] J. Calvo *et al.*, "Measurement of the attenuation length of argon scintillation light in the ArDM LAr TPC," *Astropart. Phys.*, vol. 97, pp. 186–196, 2018. DOI: 10.1016/j.astropartphys.2017.11.009. arXiv: 1611.02481 [astro-ph.IM].

[3] A. Neumeier *et al.*, "Attenuation of vacuum ultraviolet light in pure and xenon-doped liquid argon —An approach to an assignment of the near-infrared emission from the mixture," *EPL*, vol. 111, no. 1, p. 12 001, 2015. DOI: 10.1209/0295-5075/111/12001. arXiv: 1511.07725 [physics.ins-det].

[4] J. Soto-Oton, "Impact of xenon doping in the scintillation light in a large liquid-argon TPC," in *5th International Conference on Technology and Instrumentation in Particle Physics*, 2021. arXiv: 2109.05858 [physics.ins-det].

[5] C. G. Wahl, E. P. Bernard, W. H. Lippincott, J. A. Nikkel, Y. Shin, and D. N. McKinsey, "Pulse-shape discrimination and energy resolution of a liquid-argon scintillator with xenon doping," *JINST*, vol. 9, P06013, 2014. DOI: 10.1088/1748-0221/9/06/P06013. arXiv: 1403.0525 [physics.ins-det].

[6] S. Kubota, M. Hishida, S. Himi, J. Suzuki, and J. Ruan, "The suppression of the slow component in xenon-doped liquid argon scintillation," *Nucl. Instrum. Meth. A*, vol. 327, no. 1, pp. 71–74, 1993, ISSN: 0168-9002. DOI: 10.1016/0168-9002(93)91413-H.

[7] D. Akimov *et al.*, "Fast component re-emission in Xe-doped liquid argon," *JINST*, vol. 14, no. 09, P09022, 2019. DOI: 10.1088/1748-0221/14/09/P09022. arXiv: 1906.00836 [physics.ins-det].

[8] D. Fields, R. Gibbons, M. Gold, N. McFadden, S. Elliott, and R. Massarczyk, "Understanding the enhancement of scintillation light in xenon-doped liquid argon," *Nucl. Instrum. Meth. A*, p. 167 707, 2022, ISSN: 0168-9002. DOI: 10.1016/j.nima.2022.167707.

[9] E. Segreto, "Properties of liquid argon scintillation light emission," *Phys. Rev. D*, vol. 103, no. 4, p. 043 001, 2021. DOI: 10.1103/PhysRevD.103.043001.

[10] R. Acciarri *et al.*, "Effects of Nitrogen contamination in liquid Argon," *JINST*, vol. 5, P06003, 2010. DOI: 10.1088/1748-0221/5/06/P06003. arXiv: 0804.1217 [nucl-ex].

[11] C. Vogl, M. Schwarz, X. Stribl, J. Grießing, P. Krause, and S. Schönert, "Scintillation and optical properties of xenon-doped liquid argon," *JINST*, vol. 17, no. 01, p. C01031, 2022. DOI: 10.1088/1748-0221/17/01/C01031.

[12] R. Acciarri *et al.*, "Oxygen contamination in liquid Argon: Combined effects on ionization electron charge and scintillation light," *JINST*, vol. 5, P05003, 2010. DOI: 10.1088/1748-0221/5/05/P05003. arXiv: 0804.1222 [nucl-ex].

[13] A. Buzulutskov, "Photon emission and atomic collision processes in two-phase argon doped with xenon and nitrogen," *EPL*, vol. 117, no. 3, p. 39 002, 2017. DOI: 10.1209/0295-5075/117/39002. arXiv: 1702.03612 [physics.ins-det].

[14] B. J. P. Jones *et al.*, "The Effects of Dissolved Methane upon Liquid Argon Scintillation Light," *JINST*, vol. 8, P12015, 2013. DOI: 10.1088/1748-0221/8/12/P12015. arXiv: 1308.3658 [physics.ins-det].

[15] A. Hitachi, "Photon-mediated and collisional processes in liquid rare gases," *Nucl. Instrum. Meth. A*, vol. 327, no. 1, pp. 11–14, 1993, ISSN: 0168-9002. DOI: 10.1016/0168-9002(93)91398-7.

Appendix B

Failing and restoring of channels

B.1 Chronology of the SiPMs' operational state

During the operation of LLAMA in the LEGEND-200 cryostat, several SiPMs ceased working; most were subsequently recovered. Figure B.1 displays the timeline of operational conditions for all individual SiPMs. The time frame shown extends from the beginning of LLAMA's data taking in the LEGEND-200 cryostat until the beginning of 2023; the conditions have not changed since. The y-axis shows the indices of the SiPMs, from which 1 to 3 are located inside the light source and the others are situated outside (see section 5.1 for details.). A horizontal line is thin and continuous if the particular SiPM works in this time frame, while the line is thick and dashed if the SiPM fails. Vertical teal lines show time points of recovery operations, which are discussed later.

The failures occurred over more than one year, with SiPM 7 ceasing to work already one week after LLAMA's data taking commenced. The last breakdown occurred in August 2022. In total, 10 out of 16 SiPMs showed failures, out of which 8 could be recovered by two hardware interventions. Two SiPMs could not be recovered and remain unusable.

B.2 Manifestation and diagnosis of failures

B.2.1 Distorted waveforms

All SiPM failures manifest themselves in extremely unstable waveforms recorded. Often, no physical pulses can be found within them, and the photoelectron spectrum generated from recorded data is extremely distorted. Since photoelectron spectra are used further

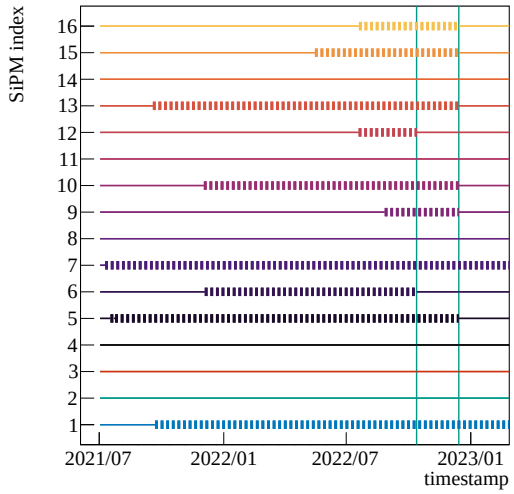

Figure B.1: Timeline of the operational state of all individual SiPMs of LLAMA in LEGEND-200. The y-axis shows the SiPMs' indices. Thin continuous lines denote SiPMs in working state, while thick dashed lines represent failing conditions. Recovery campaigns are indicated with teal vertical lines.

in the analysis[1], the malfunction becomes apparent also in high-level output. A system supervisor thus becomes aware of the problem and deactivates the supply voltage of the respective SiPM to prevent damage to it and the readout electronics, including the power supply.

Figure B.2 shows an example of such a distorted waveform (red), compared to a waveform recorded a few hours earlier in the same SiPM (blue), before its failure. Small-scale oscillations superimposed to the waveforms are noise-pickup and do not affect the functionality in any way. Conversely, the low-frequency and high-amplitude waveform distortions after the SiPM's breakdown render time and photoelectron count extractions impossible. The displayed example waveform was selected according to its successful recording - frequently, the signal exited the dynamic range of the FADC entirely.

The malfunction of SiPM 1 is peculiar, as it leads to a continuous light creation within the light source. This behavior is demonstrated using waveform recorded from the three source SiPMs, which are shown in figure B.3. The top panel shows a good event, recorded a few hours before the breakdown of SiPM 1. Detected photons follow the

[1]For example, for calculating the intensity of detected light.

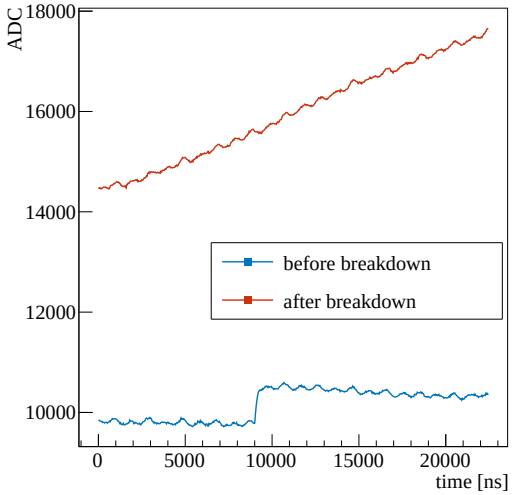

Figure B.2: Waveforms of SiPM 5 recorded just before (blue) and shortly after (red) its failure. The low-frequency distortion on the waveform after failure constitutes a primary symptom of the malfunction.

LAr scintillation time distribution. In contrast, an event recorded a few hours after the start of the malfunction (bottom panel) shows photons detected in SiPMs 2 and 3, which are not correlated to each other, i.e. indicate a continuous light emission. Also, SiPM 1 exhibits a distorted waveform with a very unstable baseline, and pulses, though visible, are too small in amplitude.

B.2.2 Hardware cause

The modular design of the readout electronics of LLAMA allows for narrowing down the source of the problem. The FADC, the PSA box, and the coaxial cables linking the latter to the connector on the cryostat's neck were excluded from causing the malfunctions by swapping channels. Hence, the problem is located on the connector at the cryostat's neck, the cables within the cryostat or LLAMA itself. Dedicated measurements conducted on the connector's socket revealed a reduced resistivity of the failing SiPMs compared to well-working channels. In operational conditions, reverse resistivity is typically larger than 100 MΩ. Some channels showed significantly less than 1 MΩ.

The loss in resistivity presumably leads to an excessive current load on the power

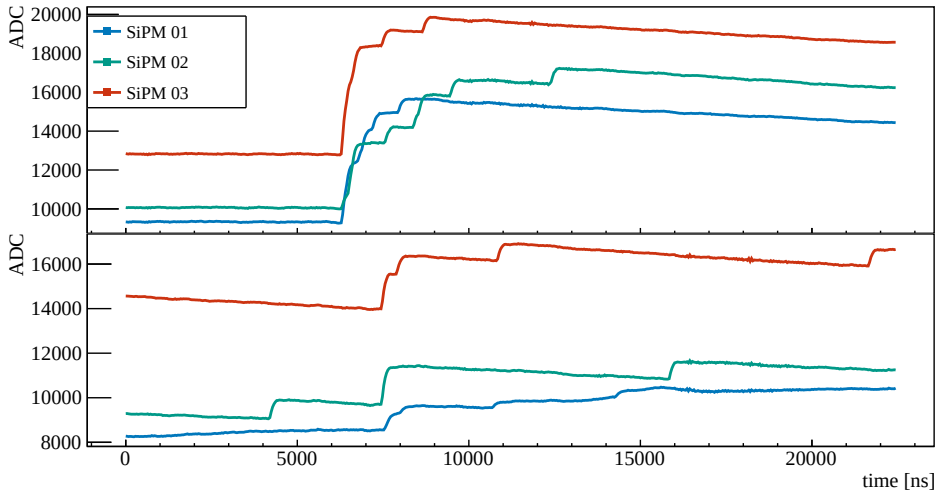

Figure B.3: Waveforms of source SiPMs recorded just before (top) and shortly after (bottom) the breakdown of SiPM 1. Its malfunction leads to permanent light emission within the source, leading to frequent detection of single photons by both other SiPMs.

supplies[2], which then produce ripples on the output voltage. As a further result, the bias voltage is decreased, leading to smaller or vanishing pulses emitted by the affected SiPMs. A shortcut between the signal/supply voltage line of SiPM 1 and the cable of the green LED might drive the LED, leading to the observed light output. Alternatively, damages or debris on the surface of SiPM 1 can lead to light emitted by its microcells, which is possible according to [2].

B.3 Recovery and prevention of malfunctions

Water condensation within the socket on the cryostat's neck was observed. While the surrounding metal parts of the neck and manifold are already cool, the bottom of the socket is especially cooled down due to the attached cables routed inside the cryostat acting as a thermal bridge. Drying the socket and the plug recovered only some SiPMs, yet the effect was transient.

A yet unidentified residue was observed on the rear wall of the socket. Figure B.4b

[2]They are rated for a maximum current output of 2 mA [1].

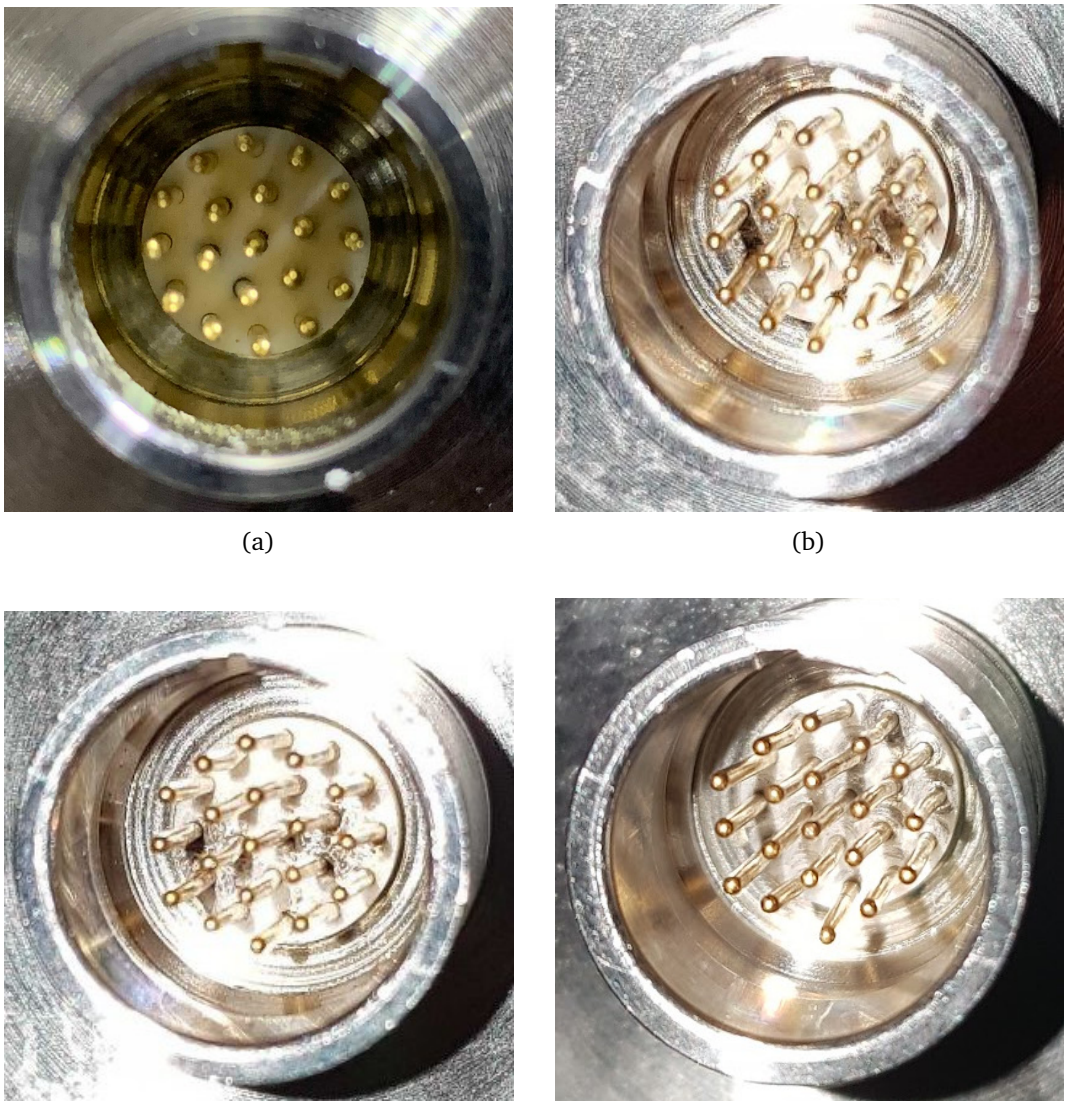

(a) (b)

(c) (d)

Figure B.4: Pictures of the connector's socket of LLAMA, which is located on the cryostat's neck. Several stages of degradation due to deposit on the rear wall are shown: in an initially clean state (a, image credit: S. Schönert), at peak amount of deposit (b), and after the 1st (c) and 2nd (d) cleaning operations.

shows the degraded socket, while figure B.4a depicts it in clean state. In an ad hoc operation on October 13th, 2022, the back wall was scratched with an ordinary wire;

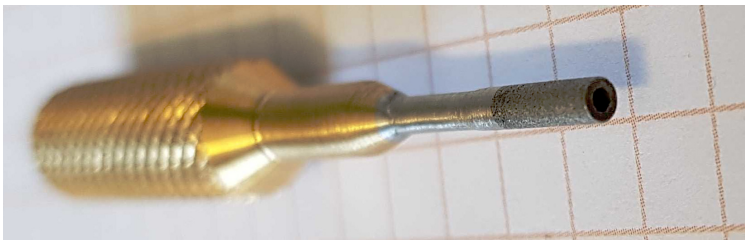

Figure B.5: Manual mechanical cleaning device featuring a diamond milling head at its tip. The milling head has been used since the 2nd cleaning campaign. Its hollow center fits over individual pins of the socket.

the result is shown in figure B.4c. Even though the 1st cleaning attempt was simple, it recovered two SiPMs and motivated the follow-up operation on December 6th, 2022.

The 2nd campaign involved a mechanical cleaning tool, whose tip is taken from a diamond[3] CNC milling head (see figure B.5). This type of milling head was used for machining the fused silica substrates employed in the liquid argon instrumentations of LEGEND-200 and GERDA [3]. Its dimensions, especially its hollow center[4] are essential for this operation since it fits over individual pins, allowing to scrape the back wall in a ring surrounding the pin. The 2nd cleaning campaign encompassed several hours of cleaning with that tool, combined with chemical treatments using oxide remover, electronics cleaners, and pressured air. The result is shown in figure B.4d.

Five SiPMs were recovered by the 2nd cleaning campaign; only two remained malfunctioning. The promising results of the 2nd cleaning campaign motivated two further attempts[5], which also involved the scraping tool. The last campaign employed a paste of sodium bicarbonate and isopropyl alcohol and rinsing with distilled water, accompanying the mechanical treatment. However, the last two campaigns neither improved nor deteriorated the situation. Thus, the reason for the malfunction of SiPMs 1 and 7 are regarded to be located within the cryostat, i.e. cannot be repaired within the runtime of LEGEND-200.

The deposit's buildup is expected to depend on the presence of liquid water in the socket. Galvanic or oxidization processes provide possible explanations. The permanently

[3] Diamond is regarded as a superior choice for scraping off even tough deposits. The Mohs hardness of diamond is 10, while the one for the aluminum oxide ceramics of the socket's back wall is 9.
[4] The milling head is hollow since it is operated water-cooled in its original purpose.
[5] These two cleaning campaigns were conducted by S. Schönert.

applied bias voltage of around 43 V can lead to the solvation of ions in the water. While the pins are gold-coated, the plug features soldered connections, providing non-noble metals.

Re-forming of the deposit is thus prevented via averting water condensation in the socket. To this end, the connector on the cryostat's neck was enclosed with a rubber sealing[6] and perpetually flushed with dry nitrogen gas. A permanent and stable nitrogen flux was established in December 2022, and LLAMA has been operating stably since.

B.4 Conclusions

The majority of LLAMA's SiPM channels failed during the operation in LEGEND-200. Deposit building up in the presence of water in the connector's socket was found to be responsible for all but two channels, and dedicated cleaning campaigns were successful. A nitrogen flush system prevents the deposit from regrowing, and LLAMA behaves stable since its permanent application.

In the future, systems similar to LLAMA should avoid water condensation in electrical connectors, e.g. by protruding the connector's location, weakening the heat-conducting effect of the cables within the cryostat. Also, the use of a larger connector and the selection of a location that is more easy to reach would ease maintenance. LLAMA's socket has a diameter of only 15 mm and is located in a spot that is hard to reach and has a partially obstructed line of sight.

The unsuccessful recovery of SiPMs 1 and 7 hints at defects located within the cryostat, which cannot be repaired without draining the cryostat, i.e. far beyond any feasibility during the runtime of LEGEND-200. This stresses the importance of keeping all parts of long-term operating devices accessible. For example, liquid argon monitoring devices planned to be employed in the UAr volume of LEGEND-1000 should be integrated into recoverable strings. In the AAr cryostat, a LLAMA-like device would presumably require a dedicated lock to be recoverable in cases of malfunctions.

On the topic of LLAMA's current operation, the persistent failure of SiPM 1 is critical since it is located within the triggered light source. Thus, it renders event selection based on both localization of scintillation events impossible and severely hampers the selection

[6] The rubber sealing was installed by P. Krause.

based on the sum of photon hits in the source (see section 5.4.1). While the cut condition on the localization of the scintillation event is removed entirely, the accepted region of the sum of photon hits was widened to $4.5 - 25$ PE. Nevertheless, LLAMA provides high-quality and vital data even after the failure of SiPMs 1 and 7 (see e.g. chapter 7), demonstrating LLAMA's capability in compensating the loss of channels.

References

[1] "Power supply for MPPC," [Online]. Available: https://www.hamamatsu.com/eu/en/product/optical-sensors/mppc/power-supply_driver-circuit/C14156.html.

[2] J. B. McLaughlin *et al.*, "Characterisation of SiPM Photon Emission in the Dark," *Sensors*, vol. 21, no. 17, 2021, ISSN: 1424-8220. DOI: 10.3390/s21175947.

[3] P. Krause, "The New Liquid Argon Veto of GERDA," *Master's thesis, TUM*, 2019.

Appendix C

Benchmarking absorption models against LEGEND-200 data

In chapter 8, it became clear that the attenuation curves measured by LLAMA in LEGEND-200 cannot be explained without additional inputs. Two possible models are derived from LLAMA data:

- Using only peripheral SiPMs in distances up to 30 cm, the attenuaion can be described with a single attenuaion length $l_{att} = (33.0 \pm 1.3)\,\text{cm}$. Using a Rayleigh scattering length of $l_{scat} = 90\,\text{cm}$, the Beer-Lambert-Law yields an absorption length of around $l_{abs} = 52\,\text{cm}$.
- A generic wavelength-dependent absorption length modeled as a step-function fits the data for all distances, providing the following parameters (see section 8.4.3):

$$l_{abs,s} = 5.6\,\text{cm},\ l_{abs,l} = 1000\,\text{cm},\ \lambda_{ths} = 133\,\text{nm}. \tag{C.1}$$

Data from the LAr instrumentation in LEGEND-200 can provide a benchmark for discriminating between both models. Precisely, spacial inhomogeneities in the photodetection efficiencies of the LAr instrumentation are probed by ^{39}Ar decays acting as an isotropic volume-distributed calibration source. These data were measured during the 60 kg phase of LEGEND-200.

The simulation of these data uses optical maps, which quantify the photodetection efficiencies within the LAr volume granularized in cubic voxels[1]. Maps are generated

[1] The voxel size of 3D maps was set to $(20\,\text{mm})^3$ for the region outside of the outer barrel and to $(10\,\text{mm})^3$ within. The shown map slices were generated using $(10\,\text{mm})^3$ voxels.

using each absorption length model using the current implementation of the LEGEND-200 geometry in MaGe. The efficiencies of the inner and outer barrels are stored in separate maps. This is done to facilitate comparisons with measurement data, in which a distinction between both barrels is possible.

Figure C.1 shows horizontal slices of optical maps for the single absorption length model. Both fiber barrels show a different efficiency distribution: The outer barrel (a) has a medium efficiency over a large part of the LAr volume, especially in the region between itself and the WLSR at $r = 700\,\text{mm}$. Conversely, the inner barrel has a low efficiency in this region while featuring a very high efficiency in the space within its radius.

The two-component model shown in figure C.2 does not show the same behavior since the inner barrel does not have a high-efficiency region.

Figure C.3 shows PE spectra summed over both barrels individually and in an event-by-event basis for simulated ^{39}Ar decays. For the simulation, a primary light yield of 40 PE/keV and a SiPM photodetection efficiency of 30 % are assumed. The spectra reflect the features of the optical maps discussed previously.

A comparison to measurement data shown in figure C.4 yields a much better agreement with the single absorption length model than the two-component model.

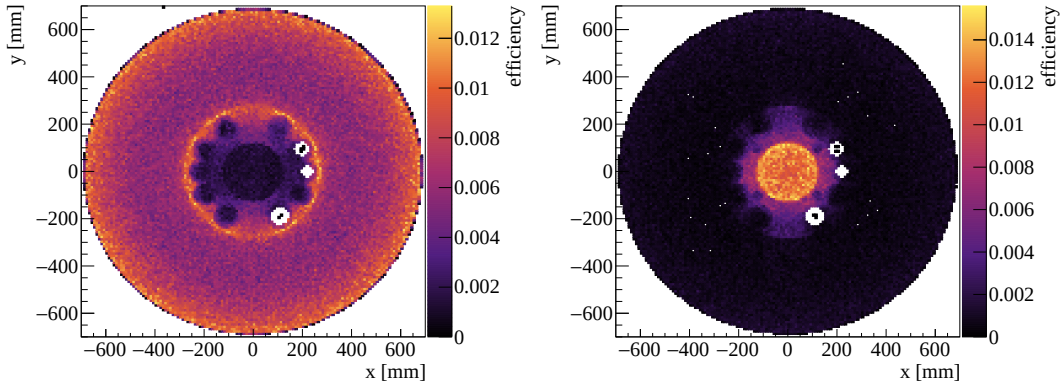

(a) (b)

Figure C.1: Slice of an optical map in XY-direction at a medium height. The optical map was produced with the MaGe framework implementing an absorption length of $l_{abs} = 52\,\text{cm}$ for LAr scintillation photons. The values correspond to the local photodetection efficiencies of the outer (a) and inner barrel (b), respectively.

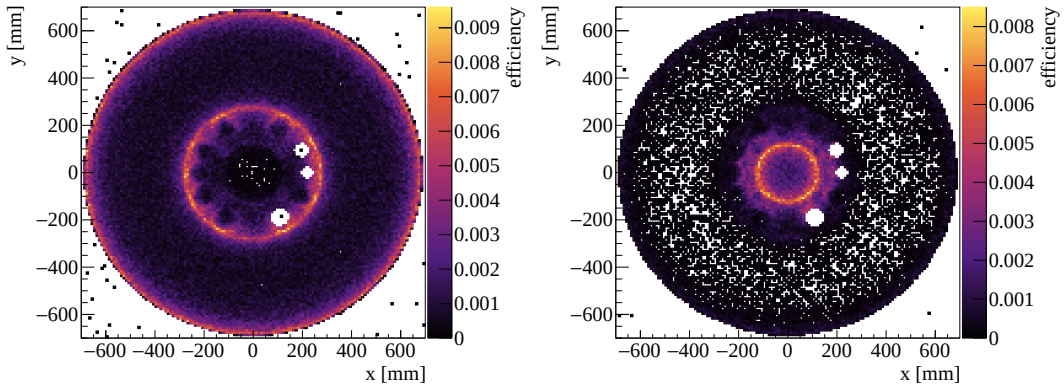

(a) (b)

Figure C.2: Slice of an optical map in XY-direction at a medium height. The optical map was produced with the MaGe framework implementing the two-absorption-length model (see text) for LAr scintillation photons. The values correspond to the local photodetection efficiencies of the outer (a) and inner barrel (b), respectively.

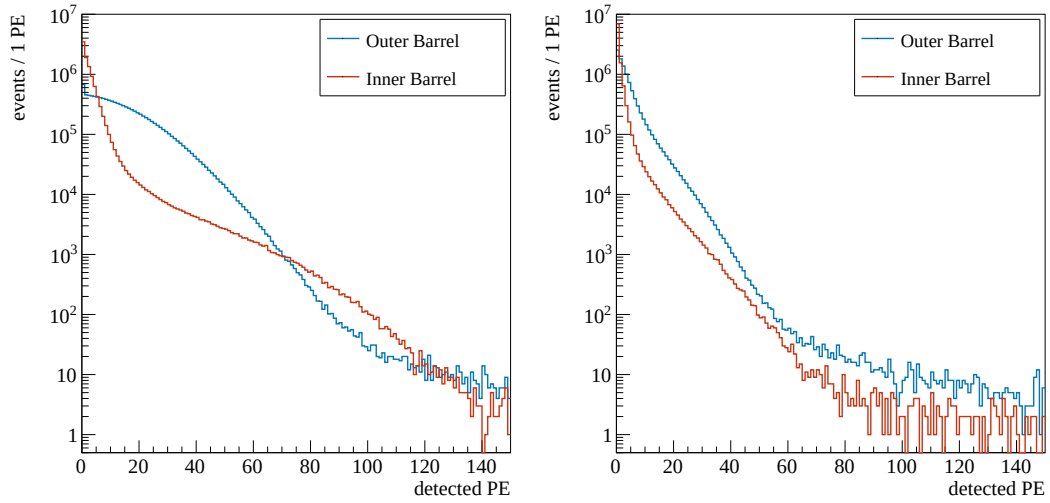

(a) (b)

Figure C.3: Simulated PE spectra summed over the outer and inner barrel, respectively. The light emissions are caused by ^{39}Ar events throughout the LAr volume. The optical models used assume a LAr absorption length of $l_{abs} = 52\,\text{cm}$ (a) and a two-component-model (b).

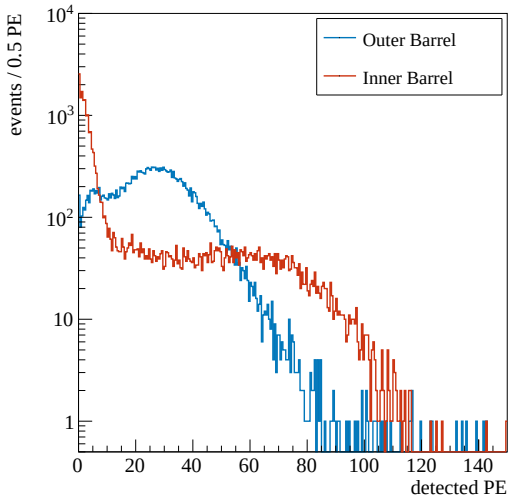

Figure C.4: Measured PE spectra summed over the outer and inner barrel, respectively. Spectra are obtained during the 60 kg phase of LEGEND-200 and are dominated by ^{39}Ar events. Data provided by P. Krause.

Acknowledgments

Finally, I want to thank everyone who, in various ways, contributed to the projects covered in this dissertation and supported me throughout the years.

I am deeply grateful to my supervisor, Stefan Schönert, for his guidance and invaluable input during my entire time in his group. Further, I want to thank also the other members of the review committee: I thank Béla Majorovits for being the second corrector, and Alejandro Ibarra for chairing my defense.

My next big *thank you* goes to the LLAMA team, without whom this project would not be possible: Patrick Krause, for all the fruitful discussions about SiPMs, liquid argon, and cryostats; Laszlo Papp, for all his efforts designing the instrument and helping with the electronics; and Stefan Schönert for his inputs on all stages of the project including the analysis. Many thanks go to the E15 workshop, especially to Harald Hess, Lukas Hein, and Georg Lerchl, for producing LLAMA's parts with amazing precision. Further thanks go to the Physics Department's electronics workshop for their valuable suggestions and for kindly providing their facilities. Thanks also to Christoph Vogl for all the projects we have worked on together, especially xenon doping and the LEGEND-200 cryostat filling campaign. I want to express my gratitude to all members of the GERDA and LEGEND collaborations for our enjoyable time together.

Many thanks go to the members of the MONUMENT collaboration, whom I met during the two nice and exciting beam times I took part in. Special thanks here to Eli Mondragón and Elisabetta Bossio for sharing most shifts and all the useful discussions we had.

My heartfelt thanks go to my colleagues from E15 (past and present), and especially to the GERDA/LEGEND subgroup: Elisabetta, Tommaso, Rosanna, Konstantin G., David, Patrick, Andi, Eli, Moritz, Luigi, Nadya, Christoph V., and Christoph W. I thank you all so much for the nice time at work and beyond!

Ich will mich sehr herzlich bei meiner Familie bedanken, für all die unglaubliche Unterstützung über Studium und Promotion. Zu guter Letzt geht ein ganz großes Dankeschön an Sandra, deren großartige und unermüdliche Hilfe mich durch die finale Phase meiner Promotion gebracht hat.